Photon-Photon processes at the International Linear Collider and BSM signatures with small mass differences

Dissertation

with the aim of achieving a doctoral degree

at the Faculty of Mathematics, Informatics and Natural Sciences

Department of Physics

of Universität Hamburg

submitted by

Kollassery Swathi Sasikumar

aus Indien

Hamburg

2020

Gutachter der Dissertation:	Dr. Jenny List Prof. Dr. Gudrid Moortgat-Pick
Zusammensetzung der Prüfungskommission:	Dr. Jenny List Prof. Dr. Gudrid Moortgat-Pick Prof. Dr. Kerstin Tackmann Prof. Dr. Dieter Horns Dr. Christian Sanders
Datum der Disputation:	25.09.2020
Vorsitzender Prüfungskommission:	Prof. Dr. Dieter Horns

To My Teachers

Abstract

The International Linear Collider is a proposed e^+e^- collider with tunable centre-of-mass energies and polarised beams. By performing high-precision measurements of Standard Model observables and searches for new particles the ILC can serve as a complementary machine to the LHC.

In supersymmetric extensions of the Standard Model, higgsino-like charginos and neutralinos are preferred to have masses of the order of the electroweak scale by naturalness arguments. Such light $\tilde{\chi}_1^{\pm}$, $\tilde{\chi}_1^0$ and $\tilde{\chi}_2^0$ states can be almost mass degenerate. Due to their mass degeneracy it is very difficult to observe the decay of such higgsinos at hadron colliders. ILC being an e^+e^- collider has the prospect of providing a very clean physics environment to observe or exclude such scenarios. However, in addition to the desired $e^+e^- \to \tilde{\chi}^+\tilde{\chi}^-$ processes, parasitic collisions of real and virtual photons radiated off the e^+e^- beams occur at the rates depending on the centre-of-mass energy (250 GeV - 1 TeV) and other beam parameters. In this thesis the effects of such $\gamma\gamma \to$ low p_T hadron overlay on the low ΔM higgsino analysis is studied. The study considers two benchmark points which exhibits mass differences of $\mathcal{O}$ [1 GeV] in the higgsino sector. In the given higgsino scenarios, the visible decay products have low transverse momenta due to the small mass differences between the higgsinos. The $\gamma\gamma \to$ low p_T hadron overlay has a very similar topology to the signal event which makes the removal of the overlay very challenging. The standard methods to remove $\gamma\gamma$ background, e.g methods based on jet clustering remain inadequate. The study presents a newly developed track grouping algorithm which is based on the concept of displaced signal and $\gamma\gamma \to$ low p_T hadron overlay vertices.

By applying the track grouping algorithm to separate $\gamma\gamma \to$ low p_T hadron tracks from the the higgsino decay tracks, an analysis has been performed using the full detector simulation for the International Large Detector (ILD). It is shown that the group tracking algorithm can very efficiently separate $\gamma\gamma \to$ low p_T hadron tracks from the the higgsino decay tracks. The results from the analysis show that even with the presence of $\gamma\gamma \to$ low p_T hadron overlay, the key observables of the higgsinos can be reconstructed with an uncertainity of a few percent. A comparison with the previous study which was performed without the inclusion of $\gamma\gamma \to$ low p_T hadron events is made to enhance the understanding about the effects of the overlay on the higgsino analysis.

Zusammenfassung

Der International Linear Collider ist ein geplanter e^+e^--Collider mit abstimmbaren Schwerpunktenergien und polarisierten Strahlen. Durch die Durchführung hochpräziser Messungen von Observablen des Standardmodells und die Suche nach neuen Teilchen kann der ILC als Komplementärmaschine zum LHC dienen.

Aus Gründen der Natürlichkeit werden in supersymmetrischen Erweiterungen des Standardmodells higgsinoartige Charginos und Neutralinos mit Massen in der Größenordnung der elektroschwachen Skala bevorzugt. Solche leichten $\tilde{\chi}_1^\pm$-, $\tilde{\chi}_1^0$- und $\tilde{\chi}_2^0$-Zustände können annähernd degeneriert bezüglich der Masse sein. Aufgrund dieser Tatsache ist es äußerst schwierig, den Zerfall solcher Higgsinos in Hadronen-Collidern zu beobachten. Da der ILC ein e^+e^--Collider ist, besteht die Möglichkeit, dass er eine sehr saubere Umgebung schafft, um solche Szenarios zu beobachten oder auszuschließen. Allerdings treten zusätzlich zu den erwünschten $e^+e^- \to \tilde{\chi}^+\tilde{\chi}^-$-Prozessen parasitäre Kollisionen der von den e^+e^--Strahlen abgestrahlten realen und virtuellen Photonen auf, wobei deren Reaktionsraten von der Schwerpunktenergie (250 GeV - 1 TeV) und von anderen Strahlparametern abhängen. In der hier vorgelegten Arbeit werden die Auswirkungen eines solchen $\gamma\gamma \to$ *Hadronen mit niedrigem* p_T-Overlays auf die Analyse von Higgsinos mit niedrigem ΔM untersucht. Im Rahmen dieser Untersuchung werden zwei Referenzpunkte betrachtet, welche Massendifferenzen der Größenordnung $\mathcal{O}$ [1 GeV] im Higgsino-Sektor aufweisen. In den gegebenen Higgsino-Szenarien haben die sichtbaren Zerfallsprodukte niedrige Transversalimpulse aufgrund der geringen Massendifferenz zwischen den Higgsinos. Die Topologie des $\gamma\gamma \to$ *Hadronen mit niedrigem* p_T-Overlays ist der des Signalereignisses sehr ähnlich, was die Beseitigung des Overlays äußerst schwierig macht. Die Standardmethoden zur Beseitigung des $\gamma\gamma$-Hintergrunds, z.B. Verfahren, die auf dem Jet-Clustering basieren, sind dabei unzureichend. Die hier vorgestellte Untersuchung führt einen neuen Spurgruppierungsalgorithmus ein, der vom Konzept der verschobenen Signal- und $\gamma\gamma \to$ *Hadronen mit niedrigem* p_T-Overlay-Vertices Gebrauch macht.

Die Nutzung des Spurgruppierungsalgorithmus zur Trennung der $\gamma\gamma \to$ *Hadronen mit niedrigem* p_T-Spuren von den Higgsino-Zerfallspuren bildete das Herzstück einer Analyse, welche die vollständigen Detektorsimulation für den International Large Detector (ILD) beinhaltete. Es wird dargelegt, dass der Spurgruppierungsalgorithmus sehr effizient $\gamma\gamma \to$ *Hadronen mit niedrigem* p_T-Spuren von den Higgsino-

Zerfallspuren trennen kann. Die Ergebnisse der Analyse zeigen, dass die Schlüsselobservablen der Higgsinos sogar beim Vorliegen eines $\gamma\gamma \rightarrow$ *Hadronen mit niedrigem* p_T-Overlays mit einer Unsicherheit von wenigen Prozent rekonstruiert werden können. Ein abschließender Vergleich mit einer vorherigen Studie, welche ohne Betrachtung der $\gamma\gamma \rightarrow$ *Hadronen mit niedrigem* p_T-Ereignisse durchgeführt wurde, dient der Verbesserung des Verständnisses der Auswirkung des Overlays auf die Higgsino-Analyse.

Contents

1. Introduction

Being in a wonderfully complex universe, it is our privilege to live in a time where enormous progress has been made towards finding answers to some unsolved mysteries of the universe. The description of our universe at a very fundamental level is the main topic of particle physics.

The Standard Model (SM) of particle physics serves as the best description of the fundamental forces and elementary particles of our universe as we perceive it today. Many of the studies which shape our understanding of the universe are carried out at high energy facilities like the particle colliders. The discovery of a Higgs boson at the CERN's Large Hadron Collider in 2012 [1] could be a portal to phenomena beyond the Standard Model which addresses the hierarchy problem and other short comings of the Standard Model. One possibility for such an extension of the Standard Model is supersymmetry (SUSY) [2]. It suppresses the quadratic divergence arising from the radiative contributions to the mass of Higgs boson due to its interaction with other particles by introducing a superpartner for every SM particle with a difference of spin by half a unit. With this it is possible to obtain the Higgs boson mass without introducing a large amout of fine tuning.

A wide range of searches for physics beyond the Standard Model is being carried out at the Large Hadron Collider. However, no supersymmetric particles or any hints for them have been found at any LHC experiments. Especially looking at stops (supersymmetric partner of the top quark) which have a significant contribution to Higgs mass due to their large Yukawa coupling, and gluinos, one can conclude that coloured spectrum of the SUSY should be rather heavy at least around the TeV scale. Nevertheless, it is possible to obtain a light electroweak SUSY sector as required by the naturalness of the Z boson along with a SM-like Higgs boson having mass consistent with that of LHC measurement.

A central feature of such natural SUSY models is that the lightest SUSY particles are the SUSY partners of the Higgs, which tend to be nearly mass degenerate if all other SUSY particles are heavy [3–5]. Such naturally mass degenerate light higgsinos have been studied in this thesis. Assuming all the other SUSY particles being heavy, the mass splittings of the higgsino-like charginos and neutralinos ($\tilde{\chi}_1^{\pm}, \tilde{\chi}_1^0$ and $\tilde{\chi}_2^0$) can be as small as a few GeV or less. Such mass degenerate higgsinos have very soft final state particles and a large missing energy as signature. Analysis of such scenarios would be quite challenging at hadron colliders like the LHC.

Analysing light higgsinos at an e^+e^- collider has certain benefits as mentioned ahead. An e^+e^- collider like the International Linear Collider (ILC) provides a very clean physics environment to observe such scenarios. This makes the measurement of even very low p_T particles possible. The ILC has a very well-determined intial energy for the beam particles. In addition, the polarized e^- and e^+ beams turn out to be very beneficial in the search of new physics especially by suppressing the SM background. All these features of the ILC form the main motivation to study such mass degenerate particles at this collider. Such a higgsino analysis was performed in [6, 7], where the events were simulated using a fast detector simulation. However, at e^+e^- colliders like the ILC, there are a few important groups of background processes. The real and virtual photons radiated off the e^+e^- beams collide to produce low p_T hadronic final state particles alongside the desired physics processes. In the higgsino scenarios studied in this thesis, visible decay products have low transverse momentum due to their small mass differences. Due to their similar natures it is quite challenging to separate the signal from the so called $\gamma\gamma$ overlay. The standard jet clustering methods to remove $\gamma\gamma$ background remains inadequate in this case. The study performed in [6, 7] did not include these $\gamma\gamma \rightarrow$ low p_T hadron backgrounds.

The study presented in this thesis is an analysis of such higgsino scenarios with the inclusion of $\gamma\gamma \rightarrow$ low p_T hadron backgrounds. Here, an alternative method for the removal of the $\gamma\gamma$ backgrounds is proposed. This work is based on a full detector simulation of the ILD concept at a centre-of-mass energy of 500 GeV. In the first part of this work, a detailed study on $\gamma\gamma \rightarrow$ low p_T hadron background events has been performed. It mainly discusses the need of a reliable simulation of the detailed properties of $\gamma\gamma$ events and the possibilities of a generator producing more realistic $\gamma\gamma$ events. The second part of the study is dedicated towards the development of an alternative method to remove the $\gamma\gamma$ background. Using a $e^+e^- \rightarrow \tilde{\chi}_1^+\tilde{\chi}_1^-\gamma$ sample overlaid with $\gamma\gamma \rightarrow$ low p_T hadron background a new track grouping algorithm is developed based on the concept of displaced vertices. The algorithm identifies and clusters the tracks from the same origin. The performance of the algorithm is studied through purity checks of the clustered tracks. The final part of the study is focused on the investigation of a supersymmetric scenario by using the algorithm developed to select signal decay tracks among the $\gamma\gamma$ background tracks. The analysis is performed along with an entire set of the possible SM and SUSY backgrounds.

This thesis is structured as follows: The theoretical concepts of the Standard Model and supersymmetry on which this entire study is based on is presented in Chapter 2. Chapter 3 gives an overview of the International Linear Collider with respect to its machine details and its advantages over hadron and circular colliders. The main two experiments of the ILC named the International Large detector (ILD) and the Silicon detector (SiD) are introduced in Chapter 4. Since the study in this

thesis is based on the simulation in ILD, a focus is mainly given on the details of the ILD and its software and simulation setups.

In Chapter 5 the setup of event generation is presented. Events generated by different generators are compared and improvements are implemented to obtain more reliable event generators for $\gamma\gamma \rightarrow$ low p_T hadron events. Details about the supersymmetric scenario considered for this study and the Standard Model backgrounds are discussed in Chapter 6. Chapter 7 presents the development and performance of a track grouping algorithm used to remove $\gamma\gamma$ background. A detailed analysis of the light higgsinos along with the full set of SM backgrounds is presented in Chapter 8. It also includes the application of the track grouping algorithm to remove the $\gamma\gamma$ background tracks from among the signal decay tracks. The chapter compares the obtained results with the previous studies [6, 7] and evaluates the performance of the track grouping algorithm for such studies. The thesis outcome is summarized in Chapter 9.

2. Theoretical Concepts

In particle physics, our understanding about the fundamental building blocks of nature and their interactions is formulated in the Standard Model of particle physics. Since its first formulation [8–10] in 1961, the theory has withstood various experimental tests, forming one of the most successful descriptions of nature. However, despite its glory, it has been evident over the years that the description provided by the Standard Model is not complete. This chapter gives an overview of the Standard Model of Particle physics. After summarizing the shortcomings of the Standard Model, the theory of supersymmetry is introduced as a potential solution. The specific models studied in this thesis and their phenomenology at e^+e^- colliders are reviewed in the last section of this chapter.

2.1. The elementary particles in the Standard Model of Particle Physics

The Standard Model of particle physics is a theory describing the fundamental particles and their interactions. In the Standard Model the elementary particles are considered to be point-like objects without any substructure. These particles are distinguished based on intrinsic properties like for instance their spin. The spin is an instrinsic form of angular momentum carried by all particles. Spin of a particle is expressed as a positive integer multiple of 1/2. The particles having a half-integer spin (e.g. $\frac{1}{2}, \frac{3}{2}$) are called as fermions and the particles with integer spins such as 0,1,2 etc.are termed as bosons. The interactions between these particles are the electromagnetic force, the weak force and the strong force. The gravitational force is explained in Einstein's theory of General Relativity and the existence of the gravitational waves was confirmed by the LIGO collaboration [11]. However, since the formulation of the gravitational force is completely different than that of the quantum field theories, it is not included in the theory of Standard Model.

The fermions are further separated into two different categories known as leptons and quarks. There are three different generations of fermions and every generation has two kinds of leptons and quarks. The quarks are categorised as up-type and down-type quarks while leptons are categorised as charged leptons and neutrinos. The generations mainly differ in terms of their masses. Besides, every fermion shown

in table 2.1 has an anti-particle with the same mass but opposite quantum additive numbers.

Fermions	Generation	Particle	Mass	Charge	Spin
Leptons	I	e neutrino: ν_e	$<$2.2 eV	0	1/2
		electron: e	0.51 MeV	-1	1/2
	II	μ neutrino: ν_μ	$<$1.7 MeV	0	1/2
		muon: μ	105.66 MeV	-1	1/2
	III	τ neutrino: ν_τ	$<$15.5 MeV	0	1/2
		tau: τ	1.78 GeV	-1	1/2
Quarks	I	up: u	2.2 MeV	2/3	1/2
		down: d	4.7 MeV	-1/3	1/2
	II	charm: c	1.28 GeV	2/3	1/2
		strange: s	96 MeV	-1/3	1/2
	III	top: t	173.5 GeV	2/3	1/2
		bottom: b	4.18 GeV	-1/3	1/2

Table 2.1.: Overview of fermions in the Standard Model. Every particle has an anti-particle with opposite charge generally denoted with a bar. The particle masses are taken from [12].

Another important nature of fermions is known as chirality. The manner in which the quantum mechanical wave function of a particle would behave is determined by this Lorentz-invariant property. Chirality has two eigen states known as *right-handedness* and *left-handedness*. Except the neutrinos all the SM fermions have been observed in both the chirality states. However, the oscillations of neutrinos predict the existence of right-handed neutrinos.

The fundamental forces like the electromagnetic force, the weak force and the strong force are mediated through bosons. The weak interaction has three mediators which are two charged $W^{\pm}$ bosons and an electrically neutral Z boson. These bosons couple to all the fermions as well as to each other. The photon is the carrier of the electromagnetic force. It couples to every particle that has an electric charge even though the photon itself is electrically neutral. The strong interaction has eight force mediators called as gluons. Gluons carry a unique charge of the strong interaction which is called as *colour*. The theoretical formulations of electromagnetic and weak interactions were unified by S. L Glashow [8], S. Weinberg [9] and A. Salam [10]. The theoretical description of strong force was later added to it by Fritzsch, Gell-Mann and Leutwyler [13] in the theory of quantum chromodynamics (QCD).

Interaction	Particle Name	Mass	Charge	Spin
Weak	$W^{\pm}$	80.39 GeV	± 1	1
	Z^0	91.19 GeV	0	1
Electromagnetic	photon: γ	0	0	1
Strong	8 gluons: g	0	0	1

Table 2.2.: The properties of SM force mediating bosons. The boson masses are taken from [12].

2.2. The principle of gauge theory

One of the basic principles the Standard Model is based on is the concept of gauge theory. The Standard Model of particle physics is a quantum field theory in which the elementary particles are formulated as quantum fields in the space-time. One of the basic requirements for the Standard Model theory is the gauge invariance under local symmetry. The discussion in this section mainly follows [14, 15].

2.2.1. The formalism of Quantum Electrodynamics (QED)

The dynamics and interactions of the quantum fields of elementary particles can be described by its *Lagrangian density*, $\mathcal{L}$. The Dirac Lagrangian of a fermion (electron) can be described as

$$\mathcal{L}_{\mathcal{D}} = i\overline{\psi}(x)\gamma^{\mu}\partial_{\mu}\psi(x) - m\overline{\psi}(x)\psi(x) \tag{2.1}$$

where $\psi(x)$ is the electron field, expressed as a four-component Dirac spinor, γ^{μ} are the Dirac matrices and m is the electron mass. Under the global gauge transformation, $\psi \rightarrow e^{i\theta}\psi$, the Dirac Lagrangian $\mathcal{L}_{\mathcal{D}}$ remains invariant. However, under local gauge transformation, i.e. $\psi \rightarrow e^{i\theta(x)}\psi$, the phase θ becomes a function of space and time, and the Lagrangian is modified. To keep the Lagrangian invariant under local transformation, a new field A_{μ} is introduced and the standard derivative ∂_{μ} is replaced with the (gauge invariant) covariant derivative:

$$\partial_{\mu} \rightarrow D_{\mu} = \partial_{\mu} - ieA_{\mu}. \tag{2.2}$$

The condition for the newly obtained Lagrangian, $\mathcal{L}_{QED}$, to be invariant under the local gauge transformation is that the mass term corresponding to the field A_{μ}, (i.e. $\frac{1}{2}m_{\gamma}^2 A_{\mu}A^{\mu}$) should be zero. For every other case, the local gauge invariance of the Lagrangian would be broken. The vector field $A_{\mu}(x)$ transforms under the gauge transformation as:

$$A_{\mu} \rightarrow A'_{\mu} + \frac{1}{e}\partial_{\mu}\theta(x) \tag{2.3}$$

The additional term in the Lagrangian describes the interaction between the gauge field and the fermions. As the mass term of A_μ has to be zero, the field can be interpreted as the electromagnetic potential and associated with the massless gauge particle photon (mediator of electrodynamics) where e is the coupling strength corresponding to the charge of the electron. The quantum electrodynamics Lagrangian also requires the kinematic term of the new field A_μ given as :

$$-\frac{1}{4}F_{\mu\nu}F^{\mu\nu} \tag{2.4}$$

which is expressed as $F_{\mu\nu} = \partial_\mu A_\nu - \partial_\nu A_\mu$. The complete Lagrangian for quantum electrodynamics can thus be expressed as :

$$\mathcal{L}_{QED} = \underbrace{i\overline{\psi}\gamma^\mu\partial_\mu\psi}_{\text{kinetic term fermion}} - \underbrace{m\overline{\psi}\psi}_{\text{mass term fermion}} - \underbrace{e\overline{\psi}\gamma^\mu A_\mu\psi}_{\text{interaction term}} - \underbrace{\frac{1}{4}F_{\mu\nu}F^{\mu\nu}}_{\text{kinetic term photon}} \tag{2.5}$$

2.2.2. Gauge structure of the Standard Model

All the particle interactions in the Standard Model are described by local gauge theories with an underlying symmetry. The fact that the local gauge transformation with respect to a certain symmetry should preserve the invariance of the Lagrangian naturally generates interactions between fermions and gauge bosons. According to Noether's theorem [16], every continuous symmetry is associated with the conservation of a quantity and hence also the symmetry of QED leads to a conserved quantum number, namely the electric charge.

The mathematical description of symmetries in the Standard Model are represented in the form of gauge groups. The *Unitary* group, $U(n)$, with unitary $n \times n$ matrices and *Special Unitary* group, $SU(n)$, with unitary $n \times n$ matrices with determinant 1 are used for this purpose.

The gauge structure of the Standard Model is given as

$$SU(3)_C \otimes SU(2)_L \otimes U(1)_Y \tag{2.6}$$

where $U(1)$ represents gauge group for quantum electrodynamics, $SU(2)$ is the gauge group for weak interactions and $SU(3)$ is the symmetry group for strong interactions.

2.2.3. The Standard Model Lagrangian

The Standard Model Lagrangian of the Standard Model given a description of the dynamics of how the elementary particles, expressed as fields, evolve in space-time and the manner in which they interact. The Standard Model Lagrangian comprises of (i) kinematic and self-coupling terms of the fermions and the gauge boson fields

(ii) coupling terms describing the interactions between gauge fields and fermions (iii) mass terms which are addressed in section ahead. The most relevant part of the $\mathcal{L}_{SM}$ is the one with kinematic and self-coupling terms expressed as:

$$\mathcal{L}_{kin} = \underbrace{-\frac{1}{4}B_{\mu\nu}B^{\mu\nu}}_{U(1)_Y} - \underbrace{\sum_{a=1}^{3}\frac{1}{4}W^a_{\mu\nu}W^{a,\mu\nu}}_{SU(2)_L} - \underbrace{\sum_{a=1}^{8}G^a_{\mu\nu}G^{a,\mu\nu}}_{SU(3)_C} \tag{2.7}$$

where the field gauge tensors are given as

$$B_{\mu\nu} = \partial_\mu B_\nu - \partial_\nu B_\mu$$

$$W^a_{\mu\nu} = \partial_\mu W^a_\nu - \partial_\nu W^a_\mu - g\sum_{b=1,c=1}^{3}\epsilon^{abc}W^b_\mu W^c_\nu \tag{2.8}$$

$$G^a_{\mu\nu} = \partial_\mu G^a_\nu - \partial_\nu G^a_\mu - g3\sum_{b=1,c=1}^{8}f^{abc}G^b_\mu G^c_\nu.$$

Here, $W^{1..3}_\mu$ are the three fields of the weak interactions and $G^{1..8}_\mu$ are the gluon fields. ϵ^{abc} is the structure constant of $SU(2)$ and f^{abc} is the structure constant of $SU(3)$. The full expression of the Standard Model Lagrangian can be found, for instance, in [17].

2.2.4. Electroweak Theory

Electromagnetic interactions as described in section 2.2.1 was unified with weak interactions to form electroweak theory ($SU(2)_L \otimes U(1)_Y$) by Glashow [8], Salam [10] and Weinberg [9]. $U(1)$ here represents a group of unitary 1×1 matrices describing weak hypercharge (Y)[1] conservation and $SU(2)$ is a group of special unitary 2×2 matrices that describes the conservation of weak isospin ($\overrightarrow{T}$). The weak isospin is a vector quantity in which "left-handed" fermions have $T = \frac{1}{2}$ and can be grouped into doublets with fermions having $T_3 = \pm\frac{1}{2}$. Electrically charged fermions are assigned T_3 value with the same sign as their electric charge. The gauge group $SU(2)$ implies that the gauge transformations only apply to left handed particles grouped into

[1]The weak hypercharge is a quantum number that relates the electric charge and third component of the weak isospin.

weak isospin doublets e.g.

$$\begin{pmatrix} \nu_e \\ \\ e \end{pmatrix}_L . \tag{2.9}$$

The hypercharge (Y) and the third component of weak isospin T_3 are related as :

$$Q = \frac{1}{2}Y + T_3, \tag{2.10}$$

where Q is the electric charge. The hypercharge for both e_L^- and and ν_e is -1, which implies that for the electric charge to be different, T_3 should be different for both of them. In the case of right handed fermions which are isospin singlets, T and T_3 are zero, since they transform into themselves under weak isospin interactions.

As described for the Lagrangian in QED, a covariant derivative is also introduced to make the Lagrangian invariant under $SU(2)_L \otimes U(1)_Y$ transformations:

$$D_\mu = \partial_\mu - ig'YB_\mu - ig\overrightarrow{T} \cdot \overrightarrow{W} \tag{2.11}$$

where B_μ is related to the hypercharge, g' is the $U(1)_Y$ coupling strength, W_μ^i with $i = 1, 2, 3$, are related to weak isospin and g is the coupling strength of $SU(2)_L$.

As described in section 2.2.1, for the Lagrangian to remain invariant under local gauge transformation, the mass term of the interaction field has to be zero. However, masses of the gauge bosons Z and $W^\pm$ imply that the electroweak theory $SU(2)_L \otimes U(1)_Y$ has to be spontaneosly broken. The mass acquirement of the gauge bosons and the breaking of symmetry is explained through the *Higgs Mechanism* [18, 19]. This is done by introducing a new complex $SU(2)$ doublet of scalar field, the Higgs field that has a weak isospin and a hypercharge.

$$\Phi = \begin{pmatrix} \Phi^+ \\ \\ \Phi^0 \end{pmatrix} = \frac{1}{\sqrt{2}} \begin{pmatrix} \Phi_2 + i\Phi_1 \\ \\ \Phi_4 + i\Phi_3 \end{pmatrix}. \tag{2.12}$$

The Higgs field has four degrees of freedom and its Lagrangian can be expressed as:

$$\mathcal{L}_{Higgs} = (\partial_\mu \Phi)^\dagger (\partial_\mu \Phi) - V(\Phi), \tag{2.13}$$

where the Higgs potential $V(\Phi)$ is given as

$$V(\Phi) = \mu^2 \Phi^\dagger \Phi + \lambda(\Phi^\dagger \Phi)^2. \tag{2.14}$$

λ is the Higgs self-coupling which in the Standard Model has a positive value while μ is a non-zero ground state or vaccum expectation value which can be negative. The minima of Higgs potential, also known as the Mexican hat potential, lies on

the circular dip (given by $\sqrt{-\mu^2/\lambda}$) of the Mexican hat like structure of the Higgs potential. This means that, among all the points on the circle, one of them has to be spontaneosly chosen as the ground state thus breaking the symmetry. The value of negative μ^2 is associated with the mass of the Higgs boson. Since the symmetry of $SU(2)_L \otimes U(1)_Y$ is broken, the weak isospin and hypercharge associated with it is no longer conserved. The spontaneous symmetry breaking of the Lagrangian generates a massless boson, known as the Goldstone boson as required by the Goldstone's theorem [20]. It was established by P.W.Higgs [18], F. Englert and R. Brout [19] that the massless Goldstone boson must not necessarily manifest as a new particle (undiscovered), but a longitudinal degree of freedom associated with the Higgs field giving mass to Z, W^+ and W^-, and generating the Higgs boson itself. However, since the symmetry of $U(1)_{QED}$ is still intact, the electric charge is conserved thus leaving the photon massless as before. Electrically neutral, the photon and the Z boson are a mixture of the neutral gauge fields W^3 and B, corresponding to the weak isospin and weak hypercharge, respectively. While the charged gauge particles mix up to form $W^\pm$ as shown below in Eq. 2.15.

$$\begin{aligned} A &= B\cos\theta_W + W^3\sin\theta_W \\ Z &= -B\sin\theta_W + W^3\cos\theta_W \\ W^\pm &= 1/\sqrt{2}(W^1 \mp iW^2) \end{aligned} \tag{2.15}$$

where θ_W is the electroweak mixing angle (also known as Weinberg angle). The QED and electroweak coupling strengths can be given as

$$e = g'\cos\theta_W = g\sin\theta_W. \tag{2.16}$$

The masses of the gauge bosons can be obtained as

$$m_W = \frac{1}{2}gv \tag{2.17}$$

$$m_Z = \frac{1}{2}v\sqrt{g^2 + g'^2} \tag{2.18}$$

$$m_\gamma = 0. \tag{2.19}$$

From the measurements of m_W and the weak coupling constant g_W one can obtain the value of $v = 246\,\text{GeV}$. With the Higgs field acquiring its vacuum expectation value, it can generate mass terms for fermions by coupling with them. These Yukawa-type couplings are different for every fermion and are expected to be proportional to their masses.

2.3. Quantum Chromodynamics

The organisational scheme for quarks which are the building blocks of strongly interacting particles was introduced by M. Gell-Mann [21] and G. Zweig [22] independently. The theory that describes the interaction between these quarks is known as Quantum Chromodynamics (QCD) [13]. QCD carries similar procedures as were carried for all the other interactions. One of the properties only carried by quarks and gluons is called *colour*. Quarks come in three different colours, *red, green* and *blue*. The derivative modified to preserve the symmetry of Lagrangian under $SU(3)$ transformations is

$$D_\mu = \partial_\mu + ig_3 \overrightarrow{\lambda} \cdot \overrightarrow{G}_\mu. \tag{2.20}$$

Eight gauge fields produced in this process are the eight gluons which mediate the strong interaction between the quarks. These gluons couple to each other which significantly effects the behaviour of the QCD couplings. The QCD couplings between the quarks becomes asymptotically weaker at high energies as the corresponding length scales between the quarks decreases and makes them behave like quasi-free particles. This feature of QCD is known as the *asymptotic freedom* [23, 24].

Conversely, when the distance between the quarks increases at lower energies, the strength of the QCD coupling increases significantly. This behaviour of the quarks is from the phenomenon known as the *colour confinement*, which states that the colour charged particles cannot be isolated and can only be observed as a colour singlet combination of quarks and gluons. Any attempt to separate a quark from its parent hadron only results in creation of new hadrons. More details about the *colour confinement* can be found in [25]. As an important effect of this feature, the high QCD coupling constant at lower energies does not allow the interaction between quarks and gluons to be treated perturbatively. Therefore, at such low energies the interactions between these particles are studied using methods like *Lattice QCD* [26, 27] or *Chiral Perturbation theory* [28].

Lattice QCD is a non-perturbative approach to solve quantum chromodynamics. In this approach, fields representing quarks are defined at lattice sites, while the gluon fields connect the neighboring sites where a is the lattice spacing. The discrete formulation of QCD rather than a continuous space-time naturally introduces a momentum cut-off at an order of $1/a$. This approximation approaches continuum QCD as the spacing between lattice sites is reduced to zero.

Chiral Perturbation theory is an effective field theory that is constructed with a Lagrangian consistent with the chiral symmetry of quantum chromodynamics together with other symmetries of parity and charge conjugation. In an effective field theory, a power ordering scheme is assigned to the theory which organizes the Lagrangian terms by some pre-determined degree of importance. In *Chiral Perturbation theory*, the Lagrangian terms are ordered based on the momentum and mass of the

quarks. The ordering allows one to keep certain important terms while safely ignore the higher order corrections. *Chiral Perturbation theory* assumes chiral symmetry, which requires that the QCD Lagrangian for left-handed and right-handed components of the quark fields should be invariant under rotations in strong isospin[2] space. This requires that the quarks should be massless. Since in real life quarks have mass, only the interactions between quarks with very small masses can be modelled using the *Chiral Perturbation theory*.

2.3.1. Quark Fragmentation and Hadronization

The process of quark fragmentation can be explained through the process of e^+e^- annihilation to hadrons as given in the figure 2.1. The initial two partons forming the quark-antiquark pair ($q\overline{q}$) are located at a very short distance from each other and behave as quasi-free particles. They are highly stimulated during the production process through e^+e^- annihilation and radiate bremstrahlung cascades of gluons, preferentially into a cone of small aperture. The emitted gluons can further split into more gluons or $q\overline{q}$ pairs as long as the amount of available energy allow.

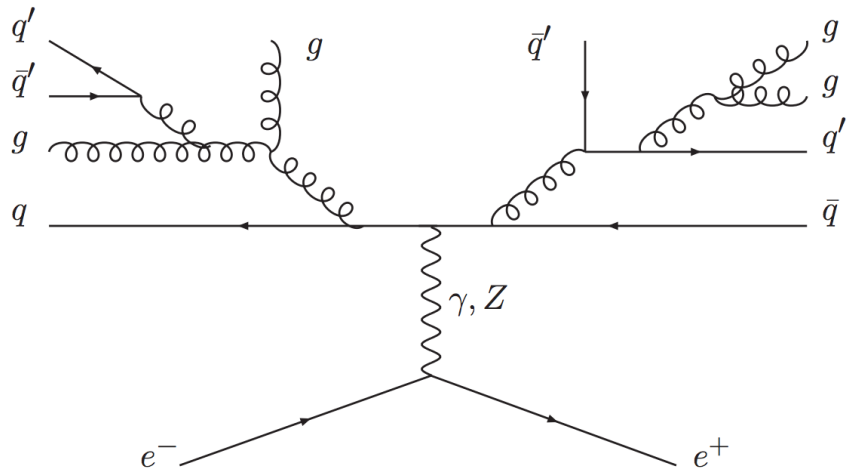

Figure 2.1.: Sketch depicting the quark-antiquark and gluon pair cascades occurring during quark fragmentation. Figure taken from [29].

However, as soon as the distance between the two initial quarks increases, a gluonic flux tube is built up between them with an energy density of $1\,\mathrm{GeV}/10^{-15}\,\mathrm{m}$ and

[2]Isospin is a vector quantity in which up and down quarks have a value of $I = \frac{1}{2}$ with the third component I_3 being $\frac{1}{2}$ for up quarks and $\frac{-1}{2}$ for down quarks.

a very small transverse size [29]. With sufficiently large separations between the two quarks ($R \sim 10^{-15}$ m), enough energy is accumulated in the flux tube which then "breaks" and produces new $q\overline{q}$ pairs. As a result, highly collimated cascades of quarks and gluons forming into hadrons are created. This model of hadronization is known as the independent hadronization process. The hadronic jets created preserve the momenta and energies of the initial quarks. Since it is not possible to observe an individual initial quarks, their properties can be determined by measuring the properties of the hadronic jets.

Similar to the independent hadronization process described above, two more methods of hadronization are used in the particle physics community. They are called as string hadronization method [30] and cluster hadronization method [31]. The general approach of the string model is similar to the independent hadronization method. However, the gluon flux tubes in this case are referred to as *strings* and they gain energy through gluons producing "kinks". The cluster hadronization has a completely different approach of producing hadrons. In this case, all the radiated gluons are split into $q\overline{q}$ pairs until only quarks are left. The quarks are then clustered into colour neutral groups which decay producing hadrons.

2.3.2. Hadron Structure

As mentioned previously, quarks are always found in bound states held together by gluons in a structure known as a hadron. The structure of a hadron was studied by probing a proton with a high resolution electron beam [32] at SLAC. These studies showed that a proton contains [33]:

- Three quarks known as the *valence* quarks
- The gluons that are the quanta of the colour field
- The quark and antiquark of the *sea* which contains quark-antiquark pairs of all flavours, with decreasing probability of increasing quark masses.

These particles were termed as *partons* by Richard Feynman. The hadron structure function, in the quantum field theory, describes the quark content of the hadron. According to the arguments by Feynman in [34] and Bjorken in [35]: In an electron-proton collision, Q^2 is defined as $-Q^2 = (E' - E)^2 - (p' - p)^2$ where E and p are the energy and three momentum of the electron before the transfer of a photon respectively and E' and p' are the energy and three momentum of the electron after the energy transfer to the nucleon. Also if x is the fraction of the four-momentum of a parton involved in the scattering, then the dependence of the hadron structure function on Q^2 for a fixed x is the Fourier transform of the charge distribution in the parton that is found at x. Which means that the structure function should only

depend on x and not change with varying value of Q^2. This was verified in studies conducted at the HERA electron-proton collider [36]. However it was also found that the structure functions are dependent on Q^2 at small values of x.

Experimentally, the distribution functions are obtained from the measurements of the deep inelastic differential cross-sections of electrons [32]. If $f(x)$ is defined as the distribution of momentum fraction for the quark of flavour f, $f(x)dx$ would be the probability that this quark carries a momentum fraction between x and $x + dx$ and $xf(x)dx$ would be the corresponding amount of momentum fraction. $\overline{f}(x)$ is the analogous function for the antiquark of f flavour and $g(x)$ is for the gluons. These functions are called parton distribution functions. The measured structure function of a hadron is the sum of the contributions of all the q and $\overline{q}$ weighted with square of charge:

$$F(x) = x \sum_f z_f^2 [f(x) + \overline{f}(x)]. \tag{2.21}$$

2.3.3. Photon Structure function in QCD

A photon may seem to be a point-like particle to the first approximation. However, quantum mechanically it can fluctuate into a fermion-antifermion pair. The process of photons fluctuating like $\gamma \leftrightarrow q\overline{q}$ are of special interest as they can interact strongly and therefore can be a reason for major parts of the γp and $\gamma\gamma$ total cross sections.

Using the Schuler-Sjöstrand model [37], a physical photon $|\gamma\rangle$ can be defined as:

$$|\gamma\rangle = \sqrt{Z_3}|\gamma_B\rangle + \sum_{V=\rho^0,\omega,\phi,j/\psi} \frac{e}{fv}|V\rangle + \sum_q \frac{e}{f_{q\overline{q}}}|q\overline{q}\rangle + \sum_{l=e,\mu,\tau} \frac{e}{f_{ll}}|l^+l^-\rangle \tag{2.22}$$

By the virtue of this superposition, a photon can be shown to interact in three different ways. The final term showing $|l^+l^-\rangle$ states can only interact strongly with partons inside the hadrons at higher orders, and can thus be neglected in the study of hadronic final states.

- A bare photon $|\gamma_B\rangle$ can interact with the incoming photons or hadrons produced in different types of processes.
- A photon may fluctuate into a vector meson since they have the same quantum properties. It fluctuates predominantly into a ρ^0 because it is the lightest vector meson.
- There may also be cases where a photon fluctuates into a $q\overline{q}$ pair of larger virtuality.

Among these, photons fluctuating into a vector meson comprises of 78% of the total $\gamma\gamma$ events [38]. The theory of vector meson dominance is presented in detail ahead.

Vector Meson Dominance

Vector Meson Dominance defines a photon as a superposition of a pure electromagnetic photon and a vector meson. The electromagnetic interaction conserves spin, parity and charge conjugation quantum numbers (J^{PC}). Heisenberg's uncertainty principle therefore allows the photon to fluctuate into another uncharged particle with same spin and (J^{PC}) for a short time. Allowed vector mesons for such fluctuations are the $\rho, \omega, \phi, J/\psi$ and Υ mesons since they have same spin, parity and charge conjugation number. Since the ρ meson is the lightest vector meson, the probability for a photon to fluctuate into a ρ is highest. These fluctuated mesons can interact with other hadrons as in Eq. 2.23:

$$[\gamma^* A \to B] = -e\frac{m_\rho^2}{2\gamma_\rho}\frac{1}{q^2 - m_\rho^2}[\rho^0 A \to B] \tag{2.23}$$

to produce a pile of hadrons [38]. A pictorial representation for this process is shown in figure 2.2. According to Eq. (2.23) a photon virtually dissociates into an on-shell

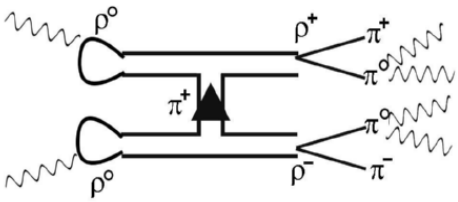

Figure 2.2.: Pictorial sketch illustrating $\gamma\gamma \to$ low p_T hadron processes

vector meson that subsequently interacts with hadron A to yield hadron B. Here, m_ρ denotes the ρ^0 meson mass, $2\gamma_\rho$ is the coupling and q^2 is the photon virtuality.

Total cross section for photon interactions

The points mentioned in the previous paragraph show that the photon exhibits hadronic properties. With the comparisons made between $\sigma(\gamma p)$ and $\sigma(\gamma\gamma)$ by Chen et.al in [39], it was shown that a photon is a hadron about $\frac{1}{400}$ of the time. The comparison of the total cross sections of different processes like $pp \to X$, $\gamma p \to$ hadrons and $\gamma\gamma \to$ hadrons are evaluated using the HPR_1R_2 model [40] and data from COMPETE [41], SELEX [42] and OPAL [43] as shown in figure 2.3. Clearly the behaviour of the curves for total cross sections of the hadronic processes and the $\gamma\gamma$ process are very similar as mentioned earlier photon is a hadron about $\frac{1}{400}$ of the time. Since the energy dependence of the crossection is the same for hadronic

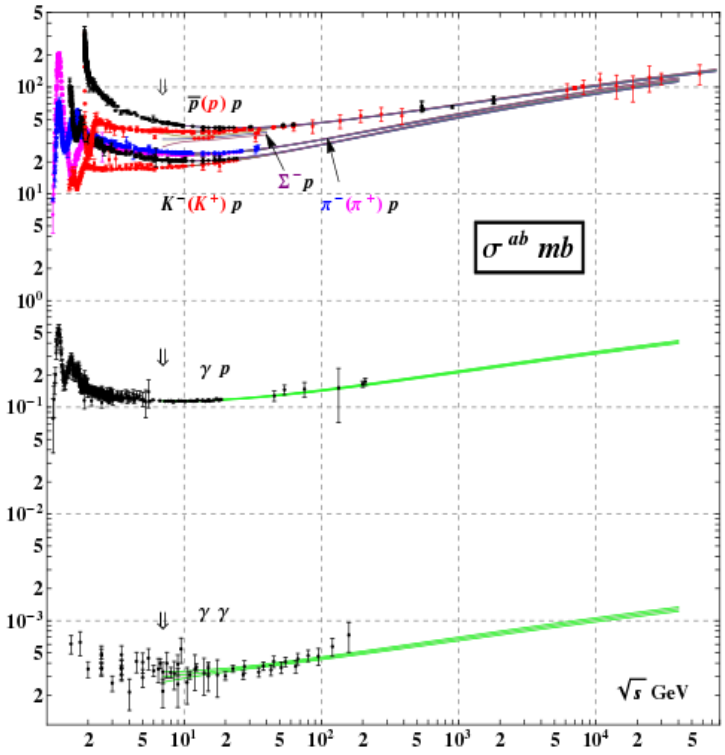

Figure 2.3.: Cross sections for hadronic,γp and $\gamma\gamma$ processes as a function of centre-of-mass energy [44]

and $\gamma\gamma$ events, the HPR_1R_2 formula alone can describe both processes. The generic form of this formula can be given as [40, 44]:

$$\sigma^{ab} = H\,log^2\left(\frac{s}{s_M^{ab}}\right) + P^{ab} + R_1^{ab}\left(\frac{s}{s_M^{ab}}\right)^{\eta_1} - R_2^{ab}\left(\frac{s}{s_M^{ab}}\right)^{\eta_2} \tag{2.24}$$

The parameters here are defined as: $H = \pi\frac{(\hbar c)^2}{M^2}$ (mb) is called the Heisenberg term, R_1 and R_2 (mb) the Regge pole contributions and P (mb) stands for the Pomeronchuk constant term. s and $s_M^{ab} = (m_a + m_b + M)^2$ are in GeV^2, m_a and m_b are the masses of initial state particles and M is a mass parameter. For $\gamma\gamma$ collisions Eq. 2.24 changes as given in Eq. 2.25 where only one Regge terms is used since both the initial particles are photons:

$$\sigma^{\gamma\gamma} = H\,log^2\left(\frac{s}{s_M^{\gamma\gamma}}\right) + P^{\gamma\gamma} + R^{\gamma\gamma}\left(\frac{s}{s_M^{\gamma\gamma}}\right)^{\eta} \tag{2.25}$$

Here, the initial state particles are the photons, $s_M^{\gamma\gamma} = 2m_\gamma + M$ and $m_\gamma = m_{\gamma^*} = m_\rho$.

2.4. Shortcomings of the Standard Model

Despite the confirmation of its predictions by numerous experiments, the Standard Model has several important short-comings [45], which will be summarized in the following.

Grand Unification : As explained in section 2.2.4, the theoretical model of electromagnetic interactions and weak interactions was successfully unified into the electroweak theory. This led to the idea that the theory of quantum chromo-dynamics also could be unified with the electroweak theory at higher energy scales. This implies that, at higher energies all the forces would couple with the same strength. However, a clear distinction in the coupling constants can be seen with their evolution at higher energy scales [46]. Thus, the Standard Model formalism can not include the unification of all three forces as shown in figure 2.4. Furthermore, as mentioned earlier, gravity also could not be accommodated in the Standard Model of particle physics.

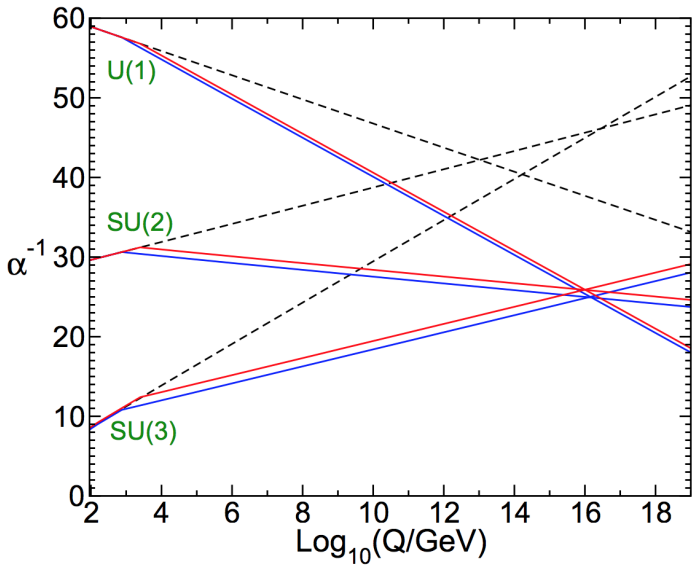

Figure 2.4.: Running couplings as a function of energy scale for different gauge groups in the Standard Model (dashed lines) and in the SUSY extension (solid lines). Gauge unification in the Standard Model is ruled out. Figure taken from [46].

The Hierarchy Problem : Theoretically, the mass of Higgs boson receives huge contributions from quantum loop corrections. The experimentally determined value

of Higgs boson's mass is $m_H \approx 125$ GeV [1]. Whereas, considering the validity of the Standard Model upto the Planck energy scale ($\Lambda_{Planck} \approx 10^{19}$ GeV), the mass of Higgs boson due to the quantum corrections becomes orders of magnitude higher than the experimentally measured value. A huge amount of fine-tuning would be required to cancel the effects of loop corrections and keep the mass of Higgs boson to the right order of magnitude.

Neutrino Masses : The Standard Model of particle physics defines neutrinos as massless particles. However, the experimental observation of neutrino oscillations between the flavours prove that the neutrinos should have some mass. The constraints on neutrino masses were obtained by experiments in cosmology and astrophysics. The first evidence on neutrino oscillations came from the Super Kamiokande experiment in 1998 [47]. The Planck experiment has provided the most recent upper limit on the sum of neutrino masses as $\sum_i m_i < 0.23$ eV at 95% CL [48], showing that the neutrinos should be lighter than the fermions by a factor of 10^{-6} [49]. Also it is not yet understood if the neutrinos are Dirac particles like other fermions or if they are Majorana particles which form their own anti-particles.

Dark Matter : Cosmological and astrophysical observables like the rotational velocity of galaxies [50, 51] and measurements of anisotropy in the cosmic microwave background [52] hint the presence of some unknown matter in the Universe. Because of its non-luminous and non-absorbing behaviour, dark matter can only be detected through its gravitational response on visible matter [53]. The cosmological parameters indicate that approximately only 5% of the universe consists of the normal visible matter, 27 % of the universe forms the dark matter and rest consists of dark energy. Since the dark matter particle is yet undetected, the possibility of this particle being massive and weakly interacting is very likely. The only candidate in the Standard Model to accommodate such a particle are neutrinos which are excluded due to their tiny masses.

Matter-Antimatter asymmetry : The Standard Model of Cosmology assumes a symmetry in the production of matter and anti-matter in the beginning of our Universe. However, the dominance of matter particles is very clearly visible in the universe, instead of them annihilating each other. The violation of the CP-symmetry (charge-conjugation parity symmetry) [54, 55] could form a potential explanation for this asymmetry. Yet, the effects of CP-violations have only been observed in the weak interactions of the quarks which is not large enough to account for the huge asymmetry in the amount of matter and anti-matter in the Universe [56].

2.5. Supersymmetry

The unsolved puzzles summarized in section 2.4 indicate that there has to be more to the theory describing the Universe rather than just the Standard Model of particle physics. One of such proposed extensions to the Standard Model is the theory of supersymmetry (SUSY) [2]. It is an appealing candidate for solving almost all the shortcomings of the Standard Model. Supersymmetry predicts that every SM particle has a supersymmetric partner with a spin that differs by 1/2. Every other property of the particle and the superparticle would be the same. Consequently, every SM boson would have a supersymmetric fermionic partner while every SM fermion would have a supersymmetric bosonic particle. The SUSY transformations of a bosonic and fermionic state is given by

$$Q\,|\text{Boson}\rangle = |\text{Fermion}\rangle\,, \quad Q\,|\text{Fermion}\rangle = |\text{Boson}\rangle\,. \tag{2.26}$$

SUSY can provide a potential dark matter candidate, which would be a lightest supersymmetric particle being stable, neutral and weakly interacting. The introduction of SUSY automatically cancels the quantum corrections between a particle and its super-partner since the fermionic loops associated with the super partners are negative in sign. As a result, the quadratically divergent loop contribution to the Higgs mass are cancelled out by contribution from super-partners. However, this is predicted with the assumption that SUSY is an exact symmetry and that the mass of the Standard Model particle and its super-partner is same. Conversely, no experimental observations to the date could confirm the presence of any SUSY particles. If the masses of the SUSY particles were exactly as that of their super-partners, they would have been already seen in the same mass range. This gives the conclusion that the supersymmetry is a broken symmetry. Nevertheless, it is also assumed that the SUSY is only softly broken and the SUSY particles maybe discovered at GeV-TeV scales.

Many different models of SUSY have been proposed, while the formulation considered for this thesis is the minimal supersymmetric extension of the Standard Model (MSSM).

2.5.1. The Minimal Supersymmetric Standard Model

The Minimal Supersymmetric Standard Model owes its name to the fact that it introduces minimal number of new particles while still ensuring that the theoretical model is phenomenologically feasible. The super-partners of SM leptons are called as sleptons while that of quarks are called as squarks. The super-partners of the SM gauge bosons have a suffix "-ino" e.g. gluino. The MSSM requires two Higgs boson doublets, with different hypercharge to ensure that *(i)* masses for both up-type and

down-type quarks are generated and *(ii)* the anomalies that occur while introducing the super-partners of Higgs are cancelled. The ratio of the vacuum expectation values of the Higgs doublet fields, $\langle H_u^0 \rangle$ and $\langle H_d^0 \rangle$, is defined as $\tan\beta$. The particle content of the MSSM is summarized in table 2.3.

Supermultiplets	S = 0	S = 1/2	S = 1	$SU(3)_C$	$SU(2)_L$	$U(1)_Y$
gluino, gluon	-	$\tilde{g}$	g	8	1	0
winos, W boson	-	$\tilde{W}^0$, $\tilde{W}^\pm$	W^0, $W^\pm$	1	3	0
bino, B boson	-	$\tilde{B}$	B	1	1	0
squarks, quarks	$(\tilde{u}_L\ \tilde{d}_L)$	$(u_L\ d_L)$	-	3	2	+1/ 6
	$\widetilde{\bar{u}}_L \equiv \tilde{u}_R$	$\bar{u}_L \equiv u_R$	-	$\bar{3}$	1	-2/3
	$\widetilde{\bar{d}}_L \equiv \tilde{d}_R$	$\bar{d}_L \equiv d_R$	-	$\bar{3}$	1	+1/3
sleptons, leptons	$(\tilde{\nu}_L\ \tilde{e}_L)$	$(\nu_L\ e_L)$	-	1	2	-1/2
	$\widetilde{\bar{e}}_L \equiv \tilde{e}_R$	$\bar{e}_L \equiv e_R$	-	1	1	+1
Higgs, Higgsino	$(H_u^+\ H_u^0)$	$(\tilde{H}_u^+\ \tilde{H}_u^0)$	-	1	2	+1/2
	$(H_d^0\ H_d^-)$	$(\tilde{H}_d^0\ \tilde{H}_d^-)$	-	1	2	-1/2

Table 2.3.: Super-fields in the MSSM model and the corresponding quantum numbers. In the case of quarks and leptons, only the first generation is presented.

The MSSM allows mixing of gauge eigenstates presented in table 2.3 to form mass eigenstates. For example, the supersymmetric partners of any fermion, namely $\tilde{f}_L$ and $\tilde{f}_R$ which are the scalar partners of respective left-handed and right-handed fermion are allowed to mix. The bino and wino mass parameters in the MSSM are defined as M_1 and M_2 respectively. μ is the higgsino mass parameter.

2.5.2. R-parity conservation and its consequences

A quantum number known as R-parity is introduced to the MSSM theory defined as:

$$R = (-1)^{3(B-L)+2S} \tag{2.27}$$

where B is the baryon number, L is the lepton number and s is the spin. The value of R for a Standard Model particle is 1 and for a SUSY particle it is -1. As a consequence of the R-parity conservation, huge restrictions are applied on the model: *(i)* SUSY particles can only be produced in pairs since every vertex should contain an even number of SUSY particles, *(ii)* the SUSY particles can only decay into odd numbers of lighter SUSY particles and their SM counterparts, *(iii)* there

should be a stable, lightest SUSY particle as the mixing between the SUSY and SM particles is forbidden by the R-parity invariance.

2.5.3. Neutralinos and Charginos

The neutral gauginos ($\tilde{B}, \tilde{W}^0$) and higgsinos ($\tilde{H}_d^0$, $\tilde{H}_u^0$) mix to produce mass eigenstates known as neutralinos.

The Lagrangian for neutralinos' mass term is given as [57–59]

$$\mathcal{L}_{\tilde{\chi}^0} = (-1/2)(\psi^0)^T \mathcal{M}_N \psi^0 + h.c., \tag{2.28}$$

where $\mathcal{M}_N$ represents the neutralino mass matrix as given in Eq. 2.29

$$\mathcal{M}_N = \begin{pmatrix} M_1 & 0 & -m_Z \sin\theta_W \cos\beta & m_Z \sin\theta_W \sin\beta \\ 0 & M_2 & m_Z \cos\theta_W \cos\beta & -m_Z \cos\theta_W \sin\beta \\ -m_Z \sin\theta_W \cos\beta & m_Z \cos\theta_W \cos\beta & 0 & -\mu \\ m_Z \sin\theta_W \sin\beta & -m_Z \cos\theta_W \sin\beta & -\mu & 0 \end{pmatrix} \tag{2.29}$$

Here, M_1 and M_2 represent the bino and wino mass parameters in the MSSM respectively, m_Z is the Z boson mass and θ_W is the weak mixing angle. Four mass eigenstates of neutralinos ($\tilde{\chi}_1^0$, $\tilde{\chi}_2^0$, $\tilde{\chi}_3^0$, $\tilde{\chi}_4^0$) are obtained by diagonalising the mass matrix. Similarly, the charged winos and higgsinos mix to form two charginos. The mass term for the charginos in Lagrangian is given as [57–59]

$$\mathcal{L}_{\tilde{\chi}^\pm} = -\frac{1}{2}(\psi^+, \psi^-) \begin{pmatrix} 0 & \mathcal{M}_C^T \\ \mathcal{M}_C & 0 \end{pmatrix} \begin{pmatrix} \psi^+ \\ \psi^- \end{pmatrix} + \text{h. c.} \tag{2.30}$$

where ψ^+=(-$i\tilde{W}^+$, $\tilde{H}_u^+$) and the mass matrix $\mathcal{M}_C$ is given as:

$$\mathcal{M}_C = \begin{pmatrix} M_2 & \sqrt{2} m_W \cos\beta \\ \sqrt{2} m_W \sin\beta & \mu \end{pmatrix} \tag{2.31}$$

Here, m_W is the W boson mass. The diagonalisation of the $\mathcal{M}_C$ matrix gives two mass eigen states called charginos given as: $\tilde{\chi}_1^\pm$, $\tilde{\chi}_2^\pm$.

Depending on the amount of mixing, charginos and neutralinos can behave either bino-like, wino-like or higgsino-like [60]. In this thesis, a scenario which has μ smaller than M_1 and M_2 where μ is in the order of electroweak scale, while M_1 and M_2 are of the order of few TeV is being investigated [61].

2.5.4. Natural Supersymmetry

As mentioned in the beginning of this section, the introduction of supersymmetry solves the problem of hierarchy in the Standard Model. Even though the introduction of super-partners cancel out the quadratic divergent terms, the logarithmic terms stay due to the breaking of SUSY. It is assumed that SUSY is broken softly which requires that the scalar particles are not too heavy as compared to their corresponding partners. The Higgs mass receives dominant contributions from the top quark and the scalar top quark masses, since they have a huge Yukawa coupling ($y_t \sim 1$). Due to the contribution of the gluino in the scalar top quark mass at one loop level, it indirectly has an effect on the Higgs boson mass. The contributions of other super-partners to the Higgs boson mass are not very significant. Consequently, naturalness puts an upper limit only on stops and gluinos while squarks and sleptons are allowed to be heavier. Such scenarios are summarised ahead as Natural SUSY [3–5].

An important aspect of the natural SUSY model is the mass of the Z boson at one-loop level. By adding one-loop level corrections to the tree level formula for Z boson mass, a direct relation between the higgsino mass parameter μ and Z boson mass can be obtained as [3]:

$$m_Z^2 = 2\frac{(m_{H_u}^2 + \sum_u)\tan^2\beta - m_{H_d}^2 - \sum_d}{1 - \tan^2\beta} - 2|\mu|^2 \tag{2.32}$$

where $\sum_u$ and $\sum_d$ are the loop corrections. The highest contribution to the loop corrections is from the scalar top quarks due to their large Yukawa coupling.

Naturalness requires that experimentally obtained results of the Higgs boson mass or Z boson mass should be theoretically obtainable without applying large fine-tuning. For this to be possible, the mass of the Z boson and the values of terms on the right hand side should be of the same order. Under large $\tan\beta$ limits Eq. 2.32 can be approximated to

$$m_Z^2 \approx -2(m_{H_u}^2 + \sum_u + |\mu|^2). \tag{2.33}$$

With the naturalness requirement, this equation demands higgsinos to be light, nearly degenerate and of the same order as of Z boson and that the mass of scalar tops gluinos to be around a few TeV. This forms the main motivation in this thesis to study light higgsinos at electroweak scale.

2.6. Light higgsinos at the Large Hadron Collider

Several studies dedicated towards the search of supersymmetric particles is conducted at the LHC experiments, CMS [62, 63] and ATLAS [64, 65]. However, the

studies related to nearly mass degenerate higgsino-like charginos and neutralino are important with respect to the studies presented in this thesis. As shown in figure 2.5, the light higgsinos are produced in hadron colliders as a $\tilde{\chi}_1^{\pm}\tilde{\chi}_2^0$ pair which decay into a highly off-shell Z or a W boson and the system is boosted by an initial state radiation (ISR) jet. The ISR jet recoils against the two $\tilde{\chi}_1^0$ and large missing transverse momentum thus allowing to select such events. The W and Z boson decay to particles with very low trasverse momentum.

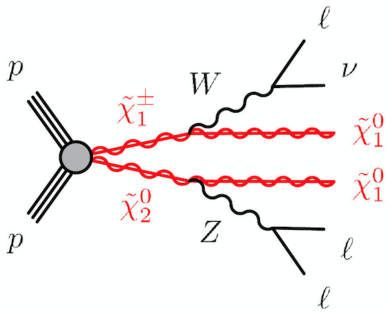

Figure 2.5.: Chargino and neutralino production at a Hadron collider [65].

Such low p_T particles can very easily be lost in a large pile of hadronic background or due to the application of trigger. Identifying and reconstructing particles with such low transverse momentum would be experimentally very challenging at hadron colliders. However, the search for SUSY scenarios with such low p_T signatures can have advantage at an e^+e^- collider e.g. the ILC. Due to a very low background environment and triggerless event selection,the search for signatures with low transverse momentum would not be experimentally as challenging as in a hadron collider.

Exclusion limit plots from the studies at ATLAS and CMS are given in figure 2.6 [65–67].

2.7. Light higgsinos at an e^+e^- Collider

Higgsinos can be produced at an e^+e^- collider via $e^+e^- \to \tilde{\chi}_1^+\tilde{\chi}_1^-$ and $e^+e^- \to \tilde{\chi}_1^0\tilde{\chi}_2^0$ through the Z boson or the γ exchange in the s-channel. Charginos can be produced via the exchange of a Z boson or a γ while only the Z boson exchange is possible for neutralinos. The production of higgsinos via t-channel and u-channel is possible via the exchange of selectrons and electron-sneutrinos. However, they are suppressed even for light selectrons/sneutrinos due to their small Yukawa coupling to higgsinos. The Feynman diagrams for higgsino production are given in figure 2.7.

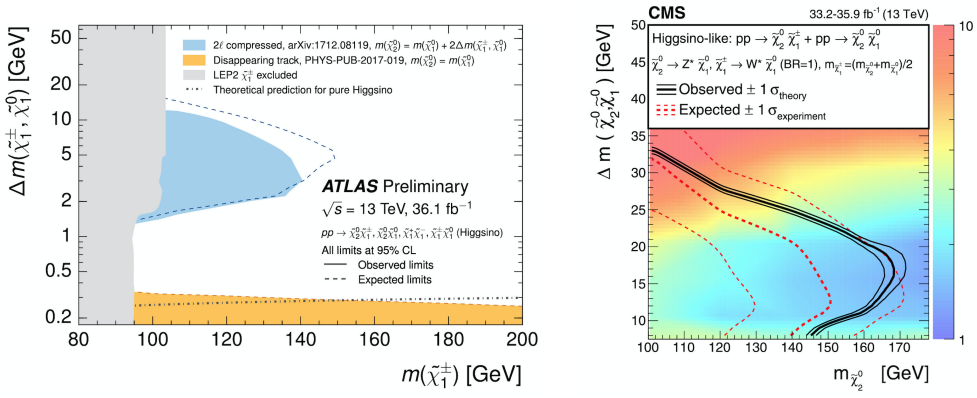

(a) (b)

Figure 2.6.: 95% CL exclusion limits set by ATLAS, CMS searches in the $\tilde{\chi}_1^{\pm}$ and $\tilde{\chi}_2^0$ vs $\tilde{\chi}_1^0$ mass plane for various simplified models of the pair production [65–67].

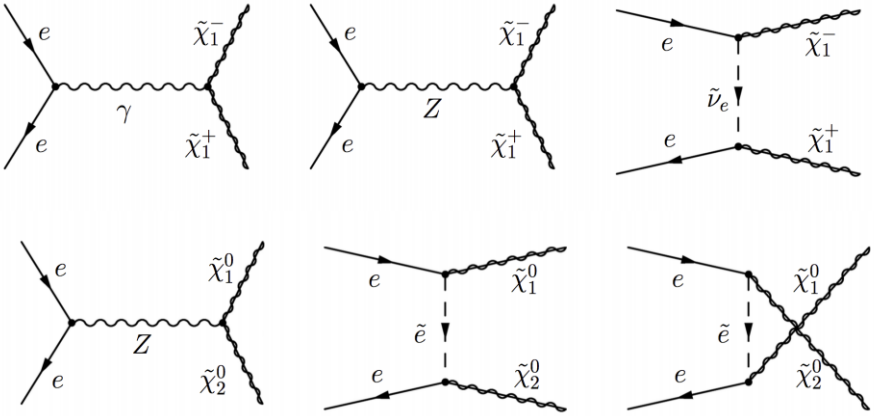

Figure 2.7.: Chargino (upper row) and neutralino (lower row) production graphs at tree level. In this scenario, t and u-channel contributions are negligible due to the small Yukawa coupling between sleptons and higgsinos.

The lightest chargino $\tilde{\chi}_1^+$ and the neutralino $\tilde{\chi}_2^0$ decay to the lightest supersymmetric particle (LSP), $\tilde{\chi}_1^0$, and an off-shell W or Z boson respectively as shown in figure. 2.8.

The $\tilde{\chi}_1^0$ may also decay to lightest chargino along with a virtual W boson as $\tilde{\chi}_2^0 \rightarrow W^{\pm}\tilde{\chi}_1^{\pm}$, but since it is kinematically highly suppressed, the branching ratio is very tiny. The radiative decay of the neutralino as $\tilde{\chi}_2^0 \rightarrow \tilde{\chi}_1^0\gamma$ is also an important decay

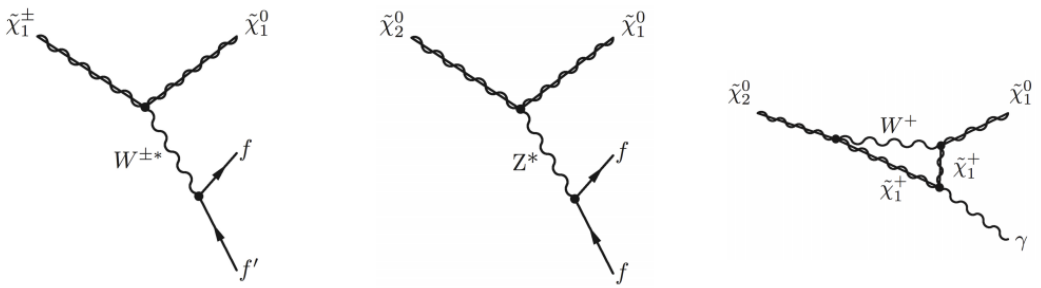

(a) $\tilde{\chi}_1^{\pm} \to \tilde{\chi}_1^0 W^{\pm *}$ **(b)** $\tilde{\chi}_2^0 \to \tilde{\chi}_1^0 W^{\pm *}$ **(c)** $\tilde{\chi}_2^0 \to \tilde{\chi}_1^0 \gamma$

Figure 2.8.: Decay channels of the lightest chargino and neutralino to the LSP and a gauge boson.

mode for small mass splitting scenarios [68].

As explained in section 2.5.4, light higgsinos are nearly mass degenerate and one can expect to have small mass splittings between them. Analysing such scenarios experimentally would depend on their mass differences. For a mass difference of the order of a GeV, an ISR photon method can be used as explained in [69]. For large mass differences, the final state particles would be quite energetic which can be used to observe them. For very small mass differences the chargino has a long lifetime. This makes the chargino to enter the detector thus leaving some signature in the tracker. Since there is an invisible decay product, a kink between the chargino track and the decay track is observed. Another important aspect would be the loss of energy by ionisation (dE/dx) which would be huge for charginos as compared to the decay products. Thus, the kink in the track and the dE/dx can be used to identify charginos with small mass splittings [70, 71]. Such scenarios were studied at LEP experiments [72–74]. One of the results showing LEP limits on the cross section as a function of the chargino mass and mass difference between the chargino and the LSP is given in figure 2.9. In the region of ΔM of $\mathcal{O}$ GeV, limits on cross section are weaker because the chargino analysis in this region requires the presence of an ISR photon. Therefore, conclusions on discovery or exclusion of any chargino signal can only be made with more data and further studies in this aspect.

A low ΔM higgsino analysis performed at the International Linear Collider showed that the key observables like the higgsino mass, the mass difference between the chargino and the LSP and the production cross section section for higgsinos could be determined with an uncertainity of a few percent [7]. The analysis considered scenarios with mass differences ($\Delta M_{\tilde{\chi}_1^{\pm},\tilde{\chi}_1^0}$) of 0.7 GeV and 1.6 GeV. In order to separate these signal events from the overwhelming background from photon-photon collisions, the presence of an ISR photon is required, which can also be used to de-

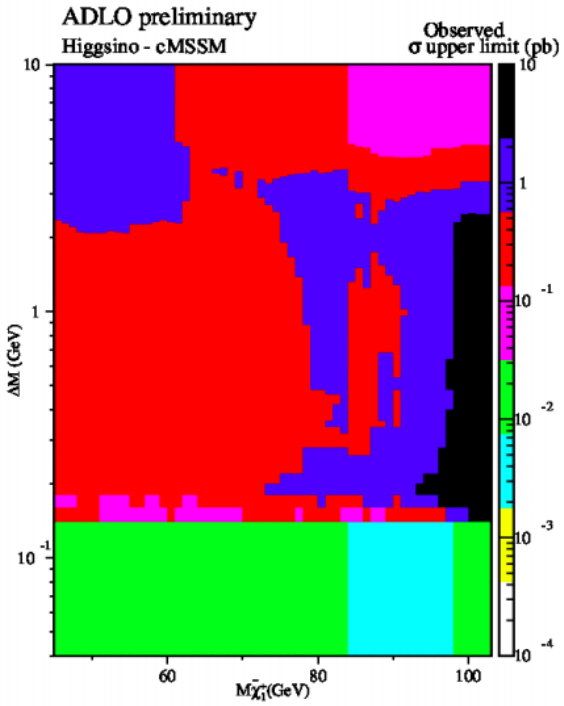

Figure 2.9.: LEP limits on the cross section as a function of the chargino mass and the mass difference between the chargino and the LSP. Figure taken from [75].

termine the chargino mass, as will be explained in section 8.6.1. Figure 2.10a shows the reconstructed value of the chargino mass vs the corresponding input value to the simulation. Figure 2.10b shows the reconstruction of mass difference between the chargino and the LSP. The plot shows that the mass reconstruction and the determination of the mass difference between the chargino and the LSP is possible at the ILC with an uncertainity of a few percent.

A drawback of this analysis was that it was performed using fast simulation and without the inclusion of one of the important backgrounds at an e^+e^- collider namely the $\gamma\gamma \rightarrow$ low p_T hadron overlay which is described in detail in chapter 5.

Other studies with larger mass gaps of $\Delta M_{\tilde{\chi}_1^\pm,\tilde{\chi}_1^0} = 3\text{-}20\,\text{GeV}$ were also performed at the International Linear Collider. The analysis performed in [76] shows that the properties of higgsinos can be measured to percent level precision. Additionally, the study also showed that with these precisions, GUT and weak scale parameters can be extracted and mass scales of unobserved sparticles can be determined from the measured masses and cross sections. SUSY parameters change with scale governed by a system of coupled differential equations called renormalization group equations

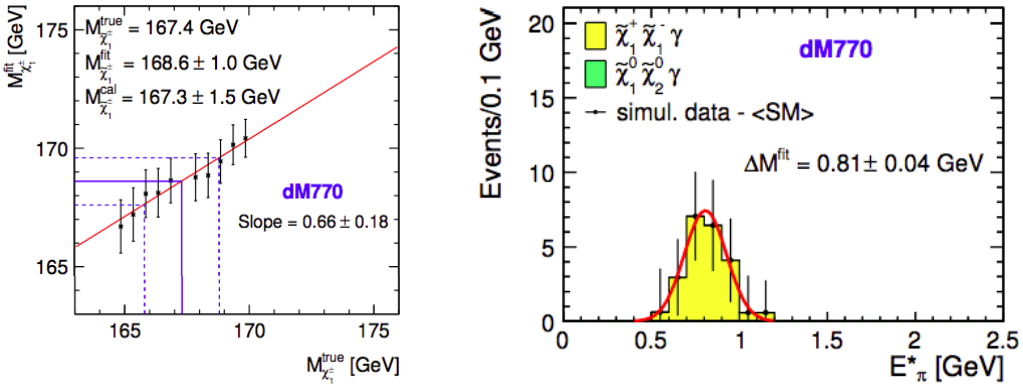

(a) (b)

Figure 2.10.: (a) The reconstructed chargino mass value as a function of the true chargino mass value. (b) The reconstruction of mass difference between the chargino and the LSP. Figure taken from [6].

(RGE). The measured masses and cross sections are given as an input to the RGEs and the three gaugino parameters M_1, M_2 and M_3 are run to the GUT scale. The gaugino masses unify at the GUT scale as can be seen in figure 2.11a. Here, M_3 as constrained from the ILC measurements at the weak scale are taken as an inout. Instead if it is assumed that M_3 unifies with M_1 and M_2 at the GUT scale, then the value of M_3 at the weak scale can be extrapolated as shown in figure 2.11b.

A recent study at the ILC evaluated cross-sections for $\tilde{\chi}^\pm_1$ pair production within a wide range of parameters [77]. This study aimed at determining conditions for lowest cross sections and compare the worst case values with an estimation of the cross section limit for the observation of light charginos at the ILC. The estimated limits were extrapolated from the studies at LEP, which would be considered as the worst-case scenario taking into account the detector and accelerator technologies. A comparison between the mass limits of the higgsino-like $\tilde{\chi}^\pm_1$ for LEP, ILC500 and ATLAS results are shown in figure 2.12. The ILC500 mass limits are extrapolated from LEP results for the Higgsino-like case. The case here considers a worst case scenario for higgsino with high sfermion masses. The study shows that the whole parameter space can be covered in a model independent way. The study concluded that the ILC can discover/exclude $\tilde{\chi}^\pm_1$ up to masses close to the kinematic limit for any mass difference.

In this thesis, Natural SUSY scenarios adopted from [6] with light higgsino-like charginos and neutralinos, $\Delta M_{\tilde{\chi}^\pm_1}$, $\Delta M_{\tilde{\chi}^0_1}$, and $\Delta M_{\tilde{\chi}^0_2}$ at electroweak scale with heavy coloured third generation particles are studied. One of the important factors of such

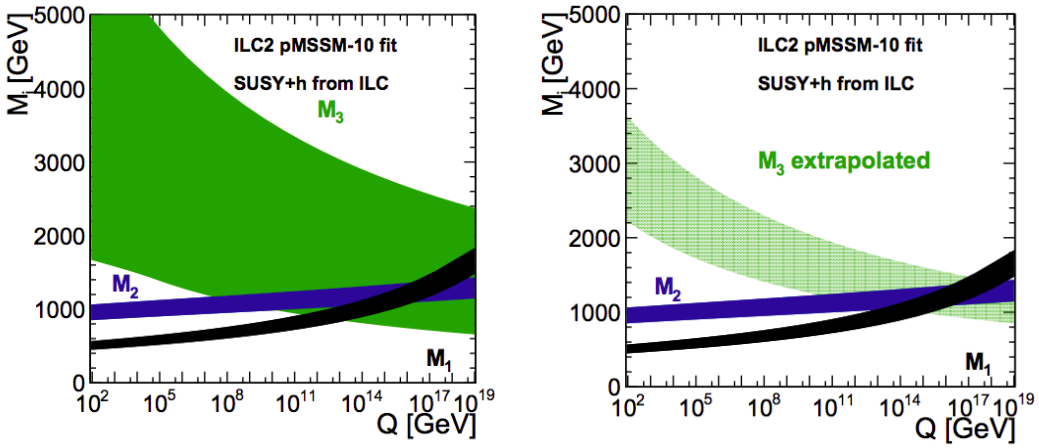

(a) (b)

Figure 2.11.: The running of gaugino masses after extracting their weak scale values from a fit to the observables. (a). Using M_3 at the weak scale as constrained from measurements. (b) M_3 is assumed to unify with the M_1 and M_2 and M_3 is ran back to the weak scale predicting gluino mass. Figure taken from [76].

a scenario is that the particles in electroweak sector are mass degenerate which results in very soft decay particles. Therefore the effects of the $\gamma\gamma \rightarrow$ low p_T hadron decays is investigated in this study. The details about such a study for the International Large Detector of the ILC will be discussed in rest of this thesis.

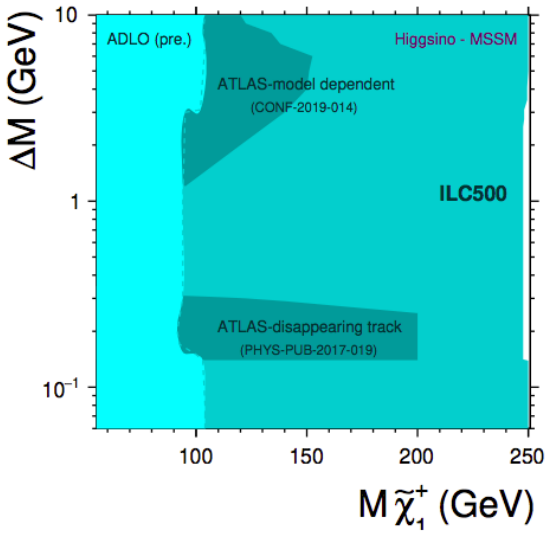

Figure 2.12.: Comparison of the $\tilde{\chi}_1^{\pm}$ mass limits for the higgsino-like case for LEP, ILC500 and LHC [65, 66]. The ILC500 mass limits are extrapolated from LEP results for the Higgsino-like case. Figure taken from [77].

3. The International Linear Collider

In the history of particle physics, e^+e^- colliders have played complementary roles in shedding light on to the properties of elementary particles. For example the top mass was predicted from the Standard Model precision measurements of the LEP experiments and was finally discovered in the predicted energy range at the Tevatron [78, 79]. Similarly was the discovery of gluon at the PETRA [80, 81] or the precise measurement of the Z boson at the LEP and the SLC [82]. The discovery of the top quark helped to put constraints on the Higgs mass in the context of the Standard Model. After the discovery of the Higgs boson at the CMS and the ATLAS experiments of the LHC [1], an e^+e^- collider can perfectly complement the hadron collider to make precision measurements of the Higgs boson.

This chapter introduces the International Linear Collider (ILC) [83] and its experimental environment. Different aspects like advantages and necessity of an e^+e^- linear collider for studies in particle physics are described. The chapter elaborates the design of the accelerator and its subsystems as can be found in different volumes of Technical Design Report (TDR) [84, 85]. The chapter also discusses the operating scenario for the ILC, its beam conditions and different kinds of machine backgrounds.

3.1. Features of e^+e^- Colliders

Some of the features of an e^+e^- collider are presented in detail sections ahead [86]. These features enable a lepton collider to form a perfectly complimentary machine to a hadron collider.

Cleanliness

An e^+e^- collider provides a very favourable environment for physics studies. Production cross sections at hadron colliders are huge. For example at LHC energies, proton-proton total cross section is roughly 100 mb and proton-proton bunch collisions occur every 25 ns. This leads to a huge number of high energetic particles. Multiplicity of processes produced at e^+e^- collider are much lower as compared to

hadron colliders. For example at International Linear Collider (ILC) which will be introduced in section 3.3, bunch crossings are spaced by 554 ns. Backgrounds are dominated by $\gamma\gamma$ collisions having a cross section six orders of magnitude smaller than the background at LHC. This leads to very clean final states at an e^+e^- collider. In the context of this study, the cleanliness is instrumental to resolve the very soft visible decay products of the higgsinos.

Democracy

The coupling of Z and photon to quarks, leptons or even for new particles from beyond the Standard Model is roughly of the same strength. Whereas at the LHC, gluon couples to all quarks and new coloured particles with same strength but not to the leptons. Due to the compositeness of protons, their PDF provides high cross sections for the production of light quarks while the production of heavy quarks has smaller cross section. Since heavy particles only constitute a small fraction of the total particles produced, a trigger system is required to reduce the amount of uninteresting events. At e^+e^- colliders there is not much hierarchy between SM and BSM physics. For example at $\sqrt{s} = 500\,\text{GeV}$ at ILC, the main SM processes in e^+e^- annhilation to quarks and leptons or to W^+W^- or to single W and Z production have cross sections at pb level and new particles coupling with about electroweak strength have cross sections of about 10 - 100 fb. Thus the BSM cross sections are more comparable to SM processes at the same time could be nicely distinguished from the SM processes. This results into an experiment without the need of any trigger system. Moreover, all final states of decaying particles can be used for physics analysis which gives the opportunity to measure absolute branching ratio and total widths. Natural SUSY scenarios with a signature of very soft visible decay particles which would be vetoed at the LHC can be studied at the ILC due to this feature.

Detail

Since the colliding particles are elementary particles, e^+e^- colliders have a very well defined centre-of-mass energy of $\sqrt{s} = 2E_{beam}$. This allows the use of kinematic information and thus gives the opportunity to make model independent measurements. Since hadrons are composite particles the exact kinematic configuration of each collision is unknown at the hadron colliders. The centre-of-mass energy is not equally distributed among the quarks and the gluons.

Another advantage of e^+e^- colliders is that the beams can be polarized. This offers an opportunity to study the processes depending on the polarization state of the initial and final state particles.

Calculability

As the initial state e^- and e^+ are elementary point-like particles they only couple to electroweak interactions. This results in very few percent level radiative corrections to the cross sections. The theorectical cross sections can be improved to a level of part-per-mil using the calculations from LEP. Since both the experimental and theorectical uncertainities are very small, the ILC stands in the advantageous position of being able to look for any deviations from precise SM cross sections. These deviations could be an indication for BSM physics.

3.2. Advantages of a Linear Collider

In contrast to the circular machines for massive protons, using electrons and positrons as beam particles in a circular collider leads to the problem of significant energy loss due to synchrotron radiation. This type of electromagnetic radiation is emitted when relativistic charged particles are subjected to an acceleration. At high energies, leptons are highly relativistic due to their small masses. The radiated photons carry away a huge amount of energy [87]. In case of the circular accelerator, the amount of energy lost, ΔE, depends on the nominal beam energy (E_{beam}), the radius of the circular beam trajectory (R) and the mass of the accelerated particle (m), as shown in the equation below:

$$\Delta E \propto \frac{E_{beam}^4}{Rm^4} \tag{3.1}$$

Since the energy loss is dependent on the particle mass, the distinction between lepton and hadron circular colliders becomes significant. The mass of the electron is almost 2000 times smaller than the proton mass due to which the expected energy loss at circular lepton colliders is much higher. The energy losses can be compensated by increasing the accelerator radius. However, this leads to increase in costs. The cost optimisations for circular colliders show a quadratic growth in costs with beam energy [88]. Considering a linear collider instead of a circular collider would be an effective alternative [89]. In this case the radius $r \to \infty$ thus making $\Delta E \to 0$. However, on the downside the particle bunches can be accelerated and collided only once. Nevertheless, besides solving the issue of synchrotron radiation, linear collider provides the flexibility of having more budget friendly higher beam energies [88]. The number of acceleration modules to achieve the desired beam energies is linearly proportional to the length of the accelerator. In fact, for centre-of-mass energies above 200 GeV, a linear collider is more cost effective than the circular one.

Another important advantage of a linear collider is that the e^- and e^+ beams can be polarised. Polarisation enables reducing the background and enhancing signal as required. For example, the Higgstrahlung process $e^+e^- \to Zh$ is enhanced by

the $\mathcal{P}(e^-, e^+)$ = (-80%,+30%) beam polarisation combination. On the other hand beam polarisation combinations like $\mathcal{P}(e^-, e^+)$ = (+80%,-30%) help the new physics searches like SUSY searches to suppress the Standard Model background. A detailed review of the benefits of electron and positron beam polarisation for the physics reach of ILC can be found in [90] and [91].

3.3. The International Linear Collider

The International Linear collider (ILC) is a proposed e^+e^- collider which will be designed such that it can be tuned between different centre-of-mass energies from 250-500 GeV with a possible upgrade to 1 TeV. The ILC is planned as a complementary machine to the LHC to perform precision measurements of known and possibly new particles. Japan shows interest in hosting the ILC and started reviews on the project. The mountainous region of Kitakami in the Iwate region of Japan is decided as the candidate site for the ILC [92]. After the Linear Collider Workshop 2016 in Morioka, significant changes with respect to the TDR times were made in the ILC plans. Motivated by the requests from the Japanese ministry to reduce the project budget, an initial funding for 250 GeV accelerator instead of 500 GeV accelerator was proposed. The final integrated luminosities gathered are supposed to be the same as previously planned: $2\,\text{ab}^{-1}$ at $\sqrt{s} = 250\,\text{GeV}$ and $4\,\text{ab}^{-1}$ at $\sqrt{s} = 500\,\text{GeV}$ and $200\,\text{fb}^{-1}$ at $\sqrt{s} = 350\,\text{GeV}$. The real-time duration of this program is ∼22 years [93].

Even though the Japanese government has declared its interest in the project, a final statement on hosting the machine is still pending owing to the negotiations with other countries for the cost sharing of the multi-billion dollar machine. Since the particle physics community in Europe was updating the European strategy for particle physics, [83, 94, 95] were submitted as updates on the recent developments of the International Linear Collider.

3.3.1. Design and Features

The ILC is presently the most advanced linear collider project. Since the analysis in this thesis is for processes at 500 GeV, the baseline design of the ILC accelerator for 500 GeV machine is presented in figure 3.1. A very brief description of the machine is given in sections ahead. A detailed review of the accelerator design and considered technologies is presented in [96] and [85]. The baseline design for the 250 GeV machine has the same properties except the length of the main linac. The detailed plan and accelerator design for 250 GeV stage of the ILC is described in [97].

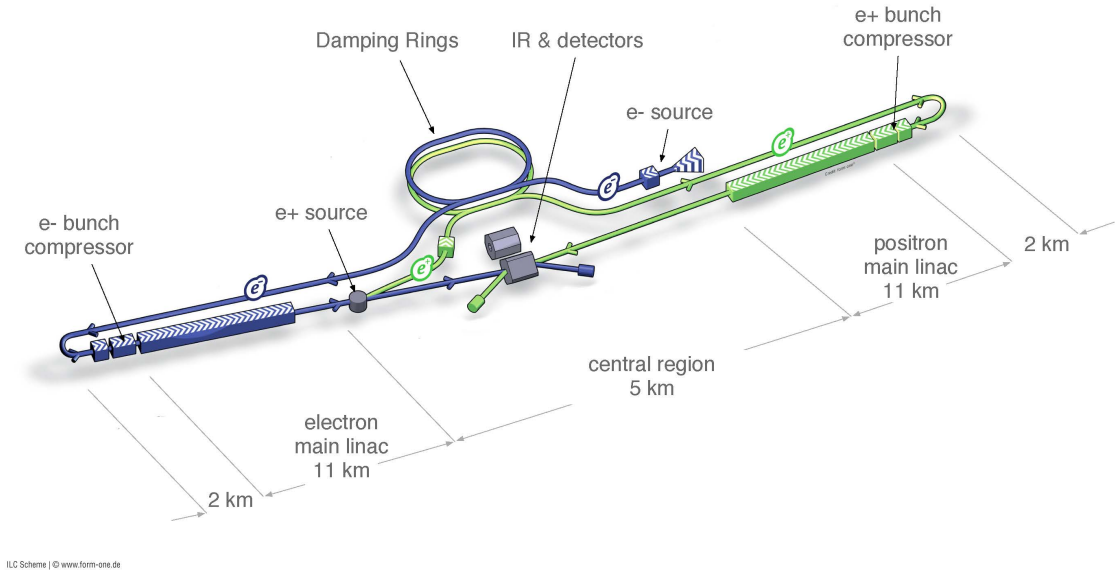

Figure 3.1.: The schematic design of International Linear Collider for 500 GeV machine. The picture is taken from [84]

Electron and positron sources

The electron beam is produced using circularly polarised laser directed at a strained gallium-arsenide (GaAs) photocathode, where electrons are emitted via the photoelectric effect. By this technique, a degree of longitudinal polarisation of 85% can be achieved, which is above the ILC design requirement of 80%. The energy of electrons is increased from the original 200 keV to 5 GeV using a pre-accelerator, before it reaches the damping rings.

Polarised positron sources are produced in a completely different process in which fully accelerated electrons with an energy of 125-250 GeV are used. This is the reason why the positron source is located after the main e^- linac, as shown in the figure 3.1. The electrons are directed through a $\approx$ 150 m long helical undulator where they produce circularly polarized photons via synchrotron radiation. These high energy photons convert into electron-positron pairs when aimed at a rotating titanium alloy target. These positrons have a polarisation of 30%. Both electron and positron have a very high emittance at this stage. To bring the emittance to the required level the beams are directed towards the damping rings.

Damping rings

The damping rings are a very important component of any linear collider. The vertical emittance of the e^+ and e^- beams have to be reduced by five orders of magnitude to reach 20 nm in order to achieve the ILC luminosity goals. Each beam comprises one damping ring each with a circumference of 3.2 km. Both the beams are guided through a 100 m long wiggler. The wiggler makes the e^- and e^+ beams to emit synchrotron radiation along with which a radio frequency (RF) module accelerates the beams only in their direction of motion. As a product the bunches become more parallel, aligned and have less emittance. Both the beams leave the damping rings with the same energy of 5 GeV as before and much lower emittance.

Ring to Main Linac

The ring to main linac is a system consisting of $\approx$ 15 km of transport line for 5 GeV beam particles, a 180° turn-around which enables feed-forward beam stabilization, spin rotators which turn the beam polarisation to desired direction and a two-stage bunch compressor to reduce the longitudinal beam size from several millimeters to a few hundred microns. The two stage compressor also accelerates the bunches from 5 GeV to 15 GeV.

Main Linac

The 15 GeV bunches are injected into two main linac systems for electron and positron and are accelerated up to an energy of 250 GeV. Each main linac consists of approximately 7400 nine-cell niobium cavities. These cavities are about 1 m long and are cooled down to about two Kelvin where the cavity material becomes superconducting. This property enables the use of a high electric field gradient of about 31.5 MeV/m. The niobium cavities are operated at a RF frequency of 1.3 GHz [85].

Beam Delivery System

The beam delivery system (BDS) forms the final part of the accelerator. It is 3.5 km long and it transports the beam bunches from the main linacs to the interaction region (IR). At the interaction region, the e^- and e^+ beams are focused and brought to a size of a few nanometers using a superconducting quadrapole and sextupole magnets. The electron and the positron bunches collide at the interaction point (IP) with a crossing angle of 14 mrad [85, 98]. The crossing angle ensures that the spent beams are safely separated from the incoming beams. The design of the ILC is such that it allows the operation of two detectors, which can be given access or taken off from the beam line via a push-pull system. The remnants of the collided beams are dumped into a 11 m long, high-pressure water dump which can absorb

as much as 14 MW which is the beam power at the highest possible energy upgrade for the ILC.

3.3.2. ILC Operating Scenario

The ILC has been designed to measure different physics processes that can be acquired at tunable centre-of-mass energy $\sqrt{s}$ = 200 - 500 GeV, with an instantaneous luminosity $L = 2 \times 10^{34}\,\mathrm{cm}^{-2}\mathrm{s}^{-1}$ at 500 GeV (upgradable to 1 TeV) and 80% polarisation for electrons and 30% polarisation for positrons [85]. The ILC operating time is divided in different ways with respect to different centre-of-mass energies and beam polarisations.

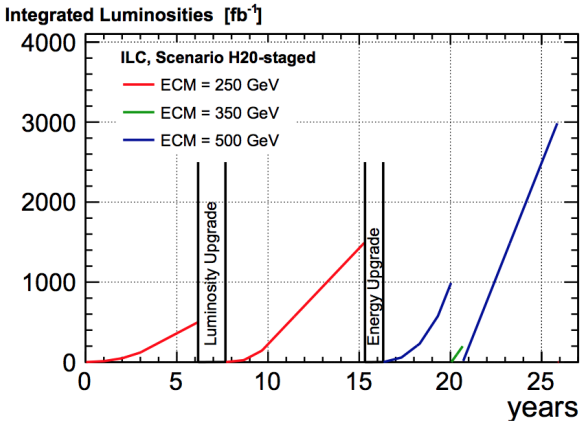

Figure 3.2.: Possible ILC running scenario with a starting energy of 250 GeV and subsequent energy upgrades [93].

Different ILC operating scenarios were studied by the ILC Parameters Joint Working Group. The details of this study are presented in [99]. These studies are based on extrapolations of physics results published in [86]. The three important aspects of the ILC physics programme are: *(i)* precision measurements of Higgs boson, *(ii)* detailed measurements of top quarks and *(iii)* search for new particles beyond the Standard Model (SM). The ILC also aims at studying other topics like the precise studies of W and Z bosons, detailed electroweak measurements, QCD etc. A complete overview of the different physics programmes at the ILC can be found in the physics volume of the Technical Design Report for the ILC [86], a summary of the physics case at the ILC [93], an interim design report as an update to the TDR [100] and an input to the European strategy 2020 [101].

The operating scenario which was recommended by the ILC Parameters Joint Working Group is termed as H20 scenario and is the most relevant for this thesis. As mentioned in section 3.3, with the intention of cost reduction, the initial stage

of operation for the ILC changed to 250 GeV instead of 500 GeV. Accordingly, an updated operating scenario where the initial stage of operation would be at a centre-of-mass energy of 250 GeV is summarised in figure 3.2. The details of this scenario is given in [99].

The data collection for different centre-of-mass energies is shown in table 3.1. At a centre-of-mass energy 500 GeV, it is possible to perform precise measurements of the Higgs coupling to the top quark and the Higgs self-coupling, as well as direct searches for new particles. At a centre-of-mass energy of 350 GeV, 200 fb^{-1} of data is collected. This enables to study the mass of top quark by performing energy threshold scan, in addition to precision measurements of the Higgs-W and Higgs-Z couplings. A data of 500 fb^{-1} is accumulated at a centre-of-mass energy of 250 GeV where the machine operates as a Higgs factory. The relevant precision measurements of Higgs are performed at this stage.

$\sqrt{s}$[GeV]		(−,+)	(+,−)	(−,−)	(+,+)
250	fraction [%]	45	45	5	5
	$\int \mathcal{L}dt$[fb^{-1}]	900	900	100	100
350	fraction [%]	67.5	22.5	5	5
	$\int \mathcal{L}dt$[fb^{-1}]	135	45	10	10
500	fraction [%]	40	40	10	10
	$\int \mathcal{L}dt$[fb^{-1}]	1600	1600	400	400

Table 3.1.: The integrated luminosities that would be accumulated at three different centre-of-mass energies. The fractions of e^- and e^+ helicities contributing to the beam are also presented [83].

The luminosity upgrade provides a further collection of 3500 fb^{-1} data at 500 GeV. Better precision measurements of top Yukawa coupling and Higgs self-coupling is possible with more accumulated data.

3.4. Beam conditions at the ILC

In this section the beam conditions at the interaction point, which define the environment for the experiments, will be discussed. The properties like luminosity, beam backgrounds etc. of the beam are mentioned in detail in further sections.

3.4.1. Beam Parameters

The cross section and the luminosity define the event rate $N_{evt} = \sigma \times \mathcal{L}$ of a certain physics process. The beam luminosity and centre-of-mass energy depend on various

other parameters that concern the ILC particle bunch structure [85]. The ILC baseline design expect a repetition rate of f_{rep} [Eq 3.2] = 5 Hz at which the bunch trains are accelerated. A bunch train consists of n_b = 1312 bunches, each of which abide $N = 2 \cdot 10^{10}$ particles. Each bunch crossing is separated by Δt_b = 554 ns. For the luminosity upgrade, number of bunches per pulse is doubled to n_b = 2625. The baseline beam parameters of the ILC are given in table 3.2.

Centre-of-mass energy	$\sqrt{s}$	GeV	250	350	500
Luminosity pulse repetition rate	f_{rep}	Hz	5	5	5
Bunch population	N	$\times 10^{10}$	2	2	2
Number of Bunches	n_b		1312	1312	1312
Bunch separation	Δt_b	ns	554	554	554
RMS bunch length	σ_z	μm	300	300	300
RMS horizontal beam size at IP	$\overline{\sigma}_x$	nm	729	684	474
RMS vertical beam size at IP	$\overline{\sigma}_y$	nm	7.7	5.9	5.9
Luminosity	$\mathcal{L}$	$\times 10^{34}\mathrm{cm}^{-2}\mathrm{s}^{-1}$	0.75	1.0	1.8
Fractional RMS energy loss	δ_{BS}	%	0.97	1.9	4.5

Table 3.2.: Summary table of the ILC baseline beam parameters for the energies 250 GeV, 350 GeV and 500 GeV ILC [85].

3.4.2. Beam Luminosity and luminosity spectrum

Figure 3.3 shows the production cross sections for various SM processes and new physics as a function of centre-of-mass energy. The cross sections are seen to be decreasing with an increasing centre-of-mass energy [102]. With higher luminosity values, better statistical evaluation and precise measurements can be performed. The luminosity is given by Eq. (3.2)

$$\mathcal{L} = \frac{n_b N^2 f_{rep}}{4\pi\sigma_x\sigma_y} H_D \tag{3.2}$$

where n_b and N are the number of colliding bunches per pulse and the number of colliding particles per bunch, f_{rep} is the pulse repetition rate and σ_x and σ_y are the bunch sizes in the transverse directions, respectively. H_D is an additional enhancement factor which accounts for non-linear effects in the beam-beam interaction which will be explained later in this section.

The distribution of centre-of-mass energies using the beam parameters introduced in section 3.4.1 is known as the luminosity spectrum. It has a peak about the nominal centre-of-mass energy and tail towards the lower energy. The beam spectra for a

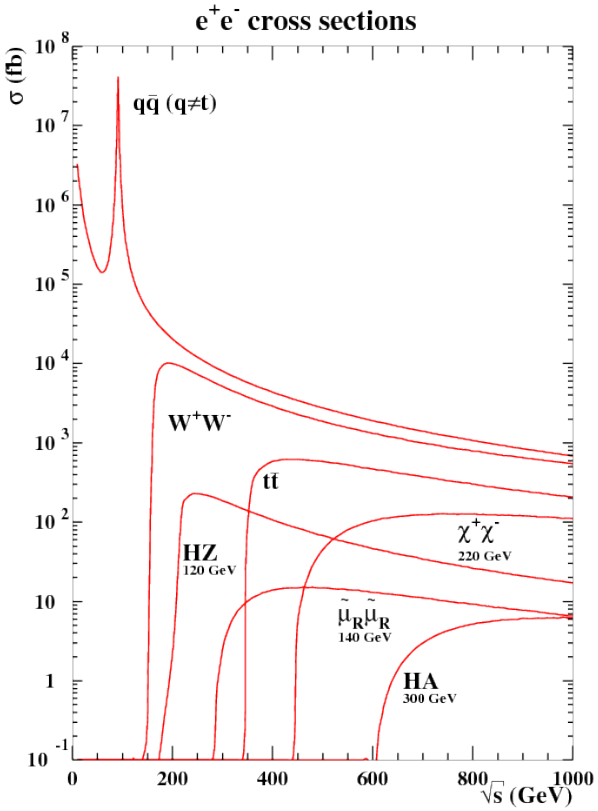

Figure 3.3.: The production cross section of the various Standard Model processes and new physics processes as a function of centre-of-mass energy at the ILC [102].

centre-of-mass energy of 500 GeV is shown in figure 3.4. The tail to lower energies is due to the nanometer-sized beams.

High luminosity for the linear collider is obtained by colliding intense bunches of nanometer-sized e^+e^- beams. The tiny bunch sizes implies that bunches have a very high space charge and are thus accompanied by a strong electric field which are compressed to a thin disc due to relativistic effects. The collective field of one bunch can exert a significant amount of force on the oncoming bunch of opposite charge. As a result the bunches are attracted towards each other and the individual particles are accelerated towards the centre of the oncoming bunch as shown in figure 3.5. This mutual attraction is called as the *pinch effect* [104, 105]. In this process, the beams are focused and the beam sizes are reduced thus increasing the luminosity. This effect is accounted for by the so called beam enhancement factor H_D in Eq. (3.2) defined as the ratio of the effective luminosity to the nominal luminosity due to

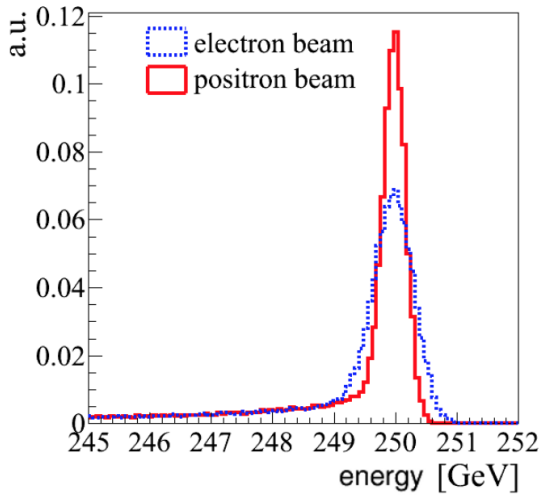

Figure 3.4.: Beam energy spectra of electron and positron beams at the interaction point for a centre-of-mass energy 500 GeV generated with `Guinea Pig`. Figure taken from [103]

.

change in beam size:

$$H_D = \frac{\overline{L}}{L} = \frac{\sigma_x \sigma_y}{\overline{\sigma}_x \overline{\sigma}_y} \tag{3.3}$$

where σ_x and σ_y are the bunch sizes and $\overline{\sigma}_x$ and $\overline{\sigma}_y$ are the reduced bunch sizes after the pinch effect. The smaller the bunch sizes the larger is H_D and higher is the luminosity. More details about the luminosity enhancement factor is given in section 3.4.4.

3.4.3. Beam Polarisation

The e^+/e^- beams at the ILC are planned to be longitudinally polarised. The production cross section for a polarised beam can be calculated as [106]:

$$\begin{aligned}\sigma(P_{e^+}, P_{e^-}) = \frac{1}{4}\{&(1+P_{e^+})(1-P_{e^-})\sigma_{RL} + (1-P_{e^+})(1+P_{e^-})\sigma_{LR} \\ &+ (1+P_{e^+})(1+P_{e^-})\sigma_{RR} + (1-P_{e^+})(1-P_{e^-})\sigma_{LL}\}\end{aligned} \tag{3.4}$$

where σ_{ij} $(i,j \in L,R)$ are the polarised cross sections where i corresponds to positron polarisation and j to the electron polarisation.

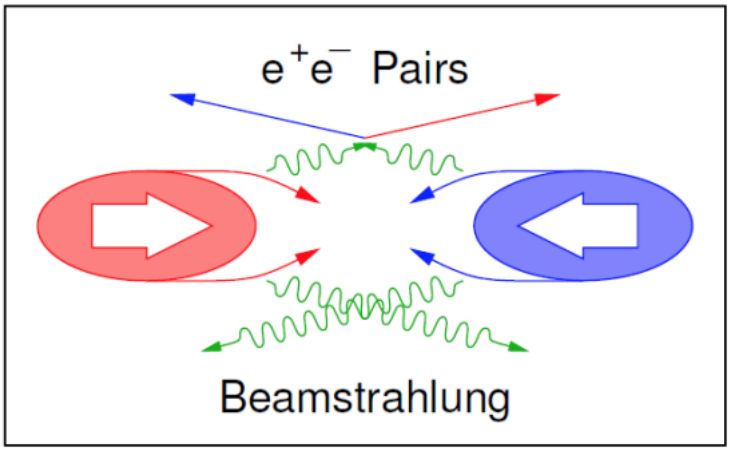

Figure 3.5.: Illustration of the pinch effect in bunch collisions. The particles of one bunch are attracted due to the electric field of the other and emit photons due to their deflection. Picture taken from [105].

Using an appropriate beam polarisation combination, the new physics searches can benefit by suppressing the Standard Model background while in some other studies e.g. Higgstrahlung processes, the signal can be enhanced. Also, for the cases where the desired signal and background have same polarisation dependence, it has to be noted that the significance of a discovery is proportional to $S/\sqrt{B}$. Therefore, even by enhancing both the signal and the background by a factor of two would improve the significance by $\sqrt{2}$. A detailed review on the benefits of electron positron beam polarisation is given in [90, 91].

3.4.4. Beam Induced Backgrounds

Beamstrahlung

As discussed in section 3.4.2, the pinch effect reduces the beam size and enhances the beam luminosity. However, the deflection of the beam particles due to the charge of the incoming bunch also results in radiation of photons. The bending of particle trajectories under the influence of the EM fields of the oncoming beam is called disruption and the radiation of photons due to this bending is known as beamstrahlung. The disruption parameter that defines the amount by which the oncoming bunch is deformed is given as [107]:

$$D_{x(y)} = \frac{2Nr_e}{\gamma}\frac{\sigma_z}{\sigma_{x(y)}(\sigma_x + \sigma_y)} \tag{3.5}$$

where N is the number of particles in a bunch, r_e is the classical electron radius, γ is the relativistic factor $E_{beam}/m_e c^2$, σ_z is the longitudinal bunch length while σ_x and σ_y are the bunch sizes in transverse direction. The overall beamstrahlung intensity is given by a global *beamstrahlung parameter* Υ_0 which is dependent on the original sizes of the beam (Eq. 3.6).

$$\Upsilon_0 = \frac{5}{6}\frac{r_e^2\gamma N}{\alpha\sigma_z(\sigma_x + \sigma_y)} \tag{3.6}$$

where α is the fine structure constant. The value of the reduced beam size (effective beam size) is determined from the luminosity enhancement factor introduced in Eq. 3.3. The luminosity enhancement factor can only be calculated analytically in $D_{x(y)} << 1$ limit. Beyond this limit the dynamics of beam-beam interaction becomes non-linear and one has to use simulations to determine the values of H_D. For $\sigma_x/\sigma_y = 1$, simulations give [108, 109]:

$$H_D = 1 + D^{1/4}\Big(\frac{D^3}{1+D^3}\Big)\Big\{ln(\sqrt{D}+1) + 2ln(0.8/A)\Big\} \tag{3.7}$$

where $A = \sigma_z/\beta^*$ and β^* is the Courant-Snyder β function [110]. Therefore for round beams, the effective beam size is roughly given as:

$$\overline{\sigma} = \sigma H_D^{-1/2}. \tag{3.8}$$

However, since in the the realistic high energy e^+e^- colliders beams are flat with $\sigma_x/\sigma_y > 5$, the value for H_D, D and A are different for x and y directions. Using Eq. 3.7 separate values for H_{D_x} and H_{D_y} are calculated. Also the field strength in a flat beam is is largely determined by σ_x rather than σ_y. Using these arguments the effective beam sizes are deduced as:

$$\overline{\sigma}_x \sim \sigma_x H_{D_x}^{-1/2}, \qquad \overline{\sigma}_y \sim \sigma_y H_{D_y}^{-1/3} \tag{3.9}$$

with the effective beam sizes estimated, the effective beamstrahlung parameter is estimated as:

$$\Upsilon = \frac{5}{6}\frac{r_e^2\gamma N}{\alpha\sigma_z(\overline{\sigma}_x + \overline{\sigma}_y)} \tag{3.10}$$

In terms of the effective beamstrahlung parameter the rate of the radiating photons with energy x is derived as [107]:

$$\overline{\nu}(x) = \frac{1}{2}\Big[(1+x)\nu_{cl} + (1-x)\nu_\gamma\Big] \tag{3.11}$$

where ν_{cl} is the number of soft photons radiated per unit time, calculated using the classical theory of radiation [109, 111]:

$$\nu_{cl} = \frac{5}{2\sqrt{3}} \frac{\alpha^2}{r_e \gamma} \Upsilon, \tag{3.12}$$

and ν_γ gives the number of hard photons where the quantum mechanical calculation gives a general formula as [109, 111]:

$$\nu_\gamma = \nu_{cl}[1 + \Upsilon^{2/3}]^{-1/2}. \tag{3.13}$$

The photons created at the interaction point results in three different types of $\gamma\gamma$ interactions. The interaction between virtual photons emitted by the e^+ and e^- bunches, the interaction between a beamstrahlung and a virtual photon and finally interaction between two beamstrahlung photons all of which result into beam backgrounds. When two photons collide, it is kinematically possible to produce a $f\overline{f}$ pair as explained in section 2.3.3. At energies below $2M_\pi$, the photon-photon collision only produce e^+e^- pairs. Once $\sqrt{s_{\gamma\gamma}}$ crosses the threshold of $2M_\pi$, the production of hadrons becomes possible which due to the strength of strong interactions dominate over the production of $\gamma\gamma \to e^+e^-$ or $\gamma\gamma \to \mu^+\mu^-$ processes. These $\gamma\gamma \to$ hadron production below $\sqrt{s_{\gamma\gamma}} < 20\,\text{GeV}$ are called as $\gamma\gamma \to$ low p_T hadron backgrounds. These backgrounds are defined in the sections below.

$\gamma\gamma$ Background

The $\gamma\gamma \to$ low p_T hadron backgrounds receive contributions from real beamstrahlung photons and virtual photons from e^+ and e^- bunches. Their cross sections highly depend on the centre-of-mass energy of e^+e^- collisions. $\gamma\gamma$ backgrounds occur at a rate of $< N > = 1.05$ events per bunch crossing at a centre of mass energy 500 GeV as will be explained in section 5.3.2. The particles produced in these interactions are typically very low p_T hadrons which appear mostly in the forward direction of the detector. These events act as a pile-up to any other physics processes. Especially, for processes which decay into very low p_T particles these backgrounds are very important. This thesis mainly focuses on developing an alternative method from the standard existing methods to remove these backgrounds. More details about these backgrounds are given in Chapter 5 and in Section 6.2.2.

e^+e^- Pair Backgrounds

e^+e^- pairs are mainly produced by scattering of two beamstrahlung photons. Typically with the given beam parameters approximately 10^5 e^+e^- pairs are created per bunch crossing. Due to their low p_T they mostly curl up in the magnetic field of the

detector. These backgrounds are important in BeamCal studies and in determining the radius of the vertex detector and shape of the beampipe. An attempt to remove the residual pair background using the newly developed method to remove the $\gamma\gamma$ background in done in this study. More details about this backgrounds are given in Section 6.2.2.

4. The International Large Detector Concept

The International Linear Collider plans to perform physics measurements using two different experiments which would share the same interaction point through a push-pull system. The two planned detectors for the ILC are the International Large detector (ILD) [83, 84, 112, 113] and the Silicon Detector (SiD) [83, 84, 114]. Both detectors are based on the particle flow approach (section 4.3). The main difference between the detectors is their central tracking system. SiD will employ a five layered silicon tracker system while ILD will be having a Time Projection Chamber. Since this thesis is based on the full detector simulation for the ILD, details of ILD are mentioned in rest of this chapter. More details about SiD can be found in [84].

4.1. Overview of detector components

A schematic view of the ILD is shown in figure 4.1. An overview of the detector components is given as follows: The most central component is the vertex detector followed by a tracking system with a time-projection chamber (TPC) as the main tracker surrounded by a complete silicon based tracking system.

The calorimetric system has an electromagnetic calometer (ECAL) and a hadronic calorimeter (HCAL). A surrounding superconducting coil provides a magnetic field of 3.5 Tesla. The detector is then enclosed by a return yoke, which is mainly employed to recover energy leakage from the calorimeters and for muon identification. The main calorimeter systems consist of a cylindrical barrel and two end caps. The detector also has calorimeters like the LumiCal, the LHCal and the BeamCal in the forward region. With LHCal the hadronic coverage is extended to the forward region while the BeamCal is closest to the beam pipes measuring pairs from beamstrahlung and neutral hadrons and the LumiCal monitors the luminosity. The studies presented ahead are performed with a detailed `GEANT4` [115] based full detector simulation for the ILD.

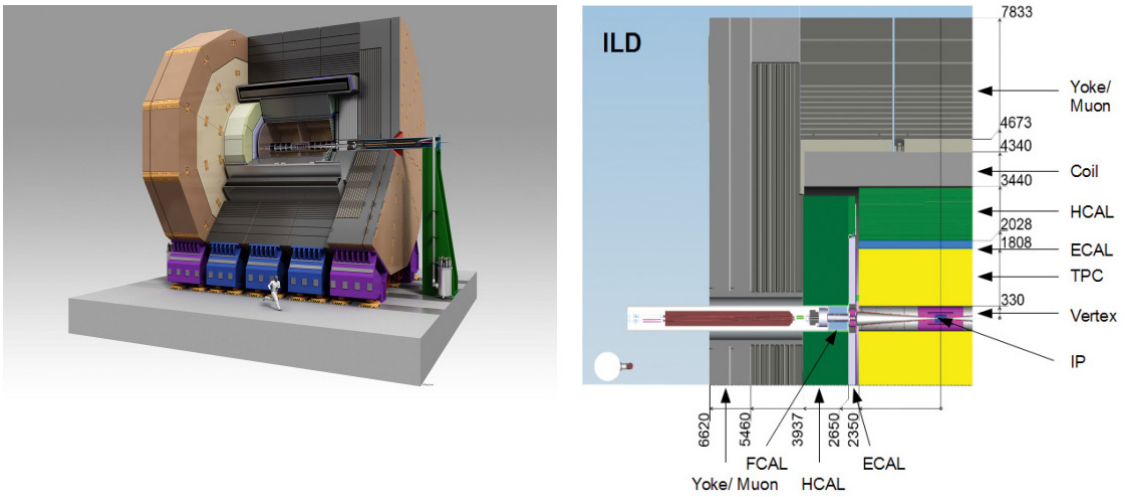

Figure 4.1.: Schematic view of the ILD detector concept. The interaction point in the quadrant view (right) is in the lower right corner of the picture. Dimensions are in mm.

4.2. Coordinate system of the detector

The coordinate system for the ILD [116] is cartesian and right-handed. Its origin is located at the nominal point of interaction. The z-axis lies between the axes of the beams and the y-axis points upwards. The crossing angle is in the horizontal plane and the incoming (outgoing) beams are in negative (positive) x-direction, as shown in the figure.

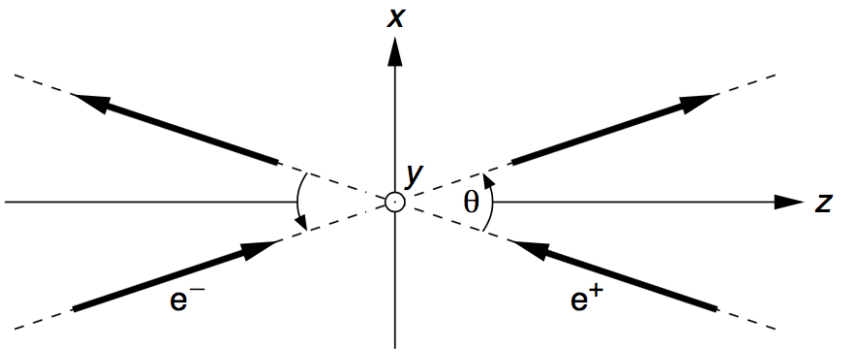

Figure 4.2.: Top view of the ILD coordinate system for a crossing angle geometry $\theta > 0$.

4.3. Particle Flow Concept

The detectors for the ILC are optimized for the particle flow concept. This implies that all the particles in an event, whether charged or neutral, are reconstructed individually [117, 118]. Depending on the particle type, the energy is measured in different sub-detectors. The momenta of the charged particles are measured in the tracking system while the energies of neutral particles are obtained through the calorimeters. This requires a very good interplay between the tracking system and the calorimeters.

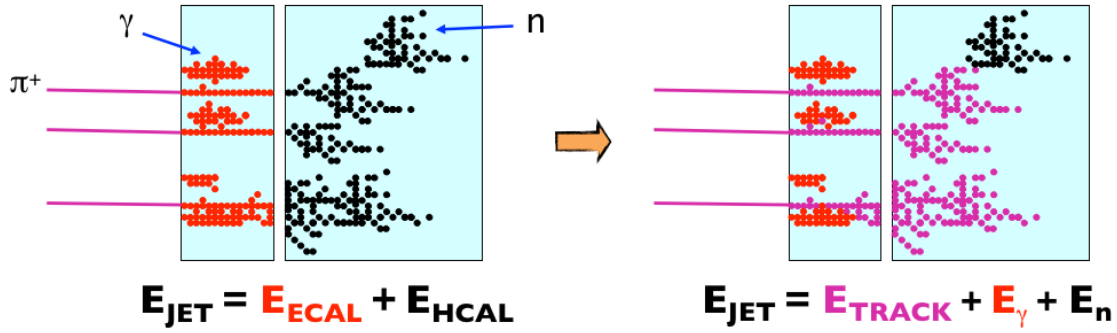

Figure 4.3.: Comparision between the traditional calorimetric approach (left) to particle flow calorimetry (right). Figure taken from [117].

Out of the total jet energies, on average 62% is carried away by charged particles, 27% by photons, 10% by long lived neutral hadrons and 1.5% by neutrinos. Traditional calorimeters evaluates jet energies by combining energy measurements from the electromagnetic calorimeter (ECAL) and the hadronic calorimeter (HCAL). With this method 72% of the jet energy is measured in HCAL which has the worst energy resolution of all detector subsystems [118].

The particle flow concept has a completely different approach where only the photon and the neutral hadron energies are measured in the calorimeters. This means that only $\sim$ 10% of the jet energy is measured in the HCAL and therefore affected by its poor energy resolution. This results in an overall energy resolution of $\sim 20\%/\sqrt{E(\mathrm{GeV})}$ [118]. However, this requires a perfect assignment of calorimeter energy deposits to correct particle tracks and a perfect separation of nearby showers. In real life this cannot be fully achieved. Thus the most most basic requirement of the detector design is to have a high granularity of the calorimeters to allow the reconstruction of individual particles and match clusters with tracks as closely as possible.

Component	Detector	Average Energy fraction	Intrinsic resolution
Charged particle $X^{\pm}$	Tracker	$\sim 0.6 E_{jet}$	$10^{-4} E^2_{X^{\pm}}$
Photon γ	ECAL	$\sim 0.3 E_{jet}$	$0.15\sqrt{E_{\gamma}}$
Neutral hadrons h^0	HCAL	$\sim 0.1 E_{jet}$	$0.55\sqrt{E_{h^0}}$

Table 4.1.: Jet energy resolutions for different types of particles. The jet energy fraction carried away by these particle types and their energy resolutions are given. Table taken from [118].

4.4. The Vertex Detector

The interaction point (IP) is surrounded by a multilayer vertex detector, consisting of three double layers of silicon pixel sensors. The vertex detector plays a very important role in detecting low p_T tracks and achieving a high performance identification of heavy flavour quarks and τ leptons. The geometry of ILD allows the innermost layer of vertex detector to have an angular coverage of $\cos|\theta| \simeq 0.96$ [84]. An impact parameter resolution of the order of $\sigma_{R-\phi} = 5 \oplus 10/[p \sin^{3/2}(\theta)]\,\mu$m is required to reach the level of precision envisioned at the ILC. The impact parameter is the transverse distance in the $R-\phi$ plane, between the point of closest approach of the particles's trajectory and the interaction point [98].

A few aspects as given ahead are taken into account while designing and optimizing the vertex detector.

Spacial Resolution: Accurate track measurements close to the IP can only be performed if the spatial resolution near IP is less than $3\,\mu$m. Such a requirement is important to achieve the goal of precise flavour tagging of heavy particles. Also, the errors that can occur in the Particle Flow reconstruction are reduced and is thus very important for separation of neighbouring tracks.

Position of first measurement: Desired flavour tagging performance can be achieved only if the first measurement of the track is made very close to the IP. Therefore the first layer of the detector should be located at a radius of nearly 1.6 cm to be as close to the beam pipe.

Material Budget: A huge number of secondary particles maybe created due to the interaction of the primary particles with the detector material. This might lead to an increased level of confusion and thus affecting the Particle flow reconstruction. To keep this in check it is important that the material budget is below 0.15% of a radiation length (X_0) per layer.

Occupancy: The occupancy of the detector's pixels must be lower than a few percent in order to reduce the potential confusion in track separation.

The ILD vertex detector is based on a cylindrical structure consisting of three, double-sided and concentric sensitive layers where each layer contains pixel sensors on both sides. Two sensors on the opposite sides of the same layer are separated by a distance of 2 mm. This ensures that, for every particle passing through all the three layers, six measurements can be performed. The material budget designated to each of the three layers is below 0.15% per layer. The radial distance (measured from the IP) occupied by the vertex detector is approximately between 16 mm to 60 mm and the first track measurement is performed at a distance of 16 mm from the IP. z_0 is the distance from the IP to the point of closest approach on the track in z-axis as presented in figure 4.6. Similarly, d_0 is the distance from the IP to the point of closest approach on the track in $x - y$ plane as can be seen in figure 4.5 [119].

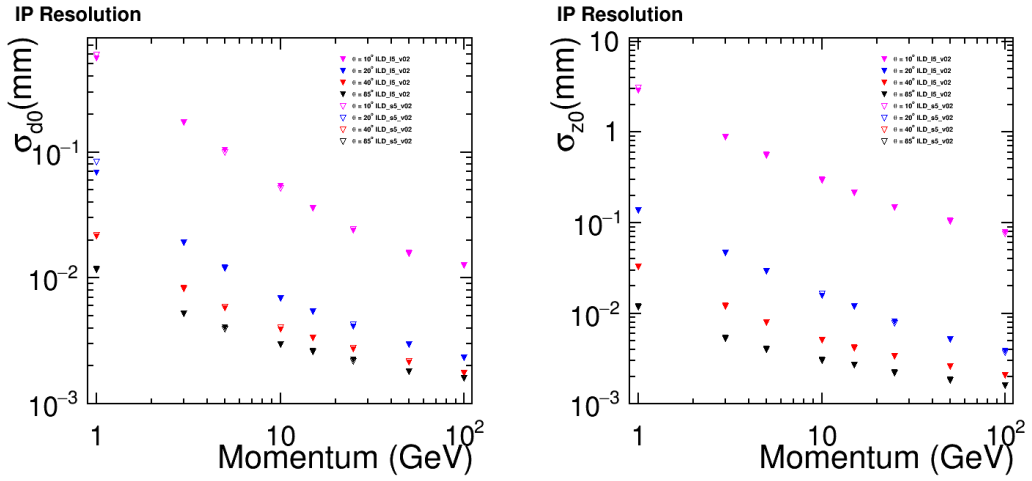

(a) (b)

Figure 4.4.: The impact parameter resolution as a function of momentum. Left: impact parameter resolution in $x - y$ plane. Right: impact parameter resolution in the z direction. Figure taken from [100].

The vertex detector performance of ILD is illustrated in figures 4.4. The left figure shows the impact parameter resolution in the $x - y$ dimension (d_0) and the right plot shows the impact parameter resolution in the z dimension (z_0).

4.5. The Tracking System and its Performance

The vertex detector is surrounded by the tracking system of which the central detector is a Time Projection Chamber (TPC). The TPC consists of a gas filled large sensitive volume with low material budget with a cathode in the centre and two anodes in the end plates. When a charged particle passes through the sensitive volume, it interacts with the atoms of the gas and ionises them. The electron-ion pairs thus created move due to the homogeneous electric field applied between the anode and the cathode. The electrons travel towards the anode while the ions travel towards the cathode. The detector is placed inside a superconducting solenoid coil which provides a magnetic field of 3.5 T in order to determine the momentum of the particles. A two-dimentional projection of particle trajectories are obtained from the readout of the amplified electron signal. An external time reference is used to measure the time between the particle passing the TPC volume and the arrival of the electron at the readout system. The third dimension of the projection of a particle trajectory (position of the track in z-direction) is obtained using the measured time and known drift velocity of the gas. A detailed description of this technique is given in [120]. The TPC is capable of recording 224 three dimentional space points per particle track and hence provide huge pattern recognition capabilities. A momentum resolution of $\delta(1/p_T) \approx 10^{-4}\,\mathrm{c/GeV}$ can be achieved as a result of large number of measurement points. Another important advantage of the TPC is the dE/dx method for particle identification. Momenta of individual particles are measured through energy loss dE per track length dx varying for different particles. The amount of energy deposited by each particle in the TPC is different for each type of particle that crosses its volume with same momentum [44]. The dE/dx measurements thus form a great tool for particle identification.

The TPC is sandwiched between the silicon part of the tracking system, which consists of Silicon Inner Tracker (SIT) and Silicon External Tracker (SET). These systems connect the TPC to the vertex detector and the calorimetric system, respectively. Particulary the SIT is very important with respect to the study presented in this thesis. The SIT improves the reconstruction of low p_T tracks and therefore plays an important role in the identification of low p_T decay tracks from the decay of charginos and low p_T background from the $\gamma\gamma$ overlay (section 3.4.4). The Forward Tracking Detector (FTD) is the last silicon detector in the tracking system. It is located in the forward region where the TPC does not have any access. The FTD is made up of seven tracking disks that are located between the beam pipe and the inner field cage of the TPC. The whole tracking system covers the polar angle region down to 7°.

The track parametrisation done at the perigee yields five different track parameters namely, the track curvature $\Omega = 1/R$, the impact parameters d_0 and z_0, and

the direction parameters ϕ_0 and $\tan\lambda = 1/\tan\theta$ [119]. Assuming that all the tracks originate at the centre of the detector and using the momentum of the particle these five parameters at the perigee are determined. The concept of track parametrisation is sketched in figure 4.5 and figure 4.6.

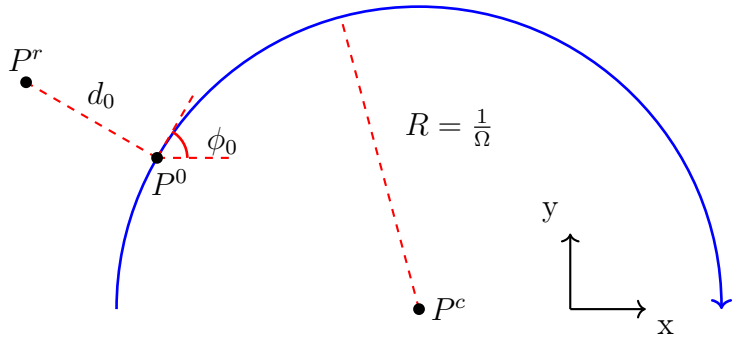

Figure 4.5.: The projection of a helix segment in the xy plane as a part of an arc with centre P^c and radius R. The direction of the particle is shown with the arrow at the arc. All the track parameters are relative to the reference point P^r. Figure taken from [119].

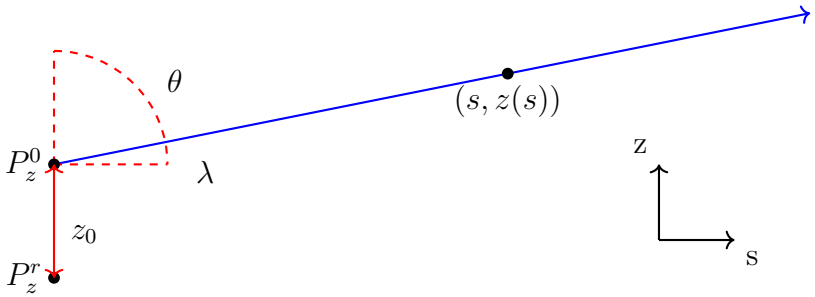

Figure 4.6.: The projection of a helix segment in the sz plane as a straight line. The variable s at a point P is the arc length in the xy plane from P^0 to P. This implies that $s = 0$ if $z = z_0$. Figure taken from [119].

The tracking performance is illustrated in figure 4.7 and figure 6.3. The transverse momentum resolution of the entire tracking system as the function of track momenta for single muon events is depicted in the plot. The momentum resolution goal for $\theta = 85°$ is reached over the entire momentum range from 1 GeV to 100 GeV. For lower angles (e.g. $\theta = 20°$) the achieved performance degrades but is still compatible

to the detector design goal.

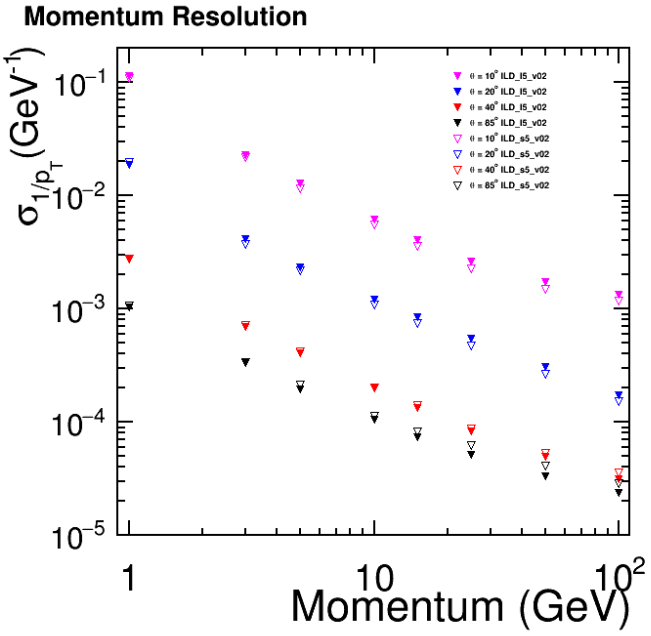

Figure 4.7.: Inverse transverse momentum resolution as a function of momentum of single muons. Figure is taken from [100].

4.6. ECAL and HCAL

The ECAL has a mechanical design which approximates a circular cylindrical shape with an octagonal prism. The separation between the energy deposits improves with the size of inner radius for the ECAL [118]. This motivates ILD to have an inner radius of 1.84 m and an outer radius of 2.028 m to allow the compact design of the ILD ECAL. To ensure that the absorber material fulfils the Particle Flow requirements, following considerations regarding the material properties are taken into account:

- A **small Molière radius** (R_M) to separate nearby showers.
- A **short radiation length** (X_0) to ensure that the electromagnetic showers start as early as possible in the ECAL.
- A **large interaction length** (λ_I) to reduce the number of hadronic showers that may start in the ECAL.

The absorber material chosen for the ILD ECAL is tungsten which has a small Molière radius of $R_M = 9\,\text{mm}$ and has a particularly large interaction length to radiation length ratio of $\lambda_I/X_0 = 99/3.5$ [84]. It also consists of a remarkable longitudinal segmentation into 30 sensitive layers which are all individually read thus being beneficial for the Particle Flow approach. The granularity of the ECAL is one of the most important factors for reducing the potential errors associated with the Particle Flow reconstruction. The cells of the ILD ECAL has an unprecedented size of $5 \times 5\,\text{mm}^2$ [121]. The performance of the ECAL design is studied through both simulations and through various test beams. The results obtained from prototypes designed by the CALICE collaboration [122] are compatible with the energy resolution values for the full ILD detector simulation [123].

The ILD envisages to have a cylindrical sampling hadronic calorimeter (HCAL) that can accommodate either scintillator tiles (analogue HCAL) or gaseous sensors (semi-digital HCAL) for the active part. It would have an inner radius of 2.058 m and an outer radius of 3.410 m. The ILD HCAL absorber requires to be non-magnetic and adequate enough to build a compact and cost-effective design. Stainless steel forms to be the best option for this purpose. It provides a satisfactory ratio between the interaction length and the electromagnetic radiation length: $\lambda_I/X_0 = 17\,\text{cm}/1.8\,\text{cm}$. An ILD HCAL tile is of the size of $3 \times 3\,\text{cm}^2$. Like the ECAL, the performance of the ILD HCAL is also studied by the CALICE collaboration through several test beams. The measured energy resolution of the analogue HCAL physics prototype is given as: $\sigma_{reco}/E_{reco} = 57.6 \pm 0.4/\sqrt{E_{beam}} \oplus 1.6 \pm 0.3 \oplus 0.18/E_{beam}$. Furthermore, with the application of software compensation techniques, the energy resolution is improved by approximately 20% thus reaching to a value of $(45.8 \pm 0.3)\%/\sqrt{E}$ in case of a stochastic term [124].

4.7. Forward Calorimeters

The LumiCal measures the luminosity on the per mille level. The Bhabha scattering events (N_{evt}) which are measured in a certain range of the polar angles and the differential cross section for the same angular range are used to measure the luminosity (L) as $L = N_{evt}/\sigma_B$. The cross section of Bhabha scattering can be determined from theory with a very high precision [125]. LumiCal covers a polar angle range of 31 to 77 mrad. A detailed simulation study on the performance of LumiCal has been made in [126]. For a beam of electrons with an energy of $E_{beam} = 250\,\text{GeV}$ the relative resolution $\sigma_E/E = a_{res}/\sqrt{E_{beam}}$ is evaluated as $a_{res} = 0.21 \pm 0.02\sqrt{\text{GeV}}$.

The BeamCal contributes to the beam tuning procedure. The energy deposited in the sensors of the BeamCal per bunch crossing allows a bunch by bunch luminosity

estimate. It also allows the determination of beam parameters with a precision of better than 10% [127]. BeamCal is hit by a huge amount of electron-positron pairs produced by beamstrahlung. The technical design of BeamCal is similar to the LumiCal as explained in [84].

The LHCal is a hadronic calorimeter located between the LumiCal and the BeamCal. The LHCal can access lower angular ranges where the main hadronic calorimeter cannot reach. For the processes like $\gamma\gamma \rightarrow$ low p_T hadronic processes where the particles have a very low transverse momentum and are in a very forward direction, this calorimeter is beneficial for enhancing the particle reconstruction.

4.8. Software Framework

An overview of the most important software tools used to generate, simulate and reconstruct the events is presented in this section. Most of the software tools are based on `LCIO` event data model.

4.8.1. The `LCIO` Event Data Model

The crucial information from the data from the experiments as well as from the Monte-Carlo simulations needs to be stored in a very clear, easily accessible and consistent way for the purposes of analysis and detector optimisation. This purpose was served by the linear collider scientific community with the development of event data model (EDM) known as `LCIO` [128].

In `LCIO`, the information is stored on an event-by-event basis which is illustrated as an `LCEvent` class. The event data is arranged into several `LCCollections` which abides a number of `LCObjects` of the same type. `LCCollections` for MCParticles, reconstructed particles, tracks etc are created where the respective quantity would be the `LCObject`. A schematic overview of the `LCIO` structure is given in figure 4.8. Different processes in the simulation and reconstruction chain are represented from left to right. The chain begins with the `MCParticle` as the main class. Generator level information on the Monte Carlo particles is stored in the `MCParticle` collection. Additional `MCParticles` can be produced as a result of the interaction of generated particles with the detector material. These particles are produced during the detector simulation and are added to the `MCParticle` collection.

The second column represents raw data classes which contain information at a very basic level as received by the subdetectors. The framework at this step is also used to analyse real data from test beams which can be used to optimise the detector design. The data received here undergoes the step of digitisation thus converting it into calometric and track hit information.

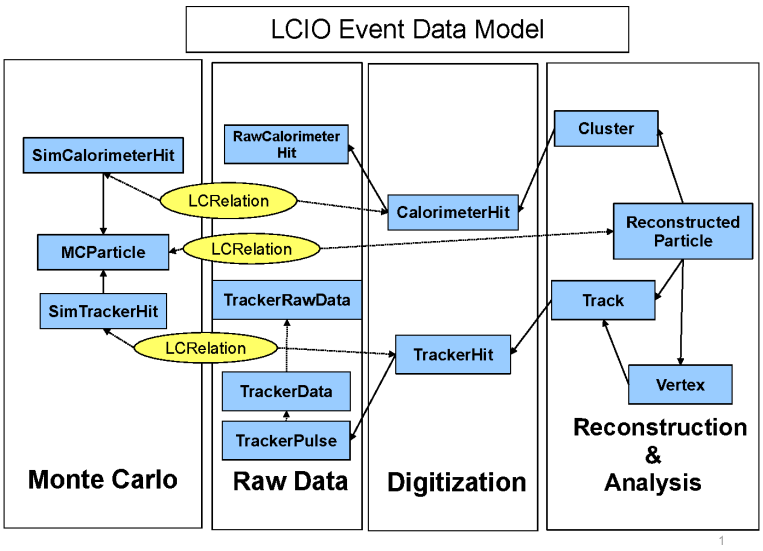

Figure 4.8.: Overview of the key data classes in the LCIO event data model. Figure taken from [129].

Using the digitised track hits, the tracking algorithms form reconstructed tracks. The Particle Flow reconstruction creates clusters using the calorimeter hits and associate the respective tracks with them giving a list of objects called as `Reconstructed Particles`. After the data processing the `LCIO` classes are stored as `SLCIO` files which are used for analysis. The Monte-Carlo processes used in this thesis are given in table 4.2.

	Processes
SUSY	$e^+e^- \to \tilde{\chi}_1^+\tilde{\chi}_1^-\gamma$ $e^+e^- \to \tilde{\chi}_1^0\tilde{\chi}_2^0\gamma$
SM	$e^+e^- \to 2f$ $e^+e^- \to 4f$ $e^+e^- \to 6f$ $e\gamma \to 3f$ $e\gamma \to 5f$ $\gamma\gamma \to 2f$ $\gamma\gamma \to 4f$

Table 4.2.: Monte-Carlo samples of SUSY and the Standard Model processes used in this thesis for $\sqrt{s} = 500\,\text{GeV}$.

4.8.2. Event Generation

The events are generated using the software tool `Whizard` [130]. `Whizard` is a program that calculates cross sections and generates events of hard scattering and decay processes that occur at high energy colliders. The program is based on leading order perturbation theory.

A certain physics model can be chosen and a list of required reactions can be given to the `Whizard` as an input. The physics model to be considered in the format prescribed by the SUSY Les Houches Accord (SLHA) [131] are presented to `Whizard` as an input for the higgsino signal samples. `Whizard` then generates matrix elements by using the program `O'mega` [132], which calculates the scattering amplitudes of processes created by polarized beams. Tree-level matrix elements are generated using this tool. Whizard is capable of producing processes having upto eight final state particles. ILC specific cases like beam polarization have been implemented into Whizard. The beamspectra for the ILD Monte-Carlo simulations are created using `Guinea Pig` [133]. An effective initial centre-of-mass energy is given by the beam spectrum of the electron and the positron beam. Using an interface with `Pythia` [134] fragmentation and hadronization of the final state are obtained and stored in `StdHep` format [135].

The higgsino processes used in this study were originally simulated for [7]. Both the signal and the background are generated using `Whizard 1.95`. Due to the nearly mass degenerate higgsinos, $\tilde{\chi}_1^{\pm}/\tilde{\chi}_2^0$ decay via highly virtual W/Z bosons. The hadronisation process for on-shell and off-shell W/Z process is different. `Herwig++` [136] has implemented such hadronisation process for the decay of τ leptons to hadrons which has a very similar pattern of decay as of charginos [137]. Using the interface to `Pythia`, the decays of the charginos and neutralinos are simulated in `Whizard` using the branching ratios calculated by `Herwig++`. It also includes the required ISR photon in the hard matrix element with respect to the corresponding beam electron or positron.

$\gamma\gamma \rightarrow$ low p_T hadron events are generated using two different event generators, `Pythia` 6.4 [134] and the so called Barklow generator. The Barklow generator is a dedicated event generator developed in the ILC community to study the low energy regime of $\gamma\gamma \rightarrow$ low p_T hadron events 5.3.1. To produce these events, `Whizard` is used as an user-interface system to produce the incoming photon spectra. Luminosity files are independently produced by `GuineaPig` called as *lumi-linker* files which are in turn used by `Whizard's` user interface code to produce incoming photon spectra. `Whizard` calls for a real photon or a virtual photon created using the equivalent photon approximation [138]. A low p_T $\gamma\gamma \rightarrow d\bar{d}$ event is created in the test mode of `Whizard` assuming constant cross section versus the centre-of-mass energy. The final state $d\bar{d}$ is discarded and the centre-of-mass energy of the incoming photons is calculated. Based on the photon-photon centre-of-mass energy of the of the incoming

photon pair, they are accepted or rejected to be considered for simulating $\gamma\gamma \rightarrow$ low p_T events. Using the energy spectra of these photons low p_T hadron events are then generated by `Pythia` or the Barklow generator based on their centre-of-mass energies [139]. More details on these generators are given in Chapter 5.

4.8.3. Detector simulation

The detector response for the events generated using above event generators are simulated using different software tools. Two different softwares used for simulations in this study are `Mokka` [140, 141] and `DD4hep` [142, 143]. The analysis studies are conducted using the samples simulated using `DD4hep`. `Mokka` performs a detailed full detector simulation based on `GEANT4` toolkit [115, 144]. `GEANT4` equips `Mokka` with a tool to simulate the passage of particles through the detector material. Event samples generated by `Whizard` and a detailed realistic model of the full detector, including dead material, labelling, support structures or gaps are provided to `Mokka` as an input. The `Mokka` version used in this study is `v01-17-11` for the detector model `ILD-o2-v05`. The output files of `Mokka` are stored in a `LCIO-SIM` format. Since the support for the maintanence of `Mokka` had ceased the detector simulation of events had to be moved to the new software, `DD4hep`.

`DD4hep` is designed by implementing improvements on the shortcomings of the detector description systems and the geometry description tools used earlier. `DD4hep` reuses the already existing software components, particularly the `ROOT` geometry package [145] which is part of the `ROOT` project [146] helping build, browse, navigate and visualize detector geometries. `DD4hep` uses `GEANT4` simulation toolkit to simulate detector response from particle collisions in complex structures. The main source of information in `DD4hep` is the geometrical representation provided by `ROOT`. For this study `DD4hep` version of `v02-00-01` for the detector model `ILD_l5_o1_v02` has been used. The output is stored in an `LCIO` format.

4.8.4. Event Reconstruction using Marlin

`Marlin` (Modular Analysis and Reconstruction for the LINear collider) is a reconstruction software used for the digitisation and event reconstruction of the simulated data [147]. This process is carried out in several steps like digitisation, tracking and clustering. Every object in the event having different structures (e.g. hits, tracks, PandoraPFOs) are stored in different collections. The individual data is read separately from the input files using a *processor* and corresponding algorithms are ran to reconstruct the data. The data handling between different *processors* and collections is done in accordance with the `LCIO` event data model.

The standard event reconstruction begins with pattern recognition in the tracking detectors using packages `Clupatra` and `FwdTracking`. The global track fitting

and combination of different track segments in various sub-detectors is done using `KalTest` and `FullLDCTracking` software packages respectively. The tracks thus reconstructed are given as an input to particle flow algorithm `PandoraPFANew` [117].

The particle flow algorithm correlates the tracks reconstructed with corresponding calorimeter clusters. These objects are then called as charged particle flow objects(PFOs) and the clusters without any tracks are reconstructed as neutral PFOs. Another important aspect of reconstruction is vertex finding, jet clustering and flavour tagging. This is done using the software packages `LCFIVertex` and `LCFIPlus` [148]. The beam induced backgrounds and other physics processes are simulated separately even though they are originating from the same bunch crossing and occur simultaneosly. Nevertheless, the processes are independent from each other since the colliding particles are different. During the reconstruction of the events the simulated detector hits from the main physics processes and beam induced backgrounds are overlaid on each other. The e^+e^- pair background is taken into account in the BeamCal reconstruction [103].

A `Marlin` version of `v01-17-11` is used in this study for reconstruction of events simulated using `Mokka`. For reconstructing events simulated using `DD4hep` a `DDMarlin` version of `v02-00-01` is used. The output from `Marlin` is stored in two different formats namely `LCIO-REC` and `LCIO-DST`. The `LCIO-REC` file contains complete information about the simulation including the hits in the detector. The `LCIO-DST` file on the other hand is a simplified version containing only necessary information for analysis.

4.8.5. `SGV` as a Fast Simulation Software

`SGV` is a fast detector simualtion software designed for e^+e^- collider studies [149]. It can simulate events approximately $\mathcal{O}(10^3)$ times faster than the full simulation. `SGV` is based on a very simplified description of the detector geometry. A detailed description of its working principle is given in [98, 149]. `SGV` accepts input files in `StdHep` [135] format and generates output in `LCIO-DST` format.

Figure 4.9 shows the tracking system used in SGV for the ILD. In the lower left corner of the figure, the silicon tracking system is depicted which is followed by ILD tracker shown in red. The layers of ECAL are shown in magenta layers which finally ends with HCAL layers in yellow. The trajectory of the charged particle in the detector through different layers is marked in black. The track-helix is followed through the detector to determine the layers which are hit by the particle.

The five track parameters explained in section 4.5 are determined in `SGV` using the Monte-Carlo truth information regarding its momentum and the starting point in the detector (IP). The specific tracker surfaces that the particle would intersect while the helix would cross the entire detector is determined and stored. `SGV` calculates a

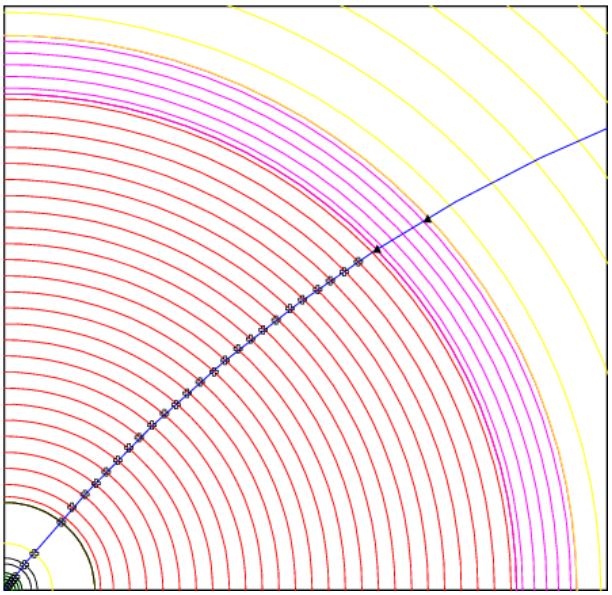

Figure 4.9.: Tracking simulation in SGV. The projection of a quadrant of the ILD in the $x-y$ plane is illustrated. The trajectory of a particle throughout the detector layers is shown. Figure taken from [149].

covariance matrix of the track parameters at the perigee using this list of interaction points of the particle in the detector. This is done by following the track from the outermost layer of the tracker to inwards. At every interaction a contribution is added in quadrature to the relevant elements of the covariance matrix. The matrix is then inverted to obtain a weight matrix. The effects of extrapolation uncertainities as well as the errors from multiple scattering [150] and energy loss that can happen due to the particle interaction with the silicon detector surfaces are added to the relevant elements of this matrix. The matrix thus obtained is inverted again and translated along the helix to the next intersected surface where the procedure is repeated until the mathematical surface representing the point of closest approach is reached. `SGV` mainly adapts the *Kalman Filter* procedure [151] to calculate the covariance matrix.

Every track whose covariance matrix can be calculated is considered to be reconstructed. The covariance matrix of a particle cannot be calculated if its trajectory intersects with very few detector layers (i.e. less than three layers). In such cases tracks are found to be missing in `SGV`. The tracking performance for `SGV` is shown in figure 4.10 In this thesis `SGV` is used to study the tracking efficiency of $\gamma\gamma \rightarrow$ low p_T hadron events that occurs at a photon-photon centre-of-mass energy below 2 GeV. The details of this study is presented in the following Chapter 5.

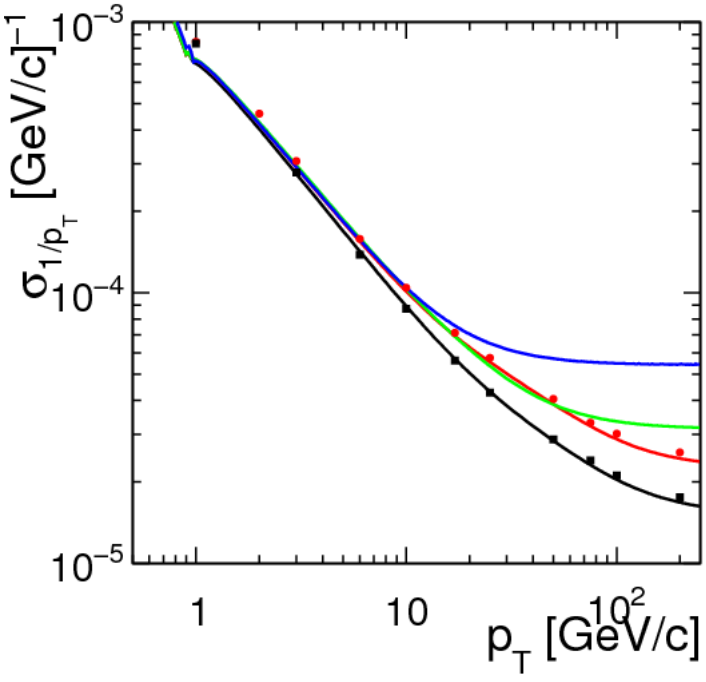

Figure 4.10.: The momentum resolution as a function of transverse momentum is presented. The lines indicate the SGV results while the dots represent results from full simulation. The blue line shows the case where only TPC is considered, green shows the results along with the VTX detector, while the red and black shows the case where SET and SIT are included respectively. Figure taken from [149].

4.9. Luminosity and Polarisation Weights

The study performed in this thesis will be presented normalised to an integrated luminosity of $\int \mathcal{L}dt = 500$ fb^{-1}. However, some of the processes do not have enough statistics. Therefore, to fulfill this criteria, a luminosity weight is assigned to each process. The weights are calculated for each process for all different helicity combinations $h(e^+e^- \in RR, LL, LR, RL)$. The luminosity weight for a given process ($proc$) and helicity (h) combination can be calculated as:

$$w_{lumi|_{proc,h}} = \frac{\int \mathcal{L}dt \cdot \sigma_{prod|_{proc,h}}}{N_{prod|_{proc,h}}} \tag{4.1}$$

where $\sigma_{prod|_{proc,h}}$ is the production cross section and $N_{prod|_{proc,h}}$ is the number of events corresponding to the given process and helicity.

In addition to the luminosity weights, the polarisation of each process should also be taken into account. The polarisation fraction for each helicity is different. The polarized cross section based on the fractions of different polarisations can be given as:

$$\sigma(P_{e^+}, P_{e^-}) = w(e^+_R e^-_L)\sigma_{RL} + w(e^+_L e^-_R)\sigma_{LR} + w(e^+_R e^-_R)\sigma_{RR} + w(e^+_L e^-_L)\sigma_{LL} \quad (4.2)$$

The polarisation weights $w(e^+_{R/L} e^-_{R/L})$ are determined using the individual partial polarisations of the positron and the electron beam for each process and helicity:

$$w(e^+_{R/L} e^-_{R/L}) = \frac{1}{4}(1 \pm P_{e^+})(1 \pm P_{e^-}) \quad (4.3)$$

The upper and lower signs in equation 4.3 corresponds to right-handed/left-handed polarisation of the beam particles respectively.

Weights	(0.0, 0.0)	(+0.3, -0.8)
$w(e^+_R e^-_L)$	0.25	0.585
$w(e^+_L e^-_R)$	0.25	0.035
$w(e^+_L e^-_L)$	0.25	0.065
$w(e^+_R e^-_R)$	0.25	0.315

Table 4.3.: The polarisation weights as $P(e^+e^-)$ used for the study performed in this thesis.

The final polarised luminosity weights applied on the events are calculated as

$$w|_{proc,h} = w_{lumi}|_{proc,h} \cdot w(e^+_{R/L} e^-_{R/L}). \quad (4.4)$$

5. $\gamma\gamma \rightarrow$ low p_T Hadron Event Generators

One of the biggest advantages of an e^+e^- collider is its low background environment (section 3.2). However, one issue in the design of e^+e^- colliders is the effect of beam-beam interaction on the physics environment. The interaction between photons created in beam induced backgrounds like beamstrahlung or in the e^+e^- interaction itself lead to the production of low p_T hadrons. These $\gamma\gamma \rightarrow$ low p_T hadron backgrounds are one of the major backgrounds at linear colliders. This chapter provides a detailed view into the nature of $\gamma\gamma \rightarrow$ low p_T hadron backgrounds and forms a foundation for developing differential methods to identify and remove this background.

5.1. Photon sources

Photons are the dominant source of low p_T hadrons at an e^+e^- collider. The $\gamma\gamma$ luminosity receives contributions from two different sources; beamstrahlung and the Weizsäcker-Williams process corresponding to real and virtual photons, respectively. Beamstrahlung, the Weizsäcker-Williams process and the $\gamma\gamma$ luminosity function are discussed in detail in this sections.

5.1.1. Beamstrahlung

As discussed in section 3.4.2, the pinch effect reduces the beam size and enhances the beam luminosity. However, the deflection of beam particles due to the charge of the incoming bunch results in radiation of photons. This phenomenon of photon radiation due to beam-beam interaction is known as beamstrahlung. The effective *beamstrahlung parameter* Υ, the number of soft photons ν_{cl}, the number of hard photons ν_γ and the rate of photons radiated with an energy x, $\overline{\nu}(x)$, are introduced in section 3.4.4. Using these parameters radiation spectrum for real photons is given as [111]:

$$f_r(x) = \frac{1}{\Gamma(1/3)}\left(\frac{2}{3\Upsilon}\right)^{1/3} x^{-2/3}(1-x)^{-1/3}\exp\left[-\frac{2x}{3\Upsilon(1-x)}\right]\cdot G(x) \tag{5.1}$$

where x is the fraction of initial beam energy carried away by the photon, Γ is the gamma function and $G(x)$ is a function of the effective beamstrahlung parameter,

$$G(x) = \frac{1-\omega}{g(x)}\Big\{1 - \frac{1}{g(x)n_\gamma}\Big[1 - e^{-g(x)n_\gamma}\Big]\Big\} + \omega\Big\{1 - \frac{1}{n_\gamma}\Big[1 - e^{-n_\gamma}\Big]\Big\}, \tag{5.2}$$

$$g(x) = 1 - \frac{\overline{\nu}}{\nu_\gamma}(1-x)^{2/3}, \tag{5.3}$$

$\omega = (1/6)\sqrt{3\Upsilon'/2}$ and $n_\gamma = \sqrt{3}\sigma_z\nu_\gamma$ is the mean number of photons radiated per electron throughout the collision [107].

5.1.2. Weizsäcker-Williams Process

The main features of the radiation of virtual photons by relativistic electrons are approximated by the Weizsäcker-Williams method [152]. The electromagnetic fields of an electron in uniform relativistic motion are predominantly transverse, with $E \approx B$ [153]. This being similar to the fields of a plane wave, it is likely that a fast electron carries a cloud of virtual photons that it can radiate if perturbed. This process is described with parameters like formation time and corresponding formation length $L_0 = vt_0$ where v is the velocity of relativistic electron. The formation length is the distance that the electron travels while a radiated wave advances one wavelength λ ahead of the projection of the electron's motion onto the direction of projection. Thus once the formation time is elapsed the radiation becomes completely independent of its source. λ is given as [152]

$$\lambda = ct_0 - vt_0\cos\theta \approx L_0(1-\beta\cos\theta) \approx L_0(\frac{1}{2\gamma^2} + \frac{\theta^2}{2}) \tag{5.4}$$

where radiation is observed at angle θ of electron trajectory.
The spectrum of such radiated photons is given as [154]

$$\begin{aligned} f_v(x,Q,E) =& c_v \cdot \frac{\alpha}{2\pi x}\Big[(1+(1-x)^2)\Big(\log\frac{Q^2}{{m_e}^2} - 1\Big) + \frac{x^2}{2}\Big(\log\frac{(1-x)}{x^2} + 2\Big) \\ &+ \frac{(2-x)^2}{2}\log\frac{(1-x)}{(Q^2/E^2+2)}\Big] \end{aligned} \tag{5.5}$$

where E is the electron beam energy, x is the fraction of the initial beam energy carried away by the photon, Q is the transverse momentum of a photon and $c_v = 0.85$.

5.2. Photon-Photon luminosity

The real and virtual photon spectra as mentioned in sections above in different combinations adds up to the photon-photon luminosity function $L_{\gamma\gamma}(x_1 x_2)$ which significantly contributes to the $\gamma\gamma$ cross sections at e^+e^- colliders. Here x_1 and x_2 are the fractions of total energy of incoming electron and positron, respectively, carried away by the colliding photons. The $\gamma\gamma$ luminosity function for e^+e^- collider

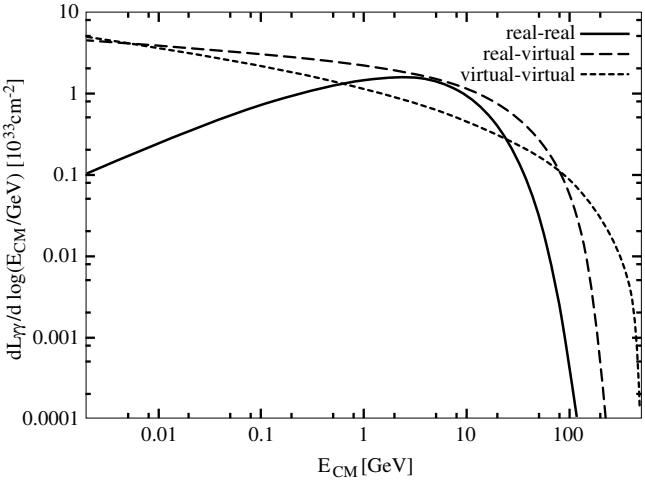

Figure 5.1.: The $\gamma\gamma$-luminosity spectra for different combinations of real and virtual photons colliding at $\sqrt{s_{ee}} = 500\,\text{GeV}$. Figure taken from [155].

as a sum of components is thus given as [39]:

$$L_{\gamma\gamma}(x_1 x_2) = \underbrace{f_v(x_1) f_v(x_2)}_{\text{virtual-virtual collision}} + \underbrace{\left[f_v(x_1) f_r(x_2) + f_r(x_1) f_v(x_2) \right]}_{\text{virtual-real collision}} + \underbrace{f_r(x_1) f_r(x_2))}_{\text{real-real collision}} \tag{5.6}$$

where $f_v(x)$ is the spectrum for virtual photons as given in Eq. 5.5 and $f_r(x)$ is the spectrum for real photons as given in Eq. 5.1. A pictorial representation of Eq. 5.6 is given by figure 5.1.

The most important $\gamma\gamma$ induced processes and their theoretical modeling is introduced in section 2.3.3. In order to calculate the total rate of $\gamma\gamma$ processes at an e^+e^- collider, the relevant energy-dependent cross sections have to be folded with the $\gamma\gamma$ luminosity spectra.

5.3. Modelling $\gamma\gamma \rightarrow$ low p_T hadron processes

A realistic modelling of $\gamma\gamma \rightarrow$ low p_T hadron processes is crucial for the development of advanced methods to mitigate these backgrounds. In this section the treatment of $\gamma\gamma \rightarrow$ low p_T hadron processes used in the ILC TDR [86] and in many physics analyses since then will be scrutinized, followed by the presentation of an improved modelling developed in the context of this thesis.

5.3.1. Status of $\gamma\gamma \rightarrow$ low p_T hadron processes in the ILC TDR

The study of $\gamma\gamma \rightarrow$ low p_T hadron processes in the ILC TDR [86] is based on two different event generators: `Pythia` 6.4 [134] for the higher $\sqrt{s_{\gamma\gamma}}$ and a dedicated generator developed by T.Barklow [39, 139] to cover the lowest $\sqrt{s_{\gamma\gamma}}$. The latter will be referred to as "the Barklow generator" in the following. Both generators are called through the ILC Whizard setup in order to ensure the correct treatment of the luminosity spectra. The transition energy is a steerable parameter. In the DBD Monte-Carlo production, the transition was set to 10 GeV by the author as can be seen in figure 5.2.

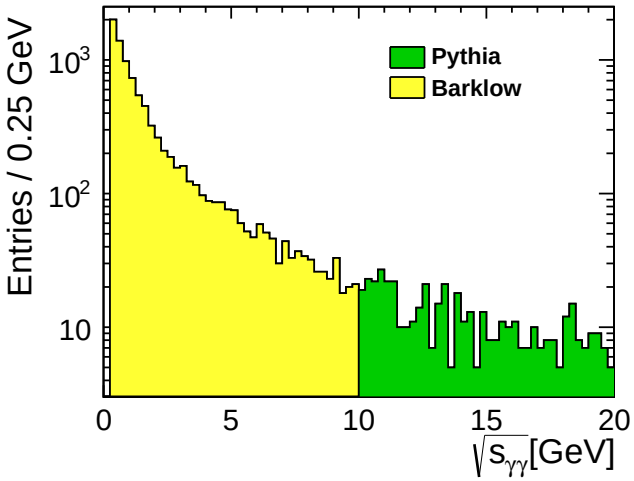

Figure 5.2.: Energy spectrum of $\gamma\gamma \rightarrow$ low p_T hadron events as a function of centre-of-mass energy. The figure shows the energy cutoff of 10 GeV below which the events are generated by the Barklow generator. Above 10 GeV the events are generated by `Pythia`.

Even though `Pythia` generates events from as low as $\sqrt{s_{\gamma\gamma}} = 10$ GeV, the total

cross section to generate $\gamma\gamma$ events up to 20 GeV is calculated using the Amaldi paramerization [156] while the cross sections for events with $\sqrt{s_{\gamma\gamma}} > 20\,\text{GeV}$, is given by `Pythia`. This is because of the incompatibility of $\gamma\gamma \rightarrow$ hadron cross sections given by `Pythia` with theoretical studies and real data cross sections from LEP [157], PETRA [158] and VEPP [159] for $\sqrt{s_{\gamma\gamma}} < 20\,\text{GeV}$ as can be seen in figure 5.3.

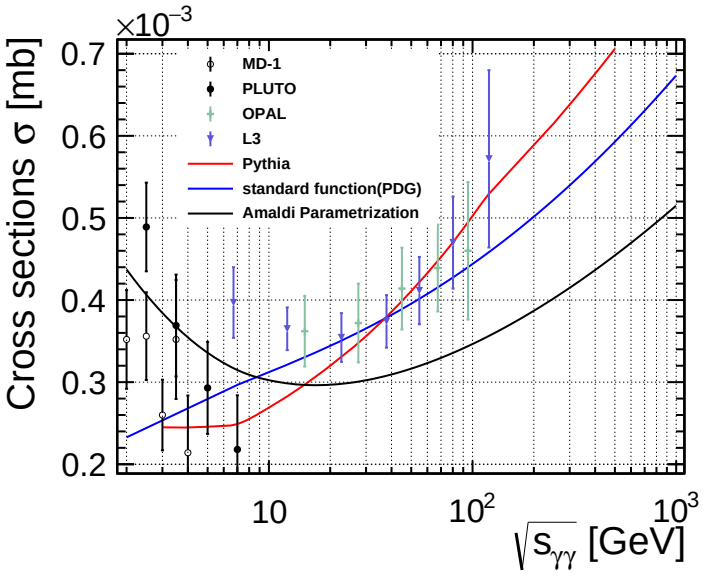

Figure 5.3.: Comparison of cross sections for $\gamma\gamma \rightarrow$ hadron processes as a function of centre of mass energy obtained from Amaldi parameterization [156], Standard paramerization [44] in PDG, Pythia and data from LEP [157], PETRA [158] and VEPP [159]

A comparison study with the cross sections for $\gamma\gamma \rightarrow$ hadron events produced by `Pythia` with the cross sections obtained from the Amaldi parametrization [156], the PDG parametrization [44] and with data from LEP [157], PETRA [158] and VEPP [159] was performed. The comparison shows that at $\sqrt{s_{\gamma\gamma}} > 20$ GeV the cross sections for $\gamma\gamma \rightarrow$ hadron processes produced by `Pythia` is in agreement with data from the LEP experiments and cross section function from the PDG. However, at $\sqrt{s_{\gamma\gamma}} < 20$ GeV the variation between data and different parameterizations is higher. In this energy regime, the Amaldi parameterization gives the best description for $\gamma\gamma \rightarrow$ low p_T hadron cross sections as given in Eq. 5.7

$$\sigma(\gamma\gamma \rightarrow \text{hadrons}) = \sigma_0 \cdot \Big\{1 + (6.30 \times 10^{-3})[\log(s)]^{2.1} + (1.96)s^{-0.37}\Big\}. \tag{5.7}$$

Therefore, the total cross section for $\sqrt{s_{\gamma\gamma}} < 20$ GeV in the $\gamma\gamma \rightarrow$ hadron generator is taken from the Amaldi parameterization. However, the cross sections for individual subprocesses in the Barklow generator are taken from measurements at different experiments wherever possible or from theoretical models, where as for all the events generated by `Pythia`, the cross sections for subprocesses are self-generated. More details about the individual cross sections are given ahead.

The $\gamma\gamma \rightarrow$ low p_T hadron events generated by `Pythia` are modelled in the following way: A variety of events like Vector Meson Dominance (VMD), direct events (DIR) and anomalous events (GVMD) [134] (section 2.3.3) with respective cross sections are produced by `Pythia`. These $\gamma\gamma$ processes can be extracted from Eq. 2.22, where the direct event, VMD and the GVMD event corresponds to the first, second and third term of the equation respectively. The cross sections for different combinations of photon-photon interaction subprocesses given by `Pythia` are shown in table 5.1. These cross sections folded with the $\gamma\gamma$ luminosity spectrum as explained in section 5.2 give the $\gamma\gamma \rightarrow$ hadron events.

Subprocess	cross section [nb]
VMD*VMD	239.2
DIR*VMD	87.52
GVMD*DIR	9.77
DIR*DIR	1.644×10^{-2}
VMD*GVMD	53.70
GVMD*GVMD	12.05

Table 5.1.: Cross sections from `Pythia` for $\gamma\gamma$ subprocesses at an e^+e^- centre-of-mass energy 500 GeV.

With the VMD induced processes having the highest cross section, vector meson particles like $\rho^0, \rho^{\pm}$ and ω are seen predominantly in $\gamma\gamma$ events. Vector mesons decay to particles like $\pi^{\pm}, \pi^0, \mu^{\pm}$ and K [44]. To compare the particle multiplicities of `Pythia` events at lower $\sqrt{s_{\gamma\gamma}}$ energies with events from Barklow generator, `Pythia` events with $\sqrt{s_{\gamma\gamma}} < 6$ GeV are chosen. Using these events, the particle multiplicities for `Pythia` events are shown in figure 5.4, figure 5.5 and figure 5.6. Figure 5.4 shows the number of charged and neutral particles per event generated by `Pythia`. In figure 5.5, the number of charged and neutral pions generated per `Pythia` event is demonstrated. Figure 5.6 shows the number of neutral rho mesons and number of charged rho mesons per event. It is expected that the cross sections for the production of neutral rho mesons is higher than that of the charged rho mesons. As can be seen in figure 5.6, there are higher number of neutral rho mesons per event than the charged rho mesons per event. Therefore, it can be concluded that

`Pythia` generates number of particles per event as expected from cross sections for the respective processes.

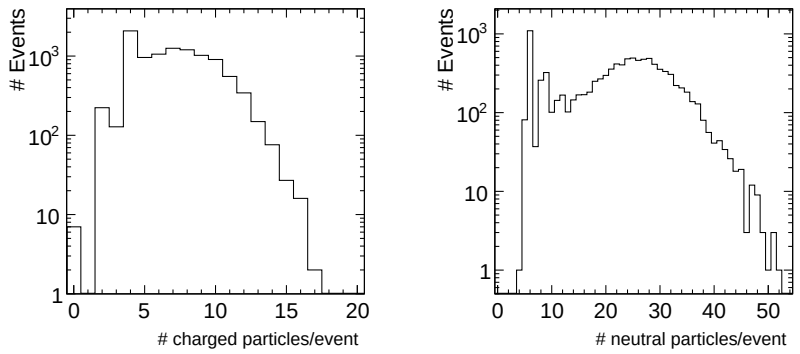

(a) (b)

Figure 5.4.: Number of charged and neutral particles per event for 10k `Pythia` generated events.

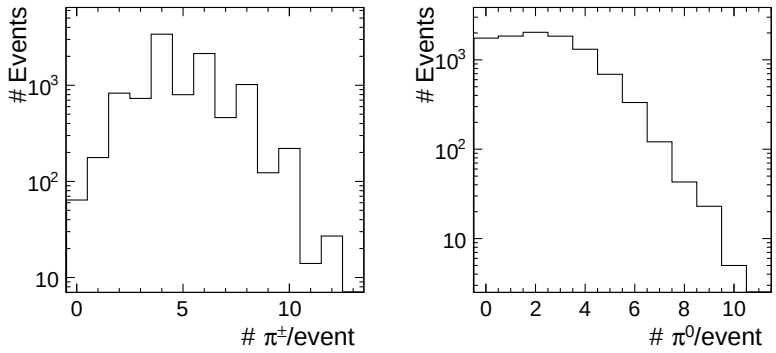

(a) (b)

Figure 5.5.: Number of charged and neutral pions per event for 10k `Pythia` generated events.

At $\sqrt{s_{\gamma\gamma}} < 10$ GeV the Barklow generator produces $\gamma\gamma \rightarrow$ low p_T hadron events with a simplified model. Events in the Barklow generator comprise of a few simple processes: $\gamma\gamma \rightarrow \pi^+\pi^-$, $\gamma\gamma \rightarrow \pi^\pm\rho^\pm$ and $\gamma\gamma \rightarrow \rho^+\rho^-$. A comparison between the particles produced by `Pythia` and the Barklow generator are given in figure 5.7. The cross sections for $\pi^+\pi^-$ pair production below 1 GeV are calculated using the chiral sum rule [160]. For $\sqrt{s_{\gamma\gamma}} > 1$ GeV, cross section values for all the other subprocesses are taken from measurements at the ARGUS collaboration [161].

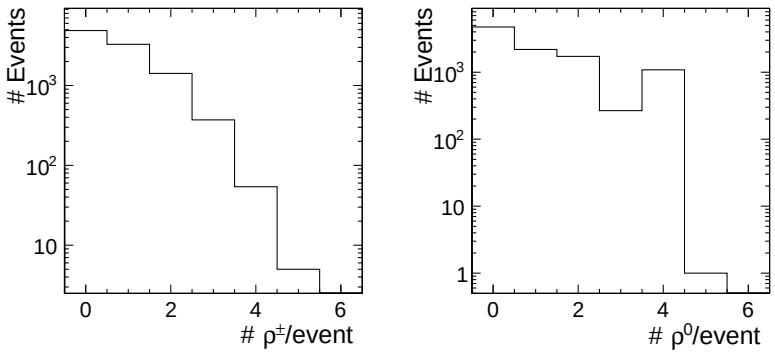

(a) (b)

Figure 5.6.: Number of charged and neutral ρ-mesons per event for 10k `Pythia` generated events.

The particles produced by the Barklow generator is given in figure 5.7b. It can be seen that the Barklow generator can only produce charged ρ-mesons, $\pi^{\pm}$, π^0 and photons whereas along with these particles `Pythia` can also produce neutral ρ-mesons, ω, K and μ. The cross section measurement for ρ^0 [162] and $\rho^{\pm}$ [163] as given in Table I of [161], shows that the cross section for producing ρ^0 (57 ± 6 nb) is higher than that for $\rho^{\pm}$ (12 ± 4 nb) at ρ threshold energy. However, as seen in figure 5.7, only $\gamma\gamma \rightarrow$ low p_T hadron events with $\rho^{\pm}$ and no ρ^0 are produced by the Barklow generator. Similarly, the Barklow generator also only generate $\pi^+\pi^+$ and no $\pi^0\pi^0$ pairs below 1 GeV. Above all these, the Barklow generator produces the $\rho^{\pm}$ meson which has a mass distribution peaked at the nominal $\rho^{\pm}$ mass as seen in figure. 5.8 but has no width.

5.3.2. Improved $\gamma\gamma \rightarrow$ low p_T hadron event generator

With several issues in the Barklow generator as mentioned in section 5.3.1, the transition energy for `Pythia` is changed from 10 GeV to 2 GeV. However, since `Pythia` is designed to equip events at higher energies, it cannot generate events for $\sqrt{s_{\gamma\gamma}} < 2$ GeV [134]. The issues in Barklow generator leaves the energy regime between $2M_{\pi}$ and 2 GeV without an efficient generator. An improved version of the Barklow generator producing such simple events should suffice to cover this low energy regime. The required corrections for the Barklow generator were implemented through discussions by the author.

The new version of the generator produces a large variety of events e.g. $\gamma\gamma \rightarrow \pi^0\pi^0, \pi^+\pi^-, \rho^0\rho^0, \rho^+\rho^-$ and other particles as shown in the figure 5.9a. The cross sections for these processes are taken from different measurements as presented in

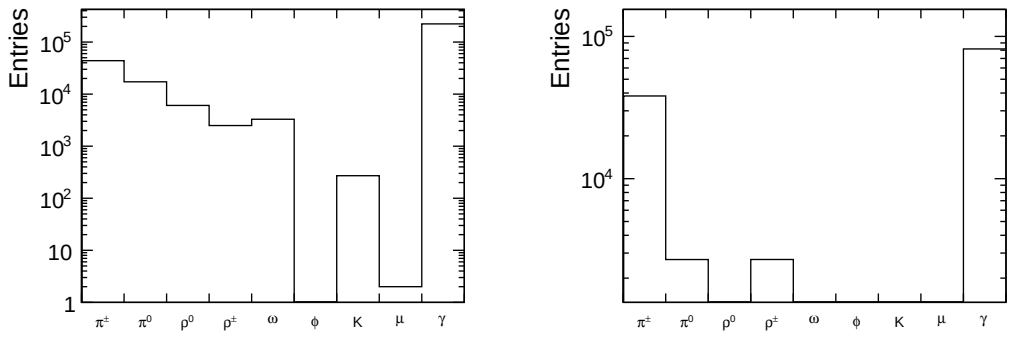

(a) (b)

Figure 5.7.: The particles produced by `Pythia` and the Barklow generator for $\sim$ 100k events. (a) particles produced by `Pythia`. (b) particles produced by Barklow generator. The difference between the variety of particles produced in both the generators is evident here.

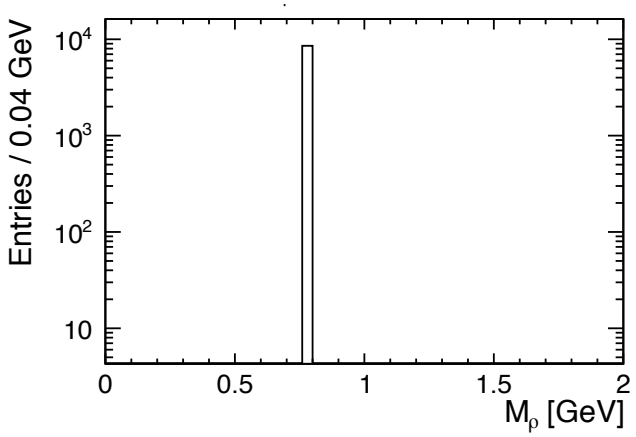

Figure 5.8.: Mass distribution for $\rho^{\pm}$ produced in the Barklow generator. ρ mesons are produced with zero-width distribution.

table 5.2.

Also as shown in figure 5.9b, the ρ meson produced by the improved Barklow generator has a Breit-Wigner's mass distribution around m_ρ.

The new energy cut-off value for transition from Pythia to the Barklow generator at 2 GeV is given in figure 5.10. The $\gamma\gamma \rightarrow$ low p_T hadron events from different combinations of real and virtual photons given as $\gamma - \gamma$ (BB), e/$\gamma - \gamma$ (WB), $\gamma - e/\gamma$ (BW) and $e/\gamma - e/\gamma$(WW) are obtained in simulation. The number of events per

Subprocess	Experiment
$\pi^+\pi^-$	PETRA [164]
$\pi^0\pi^0$	The Crystal Ball [165]
K^+K^-	PETRA [164]
K^0K^0	PETRA [164]
$\rho^+\rho^-$	ARGUS [162]
$\rho^0\rho^0$	ARGUS [163]

Table 5.2.: Cross sections measurements for sub processes in $\gamma\gamma \rightarrow$ low p_T hadron events from different experiments.

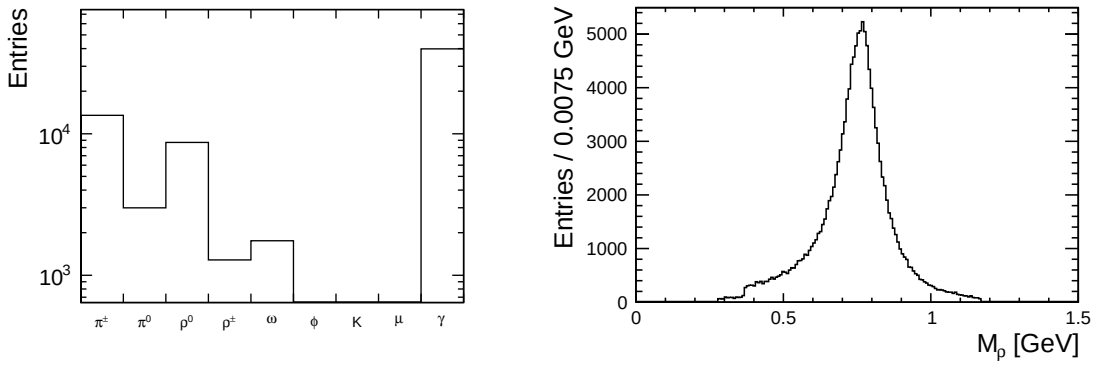

(a) (b)

Figure 5.9.: Properties of events generated by Barklow generator after the improvements were implemented. (a) particles produced in Barklow generator (b) the ρ meson mass distribution.

bunch crossing for different types of $\gamma\gamma$ processes are calculated from the cross section and luminosity as given in table 5.3. The overall $\gamma\gamma \rightarrow$ low p_T hadron events thus sums to 1.05 events/bunch crossing for $\sqrt{s} = 500\,\text{GeV}$. In the DBD production, this number was 1.2 events/bunch crossing for $\sqrt{s} = 500\,\text{GeV}$. The new setup for $\gamma\gamma \rightarrow$ hadron events is adopted as the new standard by the generator group, e.g. for the ILD IDR and the productions in future.

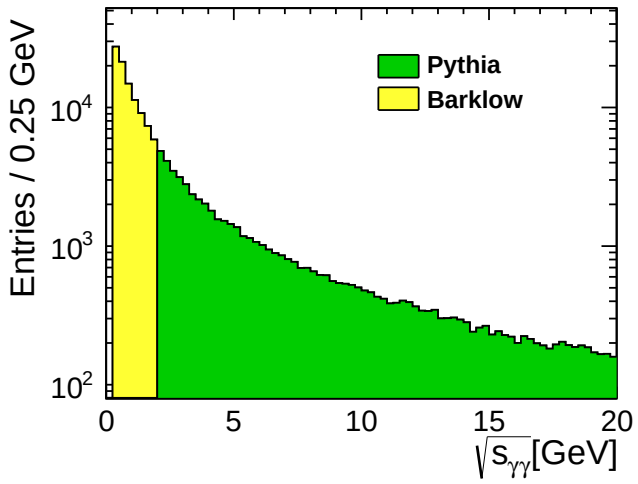

Figure 5.10.: The number of $\gamma\gamma \rightarrow$ low p_T hadron events as a function of $\gamma\gamma$ centre-of-mass energy. The figure shows the changed energy cutoff of 10 GeV to 2 GeV below which the events are generated by Barklow generator and above it the events are generated by Pythia. The events are produced at a centre-of-mass energy 500 GeV for ∼150k events.

Processes	Luminosity[cm^2s^{-1}]	Cross section[fb]	Events/BX
WW	1.7108×10^{34}	0.8127×10^{8}	0.211
WB	1.0367×10^{34}	0.9435×10^{8}	0.2460
BW	1.0269×10^{34}	0.9347×10^{8}	0.2438
BB	0.8008×10^{34}	0.1344×10^{8}	0.35003

Table 5.3.: The poissonian distribution for number of events per bunch crossing for different kinds of $\gamma\gamma \rightarrow$ low p_T events are shown. The luminosities and cross sections (taken from [139]) are used to calculate the event numbers.

5.4. Evaluation of the ILD acceptance for $\gamma\gamma \rightarrow$ hadron events with $\sqrt{s_{\gamma\gamma}} < 2\,\text{GeV}$

At $\sqrt{s_{\gamma\gamma}} < 2$ GeV, the low transverse momentum of the pions make them scatter with a small polar angle. Therefore, a study is conducted to investigate if these low p_T particles could scatter with the minimum critical angle required to be seen in the detector.

For this study, the $\gamma\gamma \rightarrow$ low p_T hadron events at a $\sqrt{s_{\gamma\gamma}} < 2$ GeV were simulated using SGV Fast Detector Simulation [149].

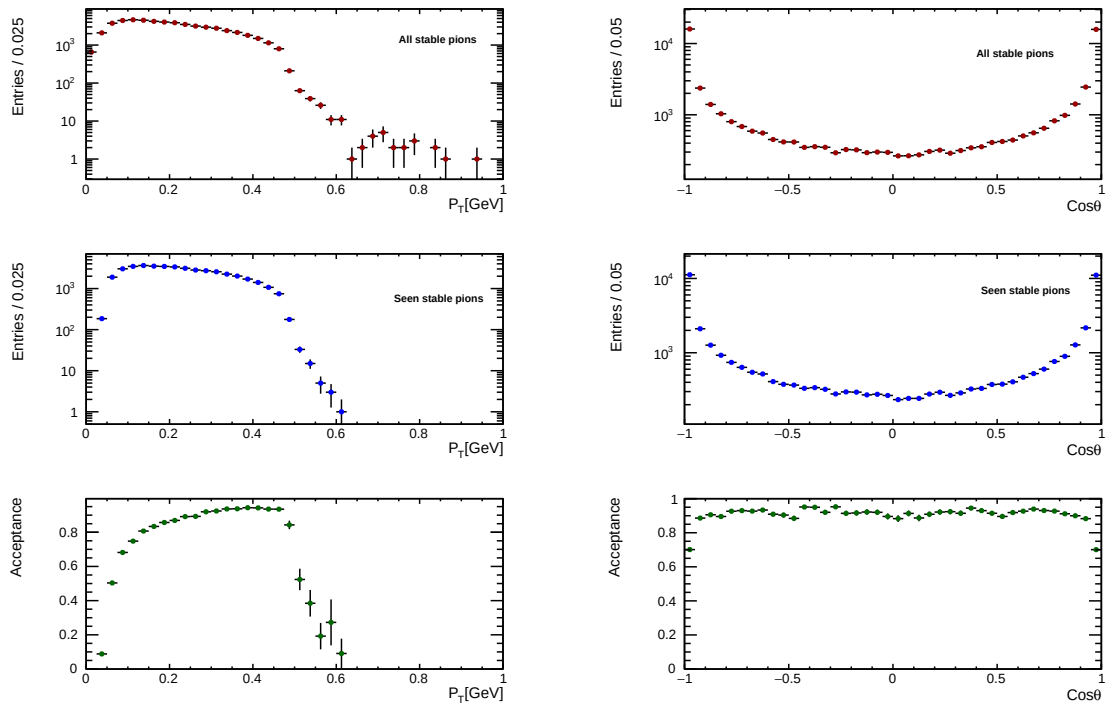

(a) (b)

Figure 5.11.: The momentum acceptance and angular acceptance of pions at a $\sqrt{s_{\gamma\gamma}} < 1$ GeV produced at a centre-of-mass energy 500 GeV for ∼120k events. Both the colliding photons radiated off the beam electrons are real.

The detector acceptance for the pions produced is determined by evaluating the momentum acceptance and angular acceptance of the detector. The process is initiated by selecting $\gamma\gamma$ events at a $\sqrt{s_{\gamma\gamma}} < 1$ GeV. The transverse momentum and polar angle of all the true pions are determined and the pions which could be reconstructed (seen) in the detector as per the SGV definition are preselected. The transverse momentum acceptance and angular acceptance are calculated as

$$\epsilon_{p_T} = \frac{p_{T_{\text{seen particles}}}}{p_{T_{\text{true particles}}}}, \quad \epsilon_\theta = \frac{\theta_{\text{seen particles}}}{\theta_{\text{true particles}}} \tag{5.8}$$

Figure 5.11 represents the case of real-real photon collion. The momentum and angular acceptance for the larger share of the particles is above 80%. The fraction

of beam particle energies carried away by a virtual photon is smaller than that of a real photon. This can make them scatter with angles smaller than the threshold angle to reach the acceptance of the detector. Thus in the case of real-virtual and virtual-virtual photon collisions, the detector acceptance reduces with increasing virtuality as shown in figure 5.12.

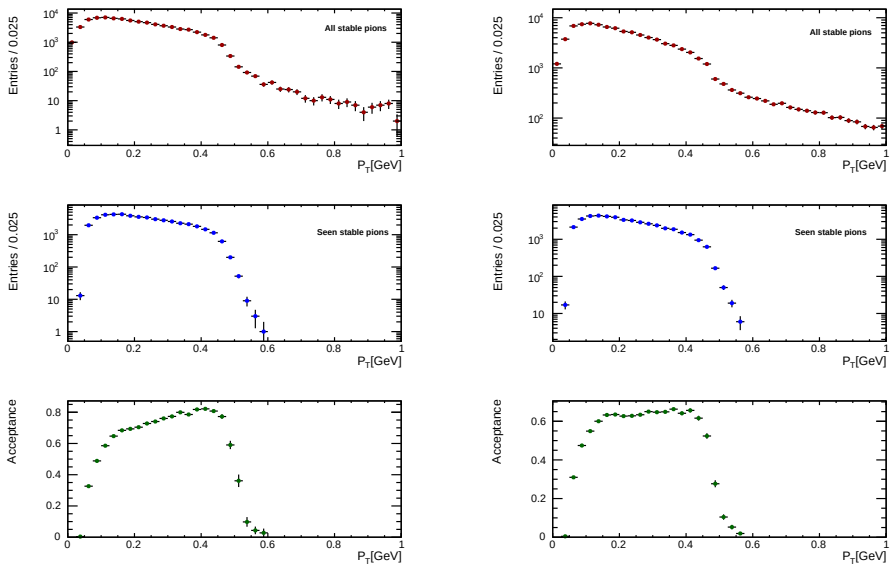

(a) (b)

Figure 5.12.: The momentum acceptance of pions at a $\sqrt{s_{\gamma\gamma}} < 1$ GeV for a centre-of-mass energy 500 GeV for ∼120k events. (a) real-virtual photon collision (b) virtual-virtual photon collisions.

Nevertheless, in all the three cases the detector acceptance for pions is above 65%. This gives the conclusion that the particles produced in $\gamma\gamma$ collisons at a $\sqrt{s_{\gamma\gamma}} <$ 2 GeV can be seen in the detector and hence it is important to model this energy regime.

5.5. Results

Backgrounds like $\gamma\gamma \rightarrow$ low p_T hadron processes are important in lepton colliders. To develop efficient methods to remove such background it is important to study and understand its basic properties. The Monte-Carlo generator producing $\gamma\gamma \rightarrow$ low p_T hadron events for DBD simulations were found to be insufficiently accurate. Even though Pythia at higher energies could produce events comprehensively, the Barklow generator produced less realistic events. The energy cutoff for Pythia to

simulate $\gamma\gamma \rightarrow$ low p_T hadron events was thus changed from 10 GeV to 2 GeV. The issues in Barklow generator were studied and respective corrections were implemented. This generator is then used to study events below 2 GeV. Integrating both the event generators at appropriate energies into Whizard, an efficient and reliable event generator is developed to study the $\gamma\gamma$ backgrounds for the ILC. The improved version of the generator thus forms the basis for the development of more sophisticated methods to identify and reject particles from the important physics events to be studied at high level precision.

6. Light Higgsinos and $\gamma\gamma \rightarrow$ low p_T Hadron Overlay Removal

Naturalness has been a guiding principle while arguing for the existence of weak-scale supersymmetry. As discussed in Chapter 2, Eq. 2.32 very well motivates investigation of light higgsinos at electroweak scale. In this chapter, low ΔM higgsinos and their branching ratios in the studied benchmark scenarios are discussed. Various Standard Model backgrounds affecting the light higgsino analysis are also discussed here. The ISR photon method which is essential to suppress some high-rate Standard Model backgrounds, is explained in detail.

6.1. Light Higgsinos at the ILC

Being an e^+e^- collider, higgsinos might be produced at the ILC via the $s-$channel exchange of a Z boson or a γ as explained in section 2.7. The analysis of such challenging physics scenarios at lepton colliders has certain advantages (section 3.1). The polarized e^- and e^+ beams can enhance the signal and suppress the background events. Since there is no trigger foreseen at the ILC, every event will be recorded. Some of the earlier studies on higgsinos at the ILC included different models and benchmark scenarios with smaller and larger mass gaps between the chargino and the LSP as given in table 6.1.

Models	Benchmark	$\Delta M_{\tilde{\chi}_1^\pm}$[GeV]	$\Delta M_{\tilde{\chi}_2^0}$ [GeV]
NUHM1	ILC1	14.6	21.3
NUHM2	ILC2	10.2	9.7
Mirage mediation	nGMM1	7.3	4.4
Mixed	dM770	0.77	1.04
gauge-gravitation	dM1600	1.6	2.7

Table 6.1.: Different benchmark scenarios and mass differences between $\tilde{\chi}_1^\pm$ and the LSP and $\tilde{\chi}_2^0$ and the LSP [7, 76].

These studies showed that the key observables e.g. higgsino masses, uncertainities

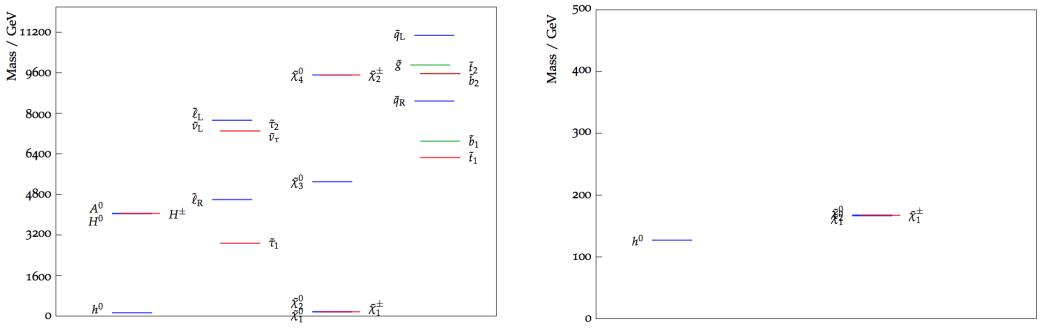

(a) (b)

Figure 6.1.: Typical example of mass spectrum of a natural SUSY including light higgsinos. Figure taken from [166].

on cross sections, mass difference between the higgsinos and the LSP, can be obtained with an uncertainity of few percent. The two benchmark scenarios taken from [7], corresponding to the last row of table 6.1 are studied in this thesis. The details of these benchmark scenarios and their branching ratios will be explained in detail in further subsections.

6.1.1. Benchmark Scenarios

Based on the mass difference between the $\tilde{\chi}_1^\pm$ and the LSP, the benchmark scenarios are referred to as the dM1600 ($\Delta M = 1.6\,\text{GeV}$) and the dM770 ($\Delta M = 0.77\,\text{GeV}$) scenario. These scenarios include a Higgs boson mass of 124 GeV and 127 GeV which are compatible with the LHC discovery ($m_h = 125.09 \pm 0.24$) [1] within the theory uncertainity of MSSM prediction of 2 GeV. The lightest chargino $\tilde{\chi}_1^\pm$ and first two neutralinos $\tilde{\chi}_1^0, \tilde{\chi}_2^0$ are almost mass degenerate. The $\tilde{\chi}_1^\pm$ has a finite lifetime of 0.3 ps in the dM1600 and 8.5 ps in the dM770 scenario [6]. For the considered benchmark scenarios, an example of the full mass spectrum can be seen in figure 6.1.

Charginos decay into an LSP and a virtual W boson ($\tilde{\chi}_1^\pm \rightarrow \tilde{\chi}_1^0 W^{\pm *}$) as explained in section 2.7. As a consequence of small mass splittings, a significant amount of energy is carried away by the LSP, leaving the visible decay products very soft. The p_T spectrum of the visible chargino decay on the generator level for both the benchmark scenarios can be seen in figure 6.2. The p_T distribution of the higgsino decay products in the dM770 case is smaller than 2 GeV.

The track reconstruction efficiency as a function of transverse momentum is shown in figure 6.3 for chargino events at $\sqrt{s} = 500\,\text{GeV}$ and $\int \mathcal{L} dt = 500\,\text{fb}^{-1}$. Tracks with p_T above 300 MeV obtain a reconstruction efficiency of almost 100%. Two decay tracks are expected in most of the chargino events from the branching ratios. The

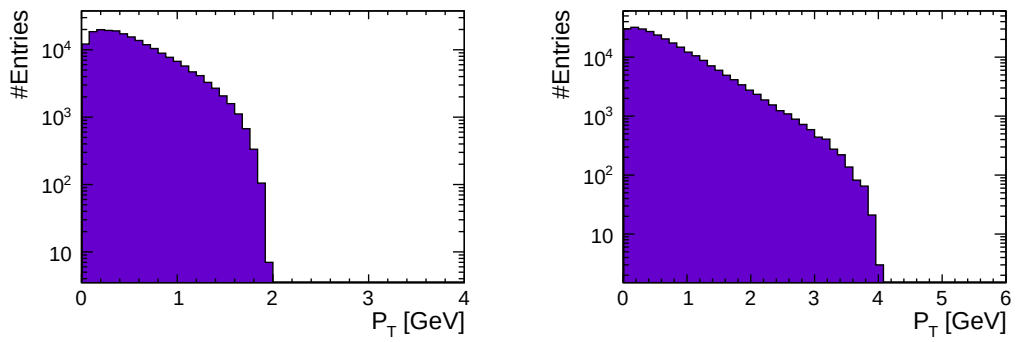

(a) (b)

Figure 6.2.: The p_T spectrum of visible chargino decay on generator level at $\sqrt{s} = 500\,\text{GeV}$ and $\int \mathcal{L}dt = 500\,\text{fb}^{-1}$. (a) dM770 scenario (b) dM1600 scenario.

efficiency for both the tracks to be reconstructed is about 61%.

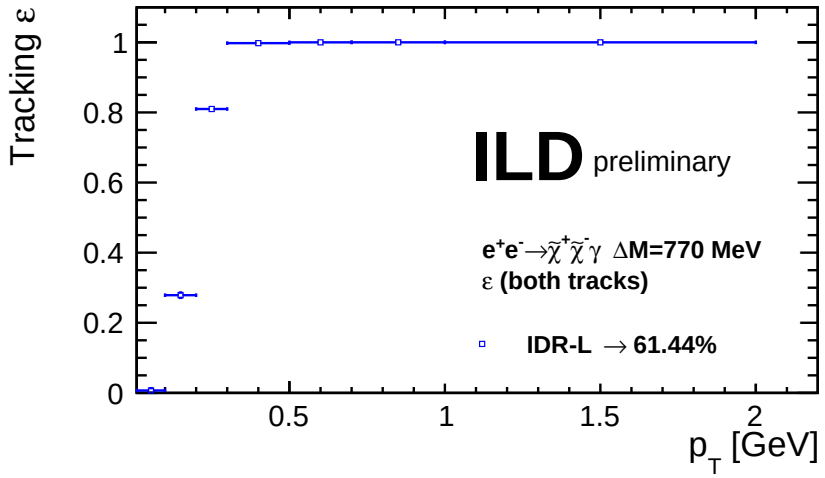

Figure 6.3.: Tracking efficiency for low p_T chargino decay tracks is shown. The tracking efficiency is found to be 100% above a $p_T > 300$ MeV. Both the decay tracks of charginos in an event are reconstructed 61% of the times. The plot is created using `v02-00-01` version of `iLCSoft`.

6.1.2. Branching Ratios

The decays of the lightest chargino $\tilde{\chi}_1^{\pm}$ and the neutralino $\tilde{\chi}_2^0$ to lightest supresymmetric particle $\tilde{\chi}_1^0$ is explained in detail in Chapter 2. The branching ratios for charginos and neutralinos are given in Table 6.2 and Table 6.3 respectively. In the dM770 scenario, charginos dominantly decay to $\pi^{\pm}\tilde{\chi}_1^0$ while the neutralinos dominantly decay to $\gamma\tilde{\chi}_1^0$. In the case of dM1600 scenario $\pi^{\pm}\pi^0\tilde{\chi}_1^0$ is the most frequent decay, while $\pi^{\pm}\tilde{\chi}_1^0$ is not more frequent than the lepton decay modes. Figure 6.4 shows the branching ratios of the chargino decays as a function of the mass difference between $\tilde{\chi}_1^{\pm}$ and $\tilde{\chi}_1^0$. The difference in the branching ratios for $\tilde{\chi}_1^{\pm}$ and $\tilde{\chi}_1^0$ are utilized to distinguish them in chargino analysis shown in Chapter 8.6.3. A semi-leptonic decay channel where the chargino decays to a pion and a $\mu^{\pm}/e^{\pm}$ are used in the analysis presented in this thesis. More details about the semi-leptonic selection is given in section 8.2.

$\tilde{\chi}_1^{\pm}$ **Decay mode**	**BR (dM1600)**	**BR (dM770)**
$e\nu\tilde{\chi}_1^0$	17.3%	15.0%
$\mu\nu\tilde{\chi}_1^0$	16.6%	13.7%
$\pi^+\tilde{\chi}_1^0$	15.5%	60.4%
$\pi^+\pi^0\tilde{\chi}_1^0$	28.5%	7.3%
$\pi^+\pi^0\pi^0\tilde{\chi}_1^0$	7.5%	0.03%
$\pi^+\pi^+\pi^-\tilde{\chi}_1^0$	7.1%	0.03%
$\pi^+\pi^+\pi^-\pi^0\tilde{\chi}_1^0$	2.4%	-
$\pi^+\pi^0\pi^0\pi^0\tilde{\chi}_1^0$	0.5%	-
$K^+\tilde{\chi}_1^0$	1.2%	3.5%
$K^0\pi^+\tilde{\chi}_1^0$	1.0%	0.03%
$K^+\pi^0\tilde{\chi}_1^0$	0.5%	0.02%

Table 6.2.: Chargino $\tilde{\chi}_1^{\pm}$ decay modes according to `Herwig++ 2.6.0`. Table taken from [6].

6.2. The SM Backgrounds

The SM processes can be classified in terms of their initial and final states. Due to the induced strong electromagnetic field between the colliding bunches, photons are emitted before the e^+e^- collisions. Hence along with the e^+e^- collisions there are

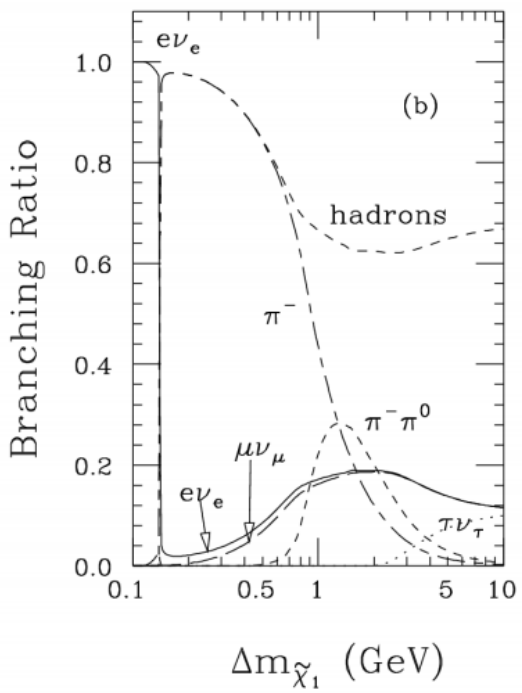

Figure 6.4.: Branching ratios of the chargino decay as a function of mass difference between the chargino and the LSP, $\Delta m_{\tilde{\chi}_1} = \Delta M_{\tilde{\chi}_1^\pm - \tilde{\chi}_1^0}$. Figure taken from [167].

$\tilde{\chi}_2^0$ **decay mode**	**BR (dM1600)**	**BR (dM770)**
$\gamma\tilde{\chi}_1^0$	23.6%	74.0%
$\nu\overline{\nu}\tilde{\chi}_1^0$	21.9%	9.7%
$e^+e^-\tilde{\chi}_1^0$	3.7%	1.6%
$\mu^+\mu^-\tilde{\chi}_1^0$	3.7%	1.5%
hadrons + $\tilde{\chi}_1^0$	44.9%	12.7%

Table 6.3.: Neutralino $\tilde{\chi}_2^0$ decay modes according to `Herwig++ 2.6.0`. Table taken from [6].

also $e^{\pm}\gamma$ and $\gamma\gamma$ collisions as explained in section 3.4.4. These three initial states constitute the classes of SM backgrounds considered in this study. The incoming photon can either be real or virtual depending on the source of photons. Figures 6.5a and 6.5b illustrate three different Standard Model background classes based on their initial particles and momentum transfer. $Q_{1,2}^2 = -p_\gamma^2$ is the virtuality of the photons in which case it is zero for real photons. Depending on the momentum transferred to the fermion pair, the scattering angle of outgoing electrons would be large enough to be within the acceptance of the detector. Smaller momentum transfer to the fermion pair results in the scattering of the outgoing electrons with a very small angle making them go down the beampipe. For example, if both the incoming electrons transfer enough momentum to the photon such that the outgoing electrons scatter with an angle large enough to be seen in the detector, then these backgrounds fall under the e^+e^- class of backgrounds. If either of the incoming electrons fails to transfer adequate amount of momentum to the photon then that electron goes down the beam pipe and only one electron is visible in the detector. Such backgrounds fall under $e^{\pm}\gamma$ category of backgrounds as shown in figure 6.5a. When both the incoming electrons scatter with a very small angle and go down the beam pipe, the backgrounds fall under the $\gamma\gamma$ category of backgrounds. Examples of the three different Standard Model background classes are given in figure 6.6. The Feynman diagram shows processes like $e^+e^- \rightarrow 4f$, $e^-\gamma \rightarrow 3f$ and $\gamma\gamma \rightarrow 2f$. Generally, the processes that have an even/odd number of intial state fermions produce an even/odd number of final state fermions. The Standard Model backgrounds considered for this analysis consists of $e^+e^- \rightarrow (2f, 4f, 6f)$, $e^{\pm}\gamma \rightarrow (1f, 3f, 5f)$ and $\gamma\gamma \rightarrow (2f, 4f)$ processes.

The low energy decay products of the SM background sometimes mimic the low p_T decay products of the signal. In the SM background processes producing tau neutrinos carry away a large amount of energy or a significant amount of energy escapes

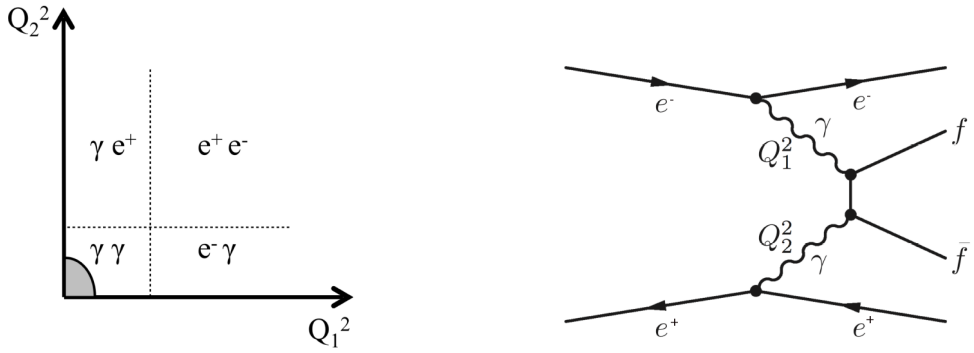

(a) (b)

Figure 6.5.: The Feynman diagram displays three different classes of Standard Model background. $Q^2_{1,2}$ is the measure of the transferred four momentum to the corresponding photon.

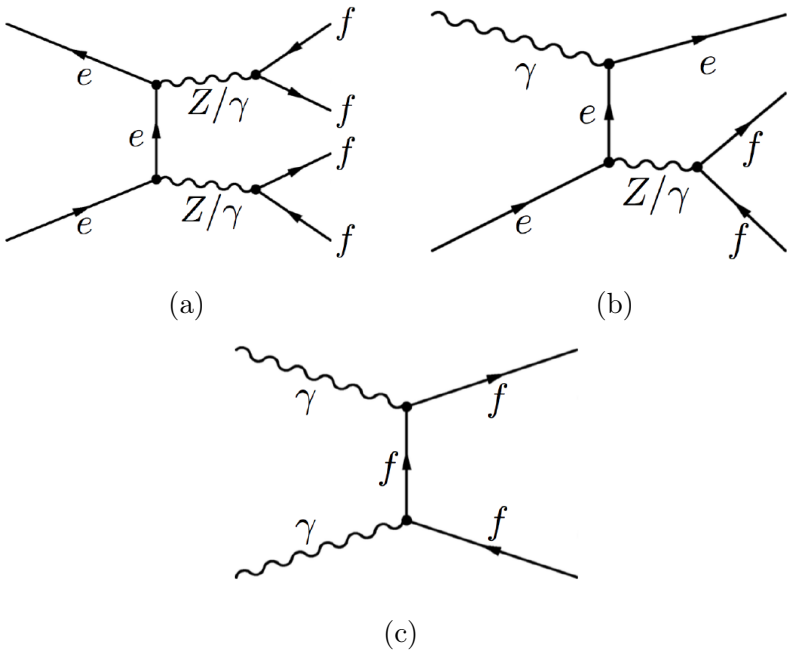

(a) (b)

(c)

Figure 6.6.: Examples of the three different classes of the Standard Model background with respect to their initial state particle i.e. e^+e^-, $e^\pm\gamma$ and $\gamma\gamma$.

with particles going in uninstrumented regions of the detector (e.g. beampipe). These backgrounds are illustrated in detail in the sections below.

Backgrounds with e^+e^- initial state : Suppressing the backgrounds that fall under the e^+e^- initial state category is easier than the $\gamma\gamma$ or $e^{\pm}\gamma$ processes with the preselection determined through the topology of the signal samples (cf. Chapter 7). However, since the $\tau^+\tau^-$ events have same signatures as the chargino signals, they are expected to be one of the dominant backgrounds in this analysis. The τ-leptons decay into a virtual W boson and ν_τ. The virtual W boson produced can decay either leptonically or hadronically. Here a large amount of energy is carried away by the invisible neutrinos and the low energetic remnant fermions mimic the signal events. The τ pairs coming out of such e^+e^- processes have their cross sections 20 times larger, $\mathcal{O}(2000)$ fb, than the signal, $\mathcal{O}(100)$ fb, for the case of the incoming electron being a left-handed and the incoming positron a being right-handed. There is no missing energy threshold for τ decays; the neutrinos can carry away any unknown amount of energy. However, the case of neutrinos carrying away a huge amount of energy leaving the τ-leptons to decay softly is rare. This allows to suppress the τ decay particles without applying very narrow cuts on the event topology.

Backgrounds with $\gamma\gamma$ initial state : The backgrounds with $\gamma\gamma$ initial state are the ones where large amount of energies are lost due to the particles going down the beampipe. These backgrounds have a very high cross section of $\mathcal{O}(10^6)$ fb for processes like $\gamma\gamma \rightarrow 2f$ and a cross section of $\mathcal{O}(100)$ fb for $\gamma\gamma \rightarrow 4f$. The $\gamma\gamma \rightarrow 2f$ class forms the dominant background which is formed in the process of $e^+e^- \rightarrow e^+e^-\gamma^*\gamma^* \rightarrow e^+e^-f\overline{f}$. The cross sections for τ-pairs produced in $\gamma\gamma$ processes are much larger than for τ - pair production from e^+e^- processes. The outgoing beam electrons in $\gamma\gamma$ process have very low transverse momenta such that they go down the beampipe carrying a large fraction of the energy. This makes the τ to decay very softly, thus mimicking the signal. These events are distinguished by the method of initial state radiation (ISR) emitted by one of the beam electrons with a certain energy and angle such that they are seen in the detector. The incoming electron or positron that radiates the photon recoils against the ISR photon. If the ISR photon has sufficient energy, then the incoming particle is deflected into the acceptance of the detector. This saves a large amount of energy that would be missed if the incoming electron or positron goes down the beampipe without being averted into the acceptance of the detector by the ISR photon. However, for the case of $\gamma\gamma \rightarrow 2f$ where the initial particles are real photons from beamstrahlung, the emission of an ISR photon is not possible since there are no charged particles in the initial state. Hence in such cases, some event selection cuts to suppress such backgrounds has to be applied.

Backgrounds with $e^{\pm}\gamma$ initial state : Like the first two cases, $e^{\pm}\gamma$ processes also

gives similar signatures with respect to the signal events. The $e^{\pm}\gamma \to 3f$ class, particularly in the t-channel diagram as shown in figure 6.6b, is a dominant class with a cross section of $\mathcal{O}(10^5)$ fb, whereas $e^{\pm}\gamma \to 5f$ has a cross section of the $\mathcal{O}(100)$fb. In this scenario an ISR photon is emitted only from one of the initial particles since the other one would be a neutral particle. Unlike $\gamma\gamma \to 2f$ class, the emitted hard ISR photon does not recoil against the beam electron. It instead recoils against the $f\overline{f}$ pair produced via the exchange of a Z boson or photon. The beam electron emitting the ISR photon transfers a very small fraction of energy to the photon and carries away a huge fraction of the energy down the beampipe. Similar to earlier cases, the large missing energy makes these events very similar to the signal events. The requirement of ISR photon in this particular case is not very helpful to remove these backgrounds.

6.2.1. Initial State Radiation Method

The initial state radiation (ISR) method is a great tool to suppress the $\gamma\gamma \to 2f$ background. This method has been used before e.g. for search of nearly mass degenerate charginos and neutralinos by the OPAL experiment at LEP [168] and at the ILC [6, 7]. The visual representation of the expected signature for signal and $\gamma\gamma \to 2f$ background without the requirement of an ISR photon in the detector is given in figure 6.7. For $\gamma\gamma \to 2f$ backgounds having virtual initial photons, both the beam electrons go down the beampipe thus causing large missing energy. This results into the presence of only a few soft remnants of the decay in the detector. However, the signal also has soft final state particles as signature since the LSPs carry away a huge fraction of energy.

The additional requirement of the presence of a hard ISR photon can solve the problem of similar final states from the signal and background. The detector sketches for this process is shown in figure 6.8. The ISR photon should have a certain angle such that it is within the acceptance of the tracking system of the detector. Only then can a PFO be distinguished as a photon or an electron. The photon should also have sufficiently high energy such that it deflects the outgoing beam electron into the acceptance of detector. This renders a signature for the two-photon background which includes an additional beam electron in it. For the signal processes, most of the energies are carried away by the LSPs. Thus the requirement of an additional ISR photon does not make any crucial differences in the signature for the signal.

6.2.2. Beam-Induced backgrounds

Apart from the main Standard Model backgrounds, beam induced backgrounds are one the major concerns for low δM higgsino analysis. As mentioned in section 3.4.4, secondary particles created in the interaction of the beamstrahlung photons might

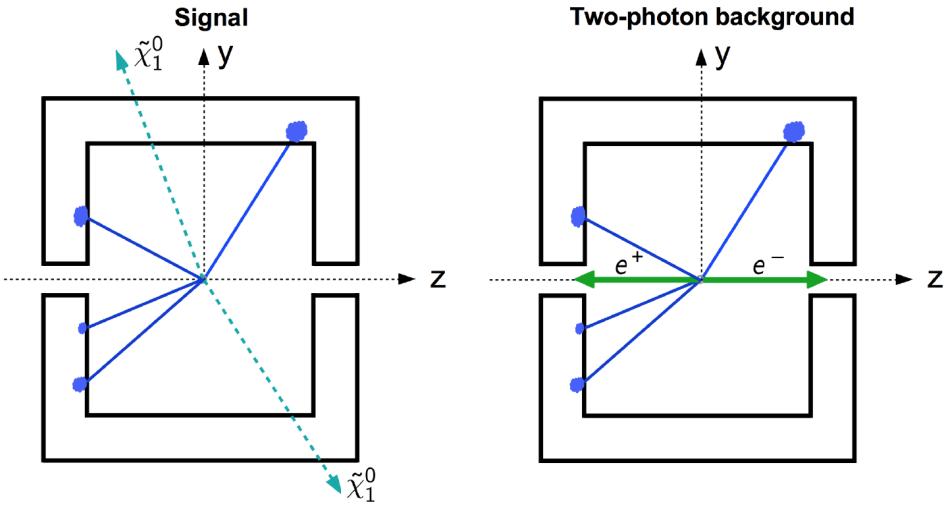

Figure 6.7.: Detector sketches for the final state particles of signal and $\gamma\gamma \to 2f$ background. Since a large fraction of energy is carried away by the LSPs ($\tilde{\chi}_1^0$), only a few soft particles are observed. In case of the background, a large fraction of energy is missing due to the beam electrons escaping through the beam pipe. Figure taken from [6].

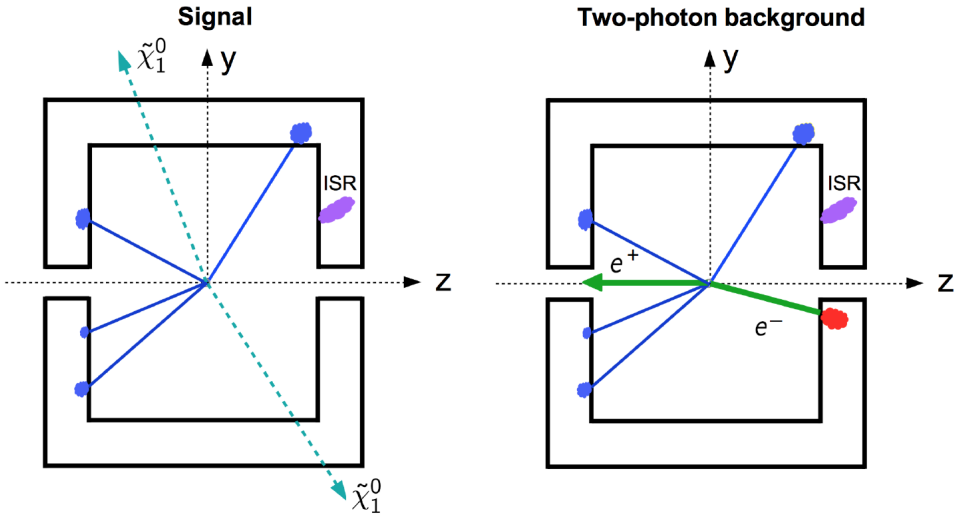

Figure 6.8.: Detector sketches for the final state particles of signal and $\gamma\gamma \to 2f$ background with the requirement of an ISR photon. The beam electron transfers energy to the ISR photon and deflects with an angle thus becoming visible in the detector. Figure taken from [6].

impact the detector performance significantly. The particles created in these interactions have very low transverse momentum which make them topologically very similar to the chargino decay products. They are dicussed in more details in further sections.

Soft e^+e^- Pair Backgrounds

Low energetic e^+e^- pairs are created when the real or virtual photons interact with each other. These processes are made apparent in figure 3.5. The production of e^+e^- pairs receive contributions from coherent [169] and incoherent [170] processes. Thereby the production of electron-positron pairs by a photon impinging on a high density bunch of electron or positrons is called coherent pair creation. Incoherent pair creation results from the interaction of two photons. Thereby, e^+e^- pair can be created through three different processes depending on the virtuality of the photon. The creation of an e^+e^- pair due to the interaction of two real beamstrahlung photons is called *Breit-Wheeler process* [171]. When one of the two interacting photons is a virtual photon then the process is called *Bethe-Heitler process* [172]. If both the interacting photons are virtual then e^+e^- pairs are created through *Landau-Lifshitz process* [173].

The soft e^+e^- pairs can be deflected into the detector with larger angles thereby creating tracks in the vertex detector and in the TPC. However, being soft particles, they mostly curl and travel along the applied magnetic field used to determine the transverse momentum of the particles. This ascertains that it is the forward region of the detector which is mainly affected by e^+e^- pairs produced. They may also backscatter into the vertex detector or into the TPC due to interactions with the material in the endcap.

Nevertheless, many additional tracks are produced by the pair background in the vertex detector, TPC and especially in forward detectors. Most of these background tracks have low transverse momentum. Since low p_T region is of high interest for the higgsino events, the background tracks cannot be reduced by vetoing tracks having p_T below a certain threshold value (e.g. $p_T < 1\,\text{GeV}$) as they would affect the low multiplicity signature of the signal events.

$\gamma\gamma \rightarrow$ low p_T hadron backgrounds

$\gamma\gamma \rightarrow$ low p_T hadron background events are explained in a very detailed fashion in Chapter 5. Real photons or virtual photons created in e^+e^- processes can interact with each other in different ways e.g.direct, VMD or GVMD as explained in section 2.3.3. Photons can fluctuate into vector mesons for a very short period of time since they have same quantum properties (section 2.3.3). The photons fluctuated into mesons interact with each other to produce low p_T final state hadrons and pho-

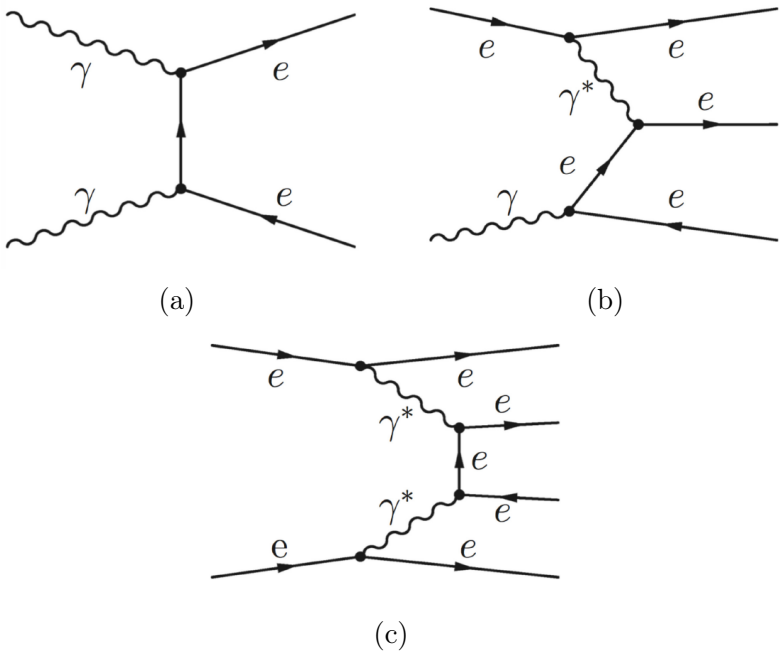

Figure 6.9.: Feynman diagrams for three different types of processes in creation of e^+e^- pairs (a) real-real photon interaction (Breit-Wheeler process) (b) real-virtual photon interaction (Bethe-Heitler process) (c) virtual-virtual photon interaction (Landau-Lifshitz process)

tons. These low p_T final state particles are most frequently found to be charged pions. As shown in section 6.1.2, charginos decay into low p_T pions 68% of the times for dM770 scenario and 63% of times for dM1600 case. Since the final state particles of $\gamma\gamma \rightarrow$ low p_T hadron backgrounds and $e^+e^- \rightarrow \tilde{\chi}^+\tilde{\chi}^-\gamma$ are dominantly low p_T pions, separating signal tracks from these overlay tracks is quite challenging.

Standard jet clustering methods e.g.k_T algorithm methods are normally used to remove $\gamma\gamma \rightarrow$ low p_T hadron backgrounds. The beam induced backgrounds are usually removed by using an exclusive k_T jet algorithm [174]. This jet clustering method involves grouping the reconstructed particles (PFO's) present in the event into jets. The distance between two reconstructed particles is then measured using Eq. 6.1

$$d_{ij} = \frac{min(p_{T_i^2}, p_{T_j^2}) \cdot \Delta R_{ij}^2}{R^2} \tag{6.1}$$

where $\Delta R_{ij}^2 = (y_i - y_j)^2 + (\phi_i - \phi_j)^2$ with $y_{i,j}$ being the rapidities, $\phi_{i,j}$ the azimuthal angle and $p_{Ti,j}$ the transverse momenta of the particles forming the pairs [98]. The pair distance is calculated for each pair of reconstructed particles and in addition the

distance between each individual PFO and the beam (d^i_{beam})is also calculated. The pair distances (d_{ij}) and the beam distances (d^i_{beam}) are compared and the minimal value is evaluated. If the calculated minimum is a pair distance then the two PFOs are merged by adding their four momenta thus gradually forming a jet. Conversely, if the beam distance is found to be the minimum value, then that particular PFO is considered to be the part of beam and is discarded. Since the hadrons produced in $\gamma\gamma \rightarrow$ low p_T hadron backgrounds have a very low transverse momentum they are found close to the beam. Thus they are expected to fulfill algorithm's condition of d^i_{beam} to be minimum for rejection. This makes the exclusive k_T clustering algorithm a useful tool to remove $\gamma\gamma$ backgrounds.

However, the use of k_T clustering algorithm to remove $\gamma\gamma \rightarrow$ low p_T hadron backgrounds in a higgsino-like chargino analysis is not feasible for two different reasons. An $e^+e^- \rightarrow \tilde{\chi}^+\tilde{\chi}^-\gamma$ event is a very low multiplicity event. The charginos dominantly decay into one charged track and sometimes additional neutral particles. Secondly, the final decay products of the $e^+e^- \rightarrow \tilde{\chi}^+\tilde{\chi}^-\gamma$ process have very low transverse momentum. These particles along with the $\gamma\gamma \rightarrow$ low p_T hadron particles fulfill the $d^i_{beam} \rightarrow min$ condition of rejection and are identified as part of the beam and finally are discarded as beam backgrounds. Thus even though the exclusive k_T clustering algorithm can be a great tool to remove $\gamma\gamma \rightarrow$ low p_T hadron backgrounds, for the particular case of $e^+e^- \rightarrow \tilde{\chi}^+\tilde{\chi}^-\gamma$ events it remains inefficient.

6.3. Possible methods to remove $\gamma\gamma$ overlay

Since the standard $\gamma\gamma \rightarrow$ low p_T hadron removal methods are not sufficient to remove these backgrounds, it is important to find an alternative method which takes the topology of signal and backgrounds into account. In further sections, possible differences between the signal and the background are discussed.

6.3.1. Displaced vertices

The photons which form the source of $\gamma\gamma \rightarrow$ low p_T hadron backgrounds are either radiated off the beam or virtually created during the e^+e^- interaction. The collision between these photons is independent of the specific e^+e^- collision from which the higgsino event originates even though they belong to the same bunch crossing. This denotes that the primary vertices of the specific e^+e^- interactions producing the signal events and the photon-photon interaction are different and thus can be displaced from each other. Figure 6.10 represents the true Monte-Carlo information of the vertices for overlay and signal particles for three example events. To make it more comparable with the real life scenario, only vertices of stable charged particles are considered since tracks are used to reconstruct vertices. Charginos have a finite

lifetime, due to which, the vertices reconstructed with the final state tracks would give the secondary vertices of the signal (figure 7.1). Thus the Monte-Carlo information of vertices where the charginos begin to decay are used in the plots. The vertices for signal and $\gamma\gamma$ overlay are separated. Even in the cases where an event is overlaid with more than one $\gamma\gamma$ overlay event, the vertices for each $\gamma\gamma$ overlay event is different and displaced. This can be interpreted as different primary vertices for signal and for $\gamma\gamma$ background. However, $e^+e^- \rightarrow \tilde{\chi}^+\tilde{\chi}^-\gamma$ have a very low multiplicity and consists only one single track from each chargino. Reconstruction of vertices with single tracks is not possible. Hence, intead of reconstructing the vertices, tracks can be grouped together as per their distances from each other on the z axis thus grouping them as signal of background groups similar to vertices. This method is explained in detail in Chapter 7.

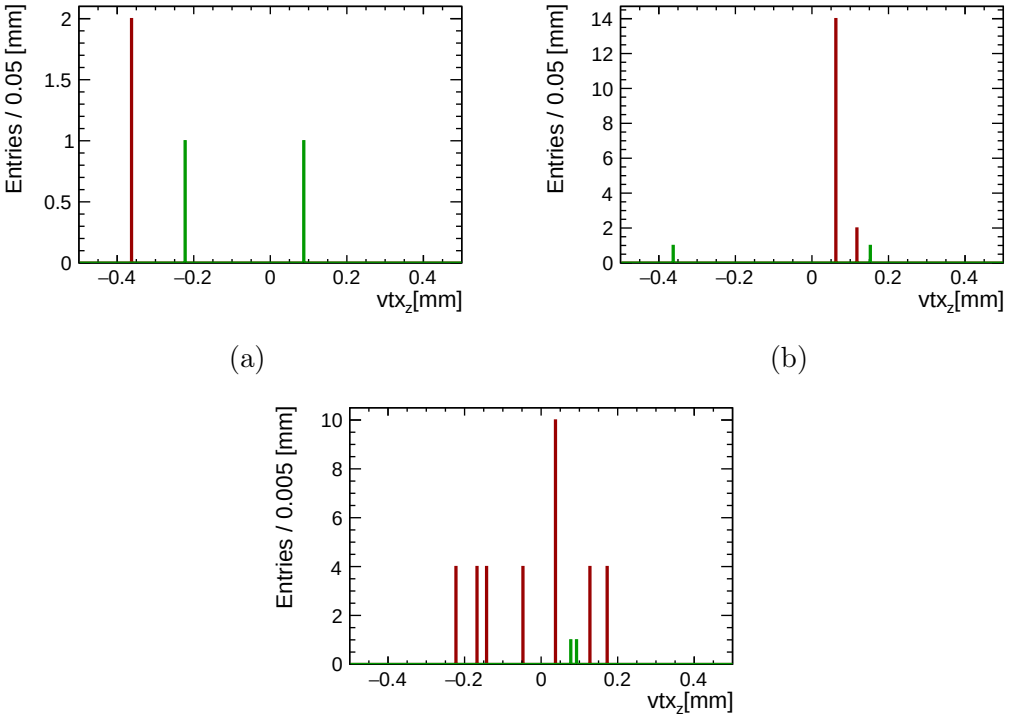

Figure 6.10.: Examples of three random events showing the positions of true primary vertices of $\gamma\gamma \rightarrow$ low p_T hadron events and secondary vertices of the higgsino events on the z axis. Green represents signal and reddish brown represents overlay.

6.3.2. Rho meson reconstruction

Vector meson dominance explains the fluctuation of photons in a vector meson are pre-dominantly charged and neutral ρ mesons 2.3.3. The production of $\rho^{\pm}$ mesons in $e^+e^- \rightarrow \tilde{\chi}^+\tilde{\chi}^-\gamma$ processes is possible but highly unlikely. For the dM770 benchmark scenario, the mass difference between $\tilde{\chi}^{\pm}$ and LSPs is exactly the mass of any ρ meson. Due to the reduced phase space from the mass difference of $\tilde{\chi}^{\pm}$ and LSPs, the formation of a $\rho^{\pm}$ or ρ^0 meson is highly unlikely. In the dM1600 benchmark scenario, the mass phase space would be large enough to produce a ρ meson. But the probability for the chargino to decay into a $\rho^{\pm}/\rho^0$ and LSP is very small. This implies that charged and neutral ρ-mesons are dominantly found in $\gamma\gamma \rightarrow$ low p_T hadron events which makes them a tag for identifying $\gamma\gamma \rightarrow$ low p_T hadron events. It is possible to reconstruct the mass of the parent meson by computing the invariant mass of their decay particles. The invariant mass from the decay particles is calculated using Eq. 6.2

$$M = \sqrt{E^2 - (P_x^2 + P_y^2 + P_z^2)} \tag{6.2}$$

where M is the invariant mass, E is the energy and P_x, P_y and P_z are the three momenta.

The $\gamma\gamma \rightarrow$ low p_T hadron events produced by the Barklow generator as mentioned in section 5.3.1 are less complex as compared to `Pythia` events. These events are chosen and differentiated into different classes with respect to their decay process. For example, they are classified as $\gamma\gamma$ events decaying to $\rho^+\rho^-$, $\rho^0\rho^0$, $\pi^0\pi^0$, $\pi^+\pi^-$ etc. Since the ρ^0 meson decays into oppositely charged pions, $\gamma\gamma \rightarrow \rho^0\rho^0$ events are chosen where two positively charged pions and two negatively charged pions are expected as $\gamma\gamma \rightarrow \rho^0\rho^0 \rightarrow \pi_i^+\pi_j^-\pi_k^+\pi_l^-$. The invariant mass of two different pion combinations as $M_{i,j}$ and $M_{k,l}$ or $M_{i,l}$ and $M_{k,j}$ are calculated using Eq. 6.2. A combination of pions is chosen by minimizing the difference between invariant mass calculated with different pion combinations and true ρ meson mass using minimization of the sum of the squared mass differences as:

$$\Delta M_{\rho^2} = [M_{i,j} - M_\rho]^2 + [M_{k,l} - M_\rho]^2 \tag{6.3}$$

where $M_\rho = 770\,\text{MeV}$ is the true mass of the ρ meson. The ΔM_{ρ^2} minimization value for two different combinations of oppositely charged pions is calculated. Figure 6.11 represents the invariant mass of different combinations of oppositely charged pions at Monte-Carlo truth level. Even though wrong combinations can sometimes be chosen over the right combination of pions, the figure shows that the calculated invariant mass mostly peaks over $770 \pm 145\,\text{MeV}$ which is the true ρ meson mass.

A similar method is applied at the reconstruction level by choosing a combination of oppositely charged tracks without cheating the pion ids from the true information.

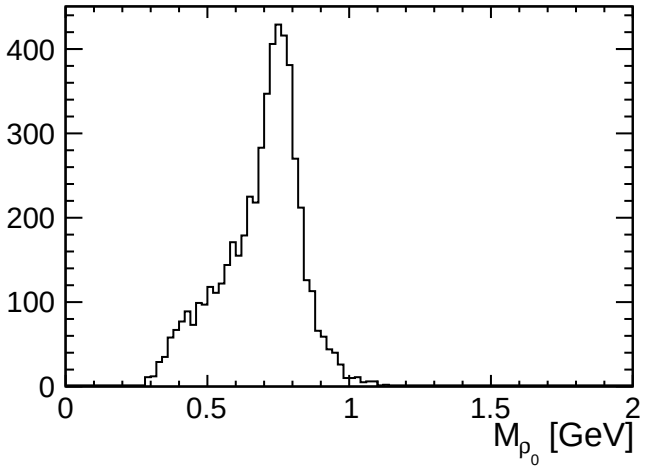

Figure 6.11.: The invariant mass of ρ^0 meson reconstructed with different combinations of oppositely charged pions at Monte-Carlo truth level by using the ΔM_{ρ^2} minimization for 2700 $\gamma\gamma \rightarrow \rho^0\rho^0 \rightarrow$ low p_T hadron events.

Invariant mass of different combinations of oppositely charged tracks are calculated and ΔM_{ρ^2} minimization method is applied over all different combinations found. Choosing the combination with minimal ΔM_{ρ^2} value, the invariant mass is plotted in figure 6.12. In this case too the calculated invariant mass mostly peaks over the true ρ meson mass.

With the use of the ρ reconstruction method, the presence of a ρ meson in a process can be detected which thus forms a tag for $\gamma\gamma \rightarrow$ low p_T hadron events. Once the tracks are grouped on the basis of their distances in z axis as mentioned in section 6.3.1, it is important to identify if a group is a signal group or a backgound group. With the ρ meson recontruction method groups from $\gamma\gamma \rightarrow$ low p_T backgrounds can be identified using a ρ meson tag. This method remains valid only for events having ρ mesons in them. These methods were investigated further and the developed new methods are explained in the chapter ahead.

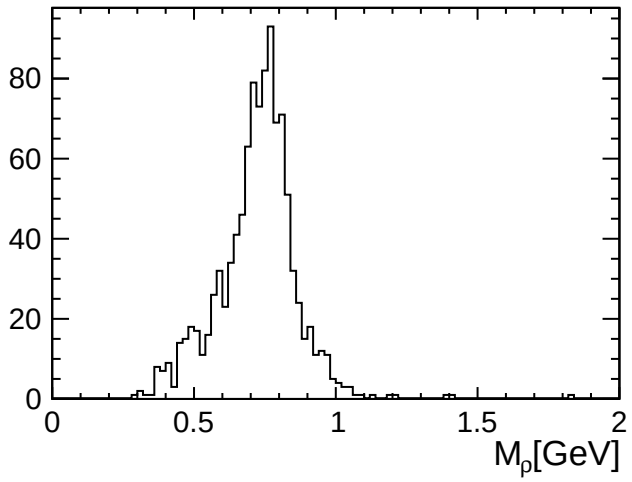

Figure 6.12.: The invariant mass of ρ^0 meson reconstructed with different combinations of oppositely charged tracks at reconstruction level using ΔM_{ρ^2} minimization for 2700 $\gamma\gamma \rightarrow \rho^0\rho^0 \rightarrow$ low p_T hadron events.

7. Development of the track grouping Algorithm

One of the important differences between $e^+e^- \to \tilde{\chi}_1^+\tilde{\chi}_1^-$ and $\gamma\gamma \to$ low p_T hadron events is that they occur at different positions on the z-axis and hence have displaced vertices with respect to each other. Also, the finite lifetime of the $\tilde{\chi}_1^\pm$ results into a large impact parameter on its decay track in the transverse plane. The $\gamma\gamma \to$ low p_T hadrons decay promptly and do not have a large impact parameter in the $x-y$ plane. However, they are longitudinally displaced from the $\tilde{\chi}_1^\pm$ decay particles. This chapter introduces an algorithm developed to group the $\tilde{\chi}_1^\pm$ decay tracks and $\gamma\gamma \to$ low p_T hadron tracks based on their longitudinal positions and differences in impact parameters.

7.1. The Standard Vertex Algorithm

The standard vertex finding algorithm for Linear Collider studies is given by `LCFIPlus`. `LCFIPlus` is a modular software framework which implements different algorithms like the vertex finding algorithm, jet finding algorithms and a multivariate analysis for flavour identification using the `TMVA` package [148]. The program can select different algorithms during run-time and can also use external programs to substitute internal algorithms. `LCFIPlus` is implemented in Marlin framework of `iLCSOFT` [175]. The standard vertex finding algorithm assumes that there is more than one charged track to form a vertex. For $\gamma\gamma \to$ low p_T hadron processes, the reconstruction of a primary vertex is possible for events with at least two charged particles if at least two tracks are reconstructed. However, for low multiplicity physics processes e.g $e^+e^- \to \tilde{\chi}_1^+\tilde{\chi}_1^-\gamma$, the reconstruction of primary vertex is not usually feasible: As stated in section 6.1.2, charginos decay into an invisible neutralino, a charged track and sometimes into other neutral particles. Charginos being long lived particles, decay into a single charged track only after a flight of a few millimeters in the detector. With only one single track and most of the energy carried away by the invisible particles, it is not feasible to extrapolate the tracks of two different charginos back to the primary point of collision. Thus the reconstruction of the primary vertex is not possible for low ΔM higgsino processes.

In such scenarios, the standard vertex fitter is not sufficient to distinguish between $\gamma\gamma \rightarrow$ low p_T hadron processes and e^+e^- interactions. This necessitates the need of an algorithm which would employ a different strategy instead of the conventional method of reconstructing the vertices. In further sections such an algorithm developed in this study, its working method and performance is discussed.

7.2. Development of the track grouping algorithm

Section 6.3.1 gives a very detailed explanation of how the interactions of photons radiated off the beam particles have displaced vertices. Consequently, the tracks originating from the $\gamma\gamma \rightarrow$ low p_T hadron overlay vertex and the $e^+e^- \rightarrow \tilde{\chi}^+\tilde{\chi}^-$ vertex would also be expected to be displaced from each other. Therefore, instead of reconstructing displaced vertices, the decay tracks of the signal and $\gamma\gamma \rightarrow$ low p_T hadron overlay can be grouped separately based on their positions in space from each other. The working method of the algorithm and the role of the track impact parameters is described in the following.

7.2.1. The role of impact parameters

The track impact parameters as introduced in detail in section 4.5 and in figures 4.5 and 4.6 serve as important tools to build a track grouping algorithm. Considering the beam spot to be 300 μm in z direction (σ_z) and nanometer sized in x (σ_x) and y (σ_y) directions as given in table 3.2, the maximum displacement among the tracks is expected in the z-axis. Since z_0 becomes the closest comparable parameter to the z-position of the true primary vertex, the best strategy to group the tracks would be to group them based on their z_0 values. In order to ensure that the z_0 value is a meaningful approximation of the z-vertex positions, the impact parameter in the $x-y$ plane (d_0) should be less than a certain threshold value. More details about this is given in section 7.2.2 and in figures 7.2b and 7.2a. For this to be feasible in low multiplicity events like $e^+e^- \rightarrow \tilde{\chi}^+\tilde{\chi}^-\gamma$, it is important that the track fit is performed efficiently. For the physics processes like $e^+e^- \rightarrow \tilde{\chi}_1^+\tilde{\chi}_1^-\gamma$ where $\tilde{\chi}_1^\pm$ have a finite life time, the particles do not always decay close to the z-axis. However, since most of the particles in $\gamma\gamma \rightarrow$ low p_T events decay immediately, they decay very close to the z-axis. In such cases, d_0 parameter gives an additional handle to separate the signal and the background.

7.2.2. Track selection for low the ΔM higgsino benchmark scenarios

The track grouping algorithm is mainly studied for the two higgsino benchmark scenarios as explained in section 6.1.1. A selection procedure is applied on the tracks based on their properties. The details of this procedure is given in the following.

For the z_0 value to be a good proxy for the z position of the promary vertex, it would be ideal if the transverse impact parameter value is minimum. Being long lived particles, charginos have high d_0 decay tracks. The smaller the mass difference between $\tilde{\chi}_1^{\pm}$ and $\tilde{\chi}_1^0$, the larger is the $\tilde{\chi}_1^{\pm}$ lifetime. Figure 7.1a and figure 7.1b show the distance in flight of $\tilde{\chi}_1^{\pm}$ for benchmark scenarios dM770 and dM1600 respectively. It is evident from the figures that charginos in the dM770 scenario have a larger life time than that in the dM1600 scenario.

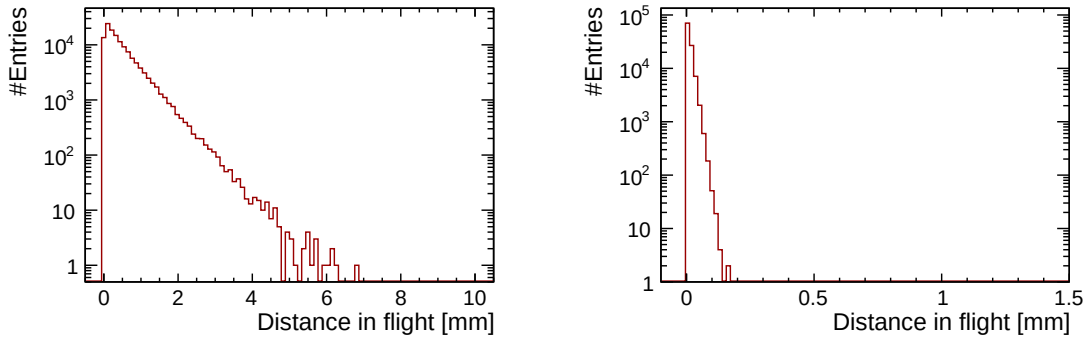

(a) (b)

Figure 7.1.: Distance in flight for charginos. a) benchmark scenario dM770 b) benchmark scenario dM1600.

Thus only the tracks having d_0 value below a certain threshold value are selected for the algorithm while the rest are treated differently. This threshold for the d_0 value is determined from figure 7.2. The plot shows the projection of d_0 in slices over the difference of the z_0 parameter of the track and the z-position of the Monte-Carlo primary vertex. Different slices represent different d_0 ranges. In the dM1600 case, the peak at $|z_0 - z_{mc}| = 0$, is the largest for the chargino decay tracks with $-0.2 < d_0 < 0.2$. Thus for the dM1600 scenario, $|d_0| = 0.2\,\text{mm}$ is taken as the threshold value. With this cut, one or more tracks in 10% of the events are lost.

Since the lifetime for the charginos in dM770 is higher the chargino decay tracks have high d_0 values as compared to dM1600 scenario. Hence, eliminating tracks with $d_0 > 0.2\,\text{mm}$ would result in loss of significant amount of signal tracks. Therefore, before applying a cut on the d_0 value, a different treatment is required for the tracks in the dM770 scenario.

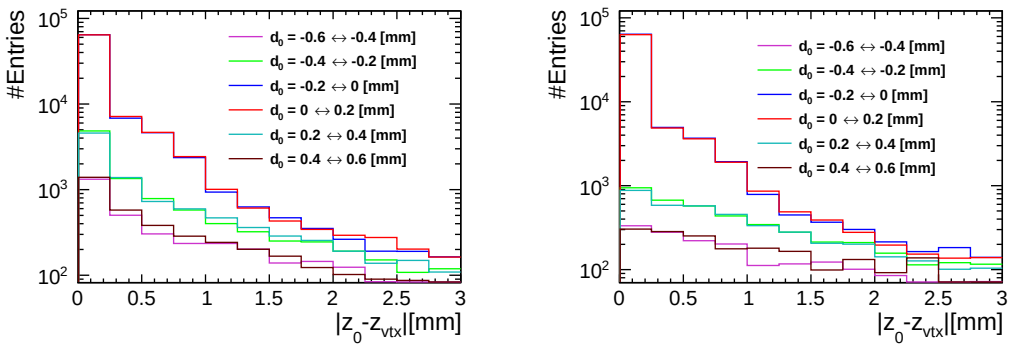

(a) (b)

Figure 7.2.: The slices of d_0 projection over $|z_0$ - $z_{vtx}|$. a) benchmark scenario dM770. b) benchmark scenario dM1600.

A detailed study on the transverse impact parameter of the signal and the $\gamma\gamma \rightarrow$ low p_T hadron overlay is performed to make an educated choice of different treatment on the signal tracks in the dM770 scenario. As mentioned in section 6.1.2, the chargino in the benchmark scenario dM770 decays into one charged particle 99.97% of the times. This denotes that every single event consists of one charged track each from both the charginos in an event. Figure 7.3 shows the d_0 and the d_0 significance for both the benchmark scenarios compared with their respective $\gamma\gamma \rightarrow$ low p_T hadron overlay tracks. The d_0 significance for a track is defined as

$$S_{d_0} = \frac{d_0}{\sigma_{d_0}} \tag{7.1}$$

where σ_{d_0} is the measurement error on d_0 value.

As seen in figure 7.3a, the d_0 distributions for signal and background are similar to each other even though charginos in the dM770 scenario have higher lifetime. However, as seen in figure 7.3c, S_{d_0} for the signal tracks is distinct from that of the $\gamma\gamma \rightarrow$ low p_T hadron tracks. This is because the $\tilde{\chi}_1^{\pm}$ tracks have a well measured impact parameter value while the $\gamma\gamma \rightarrow$ low p_T hadron tracks have a high d_0 value due to bad measurement. Since, the S_{d_0} values for the signal and the overlay are clearly separable, the track with the highest S_{d_0} value is separated from other tracks assuming it to be a signal track. The track selection procedures for the algorithm are further performed only on rest of the tracks.

Figure 7.4 shows that the S_{d_0} for each signal tracks in a particular event are noticeably different. The higher the S_{d_0} for one track, the closer is the S_{d_0} of the other track to zero. Also, the S_{d_0} for $\gamma\gamma \rightarrow$ low p_T hadron tracks is closer to zero which makes the choice of separating another track with second highest S_{d_0} value inefficient. The $\tilde{\chi}_1^{\pm}$ in the dM1600 scenario being short lived as compared to the

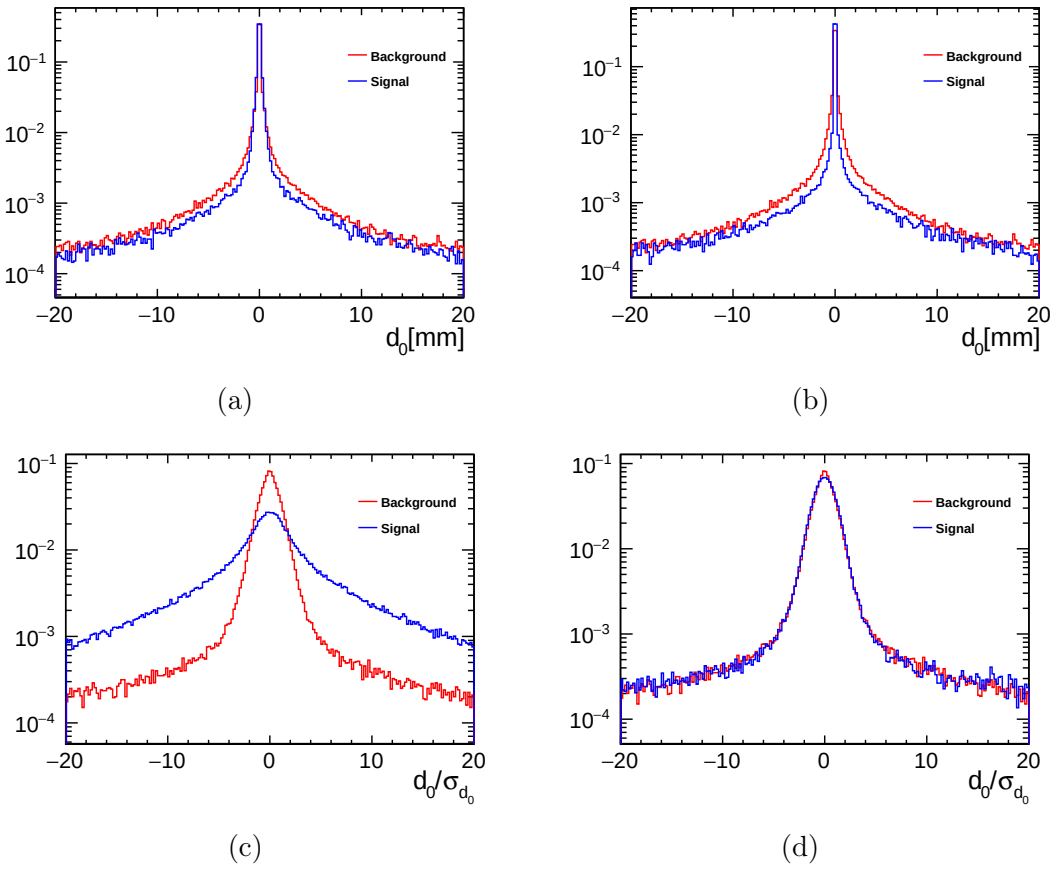

Figure 7.3.: d_0 and d_0 significance values for signal and $\gamma\gamma \rightarrow$ low p_T hadron overlay are compared with each other for different benchmark scenarios. a) d_0 for benchmark dM770. b) d_0 for benchmark dM1600. c) d_0 significance for benchmark dM770. d) d_0 significance for benchmark dM1600.

dM770 scenario, the d_0 and d_0 significance for signal and background are similar as shown in figure 7.3b and figure 7.3d. Therefore, no separation of high S_{d_0} tracks can be applied in this scenario.

The probability of the separated high S_{d_0} track being a signal track is studied and shown in figure 7.5. This study is conducted for two different samples: (i) only $\gamma\gamma \rightarrow$ low p_T hadron tracks are included and the pair background tracks are excluded (ii) both $\gamma\gamma \rightarrow$ low p_T hadron tracks and the pair background tracks are included. A number of additional particles are created through the interaction of particles in the physics processes with the detector material known as the shower particles. The impact of these particles are also considered in this study. With only the $\gamma\gamma \rightarrow$ low p_T hadron tracks and both the signal tracks reconstructed, 76 % of

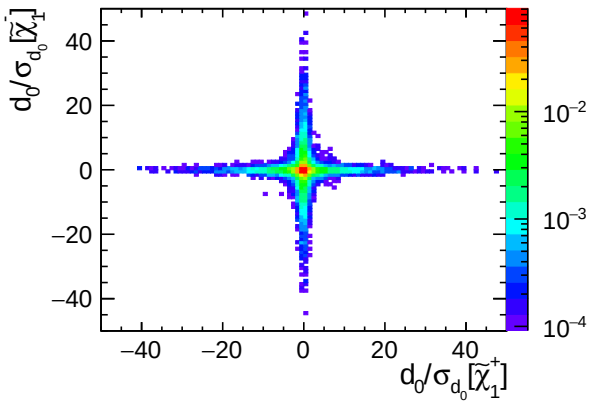

Figure 7.4.: The d_0 significance of two signal tracks in an event for dM770 benchmark scenario

.

the the separated high S_{d_0} tracks are signal tracks, 15% are the background tracks and 9% are the particles created in material interactions. With the inclusion of pair background tracks the signal efficiency reduces to 72 %, the probability of the high d_0 track being a background increases to 19% while the contribution from the shower particles stay the same. The study is repeated by including events with only one or no signal tracks reconstructed. In this case, the efficiency for the high S_{d_0} track being signal or overlay is given in figure 7.6. The efficiencies for all the cases are given in table 7.1.

This approach allows the separation of one of the two signal tracks from the overlay 76% of the times, even before passing them through the algorithm. At this stage, as the tracks with $|d_0| > 0.2$ mm values were removed in the dM1600 scenario, a d_0 threshold value is also applied on rest of the tracks in the dM770 scenario. Since charginos in dM770 scenario have higher lifetimes, it is required that the track should have $|d_0| < 0.3\,\text{mm}$ instead of $|d_0| < 0.2\,\text{mm}$ in the dM1600 scenario. With this cut, at least one of the tracks in 8% of the events are affected.

The shower particles introduced earlier in this section are created far away from the interaction point of the detector and hence have a high z_0 value. These particles can be avoided in the analysis by applying a z_0 cut on the tracks. Figure 7.7, shows the z_0 distribution for signal decay tracks and tracks from the shower particles. The z_0 value for the majority of the signal decay tracks is $|z_0| < 20\,\text{mm}$. At $|z_0| > 20\,\text{mm}$, tracks from interactions with the detector material dominate. A cut on $z_0 < 20\,\text{mm}$ impacts at least one signal track in 12% of the events. However, there are also many shower particles with $z_0 < 20\,\text{mm}$. Therefore it would be beneficial to tighten the cut if that does not influence the signal events severely. With the requirement of

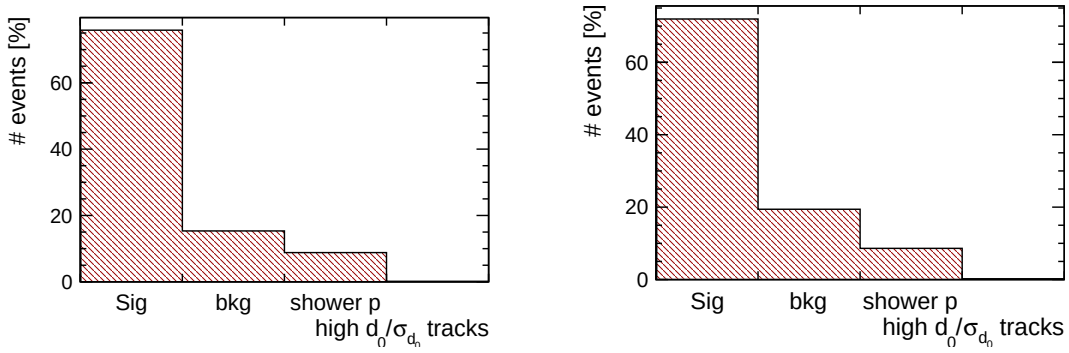

(a) (b)

Figure 7.5.: Efficiency of track with highest d_0 significance value being a signal, overlay or shower particle. These plots correspond to the sample where both the signal tracks in an event are reconstructed (a) events without pair background tracks (b) events with pair background tracks.

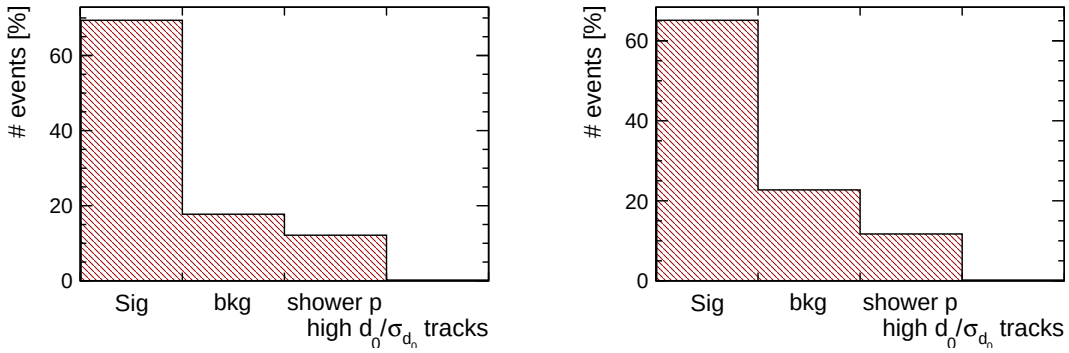

(a) (b)

Figure 7.6.: Efficiency of track with highest d_0 significance value being a signal, overlay or shower particle. All the events including the ones where both the signal tracks are not recontructed are considered. (a) events without pair background tracks (b) events with pair background tracks.

$z_0 < 15\,\text{mm}$, the signal tracks of 13% of the events are rejected which is only 1% more than the results with $|z_0| < 20\,\text{mm}$ cut. Since the cut on $z_0 < 15\,\text{mm}$ affects the events only slightly as compared to $z_0 < 20\,\text{mm}$, the tracks in this study are required to have $|z_0| < 15\,\text{mm}$.

Another important factor specific to the studies with low p_T decay tracks is that they curl due to the magnetic field of the detector. Figure 7.8 shows the event display for a chargino event. The part of the detector enclosing TPC between the

High d_0/σ_{d_0} tracks	Both signal tracks reconstructed [%]		All events [%]	
	No pair bkg	With pair bkg	No pair bkg	With pair bkg
Signal	76	72	69	65
Overlay	15	19	18	23
Shower Particles	9	9	13	12

Table 7.1.: Events having the high S_{d_0} track as a signal, overlay or a shower particle. The second and third column show events only with both the signal tracks reconstructed, wihout and with pair background respectively. The fourth and fifth column include all the events including the events where not both signal tracks are reconstructed.

Benchmark Scenario	$\lvert d_0 \rvert$ cut	$\lvert z_0 \rvert$ cut	No. of tracks
dM1600	0.2 mm	15 mm	13
dM770	0.3 mm	15 mm	13

Table 7.2.: Precuts for the algorithm in both benchmark scenarios.

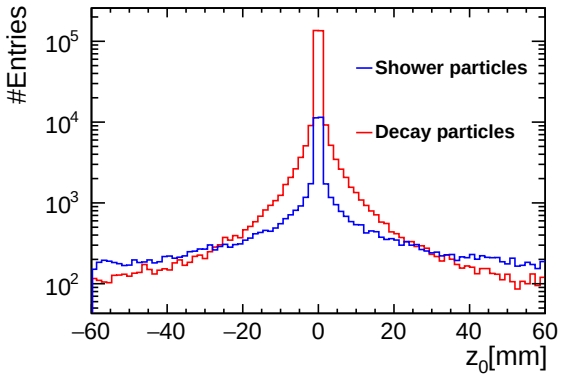

Figure 7.7.: The z_0 distribution of signal decay tracks as compared to the shower decay tracks for dM1600 scenario at $\sqrt{s} = 500$ GeV and $\int \mathcal{L}dt = 500$ fb^{-1} with $P(e^+, e^-) = (+30\%, -80\%)$.

ECAL and HCAL is shown. It gives a very good example for the vigorous curling of a track inside the TPC. The tracking efficiency for the ILD is explained in detail in section 4.5. For a transverse momentum below 1 GeV, it is highly probable for a track to curl in the magnetic field of the detector.

The reconstruction of such low p_T curler tracks is quite challenging with the

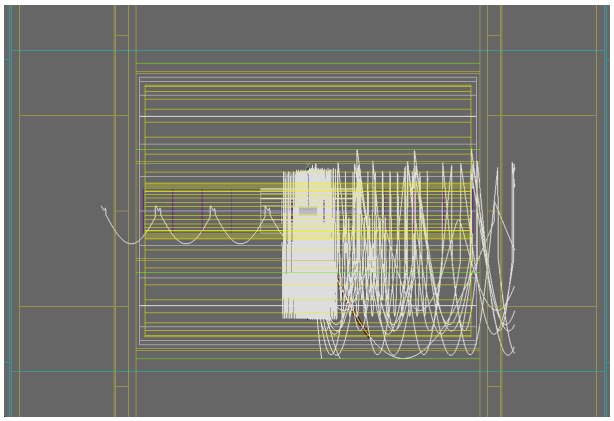

Figure 7.8.: The front view of the event display of a low p_T track curling in the magnetic field of the TPC enclosed between the ECAL and HCAL is shown. The display shows how a single track with a low transverse momentum curls vigorously due to the magnetic field of the detector.

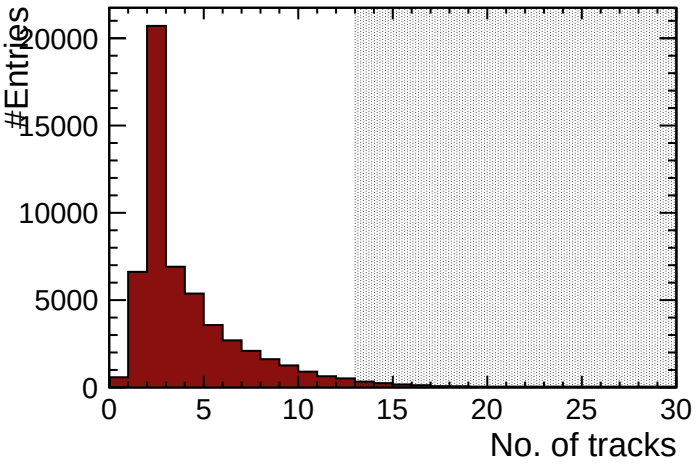

Figure 7.9.: The distribution for number of signal tracks overlaid with $\gamma\gamma \rightarrow$ low p_T hadron overlay in an event for dM1600 scenario at $\sqrt{s} = 500$ GeV and $\int \mathcal{L}dt = 500$ fb^{-1} with $P(e^+, e^-) = (+30\%, -80\%)$.

current setup of the reconstruction software. The particle trajectory hits might be reconstructed into multiple tracks for every curl even though the hits belong to one single track. Such events are avoided using another cut on the number of tracks allowed to pass through the algorithm. A histogram of the number of signal tracks including $\gamma\gamma \rightarrow$ low p_T hadron tracks in an event is given in figure 7.9. The majority of events have number of tracks below 10 in an event. From the plot it is required

that the number of tracks in an event should be below 13. Also, in the previous study it was required that the number of PFOs in an event should not be more than 15 which is comparable with choice of $ntrk < 13$. A cut at $ntrk < 13$ suppresses 2% of the signal events. The impact of the cut on the signal events is small and hence in this study it is required that any event that is considered for the algorithm should have $ntrk < 13$. The cuts applied for track selection according to the benchmark scenarios is briefed in the table 7.2.

7.2.3. The construction of track grouping algorithm

Based on the specific benchmark scenario, different selection cuts as explained above are applied on the tracks chosen to run through the algorithm. The basic requirement for grouping the tracks together is that the z_0 distance between the tracks should not be greater than a certain threshold value.

Similar to the d_0 significance value, the z_0 significance is defined as

$$S_{z_0} = \frac{z_0}{\sigma_{z_0}}. \tag{7.2}$$

In this study, the tracks are grouped based on the z_0 distance between the tracks. The algorithm is described through the flowchart given in Fig. 7.10. The z_0 distance for all different pair of track combinations is calculated with Eq. 7.3.

$$D_{ij} = \frac{z_0[i] - z_0[j]}{\sqrt{[\sigma_{z_0}[i]]^2 + [\sigma_{z_0}[j]]^2}}, \tag{7.3}$$

Identifying the track combination with smallest D_{ij} value, it is compared with a certain threshold value η. Based on such a comparison, if the z_0 difference between the two tracks is below η, then the two tracks are assumed to be originating from the same vertex and are combined together into a group. The weighted average mean position of these two tracks is then calculated with Eq. 7.4

$$\langle z \rangle = \Sigma_i \frac{z_0[i]}{\sigma_{z_0}[i]} / \Sigma_i \frac{1}{\sigma_{z_0}[i]} \tag{7.4}$$

and the weighted average error is calculated with Eq. 7.5

$$\sigma_{\langle z \rangle} = \sqrt{1/\Sigma_i \frac{1}{\sigma_{z_0}[i]}}. \tag{7.5}$$

The z_0 values and the z_0 errors of the combined two tracks are then replaced with their weighted average mean and weighted average error respectively. The z_0 significance for all different pairs of track combinations is calculated again and the pair with smallest difference is identified. After the combination of first two tracks, rest of the tracks are combined according to three protocols as given below:

- if two tracks are identified for the first time as candidates to form a group, they are combined together into a new group.
- if D_{ij} between the $\langle z \rangle / \sigma_{\langle z \rangle}$ of the group and S_{z_0} of a track is below η, then the track is accommodated into the group.
- if D_{ij} between the $\langle z \rangle / \sigma_{\langle z \rangle}$ of two different groups is below η, then the two groups are combined together into one single group.

The whole process is repeated until the pair of groups with the smallest difference is no more smaller than the given threshold value. The different groups created in the algorithm are then assumed to originate from different hard interactions.

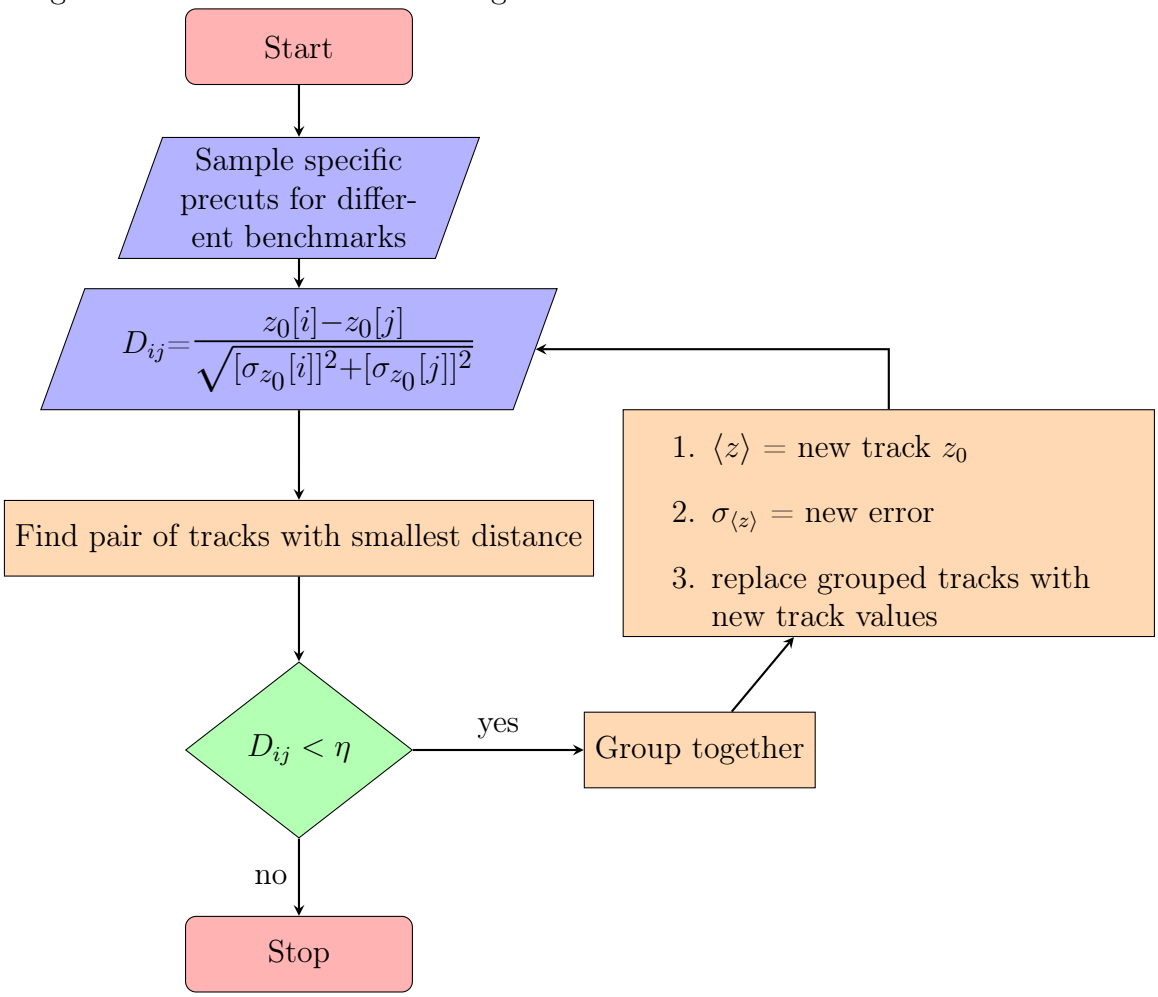

Figure 7.10.: A flowchart depicting the working mechanism of the track grouping algorithm.

Finding an optimum value for η

The optimum value for η is found using the chargino samples from both the benchmark scenarios without the inclusion of e^+e^- pair background. The number of groups created by the algorithm is expected to be similar to the number of true Monte-Carlo vertices since the ideal scenario would be where the tracks coming from the same vertex are grouped together. An optimum value for η is decided by comparing the number of groups created by the algorithm to the number of Monte-Carlo vertices for different values of η.

This is done by first counting the number of vertices in an event. The number of true Monte-Carlo primary vertices is counted for the overlay events. Since charginos have a finite life-time before decaying into the final decay products, the number of secondary vertices are counted for the charged signal particles. To emulate the separation of high S_{d_0} track which would count as a secondary vertex for the charginos in the dM770 scenario, the $N_{MC_{vtx}}$ is counted as $N_{\text{found } MC_{vtx}} - 1$. Since no high S_{d_0} track is separated for the dM1600 scenario, all the selected tracks are sorted into groups by the algorithm. If the positions of two Monte-Carlo vertices are so close that they cannot be distinguished within the detector resolution then they are considered as one single vertex. This is done in the following way: The resolution for the detector to distinguish between two Monte-Carlo vertices is given as

$$\sigma_{ij} = \sqrt{\sigma_i^2 + \sigma_j^2} \tag{7.6}$$

where σ_i and σ_j for vtx_{z_i} and vtx_{z_j} is determined from figure 4.4b based on their momentum. If difference between the positions of vtx_{z_i} and vtx_{z_j} in z-axis is less than σ_{ij} then both the vertices are combined into a single vertex. Once the number of vertices are counted and fixed, the number of groups are checked for different values of η. A full scan on several values of η is performed among which three value where η =1.6, 1.7 or 1.8 is presented in figure 7.11, figure 7.12 and figure 7.13 respectively.

As can be seen from the figures that with each increasing value of η, the fraction of events having same number of vertices and groups increase slightly. However, with increasing values of η, the concept of having separate groups is jeopardized since almost all the tracks are mostly shuffled together into one single group. More details on these figures are given in appendix A. The number of cases with two Monte-Carlo vertices corresponding to one single group of tracks also becomes higher. Therefore, it is important to have a balance in which more number of events should have the number of Monte-Carlo vertices and number of tracks same and at the same time there should not be more events whose higher number of Monte-Carlo vertices correspond to smaller number of groups due to the larger value of η. Such a balance can be maximally maintained for both the benchmark scenarios if η =1.7. Therefore, the value of η in this study is fixed as 1.7.

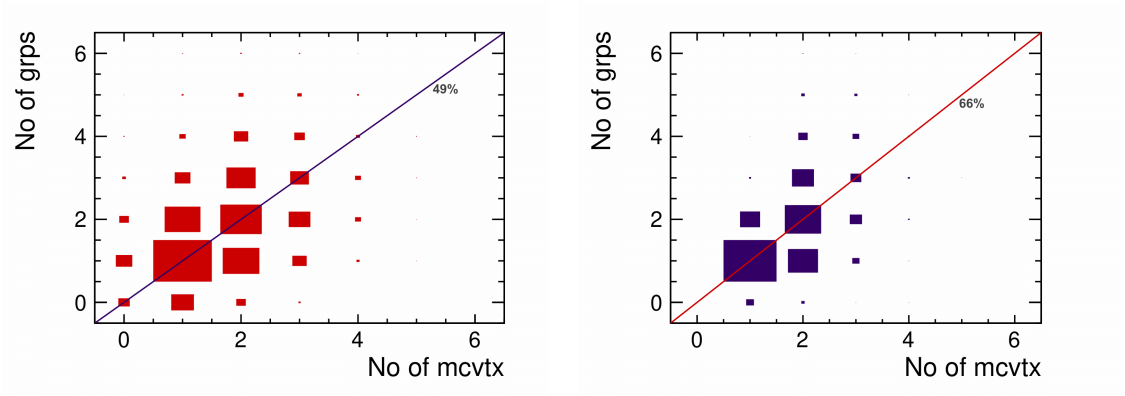

(a) (b)

Figure 7.11.: Comparison of number of true Monte-Carlo vertices with track groups obtained from the algorithm for $\eta = 1.6$. a) dM770 benchmark scenario b) dM1600 benchmark scenario

.

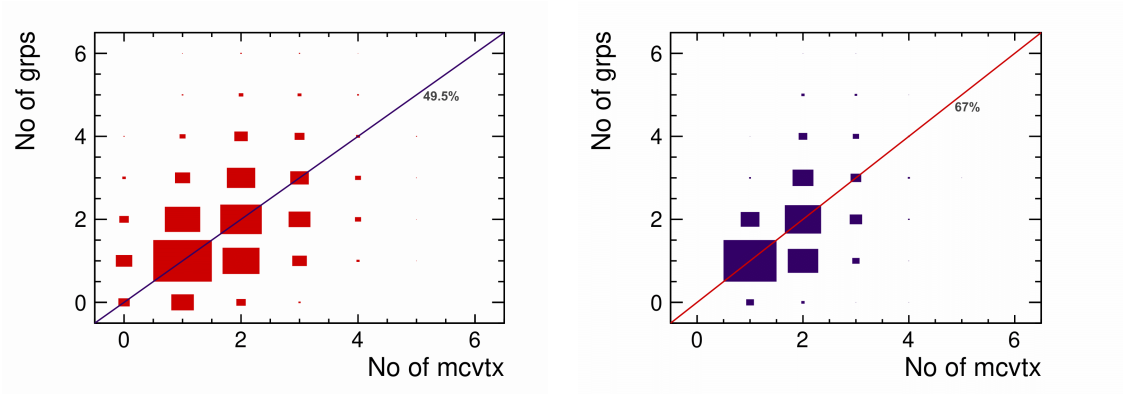

(a) (b)

Figure 7.12.: Comparison of number of true Monte-Carlo vertices with track groups obtained from the algorithm for $\eta = 1.7$. a) dM770 benchmark scenario b) dM1600 benchmark scenario

.

A comparison between the number of true Monte-Carlo vertices and the number of groups made for the sample with the inclusion of pair background. The number of true Monte-Carlo vertices is counted in the similar fashion as for the sample without the pair background and compared with the number of groups obtained from the algorithm with the η value as 1.7. The resulting distribution for the dM770 scenario is given in figure 7.14a and for the dM1600 scenario is given in figure 7.14b. The

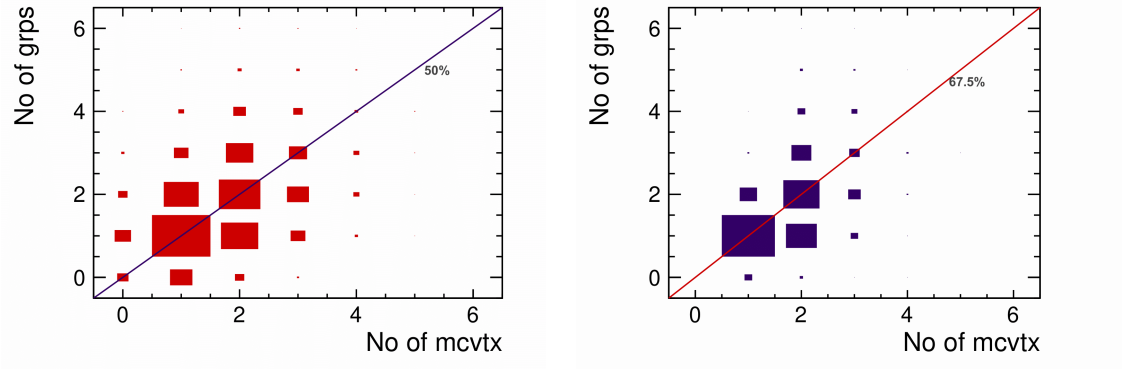

(a) (b)

Figure 7.13.: Comparison of number of true Monte-Carlo vertices with track groups obtained from the algorithm for $\eta = 1.8$. a) dM770 benchmark scenario b) dM1600 benchmark scenario

.

agreement of number of Monte-Carlo vertices and number of groups here is worse than in the case without pair background.

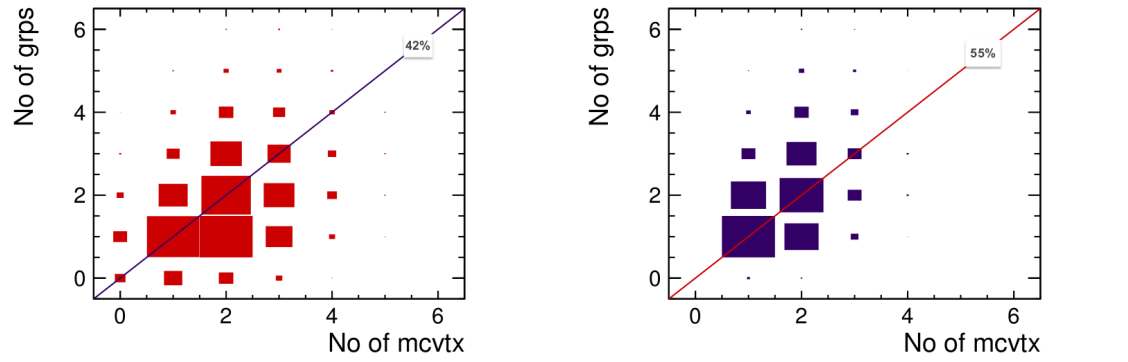

(a) (b)

Figure 7.14.: Comparison of number of true Monte-Carlo vertices with track groups obtained from the algorithm for events including the pair background. a) dM770 benchmark scenario b) dM1600 benchmark scenario.

For the dM770 scenario, in 42 % of the events the number of Monte-Carlo vertices comply with the number of groups while for the dM1600 scenario, in 55 % of the events the number of Monte-Carlo vertices and number of groups are same. The inclusion of pair background results in rise of number of Monte-Carlo vertices.

Nonetheless, the pair background tracks are more often grouped together with other tracks rather than grouped separately. Consequently, the number of groups created by the algorithm is less than the number of Monte-Carlo vertices.

7.3. Algorithm Performance

As discussed in section 7.2.2, the dM1600 and the dM770 scenario have different selection cuts for the tracks. The tracks that pass the selection cuts are run through the algorithm to group them based on their z_0 difference. The performance of the algorithm is tested through purity checks of the track groups obtained through the algorithm. The study is performed for the events where both the signal tracks are reconstructed. The main role of the algorithm is to group the selected tracks based on their z_0 value. It does not specify which group is the signal and which is the background. To check the working efficiency of the algorithm, the number of pure signal, pure background and mixed track groups are determined using the MC truth information. The study is performed for samples with and without pair backgrounds and the results are given in following sections.

Study of events without the inclusion of pair background

The track grouping algorithm efficiency for a sample without the inclusion of e^+e^- pair background is evaluated and the results are quantified in table 7.3.

Groups	dM770 [%]	dM1600 [%]
Signal	49	54
Background	33	30
Mixed	18	16

Table 7.3.: Signal, background and Mixed groups for different benchmark scenarios without the inclusion of pair background.

The number of pure signal groups, pure background groups and the groups with the mix of signal and background tracks are checked using the true Monte-Carlo information. The results of this study is given in in figure 7.15 and in table 7.3. The separation of a highest d_0 significance track in the dM770 scenario results in the reduction of signal groups compared to the dM1600 scenario. It also has to be noted that only half the signal tracks are available in each event for the dM770 scenario as the high d_0 tracks are already separated. A very efficient separation of background and signal is performed by the algorithm as only $\sim$ 16 - 18% of groups have mixed tracks in them.

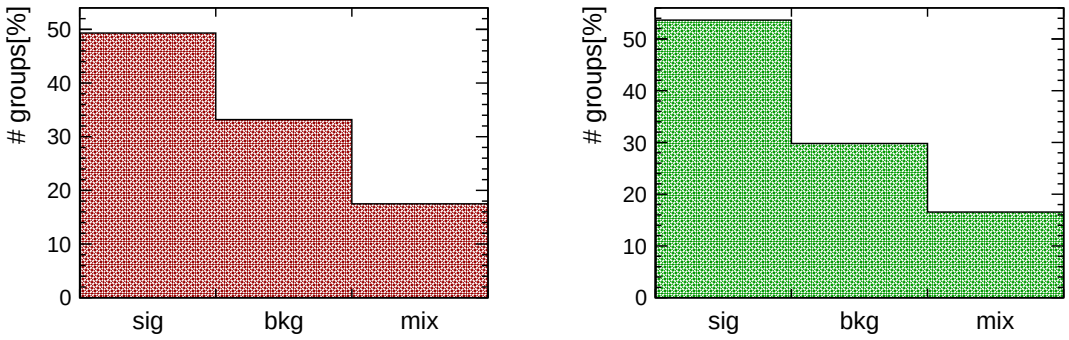

(a) (b)

Figure 7.15.: Fraction of groups obtained as pure signal, background and a mix of both is shown for events without the inclusion of pair background. a) dM770 benchmark scenario b) dM1600 benchmark scenario.

Study of events with the e^+e^- pair background

A study for $e^+e^- \to \tilde{\chi}_1^+\tilde{\chi}_1^-\gamma$ events with $\gamma\gamma \to$ low p_T hadron overlay and pair background overlay is performed. The study shows that the efficiency of the algorithm is not impacted much since the pair background tracks are more often grouped together with $\gamma\gamma \to$ to low p_T hadron tracks rather than with the signal tracks, creating less number of mixed track groups as presented in table 7.4.

Table 7.4 gives the numbers signifying the efficiency of the algorithm to separate the signal and the background. Even though the number of signal groups has dropped and the number of mixed groups are slightly higher than the mixed groups in the case of events without the inclusion of pair background, the difference is not drastic. However, the inclusion of e^+e^- pair background leads to a significant increase in pure background groups. In the dM770 scenario, number of background groups are 4% more than the signal groups. As mentioned before this is mainly because, in 75% of the events the signal tracks are separated and not included in track grouping and additionally with the inclusion of pair backgrounds the number of background groups have increased.

However, it can be concluded that the inclusion of pair background does not have a dire effect of the grouping efficiency of the algorithm.

7.4. Applications

The $e^+e^- \to \tilde{\chi}_1^+\tilde{\chi}_1^-\gamma$ analysis for dM770 and dM1600 scenarios were performed in [6, 7]. The study shows that the key observables of the higgsinos can be can be

Groups	dM770 [%]	dM1600 [%]
Signal	39	43
Background	43	35
Mixed	18	23

Table 7.4.: Signal, background and mixed groups for different benchmark scenarios for event including pair background.

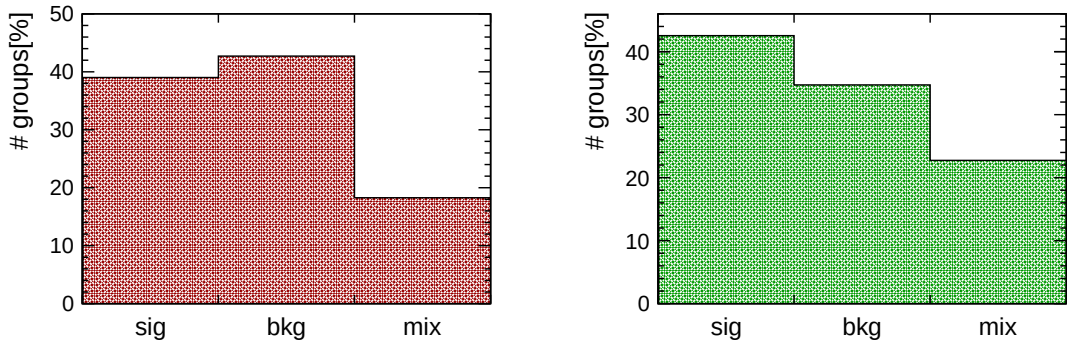

(a) (b)

Figure 7.16.: Fractions of groups obtained as pure signal, background and a mix of both is shown for events with the inclusion of pair background. a) dM770 benchmark scenario b) dM1600 benchmark scenario.

reconstructed with an uncertainity of a few percent. However, this study was performed without the inclusion of $\gamma\gamma \rightarrow$ low p_T hadron overlay or the pair background where the samples were simulated using SGV Fast simulation. The track grouping algorithm developed in this study forms a great tool to seperate signal and overlay tracks. In the following chapter, a study of $e^+e^- \rightarrow \tilde{\chi}_1^+\tilde{\chi}_1^-\gamma$ analysis is presented. The track grouping algorithm is used for fully simulated $e^+e^- \rightarrow \tilde{\chi}_1^+\tilde{\chi}_1^-\gamma$ events overlaid with $\gamma\gamma \rightarrow$ low p_T hadron background. A full analysis with the complete set of all the Standard Model backgrounds is performed and the efficiency of the track grouping algorithm to extract the signal tracks is studied and presented.

8. Low ΔM Higgsino Analysis

The study presented in this chapter mainly focuses on the impact of $\gamma\gamma \rightarrow$ low p_T hadron overlay on the low ΔM higgsino analysis. As mentioned earlier, the higgsino analysis performed in [6] was performed without the inclusion of $\gamma\gamma \rightarrow$ low p_T hadron overlay. Therefore, this study presents a comparison between [6] and the higgsino analysis with the inclusion of $\gamma\gamma \rightarrow$ low p_T hadron overlay. However, the e^+e^- pair backgrounds are not included in this study apart from its effect on the BeamCal. For convenience of comparison, [6] is termed as *HS-analysis* in further parts of this chapter.

8.1. Pre-algorithm cuts

To perform a full analysis on the low ΔM higgsino process, it is important to suppress the Standard Model background. For selection of the signal from the Standard Model background, some pre-selection cuts are applied. The events that pass the pre-selection cuts are run through the track grouping algorithm for selection of signal tracks among the $\gamma\gamma \rightarrow$ low p_T hadron tracks. The cuts used in this analysis are adapted from the *HS-analysis*. The Standard Model backgrounds used in this study are introduced in 4.2.

BeamCal Particles

The BeamCal detector as introduced in section 4.7 is one of the most forward sub-detectors of the ILD. The detector is mainly hit by a large amount of e^+e^- pair background due to which it requires some special considerations. The incoming beam electrons for the signal annihilate, thus leaving no significant activity in the BeamCal even with the requirement of an ISR photon being detected. However, for processes like $\gamma\gamma$ and γe high energetic electrons or photons are scattered with a small angle. Such photons or electrons end up in the BeamCal detector. Energies of the BeamCal clusters for different processes is shown in figure 8.1. The $e^+e^- \rightarrow \tilde{\chi}_1^+\tilde{\chi}_1^-$ events in the *HS-analysis* were simulated using SGV (section 4.8.5). As explained in section 4.8.5, the `BeamCalTagEfficiency` processor only tags events with particles in BeamCal above 40 GeV. However, as can be seen in figure 8.1, signal events can have significant BeamCal activity from particles having energy below 40 GeV in full simulation. Thus

vetoing all the events with BeamCal activity as in *HS-analysis* would result in major loss of signal events. Since the processes having major BeamCal activities (e.g. $\gamma\gamma$ and γe events) have particles found in BeacmCal with higher energies, only events having BeamCal cluster energies above 150 GeV are vetoed.

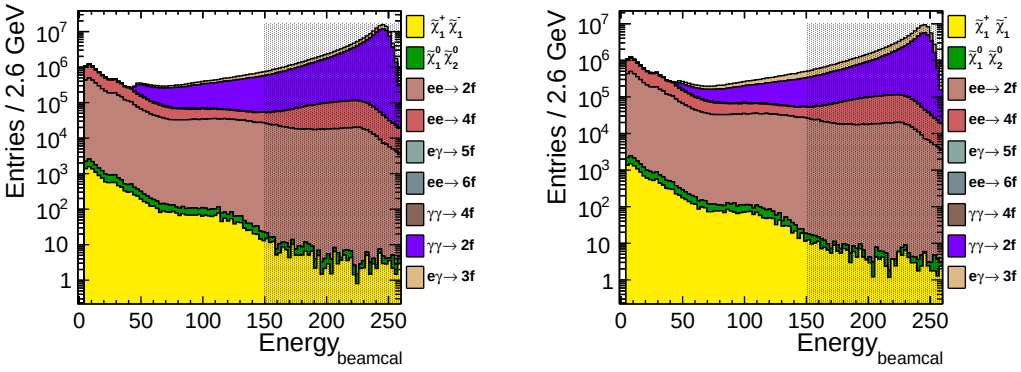

(a) (b)

Figure 8.1.: Energy of the BeamCal clusters at $\sqrt{s} = 500$ GeV and $\int \mathcal{L}dt = 500$ fb^{-1} with $P(e^+, e^-) = (+30\%, -80\%)$ for dM1600 and dM770.

Number of tracks

Utilizing the low multiplicity nature of the low ΔM higgsino processes, it was required in the *HS-analysis* that the number of PFO's in an event should not be greater than 15. Since the Standard Model hadronic events have large multiplicities, such a cut can prove quite efficient against them. Since the separation of the signal and $\gamma\gamma \rightarrow$ low p_T hadron overlay is performed using the grouping of the tracks, analysis is performed using the separated tracks which are assumed to be the signal tracks. Therefore, unlike the *HS-analysis*, tracks are used instead of the PFOs for the analysis. It is explained in section 7.2.2 that due to the nature of low p_T tracks curling in the magnetic field of the detector, a cut is required on the number of tracks allowed into the track grouping algorithm. Due to the presence of $\gamma\gamma \rightarrow$ low p_T hadrons, there are more number of tracks in an event. Therefore, the choice is made on the number of tracks which pass the first two algorithm selection cuts (second and third column of Table 7.2) instead of the total number of tracks. According to the algorithm selection criteria, if the number of tracks passing the z_0 and d_0 cuts for the algorithm is $ntrk < 13$, then the event is selected for further analysis. A cut-flow plot showing the effects of this cut is given in figure 8.2.

Initial State Radiation Photon

The signal events have a large missing energy as described in section 8.3.2. Some Standard Model background events resemble the signal events by having a large missing energy due to the loss of beam particles into the beampipe. To distinguish such events, it is required that the event has a hard ISR photon. A detailed explanation of the ISR method is given in section 6.2.1. The photon candidate is required to be within the tracking performance of the ILD with $|\cos\theta_{ISR}| < 0.9397$ corresponding to 7° and an energy $E_{ISR} > 10$ GeV. In order to ensure that the photon is within the acceptance of the tracking system, it is important to have a minimum requirement for the polar angle. If more than one candidate is found then the highest energetic photon fulfilling these criteria is chosen as the hard ISR photon.

Cutflow Analysis for pre-algorithm cuts

A pictorial representation of the cut-flow for events with all the pre-algorithm cuts at $\sqrt{s} = 500$ GeV and $\int \mathcal{L}dt = 500$ fb^{-1} with $P(e^+, e^-) = (+30\%, -80\%)$ for the dM1600 and the dM770 scenario is given in figure 8.2. An analysis on the effectiveness of these cuts along with the values in the cut-flow tables (table 8.1, table 8.2) are shown ahead.

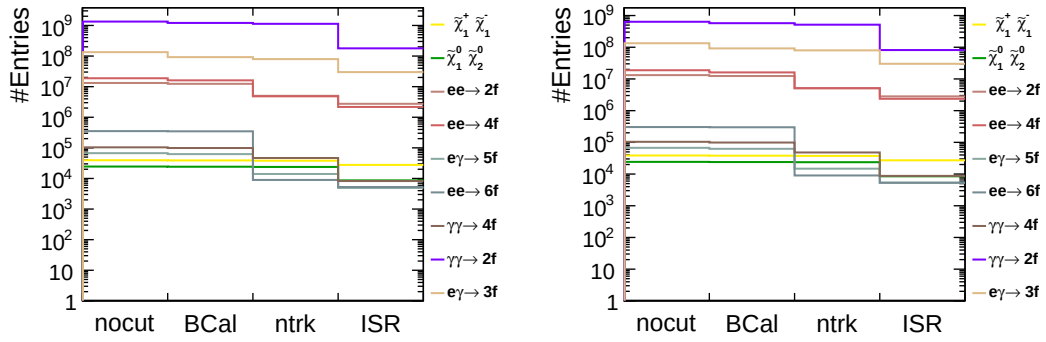

(a) (b)

Figure 8.2.: Pictorial representation of cutflow for events with all the pre-algorithm cuts at $\sqrt{s} = 500$ GeV and $\int \mathcal{L}dt = 500$ fb^{-1} with $P(e^+, e^-) = (+30\%, -80\%)$ for the dM1600 and the dM770 scenarios.

Table 8.3 and table 8.4 presents the cut-flow values for the precuts in the *HS-analysis*. A comparison of these values is made with the cutflow values in the current analysis given in table 8.1 and table 8.2. In the dM1600 scenario, the chargino events

Selection cuts	dM1600		Standard Model		
	$\tilde{\chi}_1^+\tilde{\chi}_1^-\gamma$	$\tilde{\chi}_2^0\tilde{\chi}_1^0\gamma$	$e^+e^- \to 2,4,6f$	$e\gamma \to 3,5f$	$\gamma\gamma \to 2,4f$
no cut	39368	24513	3.232461×10^7	1.34229×10^8	1.3386×10^9
BeamCal veto	38862	24191	2.87982×10^7	9.22543×10^7	1.2094×10^9
N_{trk}	38049	23794	9.8561×10^6	7.9430×10^7	1.13065×10^9
$N_{ISR}=1$	27751	8654	4.9326×10^6	2.9901×10^7	1.78609×10^8

Table 8.1.: Cut-flow table for pre-algorithm selection at $\sqrt{s}$ = 500 GeV and $\int \mathcal{L}dt$ = 500 fb^{-1} with $P(e^+,e^-)$ = (+30%, -80%) for the dM1600 scenario.

Selection cuts	dM770		Standard Model		
	$\tilde{\chi}_1^+\tilde{\chi}_1^-\gamma$	$\tilde{\chi}_2^0\tilde{\chi}_1^0\gamma$	$e^+e^- \to 2,4,6f$	$e\gamma \to 3,5f$	$\gamma\gamma \to 2,4f$
no cut	38498	24221	3.232461×10^7	1.34229×10^8	1.3386×10^9
BeamCal veto	37972	23924	2.87982×10^7	9.22543×10^7	1.2094×10^9
N_{trk}	37342	23655	1.02105×10^7	7.9941×10^7	1.13497×10^9
$N_{ISR}=1$	27150	8483	5.19609×10^6	3.01661×10^7	1.79849×10^8

Table 8.2.: Cut-flow table for pre-algorithm selection at $\sqrt{s}$ = 500 GeV and $\int \mathcal{L}dt$ = 500 fb^{-1} with $P(e^+,e^-)$ = (+30%, -80%) for the dM770 scenario.

Selection cuts	dM1600		Standard Model		
	$\tilde{\chi}_1^+\tilde{\chi}_1^-\gamma$	$\tilde{\chi}_2^0\tilde{\chi}_1^0\gamma$	$e^+e^- \to 2,4,6f$	$e\gamma \to 3,5f$	$\gamma\gamma \to 2,4f$
no cut	38672	24250	2.6434×10^7	8.8820×10^7	9.7554×10^8
BeamCal veto	38591	24187	2.6284×10^7	8.8178×10^7	9.6757×10^8
N_{RP}	38591	24185	6.4968×10^6	6.5811×10^7	6.6308×10^8
$N_{ISR}=1$	30058	9551	3.1640×10^6	1.5074×10^7	1.7752×10^8

Table 8.3.: Cut-flow table for the *HS-analysis* at $\sqrt{s}$ = 500 GeV and $\int \mathcal{L}dt$ = 500 fb^{-1} with $P(e^+,e^-)$ = (+30%, -80%) for the dM1600 scenario.

are 2% more than in the *HS-analysis* while in the dM770 scenario, they are almost similar. The number of neutralino events are also found similar in the current

Selection cuts	dM770		Standard Model		
	$\tilde{\chi}_1^+\tilde{\chi}_1^-\gamma$	$\tilde{\chi}_2^0\tilde{\chi}_1^0\gamma$	$e^+e^- \to 2,4,6f$	$e\gamma \to 3,5f$	$\gamma\gamma \to 2,4f$
no cut	38130	23940	2.6434×10^7	8.8820×10^7	9.7554×10^8
BeamCal veto	38054	23874	2.6284×10^7	8.8178×10^7	9.6757×10^8
N_{RP}	38054	23874	6.4968×10^6	6.5811×10^7	6.6308×10^8
$N_{ISR} = 1$	29675	9317	3.1640×10^6	1.5074×10^7	1.7752×10^8

Table 8.4.: Cut-flow table for for the *HS-analysis* pre-algorithm selection at $\sqrt{s} =$ 500 GeV and $\int \mathcal{L}dt = 500$ fb^{-1} with $P(e^+, e^-) = (+30\%, -80\%)$ for the dM770 scenario.

analysis and the *HS-analysis*. However, for the Standard Model background, there are 18% more number of $e^+e^- \to 2f, 4f, 6f$ events, 34% more $e^\pm\gamma \to 3f, 5f$ events and and 27% more $\gamma\gamma \to 2f, 4f$ events in this analysis than in the *HS-analysis*. For the dM1600 scenario the BeamCal cut can suppress 11% of $e^+e^- \to 2f, 4f, 6f$, 31% of $e^\pm\gamma \to 3f, 5f$ and 9.6% of $\gamma\gamma \to 2f, 4f$ while only reducing 1.2% of the signal. However, only $< 1\%$ of the Standard Model background events can be vetoed by removing events with BeamCal activity in *HS-analysis*. The presence of $\gamma\gamma \to$ low p_T hadron events makes a significant contribution in this selection cut. Photons radiated from neutral hadrons in $\gamma\gamma \to$ low p_T hadron events with high longitudinal momentum have bigger probabilities to end up in the BeamCal. Consequently, significant amount of BeamCal activity is found for events where more amount of the Standard Model background can be vetoed by removing events with BeamCal energy > 150 GeV.

A restriction on the number of tracks selected for the algorithm to be less than 13 removes 66% of remaining $e^+e^- \to 2f, 4f, 6f$ processes, 14% of $e^\pm\gamma \to 3f, 5f$ and 6.5% of $\gamma\gamma \to 2f, 4f$ while only affecting 2% of the chargino events. The *HS-analysis* required that the number of PFOs in an event should not be greater than 15. This cut allowed vetoeing 75% of the $e^+e^- \to 2f, 4f, 6f$ events, 25% of $e^\pm\gamma \to 3f, 5f$ and 31% of $\gamma\gamma \to 2f, 4f$ without loosing any signal events.

The requirement of a hard ISR photon in an event is very important. It curbs 63% of the SUSY background, 50 % of the remaining $e^+e^- \to 2f, 4f, 6f$ processes, 62% of $e^\pm\gamma \to 3f, 5f$ and 84% of $\gamma\gamma \to 2f, 4f$. However, it also affects the signal events by removing 27% of it. The impact of the ISR photon cut on the *HS-analysis* is similar but not exact. In the *HS-analysis* 60% of the SUSY background, 51% of the $e^+e^- \to 2f, 4f, 6f$ processes, 77% of $e^\pm\gamma \to 3f, 5f$ and 73% of $\gamma\gamma \to 2f, 4f$ are removed using the ISR photon cut. The cut also removes 22% of the signal in the

HS-analysis.

The events surviving the above selection cuts are chosen to run through the algorithm which is expressed in detail in rest of the thesis.

8.2. Semi-leptonic selection

Exclusive chargino decay modes like the semi-leptonic final state are helpful in reducing the Standard Model background but more importantly, it is an efficient approach towards suppressing the SUSY background e.g.neutralino processes. Neutralinos decay to an LSP and a virtual Z boson which decays fully leptonically or fully hadronically. As seen in table 6.2 charginos dominantly decay into single pions especially for the dM770 scenario. Therefore, the final states consisting of $\pi^{\pm}$ and an $e^{\pm}$ or $\mu^{\pm}$ is considered as the semi-leptonic signature for the charginos. Figure 6.4 represents the branching ratios of the chargino decay modes as a function of the mass difference between the chargino and the LSP. For the chargino - LSP mass difference below 1 GeV, the single pion final state is the dominant decay mode. Table 6.2 shows that for the dM770 scenario, a chargino decays to a single pion 60% of the time. Including the leptonic decay of the other chargino, the chargino semi-leptonic events amount to 35% of the total chargino pair events. However, in the dM1600 scenario, the chargino decaying to single pion is only 16.5%. This makes the semi-leptonic events sum up to 11% of the total events. Thus, also the decay mode where chargino decays to a charged and a neutral pion is considered which has a higher branching ratio. However, only the charged pion is considered for the semi-leptonic selection, as the selection is performed using the track groups obtained from the algorithm. Including all these decay modes, the semi-leptonic branching ratio amounts to 30% of the total events in the dM1600 scenario.

The main Standard Model background to this semi-leptonic signature are the τ-lepton pairs which can be created in $e^+e^- \to \tau^+\tau^-$, $e^{\pm}\gamma \to e^{\pm}\tau^+\tau^-$ or $\gamma\gamma \to \tau^+\tau^-$ processes. A τ-lepton decays as $\tau \to \nu_\tau W^*$, where W^* decays leptonically to $e\nu_e$ or $\mu\nu_\mu$ with a branching ratio of $BR(\tau \to l\nu_l\nu_\tau) = 17\%$ and hadronically to $\pi^{\pm}$ or $\pi^{\pm}\pi^0$ with the branching ratios of 10% and 25% respectively [44]. Whenever one of the τ decays hadronically and other leptonically, the final states are similar to the chargino signature. Therefore the suppression of τ-leptons is challenging in higgsino analysis.

The semi-leptonic selection for the dM770 and dM1600 benchmark scenarios are explained in further sections. Since the tracks for both the benchmark scenarios are shuffled differently as explained in chapter 7, the semi-leptonic selection is also different for both the benchmark scenarios.

A study for identification of low $p_T\mu$ and $\pi^{\pm}$ based on their shower shapes was performed using a fully simulated sample in [6]. However, this method is not cur-

rently used in this study for simplicity. The particle id for the search of semi-leptonic candidate is cheated using the true information from the Monte-Carlo data.

8.2.1. Semi-leptonic selection for dM770

As explained in section 7.2.2, since charginos have a longer life-time, the track with the highest d_0 value is assumed to be a chargino track and is separated from the other tracks. The positions of the true signal decay tracks within the groups and along the high d_0 track are investigated using the true Monte-Carlo information. Based on this investigation, table 8.5 gives the number of events which have a pion and a lepton in a certain position within the track group or as a high d_0 track. The position of the lepton track is presented horizontally while the position of the pion track is given vertically in table 8.5.

π \ l	d_0	**1 trk grps**	**2 trk grps**	3 trk grps	more trk grps
d_0		**39**	**6.4**	2.7	1
1 trk grps	**30**	**5.4**	1.45	0.58	0.27
2 trk grps	**5.6**	0.64	0.62	0.2	0.14
3 trk grps	2.3	0.39	0.16	0.66	0.1
more trk grps	0.76	0.12	0.16	0.08	0
Total no. grps with both trks	5				

Table 8.5.: Matrix showing the number of events in percentages based on the positions of true chargino semi-leptonic tracks after running the algorithm in the dM770 configuration for events at $\sqrt{s} = 500$ GeV.

As can be seen in the table, for 69% of the events, either of the semi-leptonic track is a high d_0 track and the other is in a single track group. Among rest of the events, the majority of the events (12%) have a high d_0 signal track and the other track in group with two tracks. Also 5% of the events have a high d_0 signal track and the other track is in three track group while 5% of the events have both the semi-leptonic signal tracks in the same group. The rest of the minority events have their tracks distributed as shown in table 8.5. The τ-leptons decay semi-leptonically proving to be the major background for semi-leptonic selection of charginos. Therefore, similar to table 8.5, a matrix showing the number of events based on the positions of the true τ semi-leptonic tracks are shown in table 8.6.

As can be seen in table 8.6, the distribution of semi-leptonic tracks for τ-leptons is similar to the chargino tracks. However, the case of a high d_0 track being a

π \ l	d_0	**1 trk grps**	**2 trk grps**	3 trk grps	more trk grps
d_0		**42.4**	**6.9**	5.2	1.27
1 trk grps	**32**	0.24	0.36	0.012	0.012
2 trk grps	**4.7**	0.15	0.05	0.06	0.012
3 trk grps	3.9	0.012	0.045	0	0
more trk grps	0.66	0.05	0	0.025	0
Total no. grps with both trks	1.8				

Table 8.6.: Matrix showing the number of events in percentages based on the positions of true τ-lepton semi-leptonic tracks after running the algorithm in the dM770 configuration for events at $\sqrt{s} = 500$ GeV.

candidate and the other candidate found in a three track group is higher for τ-lepton events as compared to the chargino events. Meanwhile, for the events where the high d_0 track is not a semi-leptonic candidate, the pion and the lepton track found in two groups with single tracks is higher for chargino events with respect to τ-lepton events. Also, the probability of the semi-leptonic candidates in one single group is 1.8% for τ-lepton events while it is 5 % for chargino events.

Based on these arguments, the semi-leptonic selection is made in a multi-layered process as explained in detail in flowchart 8.3. In the selection of semi-leptonic candidates, highest priority is given for the process where high d_0 track is a π/l and the oppositely charged l/π is found in a single track group. The second highest priority is given to the process where high d_0 track is a π/l and the oppositely charged l/π is found in a two track group. However, if both the tracks in a two track group are oppositely charged pions, then it is plausible that they are the decay products of a ρ meson from the $\gamma\gamma \rightarrow$ low p_T hadron overlay. As mentioned in section 6.3.2, the invariant mass of decay products of ρ meson sums up to the invariant mass of ρ meson itself (M_ρ=770 MeV$\pm$150 MeV). Therefore, it is required that in such cases, the invariant mass of the oppositely charged pions in a two track group should not resonate with M_ρ=770 MeV$\pm$150 MeV i.e.should not fall within 630 MeV $< M_{in} <$ 850 MeV. Similarly, in the case where the high d_0 track is a pion and the oppositely charged lepton is found in a two track group with another lepton, it is plausible that the e/μ are decayed from a τ-lepton or direct $\gamma\gamma \rightarrow e^+e^-/\mu^+\mu^-$. To suppress such groups, it is required that if a high d_0 track is a pion then the lepton candidate cannot be chosen from a two track group containing an oppositely charged lepton pair. It has to be noted that only the track group is rejected for selecting the semi-leptonic candidate and not the entire event. A very small number of events were

rejected since no semi-leptonic candidate was found as a consequence of the ρ cut and the lepton requirement.

Since the possibility of obtaining 10% of τ-lepton background for 5% of chargino events prevail with events where one of the candidates is a high d_0 track and other is found in a group with three tracks, this choice is discarded from the selection procedure. On the other hand, since $\sim$ 5% of chargino events can be obtained for 0.24% of tau events, the next priority for choosing the semi-leptonic candidates is given to events where a pion and a lepton is found in two single track groups. If the event fails to give a semi-leptonic candidate with all the above proceedures, then a lepton and pion track in a two track group are chosen as the semi-leptonic candidates.

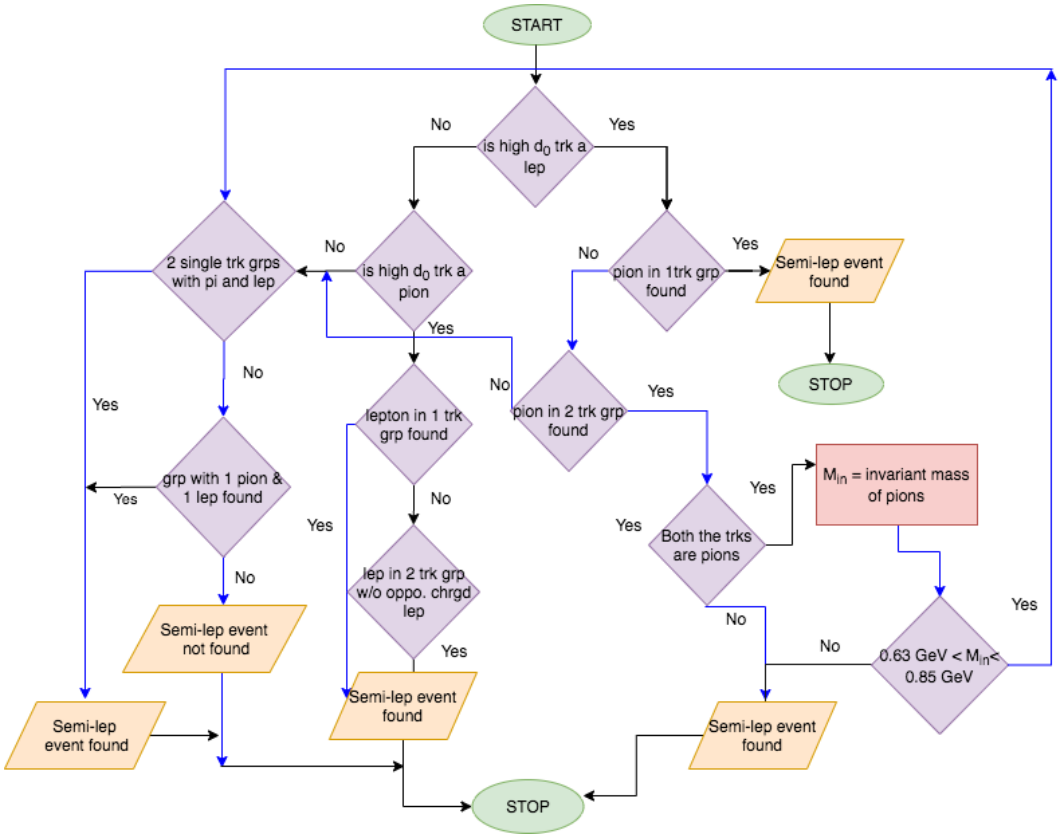

Figure 8.3.: Flowchart describing the procedure of selection of semi-leptonic candidates from the groups shuffled by the track grouping algorithm for the dM770 scenario.

Based on the selection procedure discussed above, semi-leptonic candidates are chosen for the dM770 scenario. Due to the presence of $\gamma\gamma \rightarrow$ low p_T hadron overlay,

there can be more than one semi-leptonic candidate found in an event. There are $\sim 6\,\%$ events with multi-pion candidates and $\sim 3\,\%$ events with multi-lepton candidates. The choice of a single pair of semi-leptonic candidates is based on the angle between them which is explained in section 8.3.3.

lep / π	d_0	1 trk grps	2 trk grps
d_0		31	7.5
1 trk grps	35	3.17	-
2 trk grps	14	-	-
Events with both tracks in the same group	-	-	3.1

Table 8.7.: Matrix showing the number of events in percentages based on the positions of chargino semi-leptonic candidates chosen for the dM770 scenario at $\sqrt{s} = 500$ GeV.

A matrix similar to table 8.5 for charginos and τ events achieved with the semi-leptonic selection procedure is presented in table 8.7 and table 8.8. With respect to the hierarchy of the selection, the number of events for the reconstruction level is similar to the number of events for true semi-leptonic tracks as given in table 8.5 and table 8.6. However, the number of events for high d_0 lepton with a pion in a single track group is higher than the vice-versa. This effect was not seen on the truth level. With the presence of $\gamma\gamma \rightarrow$ low p_T hadron overlay, a pool of charged pions are found in events with different decay channels. An e/μ from an event where the charginos or the τ-leptons decay di-leptonically, along with the charged pion from the $\gamma\gamma \rightarrow$ low p_T hadron overlay can imitate the signature for semi-leptonic decay.

lep / π	d_0	1 trk grps	2 trk grps
d_0		24.5	7.9
1 trk grps	42	1.3	-
2 trk grps	10.3	-	-
Events with both tracks in the same group	-	-	3.6

Table 8.8.: Matrix showing the number of events in percentages based on the positions of tau semi-leptonic candidates chosen for the dM770 scenario at $\sqrt{s} = 500$ GeV.

The selection of semi-leptonic candidates using the high d_0 track may result in high number of τ-events for following reasons. Even though the separation of high

d_0 track is a good strategy to isolate the chargino tracks from the $\gamma\gamma \rightarrow$ low p_T hadron tracks, τ-leptons also have a finite long life-time [44] similar to the charginos. Since the selection is prioritized based on the high d_0 track being a candidate, the possibility of finding a τ-event is as high as for the chargino events. Furthermore, high d_0 lepton tracks from the di-leptonic τ-decay events along with pions from $\gamma\gamma \rightarrow$ low p_T hadron events resemble the semi-leptonic decay channel and result into additional background events. As a consequence, narrowing the event selection based on the semi-leptonic decay channel is not as effective as in the *HS-analysis*.

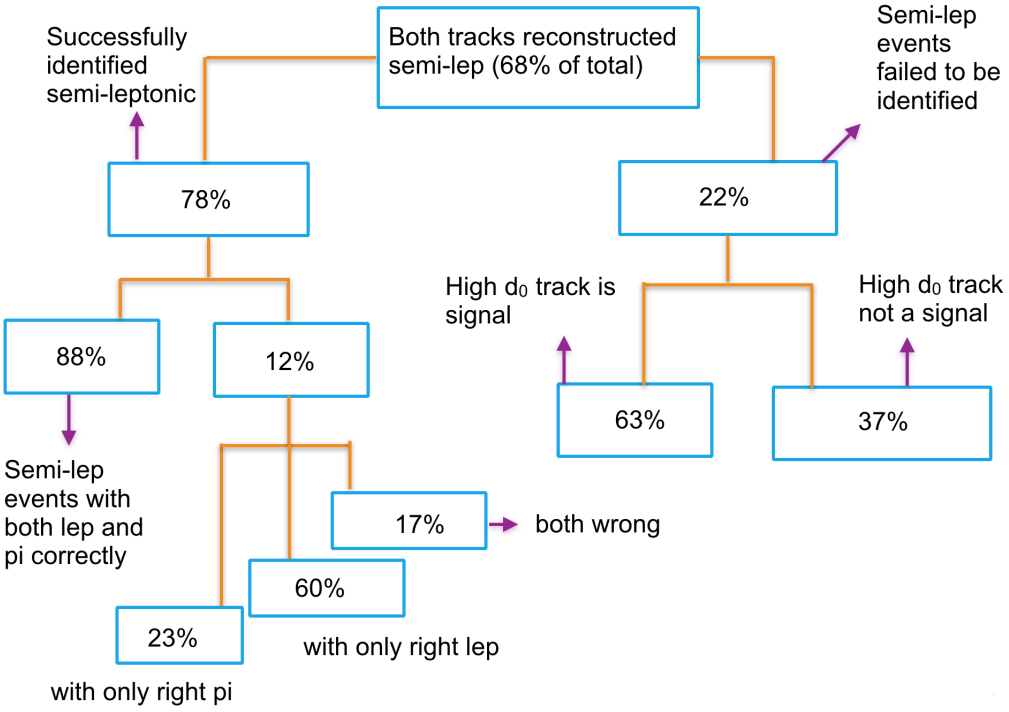

Figure 8.4.: A pictorial description of the efficiency of semi-leptonic selection procedure for the dM770 scenario for events at $\sqrt{s} = 500$ GeV.

The efficiency for selecting the right semi-leptonic chargino candidates in this process is shown through a pictorial representation in figure 8.4. For the semi-leptonic candidates to be correctly identified it is important that both the tracks are reconstructed. For the dM770 scenario due to the lower mass gap between the chargino and the LSP, the decay tracks have a very low p_T as shown in figure 6.2. Also figure 6.3 shows that the tracking efficiency for tracks with transverse momentum below 300 MeV is low. Among the total number of true semi-leptonic events only 68% of the events have both the tracks reconstructed. Even though the *HS-analysis* did not include $\gamma\gamma \rightarrow$ low p_T hadron overlay, the tracking efficiency conditions for both the

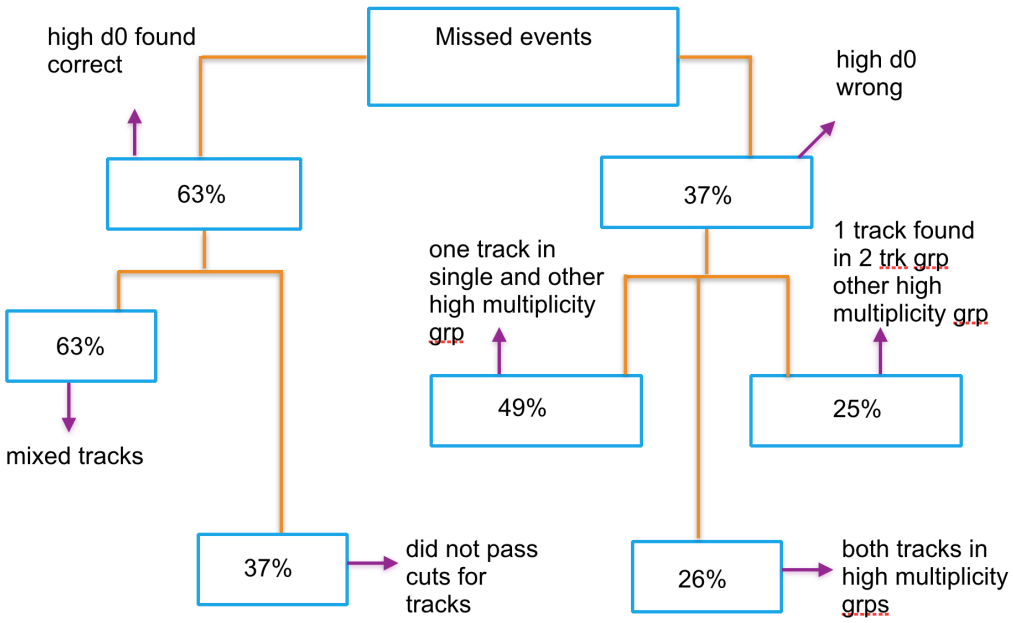

Figure 8.5.: A continuation of the pictorial description for the efficiency of semi-leptonic selection procedure for the dM770 scenario as give in figure 8.4. The picture mainly represents the reasons for failure of identifying semi-leptonic events.

analysis are same. However, it can be seen that 78% of the total events where both the tracks are reconstructed are rightly identified as semi-leptonic events. Furthermore, 88% of these events have both the π and the lepton candidates identified. In the remaining 12 % of the events either a pion or the lepton or both the candidates are chosen wrong. It can also be seen that 22% of the true semi-leptonic events are not identified. The main reason for the failure of identifying these events is that one or both the semi-leptonic tracks are grouped by the algorithm along with $\gamma\gamma \rightarrow$ low p_T hadron tracks in groups with higher number of tracks. A pictorial representation of the reasons for the failure of identifying these events are presented in figure 8.5. Among the total number of semi-leptonic events which were failed to be identified, 63% times the high d_0 track originates from a chargino decay and is thus correctly identified. However, 63% of these events have the other track in groups with mixed tracks. In 37% of the missed semi-leptonic events the signal tracks did not pass the track selection cuts for the algorithm as given in table 7.2. Among the events where the high d_0 tracks were wrongly identified, either one or both the tracks are in mixed track groups. However, since 78% of the semi-leptonic events were identified, and 88% of them have both the semi-leptonic candidates rightly identified, it can be

concluded that the semi-leptonic selection efficiency for the dM770 scenrio is good.

8.2.2. Semi-leptonic selection for dM1600

The charginos in the dM1600 scenario has smaller life-time than the charginos in the dM770 scenario. The track with highest d_0 value is not separated from the other tracks before applying the track grouping algorithm. Based on the positions of the true semi-leptonic tracks a matrix similar to table 8.5 is shown in table 8.9. However, only 16% of the semi-leptonic events have both the signal tracks in different groups. For the remaining 84% of the events both the semi-leptonic tracks are grouped together in the same group. Among them 61% of the events are in two track groups, 15% are in three track groups, 5% are in four track groups while rest are in groups with higher number of tracks in them.

π \ lep	1 trk grps	2 trk grps	3 trk grps	more trk grps
1 trk grps	8.5	1.3	0.44	0.4
2 trk grps	1.6	0.6	0.35	0.24
3 trk grps	0.6	0.2	0.13	0.20
more trk grps	0.35	0.37	0.11	0.17
trks in same grp	-	61	15	8.2

Table 8.9.: Matrix showing the number of events in percentages based on the positions of true chargino semi-leptonic tracks for the dM1600 scenario at $\sqrt{s} = 500$ GeV.

A similar table for the $\gamma\gamma \to \tau$-lepton events is shown in table 8.10. Unlike for the charginos, the majority (62%) of the events have both tracks in different groups while only 38% of the events have both the semi-leptonic tracks in the same group. The τ-leptons are long-lived particles. Most of the taus are created back-to-back and boosted longitudinally due to the ISR photon. Consequently, they are further away from each other thus making the algorithm to group them separately. This difference gives a handle on allowing less τ backgrounds as compared to the dM770 scenario.

Based on the arguments mentioned above, a procedure to select semi-leptonic candidates for the dM1600 scenario is designed and presented in a pictorial form in figure 8.6. Similar to the dM770 scenario, the semi-leptonic selection in the dM1600 scenario is a multi-layered process. The majority of the chargino events has both the the lepton and the pion in the same group. An oppositely charged pair of a π and a lepton in a two track group are selected as the semi-leptonic candidates

π \ lep	1 trk grps	2 trk grps	3 trk grps	more trk grps
1 trk grps	42	4	3.1	0.7
2 trk grps	4.1	2.3	0.6	0.7
3 trk grps	2.4	0.16	0.12	0.20
more trk grps	0.5	0.30	0	0.17
trks in same grp	-	29	5.2	4.2

Table 8.10.: Matrix showing the number of events in percentages based on the positions of true $\gamma\gamma \to \tau\tau$ semi-leptonic tracks for the dM1600 scenario at $\sqrt{s} = 500$ GeV.

with highest priority. In the case of failure, an oppositely charged pair of a π and a lepton in a three-track group is given the next priority. However, similar to the dM770 scenario, it is required that if the third track in the group is an oppositely charged pion to the selected pion candidate then the invariant mass of both the pions should not resonate the invariant mass of ρ-meson. Similarly it is also required that the third track in the group should not be an oppositely charged lepton to the selected lepton candidate to avoid the di-leptonic decay channels as mentioned in the dM770 scenario.

In case of failure, the search is extended to a pair of a π and a lepton in a four-track group. However, similar to the three-track group search, it is required that there should be no oppositely charged pion in the group with respect to the pion candidate and the invariant mass of whose combination is the invariant mass of ρ-meson (770 MeV$\pm$150 MeV). It is also required that there should not be any lepton in the group which is oppositely charged to the chosen lepton candidate. The number of events eliminated due to the rejection of groups from ρ mass cut and extra lepton cuts is given in table 8.13. If the search for semi-leptonic candidates also fails in the four-track groups, the semi-leptonic tracks are looked for in two single-track groups. Even though only 5% of the chargino semi-leptonic events have the true pion and lepton in four-track groups as compared to 8.5% of events having these tracks in two single-track groups, selection through four-track groups is given higher priority. This choice is the selection of semi-leptonic candidates for τ events which have 42% of the events where the semi-leptonic candidates are distributed in two single-track groups. The number of events based on the semi-leptonic selection procedure as mentioned above is given in table 8.11 for chargino events and in table 8.12 for τ events.

As can be seen in table 8.12, the highest fraction of events are obtained from groups with four tracks in them. Comparing this number with the true events

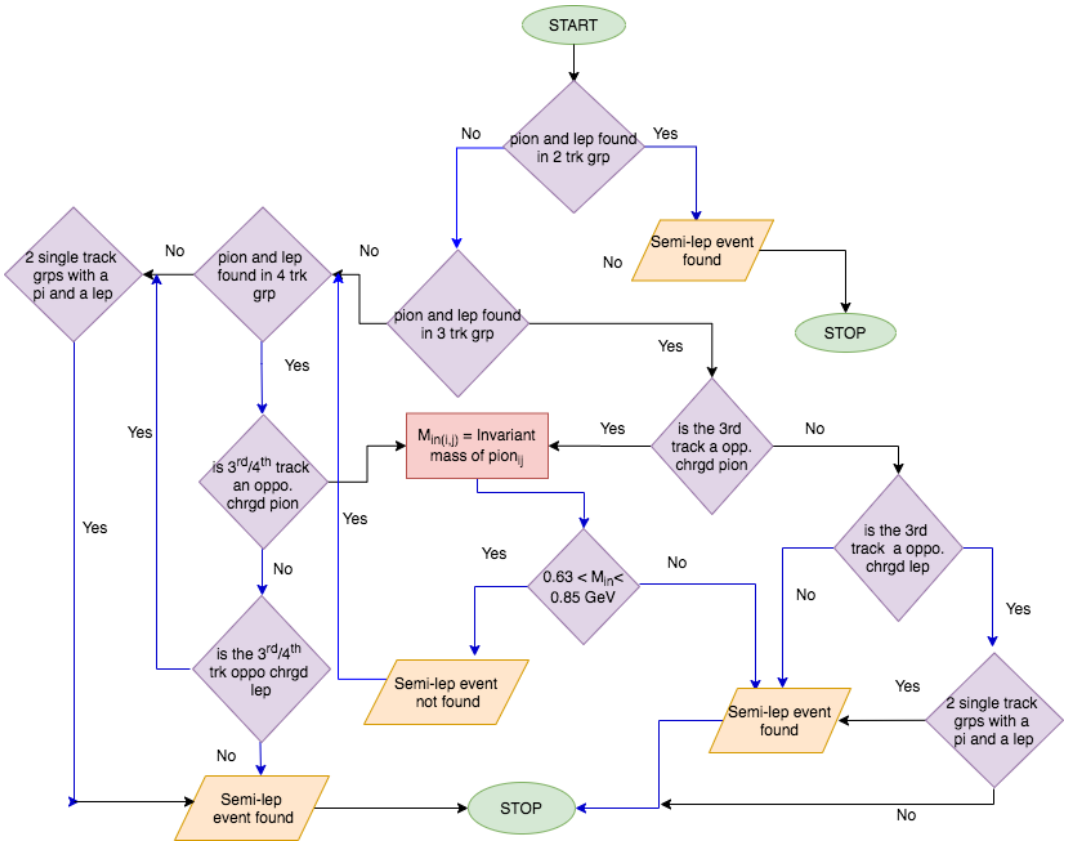

Figure 8.6.: Flowchart describing the procedure of selection of semi-leptonic candidates from the groups shuffled by the track grouping algorithm for the dM1600 scenario.

Groups	Number of semi-leptonic events found [%]
Groups with 2 tracks	64
Groups with 3 tracks	17
Groups with 4 tracks	8
2 single track groups	11

Table 8.11.: Table showing the number of chargino events in percentages based on semi-leptonic tracks selection at reconstruction level for the dM1600 scenario at $\sqrt{s} = 500$ GeV.

where both the tracks are in the four-track groups, it is clear that majority of these events are fake semi-leptonic events. However, these events can be removed with

Groups	Number of semi-leptonic events found [%]
Groups with 2 tracks	23
Groups with 3 tracks	20
Groups with 4 tracks	45
2 single track groups	12

Table 8.12.: Table showing the number of τ events in percentages based on semi-leptonic tracks selection at reconstruction level for the dM1600 scenario at $\sqrt{s} = 500$ GeV.

event-selection cuts targeted at such events as given in section 8.5. Also, as can be seen in table 8.13, the ρ mass cut and the extra lepton cut is negligible on the chargino events while the lepton cut rejects 25% of total number of $\gamma\gamma \to \tau\tau$ events. Therefore, this cut is found to be effective on removing τ background.

Group selection cuts	Number of $\tilde{\chi}_1^{\pm}$ semi-leptonic events lost [%]	Number of tau events lost [%]
ρ cut for 3 track group	0.03	0.01
Lepton cut for 3 track group	1	7
ρ cut for 4 track group	0.02	0.002
Lepton cut for 4 track group	1.2	18.5

Table 8.13.: Table showing the total number of chargino and τ events lost due to ρ-cut and extra lepton cut in percentages for the dM1600 scenario at $\sqrt{s} = 500$ GeV.

The semi-leptonic selection efficiency for the chargino events in the dM1600 scenario is shown in a pictorial representation as in figure 8.7. As mentioned before, for the semi-leptonic candidates to be correctly identified it is important that both the tracks are reconstructed. With a higher mass gap between the chargino and the LSP in the dM1600 scenario, the decay tracks have a higher transverse momentum than the decay tracks in dM770 scenario. The higher p_T enables a better track reconstruction efficiency as compared to the dM770 scenario. Consequently 84% of the true semi-leptonic chargino events have both the decay tracks reconstructed. From among these events, 79% of the events are selected as semi-leptonic events out of which 96% have both the pion and the lepton correctly identified. The results show that the semi-leptonic selection efficiency for dM1600 scenario is better than for the dM770 scenario. There are 21% of the events which were failed to be identified as semi-leptonic events because either one or both the tracks were grouped in events

with a higher number of $\gamma\gamma \rightarrow$ low p_T hadron tracks.

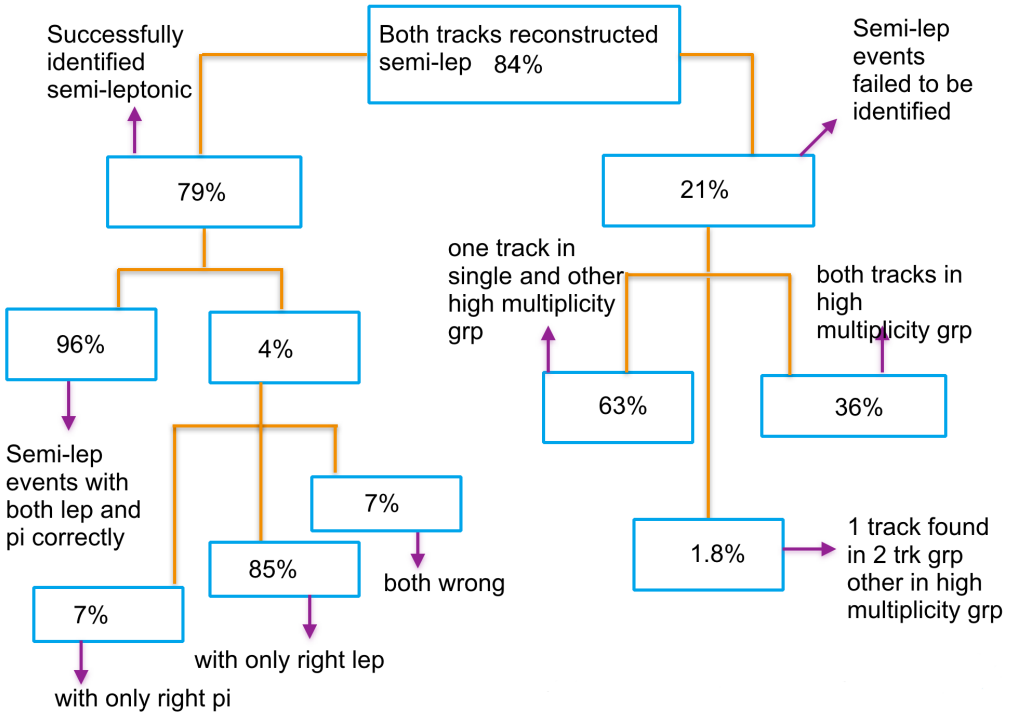

Figure 8.7.: A pictorial description of the efficiency of semi-leptonic selection procedure for the dM1600 scenario for events at $\sqrt{s} = 500$ GeV.

8.3. Post-algorithm Chargino Selection Process

The events selected through the BeamCal, ISR photon and number of track cuts are passed through the track grouping algorithm. The semi-leptonic selection for events is performed right after the algorithm. The properties of the semi-leptonic candidates are used for event selection cuts e.g. the four-momentum and the missing four-momentum cuts as can be seen in sections ahead. However, the selection of events based on identification of a semi-leptonic candidate is done only after the application of missing four-momentum selection cut for the convenience of comparison with the *HS-analysis*. A few more selection cuts applied on the surviving events are introduced in the further sections while a quantitative analysis on the efficiency of these cuts and their comparison with the *HS-analysis* is done in section 8.4.

8.3.1. Four-Momentum of Soft Particles

The reconstructed particles apart from the ISR photons were required to be 20° away from the beam axis in the *HS-analysis*. This means that every particle other than the ISR photon should fulfill the condition of $\cos theta_{\text{soft}} < 0.9397$. Charginos are produced centrally and they decay isotropically. As can be seen in figure 8.8 from the *HS-analysis*, $\cos theta_{\text{soft}}$ for the chargino decay products has a flat shape unlike the other Standard Model backgrounds which have a peak in the forward direction.

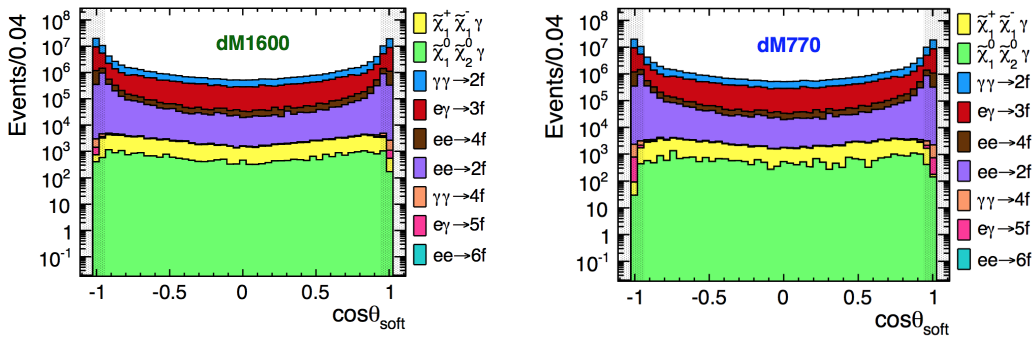

(a) (b)

Figure 8.8.: $\cos theta_{\text{soft}}$ distribution of particles in events without the inclusion of $\gamma\gamma \to$ low p_T hadron overlay at $\sqrt{s} = 500$ GeV and $\int \mathcal{L}dt = 500$ fb^{-1} with $P(e^+, e^-) = (+30\%, -80\%)$ for dM1600 and dM770. Figure taken from *HS-analysis* [6].

The $\gamma\gamma \to$ low p_T hadron overlay particles have a very low transverse momentum and are found in the forward region of the detector. Therefore, with the inclusion of $\gamma\gamma \to$ low p_T hadron overlay, such a cut would result in the loss of a huge amount of signal. Consequently, the requirement of all the particles to be 20° away from the beam axis cannot be met for the majority of the signal events. For this reason, the cut of $|\cos theta_{\text{soft}}| < 0.9397$ cannot be applied exactly as in *HS-analysis* but with certain alterations. Without the $\gamma\gamma \to$ low p_T hadron overlay, the majority of the events is expected to have tracks only from the decay particles of the $\tilde{\chi}_1^{\pm}$. To emulate a similar scenario, the $\cos theta_{\text{soft}}$ cut is modified for this analysis. For events where semi-leptonic candidates are found, $|\cos theta_{\text{soft}}|$ for the selected semi-leptonic candidates are required to be less than 0.9397 while for rest of the events $|\cos theta_{\text{soft}}|$ for all the particles should be less than 0.9397. Figure 8.9 shows the distribution of the maximum value of $\cos theta_{\text{soft}}$ of the semi-leptonic candidates for events where semi-leptonic candidates are found and the maximum value of

$\cos theta_{\text{soft}}$ among all the particles for rest of the events. With such modification, the loss in semi-leptonic signal events can be reduced while clearing away a huge amount of Standard Model background. The excluded region is shown with a shaded area which displays that a significant amount of Standard Model background is suppressed.

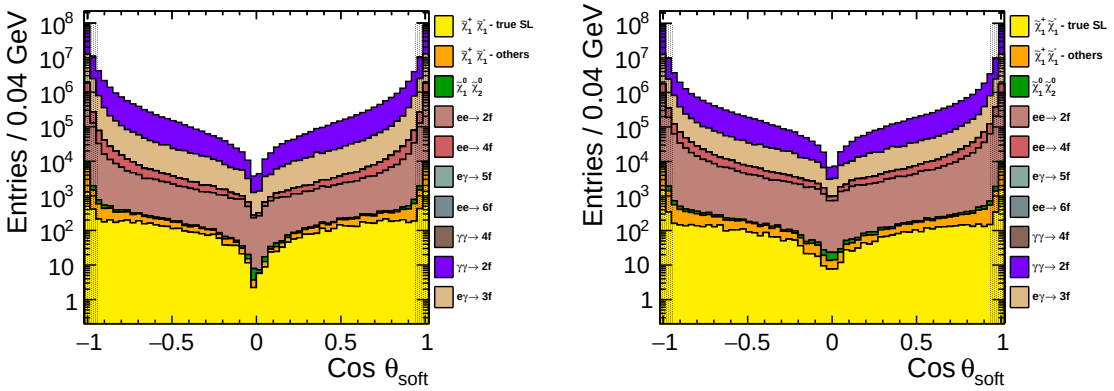

(a) (b)

Figure 8.9.: Distribution of the maximum $|\cos\theta|$ of semi-leptonic candidates for events where semi-leptonic candidates are found and maximum $|\cos\theta|$ of all the particles in rest of the events after the ISR photon cut at $\sqrt{s} = 500$ GeV and $\int \mathcal{L}dt = 500$ fb^{-1} with $P(e^+, e^-) = (+30\%, -80\%)$ for dM1600 and dM770. The excluded region is shown by the shaded area.

Since the higgsinos are nearly mass degenerate and the LSPs are carrying away a significant amount of energy, the detectable final state particles are expected to have very low energy. Figure 8.10 displays the energy distribution of the final state particles for events without $\gamma\gamma \rightarrow$ low p_T hadron overlay in *HS-analysis*. Motivated by the energy distribution it is required that no particle in an event should have energy more than 5 GeV.

However, similar to the $\cos\theta$ scenario as explained in section above, the $\gamma\gamma \rightarrow$ low p_T hadron overlay modifies the energy distribution of particles as shown in figure 8.11. As the energy distribution with overlay extends far beyond 5 GeV, eliminating events with particles of energy above 5 GeV would result in a loss of a significant amount of signal. Therefore some alternative methods to suppress background events more efficiently are studied and compared as described ahead. As discussed in section 8.3.1, without the inclusion of $\gamma\gamma \rightarrow$ low p_T hadron overlay, the signal events in the *HS-analysis* have tracks only from the decay particles of

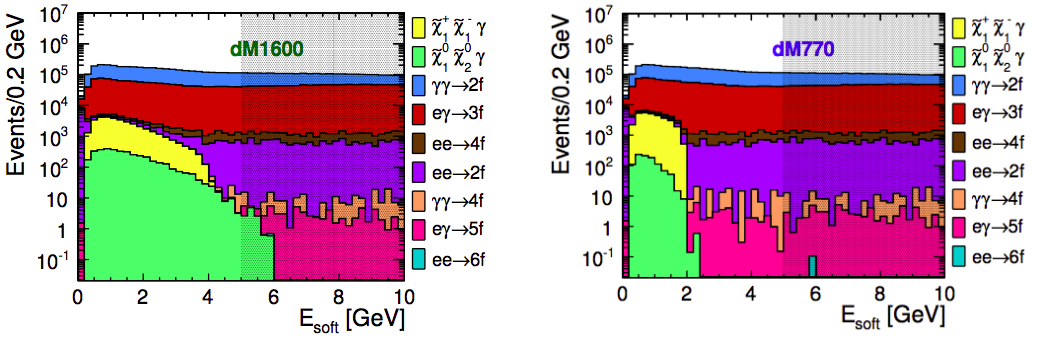

(a) (b)

Figure 8.10.: Energy distribution of particles in events without the inclusion of $\gamma\gamma \rightarrow$ low p_T hadron overlay at $\sqrt{s} = 500$ GeV and $\int \mathcal{L}dt = 500$ fb^{-1} with $P(e^+, e^-) = (+30\%, -80\%)$ for dM1600 and dM770. Figure taken from *HS-analysis* [6].

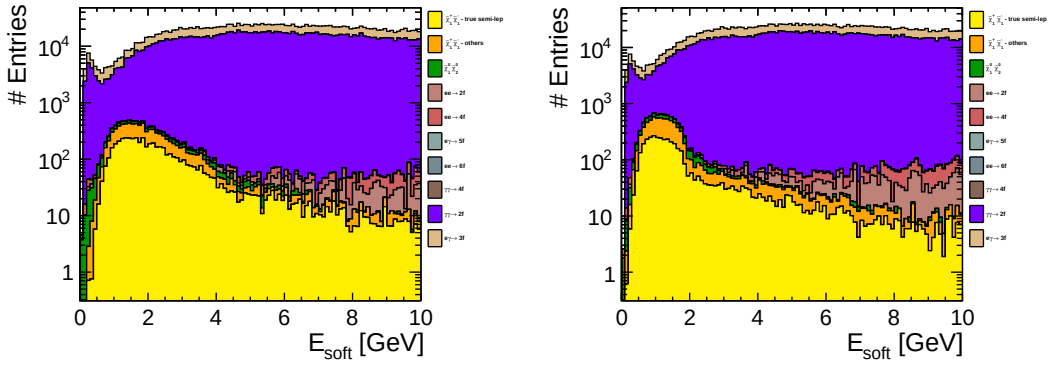

(a) (b)

Figure 8.11.: Distribution of maximum value of energy among all the particles in an event after requiring $|\cos\theta_{soft}| < 0.9397$ at $\sqrt{s} = 500\,\text{GeV}$ and $\int \mathcal{L}dt = 500\,\text{fb}^{-1}$ with $P(e^+, e^-) = (+30\%, -80\%)$ for dM1600 and dM770 .

$\tilde{\chi}_1^{\pm}$. In the dM1600 scenario, $\tilde{\chi}_1^{\pm}$ also decay into π^0 which further decay to photons. Besides from neutral decay particles of the $\tilde{\chi}_1^{\pm}$ there may also be neutral particles created by particles interacting with detector material. Using the $\tilde{\chi}_1^{\pm}$ decay tracks along with the neutral particles and $\gamma\gamma \rightarrow$ low p_T hadron overlay tracks, two different cases are studied and compared.

For the events where semi-leptonic candidates are found, the energy of the more energetic semi-leptonic candidate is called as E_{SL}, highest energy of the other tracks is known as $E_{\mathrm{oth\_trks}}$ and highest energy of neutral particles is E_{neutral}. For the events where no semi-leptonic candidate is found, E_{SL} remains zero while $E_{\mathrm{oth\_trks}}$ is assigned the value of highest energy of charged particles and E_{neutral} is the energy of highest energetic neutral particle. Using these three set of energies two different cases are discussed ahead.

$\mathbf{E_{case1}}$: In the first case it is required that E_{SL} and $E_{\mathrm{oth\_trks}} + E_{\mathrm{neutral}}$ should be less than 5 GeV. A set of 2D histograms showing E_{SL} versus $E_{\mathrm{oth\_trks}} + E_{\mathrm{neutral}}$ for the signal and the major background processes identified in *HS-analysis* e.g. $e^+e^- \to 2f$, $e^+e^- \to 4f$, $\gamma\gamma \to 2f$ and $e\gamma \to 3f$ are shown in figure 8.12 and figure 8.13 for dM1600 and dM770 scenarios respectively.

$\mathbf{E_{case2}}$: In the second case, it is required that $E_{\mathrm{SL}} + E_{\mathrm{othr\_trks}}$ and $E_{\mathrm{SL}} + E_{\mathrm{neutral}}$ should be simultaneously less than 5 GeV. A set of 2D histograms showing $E_{\mathrm{SL}} + E_{\mathrm{othr\_trks}}$ versus $E_{\mathrm{SL}} + E_{\mathrm{neutral}}$ for signal and the major background processes identified in *HS-analysis* e.g. $e^+e^- \to 2f$, $e^+e^- \to 4f$, $\gamma\gamma \to 2f$ and $e\gamma \to 3f$ are shown in figure 8.14 and figure 8.15 for dM1600 and dM770 scenarios respectively.

For comparison purpose, the energy distribution shown in figure 8.11 is referred to as $\mathrm{E_{case3}}$. After all the selection cuts introduced, three different sets of cutflow tables each with three different cases for energy cuts as explained above are presented in table 8.14, table 8.15 and table 8.16 for $\mathrm{E_{case1}}$, $\mathrm{E_{case2}}$ and $\mathrm{E_{case3}}$, respectively. A decision on the choice of the energy cut among the three cases is made based on the comparion of cutflow of the number of events as presented in section 8.3.5.

8.3.2. Missing Four-Momentum

Due to the undetected LSPs in the chargino process, a large amount of missing energy is found in the signal events. For processes like $\gamma\gamma \to 2f$ and $e\gamma \to 3f$, either one or both the beam particles may scatter under a very small angle and escape through the beampipe. However, as explained in section 8.1, the requirement of an ISR photon recoils either of the beam particles with an energy of nearly 250 GeV into the detector acceptance. With the resulting low missing energy for such events, they can be very efficiently suppressed by requiring $E_{miss} > 300$ GeV. Figure 8.16 shows the missing energy of all the different Standard Model processes along with the higgsino events. The figure clearly shows that a significant amount of the Standard Model background can be eliminated with the condition of $E_{miss} > 300$ GeV as seen in the shaded region.

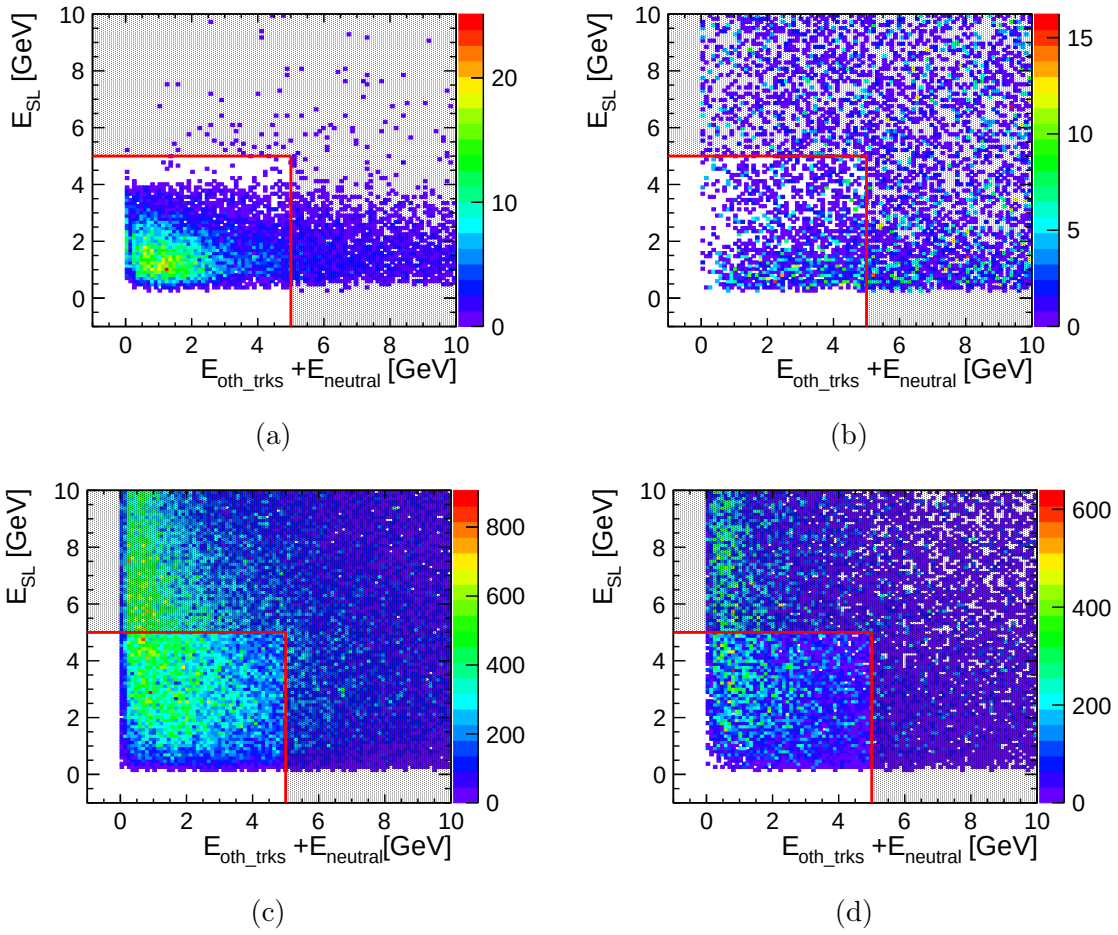

Figure 8.12.: 2D distribution for $\mathbf{E_{case1}}$ for (a) $e^+e^- \to \tilde{\chi}_1^+\tilde{\chi}_1^-$, (b) $e^+e^- \to 2f$ and $e^+e^- \to 4f$, (c) $\gamma\gamma \to 2f$ and (d) $e\gamma \to 3f$ after requiring $|\cos\theta_{soft}| < 0.9397$ at $\sqrt{s} = 500$ GeV and $\int \mathcal{L}dt = 500$ fb^{-1} with $P(e^+, e^-) = (+30\%, -80\%)$ for the dM1600 scenario. The excluded region is shown by the shaded area.

To ensure that a high missing energy for Standard Model events is not due to the beam particle escaping down the beampipe, it is required that the missing momentum vector points into the acceptance region of the detector. It is required that $|\cos\theta_{miss}| < 0.992$. The distribution of $\cos\theta_{miss}$ is given in figure 8.17.

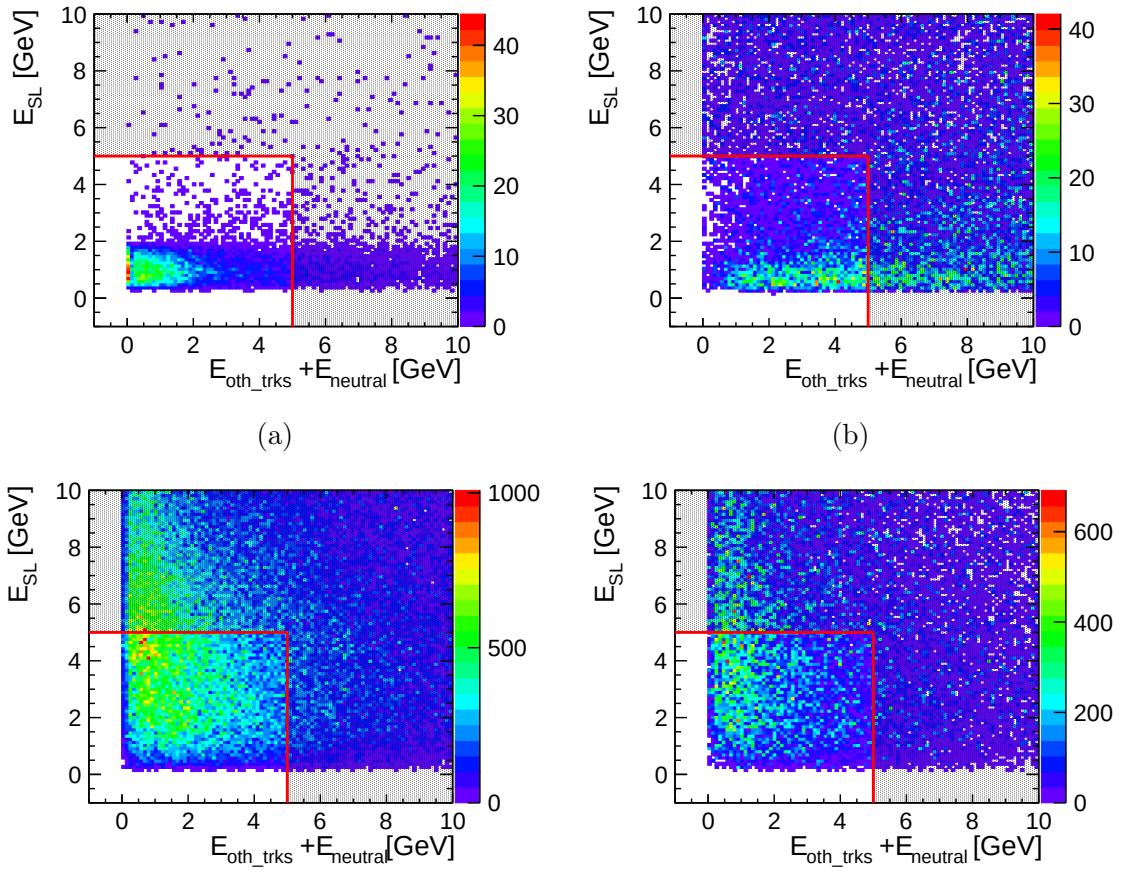

Figure 8.13.: 2D distribution for $\mathbf{E_{case1}}$ for (a) $e^+e^- \to \tilde{\chi}_1^+\tilde{\chi}_1^-$, (b) $e^+e^- \to 2f$ and $e^+e^- \to 4f$, (c) $\gamma\gamma \to 2f$ and (d) $e\gamma \to 3f$ after requiring $|\cos\theta_{soft}| < 0.9397$ at $\sqrt{s} = 500$ GeV and $\int \mathcal{L}dt = 500$ fb^{-1} with $P(e^+, e^-) = (+30\%, -80\%)$ for the dM770 scenario. The excluded region is shown by the shaded area.

8.3.3. Boosted Energy of the Pion

The requirement of a semi-leptonic final state events help suppressing the SUSY background. However, as mentioned in section 8.2, the semi-leptonic decay of the τ-lepton remains as a main challenge to eliminate such events. Therefore to handle the τ- events, a variable that represents the energy of the hadronic chargino decay products boosted into the rest frame of the chargino pair was used in the *HS-analysis*. The pion boosted energy variable from the *HS-analysis* is presented in figure 8.18.

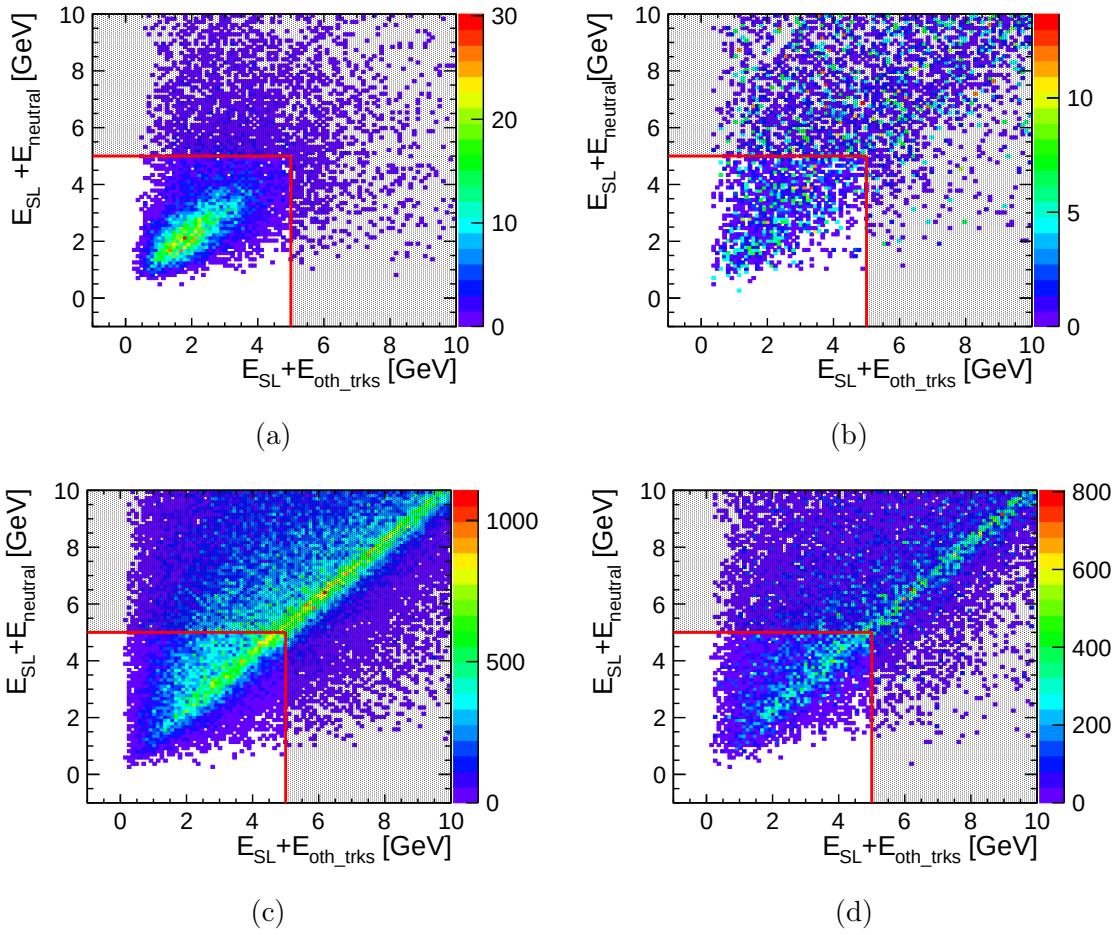

Figure 8.14.: 2D distribution for $\mathbf{E_{case2}}$ for (a) $e^+e^- \to \tilde{\chi}_1^+\tilde{\chi}_1^-$, (b) $e^+e^- \to 2f$ and $e^+e^- \to 4f$, (c) $\gamma\gamma \to 2f$ and (d) $e\gamma \to 3f$ after requiring $|\cos\theta_{soft}| < 0.9397$ at $\sqrt{s} = 500$ GeV and $\int \mathcal{L}dt = 500$ fb^{-1} with $P(e^+, e^-) = (+30\%, -80\%)$ for the dM1600 scenario. The excluded region is shown by the shaded area.

.

The pion boosted energy for the dM770 scenario is calculated as follows:

$$E_\pi^* = \frac{(\sqrt{s} - E_\gamma)E_\pi + \overrightarrow{p}_\pi \cdot \overrightarrow{p}_\gamma}{\sqrt{s'}}. \tag{8.1}$$

where $\sqrt{s'}$ is the reduced centre-of-mass energy of the system after the emission of the ISR photon, E_π and $\overrightarrow{p}_\pi$ are the energy and three-momentum of the semi-leptonic pion candidate and E_γ and $\overrightarrow{p}_\gamma$ are the energy and three-momentum of the

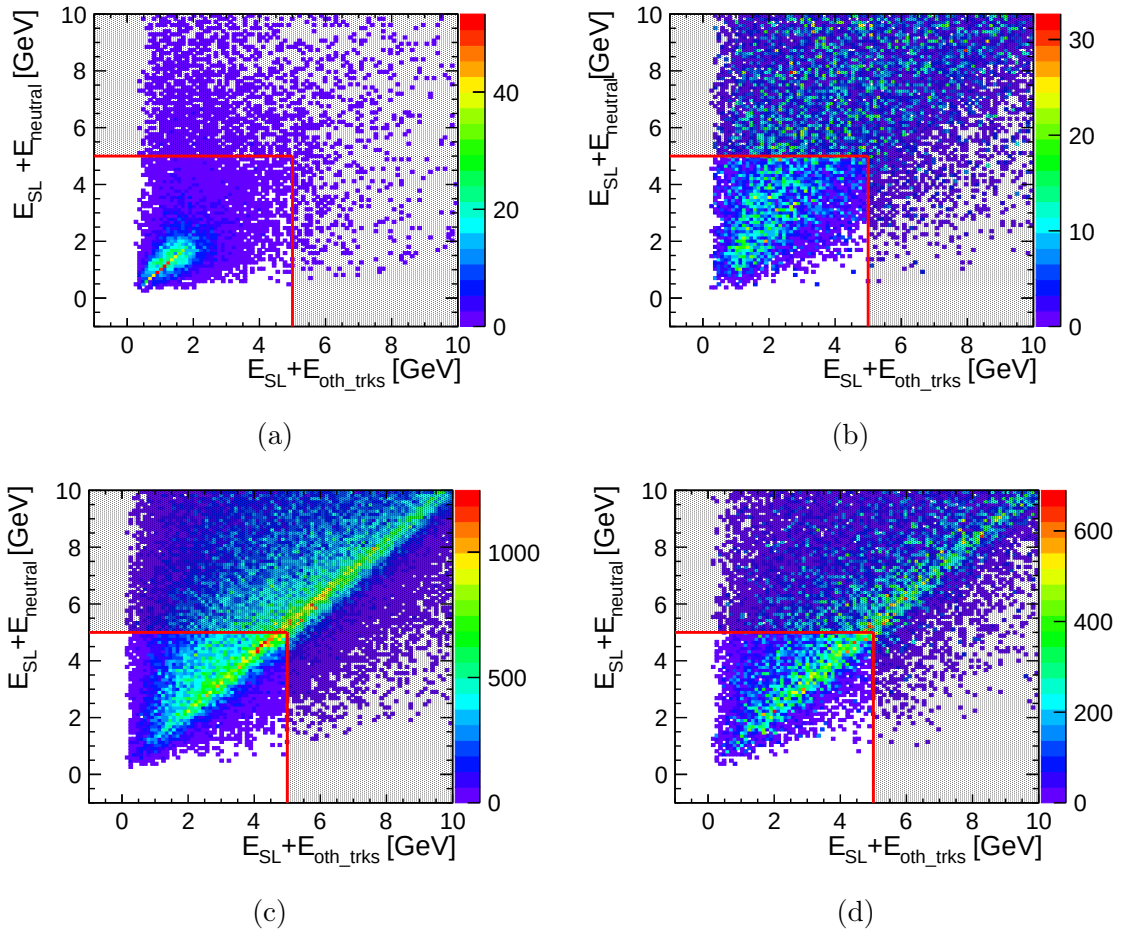

Figure 8.15.: 2D distribution for $\mathbf{E_{case2}}$ for (a) $e^+e^- \to \tilde{\chi}_1^+\tilde{\chi}_1^-$, (b) $e^+e^- \to 2f$ and $e^+e^- \to 4f$, (c) $\gamma\gamma \to 2f$ and (d) $e\gamma \to 3f$ after requiring $|\cos\theta_{soft}| < 0.9397$ at $\sqrt{s} = 500$ GeV and $\int \mathcal{L}dt = 500$ fb^{-1} with $P(e^+, e^-) = (+30\%, -80\%)$ for the dM770 scenario. The excluded region is shown by the shaded area.

.

ISR photon in that frame. The definition for s' is given as $s' = s - 2\sqrt{s}E_\gamma$ where $\sqrt{s}$ is the nominal centre-of-mass energy. Since the dM1600 scenario also has 28.8% of the charginos decaying into a $\pi^\pm$ and a π^0 as can be seen in table 6.2, the four-momentum of the two photons from the π^0 decay are added to the charged pion four-momentum. Without the inclusion of $\gamma\gamma \to$ low p_T hadron overlay particles, the only photons found in an event in the *HS-analysis* are the photons from the neutral pion in a chargino decay. Therefore adding the four-momentum of photons

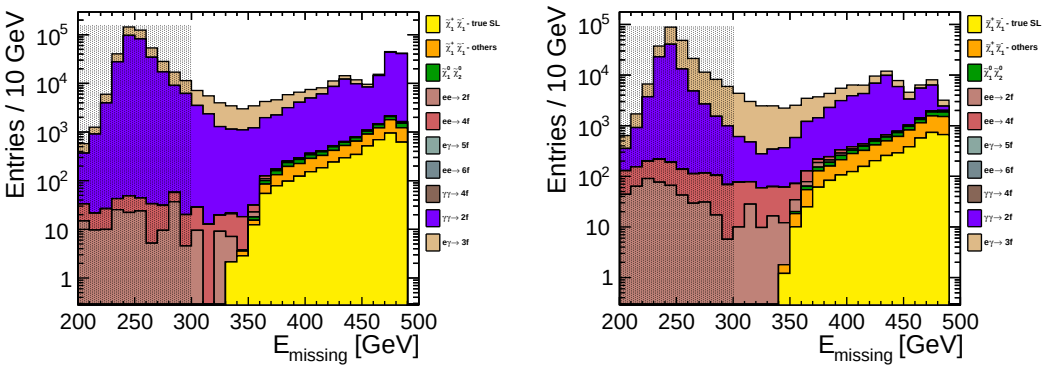

(a) (b)

Figure 8.16.: Missing energy for every event after requiring E_{soft} in the event at $\sqrt{s} =$ 500 GeV and $\int \mathcal{L}dt = 500$ fb^{-1} with $P(e^+, e^-) = (+30\%, -80\%)$ for dM1600 and dM770.

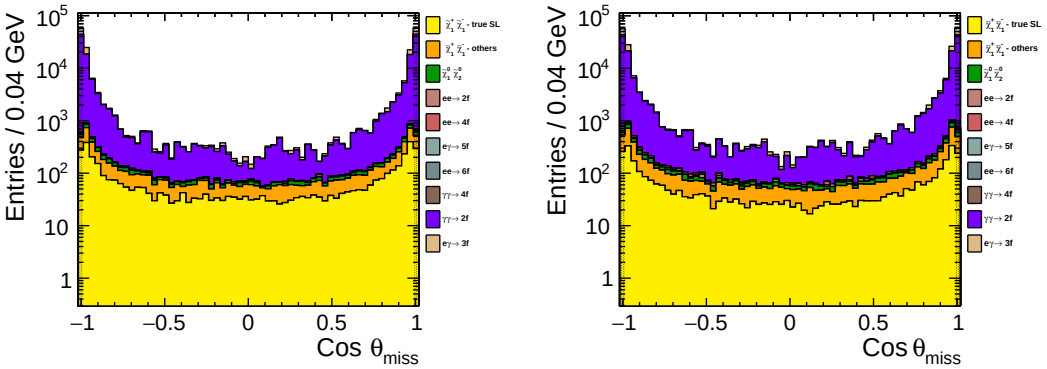

(a) (b)

Figure 8.17.: $\cos\theta$ distribution of the missing four momentum for each event after requiring $E_{miss} > 300$ GeV at $\sqrt{s} = 500$ GeV and $\int \mathcal{L}dt = 500$ fb^{-1} with $P(e^+, e^-) = (+30\%, -80\%)$ for dM1600 and dM770.

in an event would give the boosted energy of the neutral pion into the rest frame of the chargino.

However, in the current analysis, a pool of charged and neutral pions from the $\gamma\gamma \to$ low p_T hadron overlay is found. Therefore adding the four-momentum of the photons would not only include the energies of photons from the neutral pion in a chargino decay but also energies of photons from $\gamma\gamma \to$ low p_T hadrons. Therefore

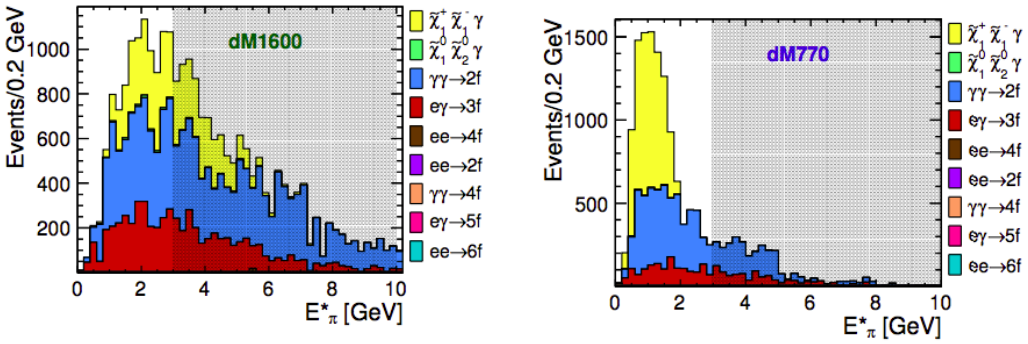

(a) (b)

Figure 8.18.: Energy of pions boosted into the rest frame of chargino pairs after the semi-leptonic decay channel selection without the inclusion of $\gamma\gamma \rightarrow$ low p_T hadron overlay at $\sqrt{s} = 500$ GeV and $\int \mathcal{L}dt = 500$ fb^{-1} with $P(e^+, e^-) = (+30\%, -80\%)$ for dM1600 and dM770 respectively. Figure taken from the *HS-analysis* [6].

the calculated boosted energy of the pions into the chargino rest frame is much higher than the actual boosted energy of the chargino decay pions as can be seen in figure 8.19. In this condition, a pion boost energy cut at 3 GeV as required in the *HS-analysis* would result in a significant amount of loss in the signal events. Therefore instead of including all the photons in an event as done in the *HS-analysis*, it is important to have appropriate methods to select photons which are part of the chargino decay process. Since the seperation of $\gamma\gamma \rightarrow$ low p_T hadron events from the main process is performed using the charged tracks in this study, the separation of neutral $\gamma\gamma \rightarrow$ low p_T particles is out of scope for this thesis. Therefore, in this analysis, the cut is only applied on the boosted energy of the charged pion decay for the dM1600 scenario even if the chargino decays to a charged and a neutral pion 28.8% of the times. scenario in this analysis. For the dM770 scenario where only the chargino decay channel of single charged pion is considered and for the events in dM1600 scenario where the charginos only decay to a charged pion, this cut remains appropriate.

The presence of $\gamma\gamma \rightarrow$ low p_T hadron overlay makes the impact of the boosted energy cut less effective than for the *HS-analysis*. The pions from $\gamma\gamma \rightarrow$ low p_T hadron overlay along with a $\mu/e^{\pm}$ from the di-leptonic final state events, emulate the signature for real semi-leptonic events allowing a significant amount of fake semi-leptonic events. The boosted energy for the wrongly picked pions from $\gamma\gamma \rightarrow$ low p_T hadron overlay as a semi-leptonic candidate is small and similar to the chargino decay pions as can be seen in figure 8.20. Due to a large peak at the lower energies for

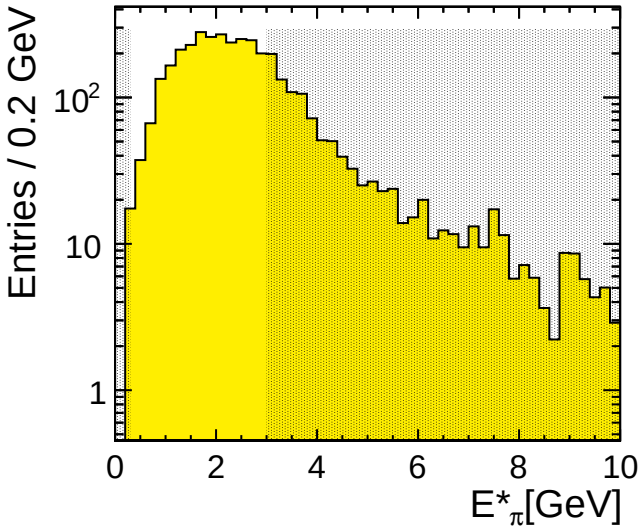

Figure 8.19.: Energy of pions boosted into the rest frame of the chargino pairs including all the four-momentum of the photons. Since no distinction can be made among the photons decayed from the neutral pions from charginos and other photons the four-momentum of all the photons are included after requiring the semi-leptonic final state cut at $\sqrt{s} = 500$ GeV and $\int \mathcal{L}dt = 500$ fb^{-1} with $P(e^+, e^-) = (+30\%, -80\%)$ for the dM1600 scenario.

the Standard Model background events, an additional requirement of $E^*_\pi > 0.3\,\mathrm{GeV}$ is applied.

In the case that several pions in the event qualify as a part of a semi-leptonic candidate, the pion which has the smallest acoplanarity angle with the lepton is chosen. For events having multi-pion and multi-lepton candidates, the pair which has the smallest acoplanarity are chosen as the semi-leptonic candidates.

8.3.4. Acoplanarity between the semi-leptonic candidates

The dominant Standard Model background left after the selection procedures mentioned above are the $\gamma\gamma \to \tau\tau$ events. These events are back-to-back in the transverse plane due to the momentum conservation and have rather high $\sqrt{s'}$: The events that survive the ISR photon cut have a low energetic ISR photon incapable of recoiling the beam particle into the acceptance range of the detector. To suppress such events, either the acoplanarity angle, which is the angle between the semi-

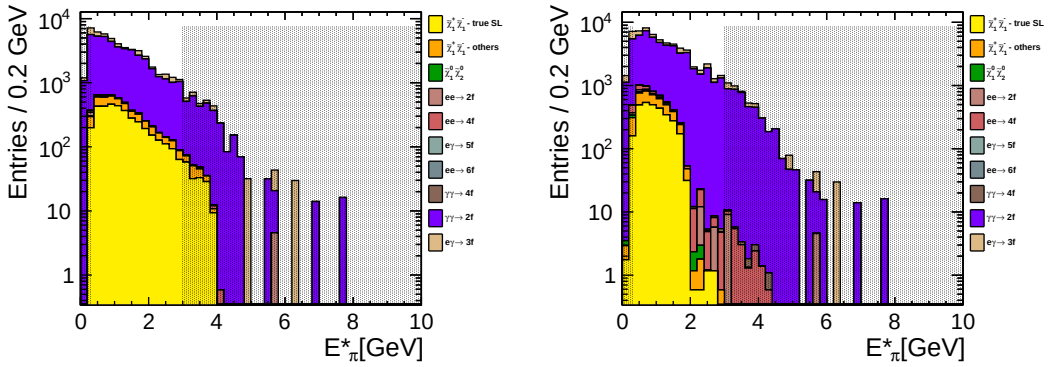

(a) (b)

Figure 8.20.: Energy of pions boosted into the rest frame of the chargino pairs after requiring the semi-leptonic final state cut at $\sqrt{s} = 500$ GeV and $\int \mathcal{L}dt = 500$ fb^{-1} with $P(e^+, e^-) = (+30\%, -80\%)$ for dM1600 and dM770 respectively.

leptonic decay products is required to be smaller than 2 rad or $\sqrt{s'} < 480$ GeV. The acoplanarity angle is calculated from the momentum of the semi-leptonic candidates as follows:

$$\Phi_{acop} = \arccos\left(\frac{\overrightarrow{p}_{\text{lep}} \cdot \overrightarrow{p}_{\text{had}}}{|\overrightarrow{p}_{\text{lep}}||\overrightarrow{p}_{\text{had}}|}\right) \tag{8.2}$$

where $\overrightarrow{p}_{\text{lep}} = p_{x_{\text{lep}}} + p_{y_{\text{lep}}}$ and $\overrightarrow{p}_{\text{had}} = p_{x_{\text{had}}} + p_{y_{\text{had}}}$ in the transverse plane. The acoplanarity angle for the dM1600 and the dM770 scenario is given is figure 8.21. This cut is very efficient in eliminating 73% of the $\gamma\gamma \to 2,4f$ and 3.4% of the $e\gamma \to 3,5f$ events at the cost of 15% of the signal events in the dM1600 scenario while it also removes 75% of the $\gamma\gamma \to 2,4f$ and 5% of the $e\gamma \to 3,5f$ events along with 17% of the signal events in the dM770 scenario.

8.3.5. Selection of energy cut

The cut-flow tables for selection of events based on the three different cases of energy cuts (E_{case1}, E_{case2} and E_{case2}) as introduced in section 8.3.1 are are given in table 8.14, table 8.15 and table 8.16. As can be seen in table 8.16, with E_{case3}, highest number of signal events are preserved as compared to the other alternatives. However, the E_{case3} energy cut is less efficient in suppressing the Standard Model background than E_{case1} and E_{case2}. With $E_{\text{case1}} < 5$ GeV, 2% more signal is obtained

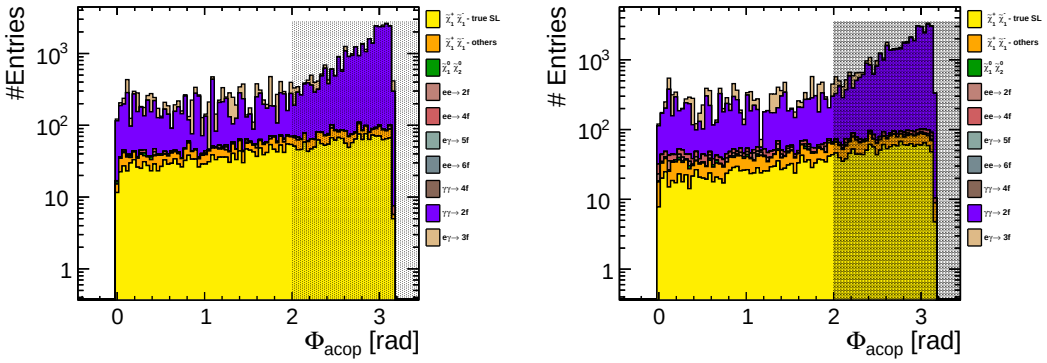

(a) (b)

Figure 8.21.: Acoplanarity angle between the leptonic and hadronic decays after the boosted pion energy cut at $\sqrt{s} = 500\,\text{GeV}$ and $\int \mathcal{L}dt = 500\,\text{fb}^{-1}$ with $P(e^+, e^-) = (+30\%, -80\%)$ for dM1600 and dM770 scenarios respectively.

as compared to $\text{E}_{\text{case2}} < 5$ GeV. However, since E_{case2} can suppress the Standard Model background in a very efficient way with a loss of only 2% signal than in E_{case1}, it is chosen as the final energy cut for this analysis.

Selection cuts	dM1600			Standard Model		
	$\tilde{\chi}_1^+\tilde{\chi}_1^-\gamma$ SL	$\tilde{\chi}_1^+\tilde{\chi}_1^-\gamma$ others	$\tilde{\chi}_1^0\tilde{\chi}_1^0\gamma$	$e^+e^- \to 2,4,6f$	$e\gamma \to 3,5f$	$\gamma\gamma \to 2,4f$
Precuts	9816	17934	8654	4.9326×10^6	2.9901×10^7	1.78609×10^8
$\lvert\cos\theta_{soft}\rvert < 0.9397$	6176	4396	1452	439969	17954349	3118228
E_{soft} (E_{case1}) < 5 GeV	4532	3628	1397	1733	203917	467310
$E_{miss} > 300$ GeV	4532	3626	1221	532	40995	174506
$\lvert\cos\theta_{miss}\rvert < 0.992$	4214	3379	1146	461	23459	103235
Semi-leptonic	3902	1297	69	279	8831	71006
$E_\pi^* < 3$ GeV	3639	1197	65	219	6472	53877
$\Phi_{acop} < 2$ or $\sqrt{s'} < 480$ GeV	3098	1018	63	193	5962	13876

Table 8.14.: Cut-flow table for the preselection at $\sqrt{s} = 500\,\text{GeV}$ and $\int \mathcal{L}dt = 500\,\text{fb}^{-1}$ with $P(e^+, e^-) = (+30\%, -80\%)$ for the dM1600 scenario with E_{case1}.

Selection cuts	dM1600			Standard Model		
	$\tilde{\chi}_1^+\tilde{\chi}_1^-\gamma$ SL	$\tilde{\chi}_1^+\tilde{\chi}_1^-\gamma$ others	$\tilde{\chi}_1^0\tilde{\chi}_1^0\gamma$	$e^+e^- \to 2,4,6f$	$e\gamma \to 3,5f$	$\gamma\gamma \to 2,4f$
Precuts	9816	17934	8654	4.9326×10^6	2.9901×10^7	1.78609×10^8
$\|\cos\theta_{soft}\| < 0.9397$	6176	4396	1452	439969	17954349	3118228
E_{soft} (E_{case2}) < 5 GeV	4366	3627	1439	1683	191951	440570
$E_{miss} > 300$ GeV	4366	3625	1264	513	39740	158348
$\|\cos\theta_{miss}\| < 0.992$	4059	3382	1184	427	22400	89598
Semi-leptonic	3746	1260	70	199	6024	40810
$E_\pi^* < 3$ GeV	3540	1176	67	171	4602	33861
$\Phi_{acop} < 2$ or $\sqrt{s'} < 480$ GeV	3020	1009	64	149	4444	9134

Table 8.15.: Cut-flow table for the preselection at $\sqrt{s} = 500\,\text{GeV}$ and $\int \mathcal{L}dt = 500\,\text{fb}^{-1}$ with $P(e^+, e^-) = (+30\%, -80\%)$ for the dM1600 scenario with E_{case2}.

Selection cuts	dM1600			Standard Model		
	$\tilde{\chi}_1^+\tilde{\chi}_1^-\gamma$ SL	$\tilde{\chi}_1^+\tilde{\chi}_1^-\gamma$ others	$\tilde{\chi}_1^0\tilde{\chi}_1^0\gamma$	$e^+e^- \to 2,4,6f$	$e\gamma \to 3,5f$	$\gamma\gamma \to 2,4f$
Precuts	9816	17934	8654	4.9326×10^6	2.9901×10^7	1.78609×10^8
$\|\cos\theta_{soft}\| < 0.9397$	6176	4396	1452	439969	17954349	3118228
E_{soft} (E_{case3}) < 5 GeV	4827	3779	1280	644	224468	536361
$E_{miss} > 300$ GeV	4827	3779	1280	540	44542	202583
$\|\cos\theta_{miss}\| < 0.992$	4487	3520	1198	438	24945	120577
Semi-leptonic	4247	1419	83	169	8086	70438
$E_\pi^* < 3$ GeV	3888	1290	78	160	6329	54150
$\Phi_{acop} < 2$ or $\sqrt{s'} < 480$ GeV	3305	1093	74	150	5793	12419

Table 8.16.: Cut-flow table for the preselection at $\sqrt{s} = 500\,\text{GeV}$ and $\int \mathcal{L}dt = 500\,\text{fb}^{-1}$ with $P(e^+, e^-) = (+30\%, -80\%)$ for the dM1600 scenario with E_{case3}.

8.4. Cut-Flow tables for Post-algorithm selection cuts

The number of events that survive after each cut for signal and the Standard Model background processes are determined. With the selection of E_{case2} as the choice for energy cut, the comparison between the *HS-analysis* and this analysis presented ahead is conducted with the results obtained using energy cut in E_{case2}.

Cut-flow analysis for the dM1600 scenario

The cut-flow analysis for the dM1600 scenario is made using the values from table 8.15 comparing it with values in table 8.17 for the *HS-analysis*.

For the dM1600 scenario, the polar angle cut introduced in section 8.3.1 vetoes 91% of $e^+e^- \to 2f, 4f, 6f$ events, 40% of $e^\pm\gamma \to 3f, 5f$ and 98% of $\gamma\gamma \to 2f, 4f$ events. It reduces about 75% of the chargino non-semileptonic events which along with a track from $\gamma\gamma \to$ low p_T hadron events mimic the semi-leptonic events. The large suppression of non-semileptonic events is due to the low transverse momentum of the $\gamma\gamma \to$ low p_T hadron tracks. The cut however impacts the semi-leptonic chargino events by suppressing 37% of it. In the *HS-analysis* this cut rejects 77% of $e^+e^- \to 2f, 4f, 6f$ events, 69% of $e^\pm\gamma \to 3f, 5f$ and 73% of $\gamma\gamma \to 2f, 4f$ events while removing 28% of the total signal events.

The energy cut for the current analysis is modified from the *HS-analysis* as described in section 8.3.1. Due to the presence of $\gamma\gamma \to$ low p_T hadron events, this cut impacts the signal events much more severely whereas the impact on the signal events in the *HS-analysis* is very small. However, it also suppresses the Standard Model background impressively. This cut suppresses 99.6% of $e^+e^- \to 2f, 4f, 6f$ events, 99% of $e^\pm\gamma \to 3f, 5f$ and 86% of $\gamma\gamma \to 2f, 4f$ events while rejecting 29% of the semi-leptonic chargino events. In the absence of $\gamma\gamma \to$ low p_T hadron events, the energy cut in the *HS-analysis* suppresses 99% of $e^+e^- \to 2f, 4f, 6f$ events, 87% of $e^\pm\gamma \to 3f, 5f$ and 74% of $\gamma\gamma \to 2f, 4f$ events while only affecting 4% of the chargino events.

Another important cut which is impacted due to the presence of $\gamma\gamma \to$ low p_T hadron events is the selection of events with semi-leptonic decay. This selection is explained in detail in section 8.2. Even though the semi-leptonic selection of events is more targeted towards eliminating the SUSY background, it could also remove the Standard Model background in the *HS-analysis* very effectively. The cut successfully vetoed 99% of $e^+e^- \to 2f, 4f, 6f$ processes, 95% of $e^\pm\gamma \to 3f, 5f$, 96% of $\gamma\gamma \to 2f, 4f$ events and 98% of the SUSY background in the *HS-analysis*. However, in the current analysis, semi-leptonic selection is not as effective in reducing the Standard Model background as in the *HS-analysis* even though it could remove

Selection cuts	dM1600		Standard Model		
	$\tilde{\chi}_1^+\tilde{\chi}_1^-\gamma$	$\tilde{\chi}_1^0\tilde{\chi}_1^0\gamma$	$e^+e^- \to 2,4,6f$	$e\gamma \to 3,5f$	$\gamma\gamma \to 2,4f$
Precuts	30058	9551	3.1640×10^6	1.5074×10^7	1.7752×10^7
$\lvert\cos\theta_{soft}\rvert < 0.9397$	21501	7318	7.1453×10^5	4.5646×10^6	4.7083×10^6
$E_{soft} < 5$ GeV	20611	6615	9092	5.9732×10^5	1.2390×10^6
$E_{miss} > 300$ GeV	20611	6615	6462	1.5822×10^5	4.6306×10^5
$\lvert\cos\theta_{miss}\rvert < 0.992$	19872	6365	5731	1.1837×10^5	3.3051×10^5
Semi-leptonic	5509	134	38	6197	13991
$E_\pi^* < 3$ GeV	4435	103	0	2635	6162
$\Phi_{acop} < 2$ or $\sqrt{s'} < 480$ GeV	3813	97	0	2564	1452

Table 8.17.: Cut-flow table for preselection in the *HS-analysis* at $\sqrt{s} = 500\,\text{GeV}$ and $\int \mathcal{L}dt = 500,\text{fb}^{-1}$ with $P(e^+,e^-) = (+30\%, -80\%)$ for the dM1600 scenario.

the neutralino events efficiently. The cut suppresses 53% of $e^+e^- \to 2f,4f,6f$ processes, 73% of $e^\pm\gamma \to 3f,5f$, 54% of $\gamma\gamma \to 2f,4f$ events and 94% of the SUSY background. As explained in section 8.2, this effect is due to the presence of $\gamma\gamma \to$ low p_T hadron tracks which along with the tracks in the process emulate the semi-leptonic events.

The selection procedure adapted from the *HS-analysis* leaves the current analysis with 3.5 times more Standard Model backgrounds and same level of signal events as compared to the *HS-analysis* . The presence of $\gamma\gamma \to$ low p_T hadron overlay results in worse signal to background ratio as compared to the *HS-analysis*.

Cut-flow analysis for the dM770 scenario

The cut-flow analysis for the dM770 scenario is made using the values from table 8.18 comparing it with values in table 8.19 for the *HS-analysis*. The polar angle cut in the dM770 scenario affects the signal more severely than in the dM1600 case due to lower transverse momentum of the decay tracks. In the dM770 scenario, the polar angle cut eliminates 84% of $e^+e^- \to 2f,4f,6f$ processes, 89% of $e^\pm\gamma \to 3f,5f$ and 90% of $\gamma\gamma \to 2f,4f$ events and removes 44% of the signal events. In this case 73% of the non-semileptonic events which mimic the semi-leptonic final state events are vetoed due to tracks from $\gamma\gamma \to$ low p_T hadron events. In the *HS-analysis* the effect on the Standard Model background is exactly same as for the dM1600 scenario while affecting only 22% of the signal events.

Selection cuts	dM770			Standard Model		
	$\tilde{\chi}_1^+\tilde{\chi}_1^-\gamma$ SL	$\tilde{\chi}_1^+\tilde{\chi}_1^-\gamma$ others	$\tilde{\chi}_1^0\tilde{\chi}_1^0\gamma$	$e^+e^- \to 2,4,6f$	$e\gamma \to 3,5f$	$\gamma\gamma \to 2,4f$
Precuts	8589	18539	8483	5.19609×10^6	3.01661×10^7	1.79849×10^8
$\lvert\cos\theta_{soft}\rvert < 0.9397$	4801	4957	1603	829576	3.44687×10^6	1.73844×10^7
$E_{soft} < 5$ GeV	3670	4063	1489	6271	217427	485589
$E_{miss} > 300$ GeV	3664	4049	1413	1203	42973	167597
$\lvert\cos\theta_{miss}\rvert < 0.992$	3409	3783	1308	1001	25479	105333
Semi-leptonic	2950	1440	126	789	8281	52628
$E_\pi^* < 3$ GeV	2912	1408	118	715	6379	44453
$\Phi_{acop} < 2$ or $\sqrt{s'} < 480$ GeV	2417	1209	111	606	6070	11233

Table 8.18.: Cut-flow table for the preselection at $\sqrt{s} = 500\,\text{GeV}$ and $\int \mathcal{L}dt = 500\,\text{fb}^{-1}$ with $P(e^+, e^-) = (+30\%, -80\%)$ for the dM770 scenario.

Selection cuts	dM770		Standard Model		
	$\tilde{\chi}_1^+\tilde{\chi}_1^-\gamma$	$\tilde{\chi}_1^0\tilde{\chi}_1^0\gamma$	$e^+e^- \to 2,4,6f$	$e\gamma \to 3,5f$	$\gamma\gamma \to 2,4f$
Precuts	29675	9317	3.1640×10^6	1.5074×10^7	1.7752×10^7
$\lvert\cos\theta_{soft}\rvert < 0.9397$	23117	7458	7.1453×10^5	4.5646×10^6	4.7083×10^6
$E_{soft} < 5$ GeV	22156	7110	9092	5.9732×10^5	1.2390×10^6
$E_{miss} > 300$ GeV	22156	7110	6462	1.5822×10^5	4.6306×10^5
$\lvert\cos\theta_{miss}\rvert < 0.992$	21558	6365	5731	1.1837×10^5	3.3051×10^5
Semi-leptonic	5489	38	19	2478	6754
$E_\pi^* < 3$ GeV	5489	38	0	1465	4755
$\Phi_{acop} < 2$ or $\sqrt{s'} < 480$ GeV	4600	36	0	1417	782

Table 8.19.: Cut-flow table for preselection in the *HS-analysis* at $\sqrt{s} = 500\,\text{GeV}$ and $\int \mathcal{L}dt = 500\,\text{fb}^{-1}$ with $P(e^+, e^-) = (+30\%, -80\%)$ for the dM770 scenario.

The energy cut suppresses 99% of $e^+e^- \to 2f, 4f, 6f$ processes, 94% of $e^\pm\gamma \to 3f, 5f$ and 97% of $\gamma\gamma \to 2f, 4f$ events along with 24% of the semi-leptonic chargino events. This cut has exact same impact on the Standard Model backgrounds and the signal events for the *HS-analysis* as in the dM1600 scenario.

Also similar to the dM1600 scenario, the semi-leptonic selection cut is less efficient to remove the Standard Model background for this analysis as compared to the *HS-analysis*. In *HS-analysis*, the semi-leptonic final state selection removes 99.6% of $e^+e^- \to 2f, 4f, 6f$ processes, 98% of $e^\pm\gamma \to 3f, 5f$ and 98% of $\gamma\gamma \to 2f, 4f$ events. In the current analysis these values vary as 21% of $e^+e^- \to 2f, 4f, 6f$ processes, 67% of $e^\pm\gamma \to 3f, 5f$ and 50% of $\gamma\gamma \to 2f, 4f$ events. However, this cut could eliminate 90% of the neutralino events.

Similar to the dM1600 scenario, the presence of $\gamma\gamma \to$ low p_T hadron overlay make the results in current analysis adverse. After the selection procedure applied there is approximately 79% signal events with respect to the *HS-analysis* and eight times more Standard Model background. The results in the dM770 scenario is worse as compared to the dM1600 scenario. The smaller mass gap between the $\tilde{\chi}_1^\pm$ and the LSP results in softer decay tracks in the dM770 scenario. Due to this, the signal suffer a big loss of events (44%) which in the dM1600 scenario was only 28%. Also as explained in section 8.2.1, the selection of semi-leptonic candidates based on the high d_0 value is a good strategy against the $\gamma\gamma \to$ low p_T hadron overlay but results in high number of τ-events due to their long life-times. As a combined effect of the signal suffering from the $\cos\theta$ cut and higher Standard Model background events passing the semi-leptonic selection criteria results in worse signal to background ratio as compared to both the *HS-analysis* and the dM1600 scenario.

8.5. Extra Cuts

The pre-conditions and targeted cuts to eliminate τ-lepton events as mentioned in the sections above suppressed the Standard Model background in *HS-analysis* very efficiently. However, due to the change in the dynamics of the event properties due to the presence of $\gamma\gamma \to$ low p_T hadron overlay, the above mentioned conditions are not sufficient to suppress the Standard Model background. Therefore, some extra stipulations which are more targeted towards the τ-lepton events are needed to eliminate the remaining backgrounds as mentioned in sections ahead.

8.5.1. Strict ISR Cut

The initial state radiation photon is the photon radiated from either of the beam particle before they annihilate to give the final state particles as can be seen in the Feynman diagram shown in figure 8.22a. As mentioned in section 8.1, the ISR photon candidate is required to be within the tracking performance of ILD with $|\cos\theta_{ISR}| < 0.9397$ corresponding to 7° and an energy $E_{ISR} > 10$ GeV. Any photon that fulfills these conditions qualify as an ISR photon candidate. However, as can be seen in the Feynman diagram for $e^+e^- \to \tau\tau$ events in figure 8.22b, the hadronically

decaying τ-lepton decays into a charged and a neutral pion which finally decays to photons. In the absence of a real ISR photon, if a photon originating from the π^0 fulfills all the required conditions for an ISR photon, the event survives the ISR photon cut even without the presence of a real ISR photon.

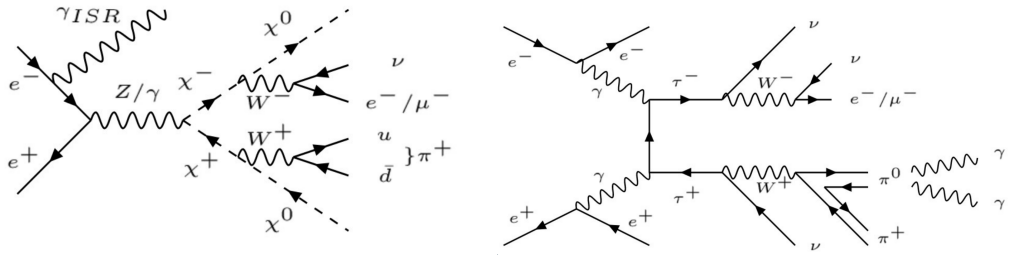

Figure 8.22.: Feynman diagrams showing $e^+e^- \to \tilde{\chi}_1^+\tilde{\chi}_1^-$ and $e^+e^- \to \tau\tau$ events. (Picture courtesy: Ulrich Einhaus).

To identify and eliminate such events a few more variables are introduced in this analysis. If the selected photon candidate is a decay particle of the π^0 from a τ-lepton, the photon would be expected to be closer to charged decay particle of the τ-lepton ($\pi^\pm$) as can be seen in figure 8.22b. Similarly, the invariant mass ($M_{\gamma\pi}$) of the photon and the $\pi^\pm$ is expected to be less than M_τ =1.7 GeV if they are the decay produts of the τ-lepton. A 2-D plot showing the angle (Φ) between the selected ISR photon candidate and the closest charged track on x-axis and their invariant mass on the y-axis is given in figure 8.23.

Any events having $M_{\gamma\pi}$ and Φ below the red lines as shown in the lower region of the plot using linear functions $y = 2x + 2$ and $y = -3x + 3$ are eliminated assuming to be the τ - events whose $M_{\gamma\pi}$ is closer to 1.7 GeV. Also since smaller number of chargino events (115 - dM770 and 418 dM1600) are expected to have $M_{\gamma\pi}$ above 18-19 GeV another cut is applied in this upper region. All the events having $M_{\gamma\pi}$ and Φ values above the line with function $y = -1.61x + 19$) are removed. Finally, since there are more $\gamma\gamma \to 2f$ and $e\gamma \to 3f$ events ($\sim$ 1200) and only $\sim$ 400 chargino events with $\Phi > 2.6$ radian, it is required that the acoplanarity between the photon candidate and the pion should not be greater than 2.6 radian. Even though this difference is not very obvious in the plot, it has to be noted that the scale for the number of entries for the chargino events and τ events are different. The strict ISR photon requirement narrows down the events from $\gamma\gamma \to$ 2f and $e\gamma \to$ 3f processes significantly. More quantitative analysis on the cut is given in section 8.5.3.

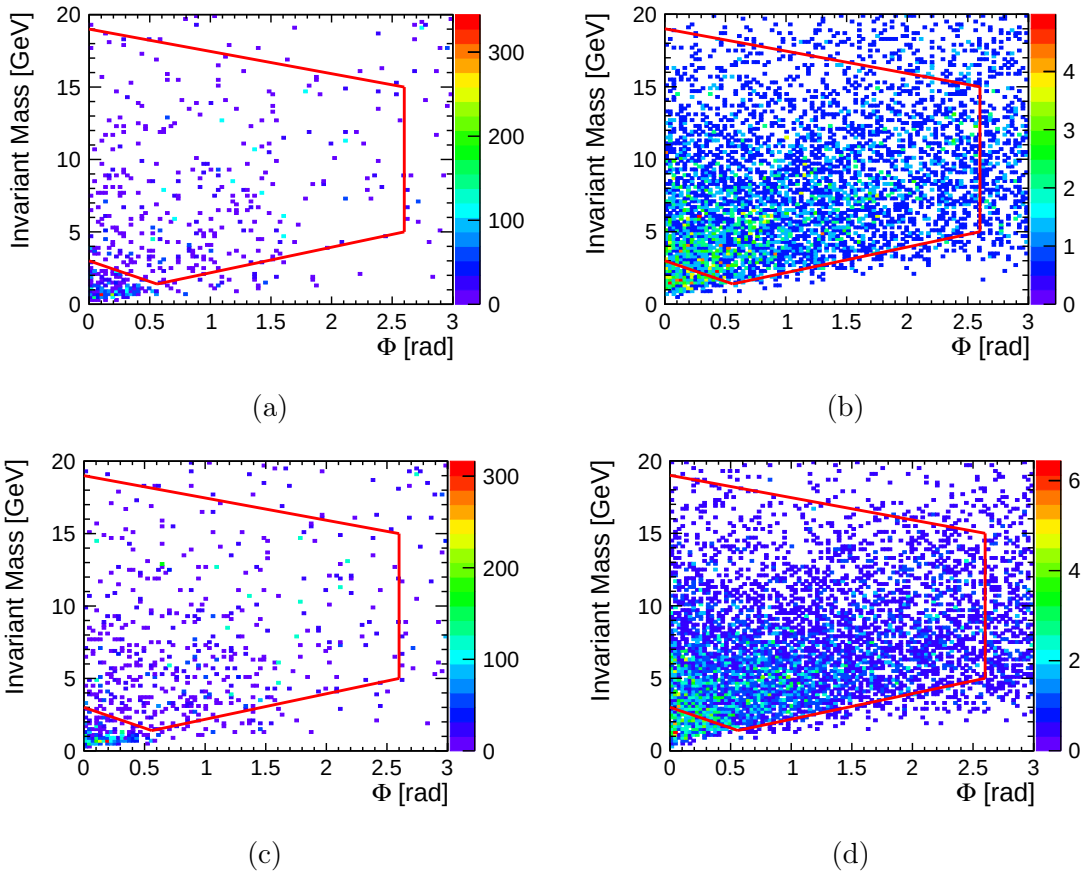

Figure 8.23.: A 2D histogram showing the angle between the selected ISR photon candidate and the nearest track and their invariant mass after the acoplanarity cut at $\sqrt{s} = 500\,\text{GeV}$ and $\int \mathcal{L}dt = 500\,\text{fb}^{-1}$ with $P(e^+, e^-)$ = (+30%, −80%). (a) τ-events from $\gamma\gamma \to 2f$ and $e\gamma \to 3f$ processes for the dM1600 scenario, (b) Chargino events for the dM1600 scenario (c) τ-events from $\gamma\gamma \to 2f$ and $e\gamma \to 3f$ processes for the dM770 scenario and (d) Chargino events for the dM7700 scenario.

8.5.2. Number of leptons

Leptons from the di-leptonic events imitating the semi-leptonic decay channel along with a pion from the $\gamma\gamma \to$ low p_T hadron overlay is discussed in section 8.2. The groups having extra leptons are excluded during semi-leptonic selection. However, it is possible that the event would survive this cut if both the leptons are not found in the same group. Therefore, as the final condition it is required that there are no events which have two oppositely charged leptons in them. A plot showing

number of oppositely charged leptons with respect to the selected lepton candidate for $\gamma\gamma$ →2f sub-processes and chargino events is shown in figure 8.24. If any event has an oppositely charged lepton with respect to the selected lepton candidate, then the event is vetoed.

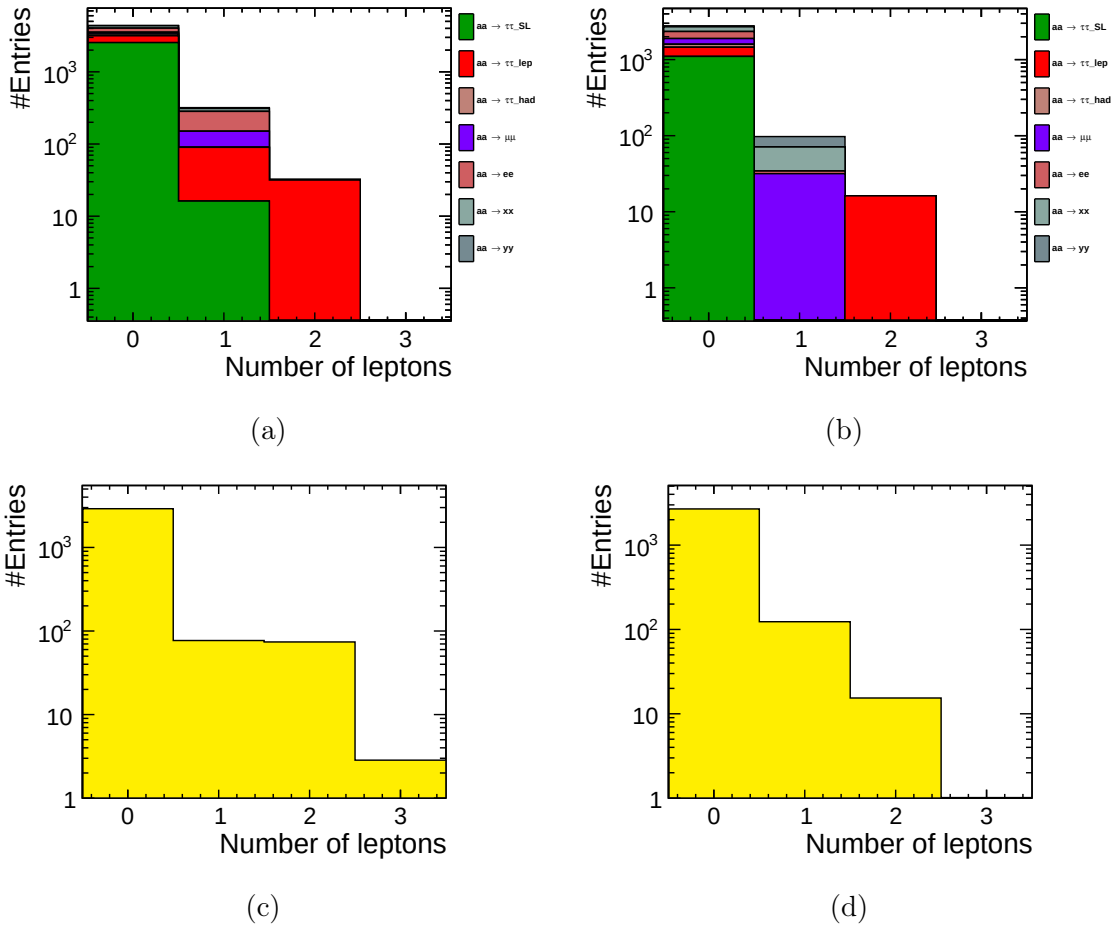

Figure 8.24.: Number of oppositely charged leptons as compared to the semi-leptonic candidate for different sub-processes of $\gamma\gamma$ →2f process and chargino events. (a) Number of leptons in $\gamma\gamma$ →2f for the dM1600 scenario, (b) Number of leptons in $\gamma\gamma$ →2f for the dM770 scenario, (c) Number of leptons in chargino events for the dM1600 scenario (d) Number of leptons in chargino events for the dM770 scenario, for $\sqrt{s} = 500\,\text{GeV}$ and $\int \mathcal{L}dt = 500\,\text{fb}^{-1}$ with $P(e^+, e^-) = (+30\%, -80\%)$.

.

8.5.3. Cut-flow analysis for the extra cuts

Selection cuts	dM1600			Standard Model		
	$\tilde{\chi}_1^+\tilde{\chi}_1^-\gamma$ SL	$\tilde{\chi}_1^+\tilde{\chi}_1^-\gamma$ others	$\tilde{\chi}_1^0\tilde{\chi}_1^0\gamma$	$e^+e^- \to 2,4,6f$	$e\gamma \to 3,5f$	$\gamma\gamma \to 2,4f$
Precuts	3020	1009	64	149	4444	9134
Strict ISR cut	2242	763	50	93	2838	3152
Lepton cut	2147	704	42	62	2652	2924
Lumi-correction	2147	704	42	62	1711	1517

Table 8.20.: Cut-flow table for final selection of events using the extra cuts and luminosity correction factor $\sqrt{s} = 500\,\text{GeV}$ and $\int \mathcal{L}dt = 500\,\text{fb}^{-1}$ with $P(e^+, e^-) = (+30\%, -80\%)$ for the dM1600 scenario.

Selection cuts	dM770			Standard Model		
	$\tilde{\chi}_1^+\tilde{\chi}_1^-\gamma$ SL	$\tilde{\chi}_1^+\tilde{\chi}_1^-\gamma$ others	$\tilde{\chi}_1^0\tilde{\chi}_1^0\gamma$	$e^+e^- \to 2,4,6f$	$e\gamma \to 3,5f$	$\gamma\gamma \to 2,4f$
Precuts	2417	1209	111	606	6070	11233
Strict ISR cut	1895	963	84	341	3530	4415
Lepton cut	1826	888	78	241	3268	4145
Lumi-correction	1826	888	78	241	2978	2201

Table 8.21.: Cut-flow table for final selection of events using the extra cuts and luminosity correction factor $\sqrt{s} = 500\,\text{GeV}$ and $\int \mathcal{L}dt = 500\,\text{fb}^{-1}$ with $P(e^+, e^-) = (+30\%, -80\%)$ for the dM770 scenario.

Using the extra cuts as explained above, the final selection of events for the chargino mass reconstruction is achieved. The strict ISR photon cut is very efficient in reducing a significant amount of Standard Model background. In the dM1600 scenario, the strict ISR cut removes 36% and 65% of the stubborn $e\gamma \to 3,5f$ and $\gamma\gamma \to 2,4f$ processes respectively. It also removes 38% of the remaining $e^+e^- \to 2,4,6f$ events. However, it also affects the chargino events by eliminates 25% of the remaining events. In the dM770 scenario, the strict ISR cut suppresses 61% of the $\gamma\gamma \to 2,4f$ events, 42% of the $e\gamma \to 3,5f$ events and 44% of $e^+e^- \to 2,4,6f$ events. It removes 22% of the signal events.

The lepton cut does not make a very significant difference but is effective in removing 6-7% of the $e\gamma \to 3,5f$ and $\gamma\gamma \to 2,4f$ backgrounds while affecting 4% of the signal events in both the dM770 and the dM1600 scenario.

An important aspect to be considered is that the cross sections for $\gamma\gamma$ and $e\gamma$ events in `Whizard` are calculated using e^+e^- luminosities instead of the luminosities of the radiated photons. The luminosity weights as explained in section 4.9 correspond to the e^+e^- luminosity instead on $\gamma\gamma$ luminosity for processes with photons as initial colliding particles. This gives more number of $e\gamma \to 3,5f$ and $\gamma\gamma \to 2,4f$ events than what they should be. Therefore, a correction factor has to implemented to the luminosity weights which was not considered in the *HS-analysis*. The luminosity is different for real photons since virtual photons imply that the initial colliding particles are e^+ or e^-. The correction factors based on the nature of initial colliding particle is given in table 8.22.

Process	Weight correction (c)
$\gamma\gamma$	0.583
$e\gamma$	0.676
γe	0.67
e^+e^-	1

Table 8.22.: Luminosity correction factors to the events based on if the initial colliding particle is a real photon or e^+/e^-.

Based on if the initial colliding particle is a real or virtual photon, the respective correction factor mentioned in table 8.22 is applied on the process. The final selection of events after the correction factors applied is given in the last row of table 8.20 and table 8.21.

8.6. Results

The events that survived all the cuts are finally used to reconstruct the chargino mass as will be discussed ahead. The separated semi-leptonic chargino events and the events survived from other chargino decay modes are added together as signal for mass reconstruction since their presence as signal or SUSY background would not make any difference in the shape of the signal curve. A comparison of signal to background ratios for this analysis and the *HS-analysis* is performed. Also, the uncertainities on the polarised cross sections are calculated and presented in sections ahead.

8.6.1. Chargino Mass Reconstruction

The reduced centre-of-mass energy is defined in section 8.3.3 as $s' = s - 2\sqrt{s}E_\gamma$. The recoil mass against the ISR photon can be presented as:

$$M_{recoil} = \sqrt{s - 2E_\gamma\sqrt{s}} = \sqrt{s'}. \tag{8.3}$$

When both the charginos are produced at rest, the reduced centre-of-mass energy is minimum. The mass of both the charginos produced being the same, Eq. 8.3 can be given as

$$\sqrt{s'|_{thresh}} = 2M_{\tilde{\chi}_1^\pm} \tag{8.4}$$

where $\sqrt{s'|_{thresh}}$ is the minimum value of the reduced centre-of-mass energy at threshold. Therefore,

$$M_{\tilde{\chi}_1^\pm} = \frac{1}{2}\sqrt{s'|_{thresh}} = \frac{1}{2}\sqrt{s - 2\sqrt{s}E_\gamma|_{thresh}}. \tag{8.5}$$

Since the impact of the crossing angle on the four-momentum was not considered in the *HS-analysis*, it is not included in this analysis either to maintain consistency. However, this would not affect the uncertainty values even though small bias for the central value is not unexpected. Using Eq. 8.5, the mass of the charginos can be determined. Figure 8.25 shows the distribution of the reduced centre-of-mass energy for all the events that passed the chargino selection cuts at $\sqrt{s} = 500\,\text{GeV}$ and $\int \mathcal{L}dt = 500\,\text{fb}^{-1}$ with $P(e^+, e^-) = (+30\%, -80\%)$ for both the benchmark scenarios. The Standard Model Background is shown in red, the SUSY background is given in green and the signal is represented in yellow.

The reduced centre-of-mass energy distribution in the *HS-analysis* is given in figure 8.26. As presented in table 8.15 and table 8.17, the number of signal events in the *HS-analysis* is 44% larger than in this analysis. The signal in figure 8.26 is more prominent than in figure 8.25. The shape of the recoil mass distribution for background is quite different now from the *HS-analysis*: While the low recoil mass region is less populated due to harsher cuts, no cuts could be found so far to reduce the background in the high recoil mass region to the level achieved in the *HS-analysis*.

A comparison between the number of signal events in this analysis and the *HS-analysis* for both the benchmark scenarios is given in figure 8.27 where S_S is the number of signal events in this analysis while S_H is the signal in the *HS-analysis*. A similar plot for the ratio between the number of Standard Model background events in the current analysis and the *HS-analysis* is given in figure 8.28 where B_S refers to background in this analysis while B_H is the amount of background in the *HS-analysis*. In the region near the endpoint, which is decisive for the mass

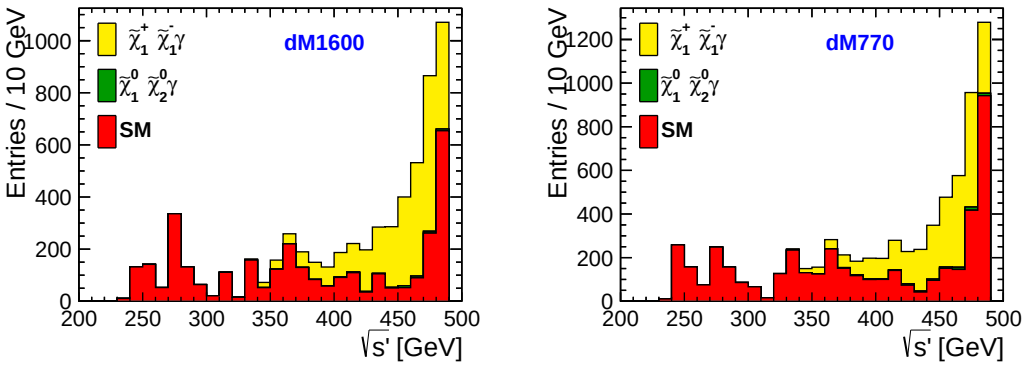

(a) (b)

Figure 8.25.: Distribution of the reduced centre-of-mass energy of the system recoiling against the hard ISR photon for all events passing through the chargino selection cuts at $\sqrt{s} = 500\,\text{GeV}$ and $\int \mathcal{L}dt = 500\,\text{fb}^{-1}$ with $P(e^+, e^-) = (+30\%, -80\%)$ for dM1600 and dM770 respectively.

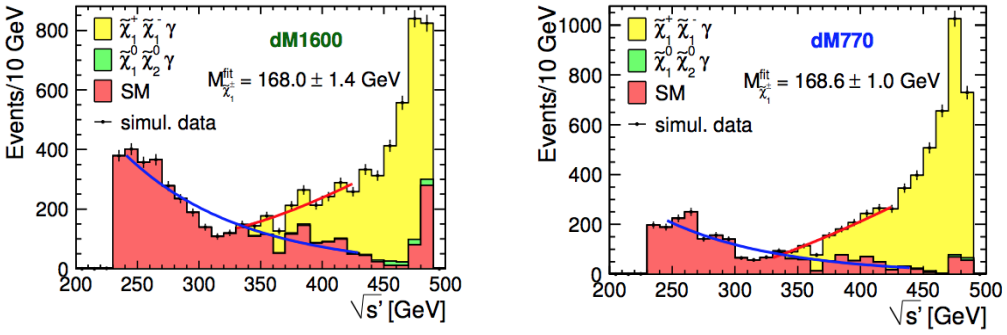

(a) (b)

Figure 8.26.: Distribution of the reduced centre-of-mass energy of the system recoiling against the hard ISR photon for all events passing through the chargino selection cuts at $\sqrt{s} = 500\,\text{GeV}$ and $\int \mathcal{L}dt = 500\,\text{fb}^{-1}$ with $P(e^+, e^-) = (+30\%, -80\%)$ for dM1600 and dM770 respectively in the *HS-analysis* [6].

reconstruction, the error bars are huge due to lack of enough statistics. Therefore, taking the average value of S_S/S_H of the first few bins in the endpoint region it could be estimated that the signal in this analysis is $\sim 40\%$ worse for dM1600 scenario

and $\sim$ 37% worse for the dM770 scenario. In the case of background ratios, the average values of nearby bins in the endpoint region gives $\sim$ 30% less background for the dM1600 scenario and approximately two times more background in the dM770 scenario.

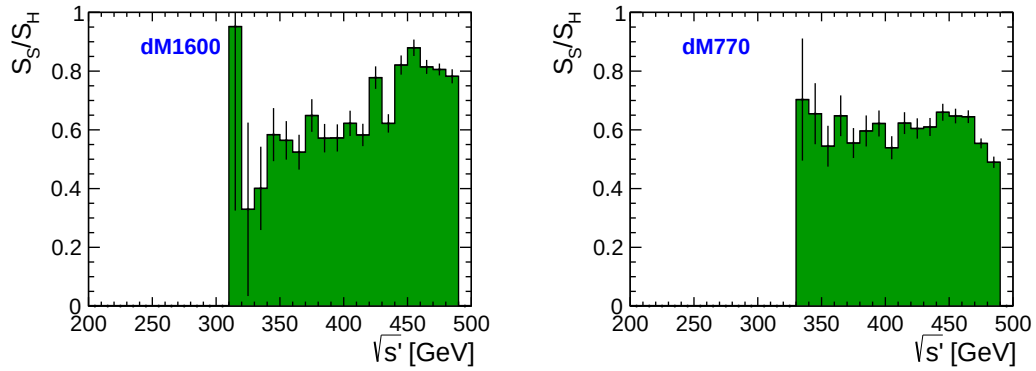

(a) (b)

Figure 8.27.: The bin-by-bin ratio of number of signal events in this analysis to number of signal events in the *HS-analysis* at $\sqrt{s} = 500\,\text{GeV}$ and $\int \mathcal{L}dt = 500\,\text{fb}^{-1}$ with $P(e^+, e^-) = (+30\%, -80\%)$ for dM1600 and dM770, respectively.

For chargino mass extraction, a fit is performed on histograms in figure 8.25 similar to figure 8.26 in the *HS-analysis*. With a loose cut on $E_{\text{miss}} > 300\,\text{GeV}$, a signal independent Standard Model region is obtained at lower $\sqrt{s'}$. The level of the Standard Model background is fixed by fitting an exponential function with two free parameters, $f_{SM}(x) = p_1 \cdot e^{-p_2 \cdot x}$. As mentioned in section 4.9, luminosity weights are assigned to all the samples so that the statistics corresponds to an integrated luminosity of $\int \mathcal{L}dt = 500\ \text{fb}^{-1}$. Therefore the errors on each bin is calculated as:

$$\Delta N_w = \sqrt{\Sigma_i w_i^2} \tag{8.6}$$

where, ΔN_w is the error on the bin and w_i is the weight on a certain process.

Different trials of fits on the Standard Model background in different $\sqrt{s'}$ ranges are shown in figure B.1 of appendix B. The range on which the function can be fitted for minimum χ^2/ndf is chosen for the the Standard Model background which is shown in figure 8.29.

A linear function is added on top of the exponential Standard Model fit function to model the signal contribution. The Standard Model background is expected to be separated by fixing its level using a fit function such that the linear function added

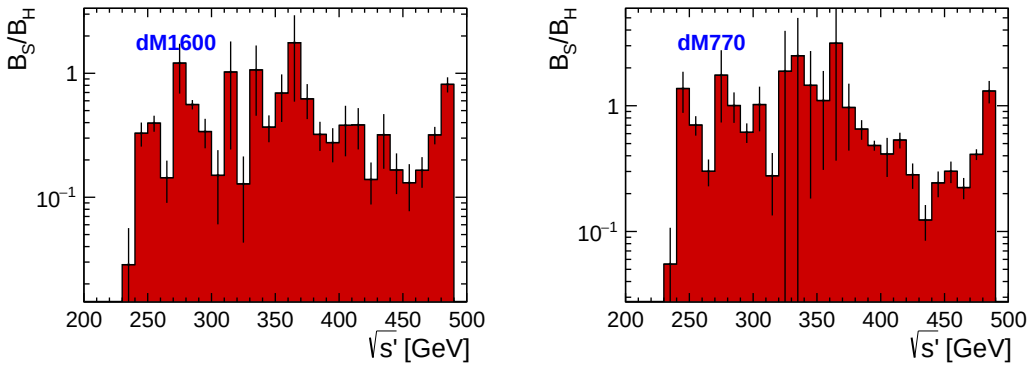

(a) (b)

Figure 8.28.: The bin-by-bin ratio of the number of signal events in the current analysis over the number of signal events in the *HS-analysis* at $\sqrt{s} = 500\,\text{GeV}$ and $\int \mathcal{L}dt = 500\,\text{fb}^{-1}$ with $P(e^+, e^-) = (+30\%, -80\%)$ for dM1600 and dM770, respectively.

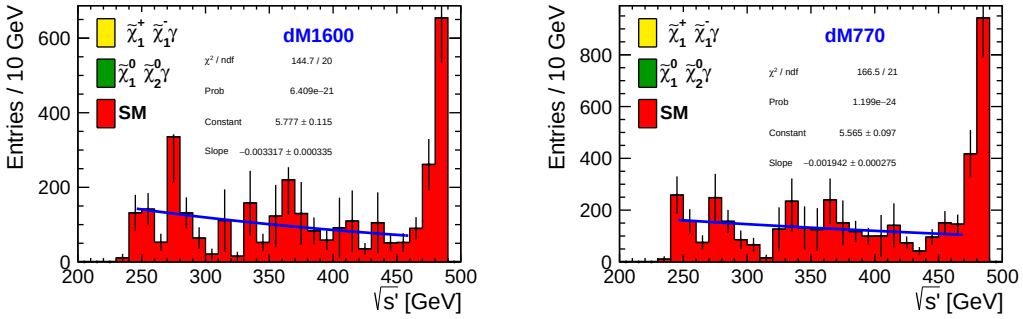

(a) (b)

Figure 8.29.: Fitting the Standard Model background for minimum χ^2/ndf value at $\sqrt{s} = 500\,\text{GeV}$ and $\int \mathcal{L}dt = 500,\text{fb}^{-1}$ with $P(e^+, e^-) = (+30\%, -80\%)$ for dM1600 and dM770, respectively.

on the top would have zero y-intercept. The new function to fit the entire data is defined as $f_{data}(x) = p_1 + p_2 \cdot x + p_3 \cdot e^{-p_4 \cdot x}$. The Standard Model free parameters p_3 and p_4 are fixed with the values obtained from the fit performed on the Standard Model only histogram. While fitting a function on the histograms, errors calculated using Eq. 8.6 are used to obtain minimum χ^2/ndf value. Several trials for different $\sqrt{s'}$ ranges are performed as shown in figure B.2 in appendix B. Once the $\sqrt{s'}$ ranges

for the reasonable χ^2/ndf values are obtained, the errors on each bin are replaced with $\sqrt{N}$, where N is the number of entries in each bin. This is because in real data scenario, the statistics corresponds to the given luminosity and no weights need to be assigned to the events in a process. Therefore the errors on each bin would correspond to $\sqrt{N}$ in each bin. The combined fit function is then applied in the ranges where the χ^2/ndf was found to be minimum using ΔN_w in green line. The final histograms with the combined fit applied for both the benchmark scenarios are shown in figure 8.30.

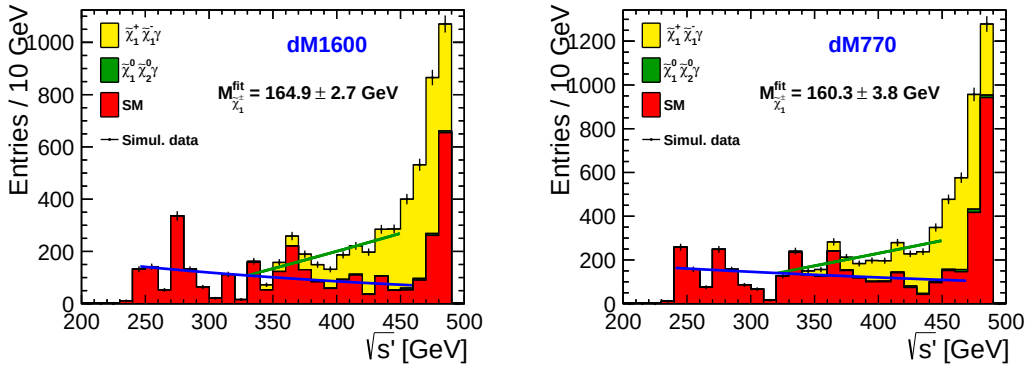

(a) (b)

Figure 8.30.: The reduced centre-of-mass energy ($\sqrt{s'}$) of the system recoiling against the hard ISR photon for events passing the chargino selection cuts at $\sqrt{s} = 500\,\text{GeV}$ and $\int \mathcal{L}dt = 500\,\text{fb}^{-1}$ with $P(e^+, e^-) = (+30\%, -80\%)$ for dM1600 and dM770, respectively. $M_{\tilde{\chi}^\pm_1}$ is determined from the linear fit to the distribution near the endpoint.

The point where the Standard Model and the data fit intersects, is then the required $\sqrt{s'}|_{thresh}$ of the signal distribution and the mass of chargino is thus determined using Eq. 8.5. The chargino masses evaluated using the fit values at $\sqrt{s} = 500\,\text{GeV}$ and $\int \mathcal{L}dt = 500\,\text{fb}^{-1}$ with $P(e^+, e^-) = (+30\%, -80\%)$ are:

$$\text{dM1600 scenario :} \quad M_{\tilde{\chi}^\pm_1} = 164.9 \pm 2.7\,\text{GeV} \tag{8.7}$$

$$\text{dM770 scenario :} \quad M_{\tilde{\chi}^\pm_1} = 160.3 \pm 3.8\,\text{GeV} \tag{8.8}$$

The input values for the chargino masses are $M_{\tilde{\chi}^\pm_1} = 165.77\,\text{GeV}$ and $M_{\tilde{\chi}^\pm_1} = 167.36\,\text{GeV}$ in the dM1600 and the dM770 scenarios, respectively. The central values of the fitted chargino masses agree with the input values within 0.3 and 1.8 standard deviations. The fitted value of the chargino masses for the *HS-analysis* is

$M_{\tilde{\chi}_1^\pm} = 168.0 \pm 1.4\,\text{GeV}$ and $M_{\tilde{\chi}_1^\pm} = 168.6 \pm 1.0\,\text{GeV}$ for the dM1600 and the dM770 scenarios which agree with the central values within 1.6 and 1.2 standard deviations, respectively. For both the current analysis and the *HS-analysis*, the obtained chargino mass values are reasonable with the simulation input values. However, it is to be noted that the uncertainty on the fitted masses for this analysis is higher than that for the *HS-analysis*. The uncertainty in the current analysis is 1.9 times higher for the dM1600 case and 3.8 times higher for the dM770 scenario as compared to the *HS-analysis*. For the dM1600 scenario, it can be determined from $\sqrt{N_{S_H}/N_{S_S}}$ (N_{S_H}: number of signal events in the *HS-analysis*, N_{S_S}: number of signal events in current analysis) how worse the expected uncertainty on the obtained mass can be with respect to the *HS-analysis*. Using the number of signal events for the current analysis and the *HS-analysis* from table 8.17 and table 8.20,

$$\sqrt{N_{S_H}/N_{S_S}} = \sqrt{3813/2147} = 1.33. \tag{8.9}$$

This implies that, given the Standard Model background is same for the current analysis and the *HS-analysis* the expected uncertainty value on the obtained mass value would be $\sim 33\%$ worse. However, since the number of background events for the current analysis is smaller than that for the *HS-analysis*, the expected uncertainty on the obtained mass would be expected to be between $20 - 30\%$ worse than the *HS-analysis*. Nevertheless, the uncertainty on the mass obtained through the fits are higher than the expected values. The higher uncertainties can be attributed to the given reasons:

As mentioned earlier, due to the lack of required Monte-Carlo statistics, weights are assigned to each processes. Particularly for processes like $\gamma\gamma \to 2f$ and $e\gamma \to 3f$ with large cross sections, the available Monte-Carlo statistics is too low. Therefore large luminosity weights are assigned to these events to correspond to the number of events for $\mathcal{L}dt = 500\,\text{fb}^{-1}$. Consequently, large bin-to-bin fluctuations are observed for the Standard Model curve as shown in figure 8.25. These fluctuations were smeared out to the neighbouring bins in the *HS-analysis* thus making the Standard Model background curve smoother. However, such a smearing is not performed in the current analysis thus leaving the Standard Model curve highly fluctuating. Since the minimum χ^2/ndf values for the fit are obtained using the errors on the Monte-Carlo statistics, the large error bars due to lack of statistics also reflects on the obtained uncertainties on the reconstructed chargino masses in both the benchmark scenarios. However, such an effect would not be expected with higher Monte-Carlo statistics or even in the real experiment. Therefore, it can be understood that the larger uncertainty is only an artefact of the lack of Monte-Carlo statistics and the uncertainties on the chargino masses in this study would be smaller with appropriate amount of statistics.

8.6.2. Measurement of Polarised Chargino Cross Sections

The precision on the polarised cross sections can be estimated assuming that the background is known precisely using the equation [176]

$$\frac{\delta\sigma}{\sigma} = \frac{1}{\sqrt{\epsilon \cdot \pi \cdot \sigma \cdot \int \mathcal{L}dt}}. \tag{8.10}$$

where ϵ is the efficiency and π is the purity obtained from the events that pass the event selection cuts. The efficiency (ϵ) and purity (π) are defined as:

$$\epsilon = \frac{N_{\text{selected signal events}}}{N_{\text{generated signal events}}} \tag{8.11}$$

$$\pi = \frac{N_{\text{selected signal events}}}{N_{\text{selected signal events}} + N_{\text{selected background events}}}. \tag{8.12}$$

where $N_{\text{selected signal events}}$ include total number of selected chargino semi-leptonic events and $N_{\text{generated signal events}}$ has the total number of generated semi-leptonic events. $N_{\text{selected background events}}$ includes the sum of the SUSY and the SM background in which, SUSY events include neutralino and surviving chargino events from other decay modes.

A bin to bin $S/\sqrt{S+B}$ ratio for the current analysis and the *HS-analysis* is shown in figure 8.31. The estimated precision on the polarised cross sections are calculated for the events in the bins which has $S/\sqrt{S+B}$ values greater than zero.

The efficiency (ϵ), purity (π) and relative statistical precision on the visible cross sections are calculated without including the branching ratios as given in table 8.23. The table also shows the corresponding values for the *HS-analysis*. The achievable statistical uncertainities on the polarised cross sections in the *HS-analysis* as given in the last row of tabel 8.23 are 1.9% and 1.6% for dM1600 and dM770 scenarios respectively. In the current analysis, smaller number of signal events as compared to the *HS-analysis* as an effect of the $\gamma\gamma \rightarrow$ low p_T hadron overlay results in worse statistical uncertainities on the polarised cross section. The statistical uncertainities that can be achieved on the polarised cross sections with the presence of $\gamma\gamma \rightarrow$ low p_T hadron overlay at a $\sqrt{s} = 500\,\text{GeV}$ and $\int \mathcal{L}dt = 500\,\text{fb}^{-1}$ with $P(e^+, e^-)=$ (+30%, -80%) are 2.3 and 2.9 for the dM1600 and dM770 scenarios respectively. However, with a three times larger statistics at a higher luminosity of 1600 fb^{-1}, the uncertainities on the polarised cross sections can be reduced and measured more precisely. Similar to the chargino mass extraction, the uncertainty on the polarised cross section for the dM770 scenario is worse than the dM1600 scenario in this analysis while the uncertainty for the dM770 scenario is better than the dM1600 scenario in the *HS-analysis*.

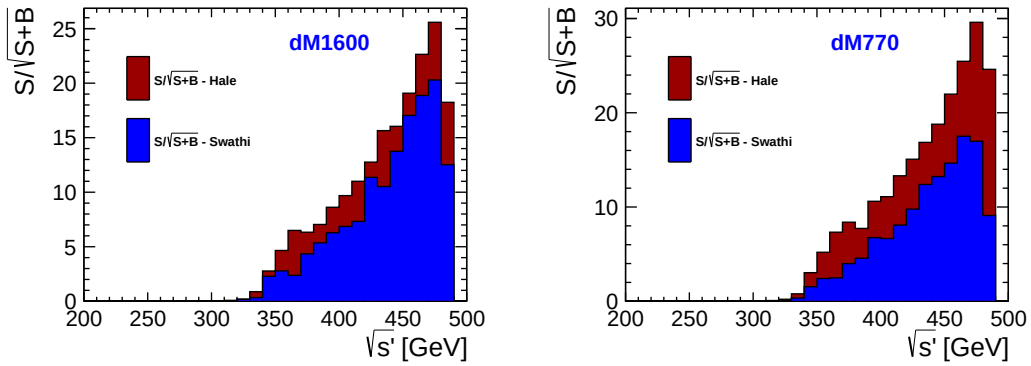

(a) (b)

Figure 8.31.: A distribution of bin to bin $S/\sqrt{S+B}$ ratio for the current analysis and the *HS-analysis* at $\sqrt{s} = 500$ GeV and $\int \mathcal{L}dt = 500$ fb^{-1} with $P(e^+, e^-) = (+30\%, -80\%)$ for dM1600 and dM770 respectively.

	Current Analysis		*HS-analysis*	
	dM1600	dM770	dM1600	dM770
$\int \mathcal{L}dt$	500 fb^{-1}	500 fb^{-1}	500 fb^{-1}	500 fb^{-1}
σ	78.7 fb	77.0 fb	78.7 fb	77.0 fb
BR of selected mode(s)	30.5	34.7	30.5	34.7
efficiency ϵ	13%	13.7%	9.9%	12.1%
purity π	35%	22%	70.1%	85.3%
$\delta\sigma/\sigma$	2.3%	2.9 %	1.9%	1.6%

Table 8.23.: A comparison of efficiency, purity and relative statistical precision on the visible cross section for charginos for the current analysis and the *HS-analysis* with $P(e^+, e^-) = (+30\%, -80\%)$ for dM1600 and dM770 without branching ratio.

8.6.3. Reconstruction of Chargino-LSP Mass difference

Being nearly mass degenerate, the mass difference between the chargino and the LSP is very small. However, the chargino-LSP mass difference can be obtained from the energy of the chargino decay products boosted into the chargino rest frame as introduced in Eq. 8.1.

Figure 8.32 shows the reconstruction of chargino-LSP mass difference using the

boosted energy of the chargino decay products in the *HS-analysis*.

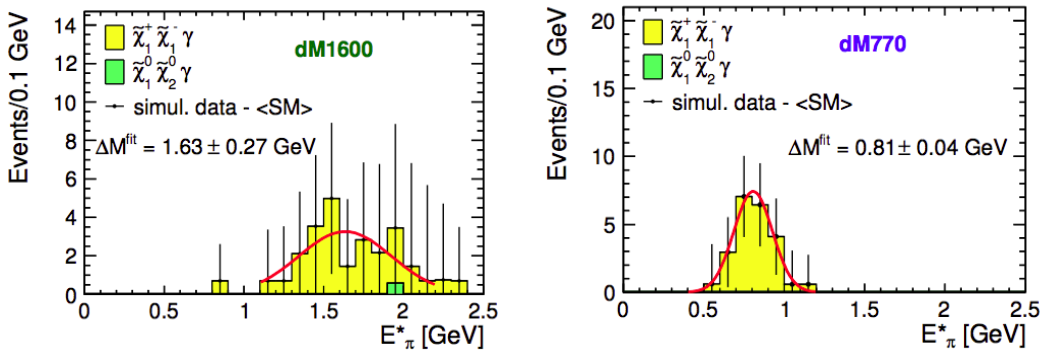

(a) (b)

Figure 8.32.: The chargino-LSP mass difference reconstructed using the E_{π^*} in the *HS-analysis* at $\sqrt{s} = 500\,\text{GeV}$ and $\int \mathcal{L}dt = 500\,\text{fb}^{-1}$ with $P(e^+, e^-) =$ (+30%, -80%) for dM1600 and dM770 respectively.

However, as explained in section 8.3.3, the chargino decays to a charged and a neutral pion 28% of the times in the dM1600 scenario. To obtain the chargino-LSP mass difference, the energy of all the decay particles boosted into the chargino rest frame has to be considered. The selection of the charged semi-leptonic pion candidate from among the chargino and $\gamma\gamma \rightarrow$ low p_T hadron tracks was performed using the groups obtained from the track grouping algorithm. However, no method has been developed to select neutral decay particles ($\pi^0 \rightarrow \gamma\gamma$) from the pool of photons coming from the chargino and the $\gamma\gamma \rightarrow$ low p_T hadron decays. Therefore, the reconstruction of chargino-LSP mass difference using the boosted energy of the chargino decay products in the chargino rest frame would not be possible unless a method to select photon candidates for the chargino decay is developed.

In the dM770 scenario, only the decay channel with single charged pion is considered and hence the issue of selecting the appropriate neutral pion decay does not arise in this case. However, as can be seen in table 8.21, the number of chargino events left after application of selection cuts is only 59% of the events in the *HS-analysis*. The lack of sufficient statistics would result in large uncertainties. At a higher luminosity of $\int \mathcal{L}dt = 1600\,\text{fb}^{-1}$, ~ 3 times more data can be achieved using which more precise values can be obtained for chargino-LSP mass difference.

9. Conclusions

The discovery of the Higgs boson particle in 2012 was a milestone in the history of particle physics. However, along with its discovery arose the questions about its mass of the order of the weak scale inspite of the quadratic divergences caused by the large loop corrections. One of the proposed theories to explain the mass of Higgs boson by cancelling the quadratic divergences is Supersymmetry. To avoid the regeneration of any divergences on the Higgs mass or the Z boson, it is required that the scalar tops and the gluinos are in the TeV scales and the higgsinos have their masses in the electroweak scale. If SUSY particles exist with masses accessible at a centre-of-mass energy of 500 GeV, then an e^+e^- collider like the International Linear Collider could measure the masses and cross sections of these particles with high precision. Such a study was performed in [6] which considered three light higgsino-like charginos and neutralinos, $\tilde{\chi}_1^\pm$, $\tilde{\chi}_1^0$ and $\tilde{\chi}_2^0$ with mass splittings of a few GeV.

The International Linear Collider being an e^+e^- collider provides a very clean physics environment to observe such scenarios. However, the processes like $\gamma\gamma \rightarrow$ low p_T hadron overlay as a result of collisions of real and virtual photons radiated off the e^+e^- beams occur at the rates depending on the centre-of-mass energy (250 GeV - 1 TeV). The study performed in [6] was done without the inclusion of $\gamma\gamma \rightarrow$ low p_T hadron overlay. In this thesis, the effect of $\gamma\gamma \rightarrow$ low p_T hadron overlay on the higgsino analysis is studied and compared with the study in [6].

To develop an effective method to remove $\gamma\gamma \rightarrow$ low p_T hadron overlay it was important to study this process in detail. In the first part of this thesis, the Monte-Carlo generators that produce $\gamma\gamma \rightarrow$ low p_T hadron overlay e.g. `Pythia` and the Barklow generator were studied and significantly improved to provide more realistic $\gamma\gamma \rightarrow$ low p_T hadron events.

The second part of the thesis is dedicated to develop a differential method to separate $\gamma\gamma \rightarrow$ low p_T hadron overlay from the higgsino decay tracks. The potential of the ILC to find light higgsinos is studied in two benchmark scenarios based on the mass difference between $\tilde{\chi}_1^\pm$ and $\tilde{\chi}_1^0$. The two considered benchmark scenarios have mass differences as 1.6 GeV (dM1600) and 770 MeV (dM770). These samples are produced using a full detector simulation at a $\sqrt{s}$ =500 GeV and an integrated luminosity of $\int \mathcal{L}dt = 500$ fb^{-1} for polarisation combination of $P(e^+, e^-) = (+30\%, -80\%)$.

A track grouping algorithm that categorizes tracks based on their z_0 difference is developed. Since signal have displaced vertices from $\gamma\gamma \rightarrow$ low p_T hadron overlay, it is expected that the grouping of the tracks based on their z_0 difference would separate the signal tracks and the $\gamma\gamma \rightarrow$ low p_T hadron overlay tracks into different groups. The additional effect of the longer lifetime of the signal enhances the separation since $\gamma\gamma \rightarrow$ low p_T hadrons do not have a lifetime and decay immediately.

The studies establish that the track grouping algorithm separates chargino decay tracks and $\gamma\gamma \rightarrow$ low p_T hadron tracks very efficiently. It is also found that the inclusion of pair background tracks do not deteriorate the algorithm performance significantly.

In the final part of the thesis, an impact of $\gamma\gamma \rightarrow$ low p_T hadron overlay on low ΔM higgsino analysis is studied and compared with the study in [6]. A hard ISR photon is required to suppress the Standard Model backgrounds arising from beam-beam interactions. The chargino event selection criteria in this study is adapted from the *HS-analysis*. However, certain modifications were applied to a few cuts to suit the needs of suppressing the effects of $\gamma\gamma \rightarrow$ low p_T hadron overlay on loss of signal events and vetoing the Standard Model background.

After the final selection of events, the mass reconstrution for charginos is performed for both the benchmark scenarios. Fitted masses of of $164.9 \pm 2.7\,\text{GeV}$ for dM1600 and $160.3 \pm 3.8\,\text{GeV}$ for dM770 scenario are obtained with a standard deviation of 0.3 and 1.8, respectively, with the input central mass value of the chargino. However, as compared to the *HS-analysis* the uncertainties on the current results are 1.9 times worse and 3.8 times worse for the dM1600 and the dM770 scenarios, respectively. However, it was argued that higher uncertainties could be a result of low Monte-Carlo statistics at the recoil mass threshold region ($\sqrt{s'|thresh}$). This analysis can obtain chargino masses with smaller uncertainties with sufficient Monte-Carlo events for the given luminosity.

The uncertainties on the polarised cross sections are found to be 2.3% for the dM1600 scenario and 2.9% for the dM770 scenario whereas in the *HS-analysis* these values were 1.9% and 1.6% respectively. However, with luminosity upgrades at the ILC one could expect to obtain results with smaller errors and uncertainty values as a result of higher statistics.

The study in this thesis showed for the first time that signatures of such fragile low ΔM higgsino processes can be discovered and measured at the ILC even in the presence of $\gamma\gamma \rightarrow$ low p_T hadron overlay. Even with the statistical uncertainties worsening due to the presence of $\gamma\gamma \rightarrow$ low p_T hadron overlay to about $\sim 1\% - 2\%$, the obtained results are highly precise.

Outlook

The study performed in this thesis was successful in observing some of the key observables for the considered Natural SUSY benchmark scenarios in the presence of $\gamma\gamma \rightarrow$ low p_T hadron overlay. However, some of the aspects that were not covered in this thesis paves a way to further this research. One of the important aspects is that the e^+e^- pair backgrounds were not included in the analysis of the chargino processes. However, the track grouping algorithm was also studied for the events with the inclusion of pair background and the results are found reasonably good. The inclusion of pair background would mainly affect the efficiency for semi-leptonic selection due to the presence of $e^{\pm}$ tracks. The solution for this issue is to only consider μ channel decay for the semi-leptonic selection. Another important aspect is that the semi-leptonic selection is performed by cheating the particle ids from true information. Using the particle identification method for low p_T tracks at reconstrution level developed in [6], more realistic studies can be performed. One final aspect is the study of mass difference between the $\tilde{\chi}_1^{\pm}$ and $\tilde{\chi}_1^0$. For the dM1600 scenario, it is important to have a method which can identify the photons that decay from charginos. Only by including the energies and three-momentum of such photons, the boost energy of chargino decay particles into the chargino rest frame can be rightly reconstructed. For the dM770 scenario, more statistics is required to reconstruct the mass difference between the $\tilde{\chi}_1^{\pm}$ and the LSP which could be achieved at higher luminosity upgrades.

Bibliography

[1] G. Aad. "Combined Measurement of the Higgs Boson Mass in pp Collisions at $\sqrt{s} = 7$ and 8 TeV with the ATLAS and CMS Experiments". In: *Phys. Rev. Lett.* 114.19 (May 2015). DOI: 10.1103/PhysRevLett.114.191803. URL: https://journals.aps.org/prl/abstract/10.1103/PhysRevLett.114.191803.

[2] J. Wess and B. Zumino. "Supergauge transformations in four dimensions". In: *Nuclear Physics B* 70.1 (Feb. 1974). ISSN: 0550-3213. DOI: 10.1016/0550-3213(74)90355-1. URL: http://www.sciencedirect.com/science/article/pii/0550321374903551.

[3] Howard Baer et al. "Natural Supersymmetry: LHC, dark matter and ILC searches". In: *J. High Energ. Phys.* 2012.5 (May 2012). ISSN: 1029-8479. DOI: 10.1007/JHEP05(2012)109. URL: http://arxiv.org/abs/1203.5539.

[4] Michele Papucci, Joshua T. Ruderman, and Andreas Weiler. "Natural SUSY Endures". In: *J. High Energ. Phys.* 2012.9 (Sept. 2012). ISSN: 1029-8479. DOI: 10.1007/JHEP09(2012)035. URL: http://arxiv.org/abs/1110.6926.

[5] Jonathan L. Feng. "Naturalness and the Status of Supersymmetry". In: *Annu. Rev. Nucl. Part. Sci.* 63.1 (Oct. 2013). ISSN: 0163-8998, 1545-4134. DOI: 10.1146/annurev-nucl-102010-130447. URL: http://arxiv.org/abs/1302.6587.

[6] Hale Sert. "Light Higgsinos at the ILC: Precision Measurements and Detector Requirements". PhD thesis. Universität Hamburg, Diss., 2015, 2016. URL: https://bib-pubdb1.desy.de//record/293539.

[7] Mikael Berggren et al. "Tackling light higgsinos at the ILC". In: *Eur. Phys. J. C* 73.12 (Dec. 2013). ISSN: 1434-6044, 1434-6052. DOI: 10.1140/epjc/s10052-013-2660-y. URL: http://arxiv.org/abs/1307.3566.

[8] Sheldon L. Glashow. "Partial-symmetries of weak interactions". In: *Nuclear Physics* 22.4 (Feb. 1961). ISSN: 0029-5582. DOI: 10.1016/0029-5582(61)90469-2. URL: http://www.sciencedirect.com/science/article/pii/0029558261904692.

[9] Steven Weinberg. "A Model of Leptons". In: *Phys. Rev. Lett.* 19.21 (Nov. 1967). DOI: 10.1103/PhysRevLett.19.1264. URL: https://link.aps.org/doi/10.1103/PhysRevLett.19.1264.

[10] A. Salam and J. C. Ward. "Electromagnetic and weak interactions". In: *Physics Letters* 13.2 (Nov. 1964). ISSN: 0031-9163. DOI: 10.1016/0031-9163(64)90711-5. URL: http://www.sciencedirect.com/science/article/pii/0031916364907115.

[11] The LIGO Scientific Collaboration and the Virgo Collaboration. "Observation of Gravitational Waves from a Binary Black Hole Merger". In: *Phys. Rev. Lett.* 116.6 (Feb. 2016). ISSN: 0031-9007, 1079-7114. DOI: 10.1103/PhysRevLett.116.061102. URL: http://arxiv.org/abs/1602.03837.

[12] Particle Data Group et al. "Review of Particle Physics". In: *Phys. Rev. D* 98.3 (Aug. 2018). DOI: 10.1103/PhysRevD.98.030001. URL: https://link.aps.org/doi/10.1103/PhysRevD.98.030001.

[13] H. Fritzsch, M. Gell-Mann, and H. Leutwyler. "Advantages of the color octet gluon picture". In: *Physics Letters B* 47.4 (Nov. 1973). ISSN: 0370-2693. DOI: 10.1016/0370-2693(73)90625-4. URL: http://www.sciencedirect.com/science/article/pii/0370269373906254.

[14] David Griffiths. *Introduction to Elementary Particles*. John Wiley & Sons, Sept. 2008. ISBN: 978-3-527-61847-7.

[15] Ulrich Mosel. *Fields, Symmetries, and Quarks*. 2nd ed. Theoretical and Mathematical Physics. Berlin Heidelberg: Springer-Verlag, 1999. ISBN: 978-3-540-65235-9. URL: https://www.springer.com/de/book/9783540652359.

[16] Emmy Noether. "Invariant variation problems". In: *Transport Theory and Statistical Physics* 1.3 (Jan. 1971). ISSN: 0041-1450. DOI: 10.1080/00411457108231446. URL: https://doi.org/10.1080/00411457108231446.

[17] W. N. Cottingham and D. A. Greenwood. "An introduction to the standard model of particle physics". In: (Apr. 2007).

[18] P. W. Higgs. "Broken symmetries, massless particles and gauge fields". In: *Physics Letters* 12.2 (Sept. 1964). ISSN: 0031-9163. DOI: 10.1016/0031-9163(64)91136-9. URL: http://www.sciencedirect.com/science/article/pii/0031916364911369.

[19] F. Englert and R. Brout. "Broken Symmetry and the Mass of Gauge Vector Mesons". In: *Phys. Rev. Lett.* 13.9 (Aug. 1964). DOI: 10.1103/PhysRevLett.13.321. URL: https://link.aps.org/doi/10.1103/PhysRevLett.13.321.

[20] Jeffrey Goldstone, Abdus Salam, and Steven Weinberg. "Broken Symmetries". In: *Phys.Rev.* 127 (Aug. 1962). DOI: 10.1103/PhysRev.127.965. URL: https://inspirehep.net/literature/12290.

[21] Murray Gell-Mann. "A Schematic Model of Baryons and Mesons". In: *Phys.Lett.* 8 (1964). DOI: 10.1016/S0031-9163(64)92001-3. URL: https://inspirehep.net/literature/11880.

[22] G. Zweig. "An SU(3) model for strong interaction symmetry and its breaking. Version 2". In: (Feb. 1964). URL: https://inspirehep.net/literature/4674.

[23] David J. Gross and Frank Wilczek. "Ultraviolet Behavior of Non-Abelian Gauge Theories". In: *Phys. Rev. Lett.* 30.26 (June 1973). DOI: 10.1103/PhysRevLett.30.1343. URL: https://link.aps.org/doi/10.1103/PhysRevLett.30.1343.

[24] H. David Politzer. "Reliable Perturbative Results for Strong Interactions?" In: *Phys. Rev. Lett.* 30.26 (June 1973). DOI: 10.1103/PhysRevLett.30.1346. URL: https://link.aps.org/doi/10.1103/PhysRevLett.30.1346.

[25] R. Alkofer and J. Greensite. "Quark confinement: the hard problem of hadron physics". In: *J. Phys. G: Nucl. Part. Phys.* 34.7 (May 2007). ISSN: 0954-3899. DOI: 10.1088/0954-3899/34/7/S02. URL: https://doi.org/10.1088%2F0954-3899%2F34%2F7%2Fs02.

[26] Kenneth G. Wilson. "Confinement of quarks". In: *Phys. Rev. D* 10.8 (Oct. 1974). DOI: 10.1103/PhysRevD.10.2445. URL: https://link.aps.org/doi/10.1103/PhysRevD.10.2445.

[27] HPQCD and UKQCD Collaborations et al. "High-Precision Lattice QCD Confronts Experiment". In: *Phys. Rev. Lett.* 92.2 (Jan. 2004). DOI: 10.1103/PhysRevLett.92.022001. URL: https://link.aps.org/doi/10.1103/PhysRevLett.92.022001.

[28] S. Scherer. "Introduction to Chiral Perturbation Theory". In: *Advances in Nuclear Physics* (Oct. 2002). URL: http://arxiv.org/abs/hep-ph/0210398.

[29] A. Ali and G. Kramer. "JETS and QCD: a historical review of the discovery of the quark and gluon jets and its impact on QCD". In: *EPJ H* 36.2 (Sept. 2011). ISSN: 2102-6467. DOI: 10.1140/epjh/e2011-10047-1. URL: https://doi.org/10.1140/epjh/e2011-10047-1.

[30] Bo Andersson. *The Lund Model*. Cambridge Monographs on Particle Physics, Nuclear Physics and Cosmology. Cambridge: Cambridge University Press, 1998. ISBN: 978-0-521-42094-5. URL: https://www.cambridge.org/core/books/lund-model/F9442FBA5696D5DE0D0E8D46F70C34C7.

[31] G. Marchesini and B. R. Webber. "Simulation of QCD Jets Including Soft Gluon Interference". In: *Nucl.Phys.B* 238 (Feb. 1983). DOI: 10.1016/0550-3213(84)90463-2. URL: https://inspirehep.net/literature/189506.

[32] M. Breidenbach et al. "Observed Behavior of Highly Inelastic Electron-Proton Scattering". In: *Phys. Rev. Lett.* 23.16 (Oct. 1969). DOI: 10.1103/PhysRevLett.23.935. URL: https://link.aps.org/doi/10.1103/PhysRevLett.23.935.

[33] Alessandro Bettini. *Introduction to Elementary Particle Physics*. Cambridge University Press, 2008. DOI: 10.1017/CBO9780511809019. URL: https://www.cambridge.org/core/books/introduction-to-elementary-particle-physics/FB7841E74DFEE051D81AD953E81E10DE.

[34] Richard P. Feynman. "Very High-Energy Collisions of Hadrons". In: *Phys. Rev. Lett.* 23.24 (Dec. 1969). DOI: 10.1103/PhysRevLett.23.1415. URL: https://link.aps.org/doi/10.1103/PhysRevLett.23.1415.

[35] J. D. Bjorken. "Asymptotic Sum Rules at Infinite Momentum". In: *Phys. Rev.* 179.5 (Mar. 1969). DOI: 10.1103/PhysRev.179.1547. URL: https://link.aps.org/doi/10.1103/PhysRev.179.1547.

[36] ZEUS Collaboration. "Measurement of the neutral current cross section and F2 structure function for deep inelastic e+p scattering at HERA". In: *Eur. Phys. J. C* 21.3 (July 2001). ISSN: 1434-6044, 1434-6052. DOI: 10.1007/s100520100749. URL: http://arxiv.org/abs/hep-ex/0105090.

[37] Gerhard A. Schuler and Torbjörn Sjöstrand. "A scenario for high-energy gamma-gamma interactions". In: 73.4 (Mar. 1997). ISSN: 0170-9739, 1431-5858. DOI: 10.1007/s002880050359. URL: http://arxiv.org/abs/hep-ph/9605240.

[38] Dieter Schildknecht. "Vector Meson Dominance". In: *arXiv:hep-ph/0511090* (Nov. 2005). URL: http://arxiv.org/abs/hep-ph/0511090.

[39] Pisin Chen, Timothy L. Barklow, and Michael E. Peskin. "Hadron production in gamma-gamma collisions as a background for e+e- linear colliders". In: *Physical Review D* 49.7 (Apr. 1994). ISSN: 0556-2821. DOI: 10.1103/PhysRevD.49.3209. URL: http://arxiv.org/abs/hep-ph/9305247.

[40] J. R. Cudell et al. "Hadronic scattering amplitudes: medium-energy constraints on asymptotic behaviour". In: *Physical Review D* 65.7 (Mar. 2002). ISSN: 0556-2821, 1089-4918. DOI: 10.1103/PhysRevD.65.074024. URL: http://arxiv.org/abs/hep-ph/0107219.

[41] J. R. Cudell et al. "High-energy forward scattering and the Pomeron: Simple pole versus unitarized models". In: *Phys. Rev. D* 61.3 (Jan. 2000). DOI: 10.1103/PhysRevD.61.034019. URL: https://link.aps.org/doi/10.1103/PhysRevD.61.034019.

[42] The SELEX Collaboration and U. Dersch. "Total Cross Section Measurements with pi-, Sigma- and Protons on Nuclei and Nucleons around 600 GeV/c". In: *Nuclear Physics B* 579.1-2 (July 2000). ISSN: 05503213. DOI: 10.1016/S0550-3213(00)00204-2. URL: http://arxiv.org/abs/hep-ex/9910052.

[43] The OPAL Collaboration and G. Abbiendi. "Total Hadronic Cross-Section of Photon-Photon Interactions at LEP". In: *Eur. Phys. J. C* 14.2 (May 2000). ISSN: 1434-6044, 1434-6052. DOI: 10.1007/s100520000352. URL: http://arxiv.org/abs/hep-ex/9906039.

[44] J. Beringer et al. "Review of Particle Physics (RPP)". In: *Phys.Rev.* D86 (2012). DOI: 10.1103/PhysRevD.86.010001.

[45] John Ellis. "Outstanding questions: physics beyond the Standard Model". In: *Philosophical Transactions of the Royal Society A: Mathematical, Physical and Engineering Sciences* (Feb. 2012). URL: https://royalsocietypublishing.org/doi/abs/10.1098/rsta.2011.0452.

[46] Stephen P. Martin. "A supersymmetry primer". In: *Perspectives on Supersymmetry*. Vol. Volume 18. Advanced Series on Directions in High Energy Physics Volume 18. WORLD SCIENTIFIC, July 1998. ISBN: 978-981-02-3553-6. URL: https://www.worldscientific.com/doi/abs/10.1142/9789812839657_0001.

[47] Super-Kamiokande Collaboration et al. "Evidence for Oscillation of Atmospheric Neutrinos". In: *Phys. Rev. Lett.* 81.8 (Aug. 1998). DOI: 10.1103/PhysRevLett.81.1562. URL: https://link.aps.org/doi/10.1103/PhysRevLett.81.1562.

[48] Planck Collaboration et al. "Planck 2015 results. XIII. Cosmological parameters". In: *A&A* 594 (Oct. 2016). ISSN: 0004-6361, 1432-0746. DOI: 10.1051/0004-6361/201525830. URL: http://arxiv.org/abs/1502.01589.

[49] Francesco Capozzi et al. "Global constraints on absolute neutrino masses and their ordering". In: *Phys. Rev. D* 95.9 (May 2017). ISSN: 2470-0010, 2470-0029. DOI: 10.1103/PhysRevD.95.096014. URL: http://arxiv.org/abs/1703.04471.

[50] K. G. Begeman, A. H. Broeils, and R. H. Sanders. "Extended rotation curves of spiral galaxies: dark haloes and modified dynamics". In: *Mon Not R Astron Soc* 249.3 (Apr. 1991). ISSN: 0035-8711. DOI: 10.1093/mnras/249.3.523. URL: https://academic.oup.com/mnras/article/249/3/523/1005565.

[51] Stephen M. Kent. "Dark matter in spiral galaxies. II - Galaxies with H I rotation curves". In: *The Astronomical Journal* 93 (Apr. 1987). ISSN: 0004-6256. DOI: 10.1086/114366. URL: http://adsabs.harvard.edu/abs/1987AJ.....93..816K.

[52] Eiichiro Komatsu et al. "Results from the Wilkinson Microwave Anisotropy Probe". In: *Prog Theor Exp Phys* 2014.6 (June 2014). DOI: 10.1093/ptep/ptu083. URL: https://academic.oup.com/ptep/article/2014/6/06B102/1562681.

[53] Gianfranco Bertone, Dan Hooper, and Joseph Silk. "Particle Dark Matter: Evidence, Candidates and Constraints". In: *Physics Reports* 405.5-6 (Jan. 2005). ISSN: 03701573. DOI: 10.1016/j.physrep.2004.08.031. URL: http://arxiv.org/abs/hep-ph/0404175.

[54] Andrei D. Sakharov. "Violation of CP invariance, C asymmetry, and baryon asymmetry of the universe". In: *Sov. Phys. Usp.* 34.5 (1991). ISSN: 0038-5670. DOI: 10.1070/PU1991v034n05ABEH002497. URL: https://iopscience.iop.org/article/10.1070/PU1991v034n05ABEH002497/meta.

[55] Mark Trodden. "Baryogenesis and Leptogenesis". In: *eConf* (2004). URL: http://arxiv.org/abs/hep-ph/0411301.

[56] Patrick Huet and Eric Sather. "Electroweak baryogenesis and standard model CP violation". In: *Phys. Rev. D* 51.2 (Jan. 1995). DOI: 10.1103/PhysRevD.51.379. URL: https://link.aps.org/doi/10.1103/PhysRevD.51.379.

[57] H. E. Haber and G. L. Kane. "The search for supersymmetry: Probing physics beyond the standard model". In: *Physics Reports* 117.2 (Jan. 1985). ISSN: 0370-1573. DOI: 10.1016/0370-1573(85)90051-1. URL: http://www.sciencedirect.com/science/article/pii/0370157385900511.

[58] John F. Gunion. "Two-body decays of neutralinos and charginos". In: *Phys. Rev. D* 37.9 (1988). DOI: 10.1103/PhysRevD.37.2515.

[59] P. Binétruy. "Supersymmetry: Theory, Experiment, and Cosmology". In: *Supersymmetry: Theory* (2006). URL: https://ui.adsabs.harvard.edu/2006stec.book.....B/abstract.

[60] T. Han, S. Padhi, and S. Su. "Electroweakinos in the Light of the Higgs Boson". In: *Phys. Rev. D* 88.11 (Dec. 2013). ISSN: 1550-7998, 1550-2368. DOI: 10.1103/PhysRevD.88.115010. URL: http://arxiv.org/abs/1309.5966.

[61] S. Heinemeyer, W. Hollik, and G. Weiglein. "Electroweak Precision Observables in the Minimal Supersymmetric Standard Model". In: *Physics Reports* 425.5-6 (Mar. 2006). ISSN: 03701573. DOI: 10.1016/j.physrep.2005.12.002. URL: http://arxiv.org/abs/hep-ph/0412214.

[62] A. M. Sirunyan et al. "Search for gauge-mediated supersymmetry in events with at least one photon and missing transverse momentum in pp collisions at s=13TeV". In: *Physics Letters B* 780 (May 2018). ISSN: 0370-2693. DOI: 10.1016/j.physletb.2018.02.045. URL: http://www.sciencedirect.com/science/article/pii/S0370269318301552.

[63] A. M. Sirunyan et al. "Search for supersymmetry in events with a photon, a lepton, and missing transverse momentum in proton-proton collisions at $\sqrt{s} = 13$TeV". In: *J. High Energ. Phys.* 2019.1 (Jan. 2019). ISSN: 1029-8479. DOI: 10.1007/JHEP01(2019)154. URL: https://doi.org/10.1007/JHEP01(2019)154.

[64] M. Aaboud et al. "Search for the direct production of charginos and neutralinos in final states with tau leptons in $\sqrt{s} = 13$TeV pp collisions with the ATLAS detector". In: *Eur. Phys. J. C* 78.2 (Feb. 2018). ISSN: 1434-6052. DOI: 10.1140/epjc/s10052-018-5583-9. URL: https://link.springer.com/article/10.1140/epjc/s10052-018-5583-9.

[65] ATLAS Collaboration et al. "Search for electroweak production of supersymmetric states in scenarios with compressed mass spectra at $\sqrt{s} = 13$TeV with the ATLAS detector". In: *Phys. Rev. D* 97.5 (Mar. 2018). DOI: 10.1103/PhysRevD.97.052010. URL: https://link.aps.org/doi/10.1103/PhysRevD.97.052010.

[66] ATLAS Collaboration. *Search for direct pair production of higgsinos by the reinterpretation of the disappearing track analysis with 36.1 fb^{-1} of $\sqrt{s} = 13$ TeV data collected with the ATLAS experiment*. Geneva, Dec. 2017. URL: https://cds.cern.ch/record/2297480.

[67] Anadi Canepa. "Searches for supersymmetry at the Large Hadron Collider". In: *Reviews in Physics* 4 (Nov. 2019). ISSN: 2405-4283. DOI: 10.1016/j.revip.2019.100033. URL: http://www.sciencedirect.com/science/article/pii/S2405428318300091.

[68] Howard E. Haber and Daniel Wyler. "Radiative Neutralino Decay". In: *Nucl. Phys. B* 323 (1989), pp. 267–310. DOI: 10.1016/0550-3213(89)90143-0. URL: http://inspirehep.net/record/263846.

[69] Mikael Berggren et al. "Electroweakino Searches: A Comparative Study for LHC and ILC (A Snowmass White Paper)". In: (Sept. 2013). URL: http://arxiv.org/abs/1309.7342.

[70] The OPAL Collaboration and K. Ackerstaff et al. "Search for stable and longlived massive charged particles in e^+e^- collisions at $\sqrt{s}$ = 130-GeV to 209-GeV". In: *Physics Letters B* 433.1-2 (Aug. 1998). ISSN: 03702693. DOI: 10.1016/S0370-2693(98)00518-8. URL: http://arxiv.org/abs/hep-ex/9803026.

[71] The OPAL collaboration. "Search for Stable and Long-Lived Massive Charged Particles in e^+e^- Collisions at $\sqrt{s}$ = 183-209 GeV". In: *Physics Letters B* 572.1-2 (Oct. 2003). ISSN: 03702693. DOI: 10.1016/S0370-2693(03)00639-7. URL: http://arxiv.org/abs/hep-ex/0305031.

[72] The DELPHI Collaboration and J. Abdallah. "Searches for supersymmetric particles in e^+e^- collisions up to 208 GeV and interpretation of the results within the MSSM". In: *Eur. Phys. J. C* 31.4 (Dec. 2003). ISSN: 1434-6044, 1434-6052. DOI: 10.1140/epjc/s2003-01355-5. URL: http://arxiv.org/abs/hep-ex/0311019.

[73] R Barate et al. "Search for Supersymmetric Particles in e^+e^- Collisions at $\sqrt{s}$ up to 202 GeV and Mass Limit for the Lightest Neutralino". In: *Physics Letters B* 499 (Feb. 2001). DOI: 10.1016/S0370-2693(01)00015-6.

[74] OPAL Collaboration. *New Particle Searches in e^+e^- Collisions at $\sqrt{s}$ = $200 - 209 GeV$*. Feb. 2001. URL: https://cds.cern.ch/record/837791.

[75] *LEP2 SUSY WORKING GROUP Charginos*. URL: http://lepsusy.web.cern.ch/lepsusy/www/inoslowdmsummer02/charginolowdm_pub.html.

[76] Howard Baer et al. "ILC as a natural SUSY discovery machine and precision microscope: From light Higgsinos to tests of unification". In: *Phys. Rev. D* 101.9 (May 2020). DOI: 10.1103/PhysRevD.101.095026. URL: https://link.aps.org/doi/10.1103/PhysRevD.101.095026.

[77] María Teresa Núñez Pardo de Vera, Mikael Berggren, and Jenny List. "Chargino production at the ILC". In: (Feb. 2020). URL: http://arxiv.org/abs/2002.01239.

[78] The CDF Collaboration. "Observation of Top Quark Production in Pbar-P Collisions". In: *Physical Review Letters* 74.14 (Apr. 1995). ISSN: 0031-9007, 1079-7114. DOI: 10.1103/PhysRevLett.74.2626. URL: http://arxiv.org/abs/hep-ex/9503002.

[79] S. Abachi. "Observation of the Top Quark". In: *Physical Review Letters* 74.14 (Apr. 1995). ISSN: 0031-9007, 1079-7114. DOI: 10.1103/PhysRevLett.74.2632. URL: http://arxiv.org/abs/hep-ex/9503003.

[80] D. P. Barber et al. “Discovery of Three-Jet Events and a Test of Quantum Chromodynamics at PETRA”. In: *Phys. Rev. Lett.* 43.12 (Sept. 1979), pp. 830–833. DOI: 10.1103/PhysRevLett.43.830. URL: https://link.aps.org/doi/10.1103/PhysRevLett.43.830.

[81] Ch. Berger et al. “Evidence for gluon bremsstrahlung in e+e annihilations at high energies”. In: *Physics Letters B* 86.3 (Oct. 1979). ISSN: 0370-2693. DOI: 10.1016/0370-2693(79)90869-4. URL: http://www.sciencedirect.com/science/article/pii/0370269379908694.

[82] The ALEPH Collaboration et al. “Precision Electroweak Measurements on the Z Resonance”. In: *Physics Reports* 427.5-6 (May 2006). ISSN: 03701573. DOI: 10.1016/j.physrep.2005.12.006. URL: http://arxiv.org/abs/hep-ex/0509008.

[83] Philip Bambade et al. “The International Linear Collider: A Global Project”. In: (Mar. 2019). URL: https://arxiv.org/abs/1903.01629v3.

[84] Ties Behnke et al. “The International Linear Collider Technical Design Report - Volume 1: Executive Summary”. In: (June 2013). URL: http://arxiv.org/abs/1306.6327.

[85] Chris Adolphsen et al. “The International Linear Collider Technical Design Report - Volume 3.II: Accelerator Baseline Design”. In: (June 2013). URL: http://arxiv.org/abs/1306.6328.

[86] Howard Baer et al. “The International Linear Collider Technical Design Report - Volume 2: Physics”. In: (June 2013). URL: http://arxiv.org/abs/1306.6352.

[87] K.A. Olive. “Review of Particle Physics”. In: *Chinese Physics C* 40.10 (Oct. 2016). ISSN: 1674-1137. DOI: 10.1088/1674-1137/40/10/100001. URL: http://stacks.iop.org/1674-1137/40/i=10/a=100001?key=crossref.5ca5f9c166adc59f41e03a802b715c19.

[88] B. Richter. “Very high energy electron-positron colliding beams for the study of weak interactions”. In: *Nuclear Instruments and Methods* 136.1 (July 1976). ISSN: 0029554X. DOI: 10.1016/0029-554X(76)90396-7. URL: http://linkinghub.elsevier.com/retrieve/pii/0029554X76903967.

[89] M. Tigner. “A possible apparatus for electron clashing-beam experiments”. In: *Il Nuovo Cimento* 37.3 (June 1965). ISSN: 0029-6341, 1827-6121. DOI: 10.1007/BF02773204. URL: http://link.springer.com/10.1007/BF02773204.

[90] Keisuke Fujii et al. “The role of positron polarization for the inital $\sqrt{s} = 250$ GeV stage of the International Linear Collider”. In: (Jan. 2018). URL: http://arxiv.org/abs/1801.02840.

[91] G. Moortgat-Pick et al. "The role of polarized positrons and electrons in revealing fundamental interactions at the Linear Collider". In: *Physics Reports* 460.4-5 (May 2008). ISSN: 03701573. DOI: 10.1016/j.physrep.2007.12.003. URL: http://arxiv.org/abs/hep-ph/0507011.

[92] K. Kawagoe et al. *Press release: Announcement of the results of the ILC candidate site evaluation in Japan*. Mar. 2019. URL: http://ilc-str.jp/topics/2013/08281826/.

[93] Keisuke Fujii et al. "Physics Case for the 250 GeV Stage of the International Linear Collider". In: (Oct. 2017). URL: http://arxiv.org/abs/1710.07621.

[94] Hiroaki Aihara et al. "The International Linear Collider. A Global Project". In: (Jan. 2019). URL: http://arxiv.org/abs/1901.09829.

[95] Philip Bambade et al. "The International Linear Collider. A European Perspective". In: (Jan. 2019). URL: http://arxiv.org/abs/1901.09825.

[96] Nan Phinney, Nobukasu Toge, and Nicholas Walker. "ILC Reference Design Report Volume 3 - Accelerator". In: (Dec. 2007). URL: http://arxiv.org/abs/0712.2361.

[97] Lyn Evans and Shinichiro Michizono. "The International Linear Collider Machine Staging Report 2017". In: (Nov. 2017). URL: http://arxiv.org/abs/1711.00568.

[98] Madalina Chera and Jenny List. "Particle Flow: From First Principles to Gaugino Property Determination at the ILC". PhD thesis. Hamburg: Verlag Deutsches Elektronen-Synchrotron, 2018. URL: https://inspirehep.net/files/7cc3f17c3f939281d68cf188ccee659f.

[99] T. Barklow et al. "ILC Operating Scenarios". In: (June 2015). URL: http://arxiv.org/abs/1506.07830.

[100] The ILD Collaboration. "International Large Detector: Interim Design Report". In: (Mar. 2020). URL: http://arxiv.org/abs/2003.01116.

[101] Richard Keith Ellis et al. *Physics Briefing Book: Input for the European Strategy for Particle Physics Update 2020*. Oct. 2019. eprint: 1910.11775. URL: https://arxiv.org/abs/1910.11775.

[102] LHC/LC Study Group et al. "Physics Interplay of the LHC and the ILC". In: *Physics Reports* 426.2-6 (Apr. 2006). ISSN: 03701573. DOI: 10.1016/j.physrep.2005.12.003. URL: http://arxiv.org/abs/hep-ph/0410364.

[103] Moritz Habermehl. "Dark Matter at the International Linear Collider". In: (2018). DOI: 10.3204/PUBDB-2018-05723.

[104] Stéphane Poss and André Sailer. "Luminosity Spectrum Reconstruction at Linear Colliders". In: *The European Physical Journal C* 74.4 (Apr. 2014). ISSN: 1434-6044, 1434-6052. DOI: 10.1140/epjc/s10052-014-2833-3. URL: http://arxiv.org/abs/1309.0372.

[105] Adrian Vogel. "Beam-induced backgrounds in detectors at the ILC". In: (2008). DOI: 10.3204/DESY-THESIS-2008-036.

[106] C. Rimbault, K. Mönig, and Daniel Schulte. "Incoherent pair generation in a beam-beam interaction simulation". In: *Physical Review Special Topics - Accelerators and Beams* 9 (Mar. 2006). DOI: 10.1103/PhysRevSTAB.9.034402.

[107] Pisin Chen. "Beamstrahlung and the QED, QCD backgrounds in linear colliders". In: (1992). URL: https://inspirehep.net/literature/338709.

[108] Kaoru Yokoya and Pisin Chen. "Beam-beam phenomena in linear colliders". In: *Frontiers of Particle Beams: Intensity Limitations*. Ed. by M. Dienes, M. Month, and S. Turner. Lecture Notes in Physics 400. Springer Berlin Heidelberg, 1992. ISBN: 978-3-540-55250-5 978-3-540-46797-7. DOI: 10.1007/3-540-55250-2_37. URL: http://link.springer.com/chapter/10.1007/3-540-55250-2_37.

[109] Pisin Chen. "An Introduction to Beamstrahlung and Disruption". In: *Lect. Notes Phys.* 296 (1988). Ed. by M. Month and S. Turner, p. 495. URL: https://inspirehep.net/literature/248920.

[110] E. D. Courant and H. S. Snyder. "Theory of the Alternating-Gradient Synchrotron". In: *Annals of Physics* 281.1 (Apr. 2000). ISSN: 0003-4916. DOI: 10.1006/aphy.2000.6012. URL: http://www.sciencedirect.com/science/article/pii/S0003491600960123.

[111] Pisin Chen. "Differential luminosity under multiphoton beamstrahlung". In: *Phys. Rev. D* 46.3 (Aug. 1992). DOI: 10.1103/PhysRevD.46.1186. URL: http://link.aps.org/doi/10.1103/PhysRevD.46.1186.

[112] Toshinori Abe et al. "The International Large Detector: Letter of Intent". In: (2010). DOI: 10.2172/975166. URL: http://inspirehep.net/record/851300.

[113] Ties Behnke. "The ILD Detector at the ILC". In: (Dec. 2019). URL: https://arxiv.org/abs/1912.04601.

[114] H. Aihara, P. Burrows, and M. Oreglia. "SiD Letter of Intent". In: (Oct. 2009). URL: http://arxiv.org/abs/0911.0006.

[115] S. Agostinelli et al. "Geant4—a simulation toolkit". In: *Nuclear Instruments and Methods in Physics Research Section A: Accelerators, Spectrometers, Detectors and Associated Equipment* 506.3 (July 2003). ISSN: 0168-9002. DOI: 10.1016/S0168-9002(03)01368-8. URL: http://www.sciencedirect.com/science/article/pii/S0168900203013688.

[116] A. Vogel. "The coordinate system for LDC detector studies". In: (2005). URL: https://inspirehep.net/literature/704358.

[117] J. S. Marshall and M. A. Thomson. "The Pandora Particle Flow Algorithm". In: (Aug. 2013). URL: http://arxiv.org/abs/1308.4537.

[118] M. A. Thomson. "Particle Flow Calorimetry and the PandoraPFA Algorithm". In: *Nuclear Instruments and Methods in Physics Research Section A: Accelerators, Spectrometers, Detectors and Associated Equipment* 611.1 (Nov. 2009). ISSN: 01689002. DOI: 10.1016/j.nima.2009.09.009. URL: http://arxiv.org/abs/0907.3577.

[119] Thomas Krämer. "Track Parameters in LCIO". In: (2006). URL: http://flc.desy.de/lcnotes/notes/localfsExplorer_read?currentPath=/afs/desy.de/group/flc/lcnotes/LC-DET-2006-004.pdf.

[120] Keisuke Fujii. *Time Stamping - CDC/TPC comparison studeis*. URL: https://www-jlc.kek.jp/jlc/sites/default/files/groups/tpc/talks/T0.CDCvsTPC.pdf.

[121] The ILD Concept Group. "The International Large Detector: Letter of Intent". In: (June 2010). URL: http://arxiv.org/abs/1006.3396.

[122] *Calice webpage*. URL: https://twiki.cern.ch/twiki/bin/view/CALICE/WebHome.

[123] C. Adloff et al. "Response of the CALICE Si-W electromagnetic calorimeter physics prototype to electrons". In: *Nuclear Instruments and Methods in Physics Research Section A: Accelerators, Spectrometers, Detectors and Associated Equipment* 608.3 (Sept. 2009). ISSN: 0168-9002. DOI: 10.1016/j.nima.2009.07.026. URL: http://www.sciencedirect.com/science/article/pii/S0168900209014673.

[124] C. Adloff et al. "Hadronic energy resolution of a highly granular scintillator-steel hadron calorimeter using software compensation techniques". In: *J. Inst.* 7.09 (Sept. 2012). ISSN: 1748-0221. DOI: 10.1088/1748-0221/7/09/P09017. URL: https://doi.org/10.1088%2F1748-0221%2F7%2F09%2Fp09017.

[125] M. Czakon, J. Gluza, and T. Riemann. "The planar four-point master integrals for massive two-loop Bhabha scattering". In: *Nuclear Physics B* 751.1-2 (Sept. 2006). ISSN: 05503213. DOI: 10.1016/j.nuclphysb.2006.05.033. URL: http://arxiv.org/abs/hep-ph/0604101.

[126] H. Abramowicz et al. “Forward instrumentation for ILC detectors”. In: *J. Inst.* 5.12 (2010). ISSN: 1748-0221. DOI: 10.1088/1748-0221/5/12/P12002. URL: http://stacks.iop.org/1748-0221/5/i=12/a=P12002.

[127] Ch Grah and A. Sapronov. “Beam parameter determination using beamstrahlung photons and incoherent pairs”. English. In: *Journal of Instrumentation* 3.10 (2008). ISSN: ISSN 1748-0221. DOI: 10.1088/1748-0221/3/10/P10004. URL: http://inis.iaea.org/Search/search.aspx?orig_q=RN:41013913.

[128] Frank Gaede et al. “LCIO - A persistency framework for linear collider simulation studies”. In: (June 2003). URL: http://arxiv.org/abs/physics/0306114.

[129] S. Aplin et al. “LCIO: A persistency framework and event data model for HEP”. In: *2012 IEEE Nuclear Science Symposium and Medical Imaging Conference Record (NSS/MIC)*. Oct. 2012. DOI: 10.1109/NSSMIC.2012.6551478.

[130] *WHIZARD – Hepforge*. URL: https://whizard.hepforge.org/.

[131] B. C. Allanach et al. “SUSY Les Houches Accord 2”. In: *Computer Physics Communications* 180.1 (Jan. 2009). ISSN: 00104655. DOI: 10.1016/j.cpc.2008.08.004. URL: http://arxiv.org/abs/0801.0045.

[132] Mauro Moretti, Thorsten Ohl, and Juergen Reuter. “O’Mega: An Optimizing Matrix Element Generator”. In: *arXiv:hep-ph/0102195* (Feb. 2001). URL: http://arxiv.org/abs/hep-ph/0102195.

[133] Daniel Schulte. “Study of Electromagnetic and Hadronic Background in the Interaction Region of the Tesla Collider”. PhD thesis. Universität Hamburg, Diss., 1996, 1996. URL: https://inspirehep.net/literature/888433.

[134] Torbjorn Sjostrand, Stephen Mrenna, and Peter Skands. “PYTHIA 6.4 Physics and Manual”. In: *Journal of High Energy Physics* 2006.05 (May 2006). ISSN: 1029-8479. DOI: 10.1088/1126-6708/2006/05/026. URL: http://arxiv.org/abs/hep-ph/0603175.

[135] L. Garren. *Notes about StdHep - HepPDT - Fermilab Redmine*. URL: https://cdcvs.fnal.gov/redmine/projects/heppdt/wiki/Notes_about_StdHep.

[136] M. Bahr et al. “Herwig++ Physics and Manual”. In: *Eur. Phys. J. C* 58.4 (Dec. 2008). ISSN: 1434-6044, 1434-6052. DOI: 10.1140/epjc/s10052-008-0798-9. URL: http://arxiv.org/abs/0803.0883.

[137] David Grellscheid and Peter Richardson. “Simulation of Tau Decays in the Herwig++ Event Generator”. In: (Oct. 2007). URL: http://arxiv.org/abs/0710.1951.

[138] Cristian Pisano. "Testing the Equivalent Photon Approximation of the Proton in the Process $ep \to \nu WX$". In: *Eur. Phys. J. C* 38.1 (Dec. 2004). ISSN: 1434-6044, 1434-6052. DOI: 10.1140/epjc/s2004-02017-x. URL: http://arxiv.org/abs/hep-ph/0408101.

[139] Timothy L. Barklow and Swathi Sasikumar. *Private Discussion with Tim Barklow*.

[140] P. Mora de Freitas and H. Videau. "Detector simulation with MOKKA / GEANT4: Present and future". In: (Aug. 2002). URL: https://inspirehep.net/literature/609687.

[141] *Mokka Webpage*. URL: https://llrforge.in2p3.fr/trac/Mokka/.

[142] *AIDASoft/DD4hep*. Sept. 2019. URL: https://github.com/AIDASoft/DD4hep.

[143] M. Frank et al. "DD4hep: A Detector Description Toolkit for High Energy Physics Experiments". In: *J. Phys.: Conf. Ser.* 513.2 (June 2014). ISSN: 1742-6596. DOI: 10.1088/1742-6596/513/2/022010. URL: https://doi.org/10.1088%2F1742-6596%2F513%2F2%2F022010.

[144] J. Allison et al. "Geant4 developments and applications". In: *IEEE Transactions on Nuclear Science* 53.1 (Feb. 2006). ISSN: 0018-9499. DOI: 10.1109/TNS.2006.869826.

[145] R Brun, A Gheata, and M Gheata. "The ROOT geometry package". In: *Nuclear Instruments and Methods in Physics Research Section A: Accelerators, Spectrometers, Detectors and Associated Equipment*. Proceedings of the VIII International Workshop on Advanced Computing and Analysis Techniques in Physics Research 502.2 (Apr. 2003). ISSN: 0168-9002. DOI: 10.1016/S0168-9002(03)00541-2. URL: http://www.sciencedirect.com/science/article/pii/S0168900203005412.

[146] Rene Brun and Fons Rademakers. "ROOT — An object oriented data analysis framework". In: *Nuclear Instruments and Methods in Physics Research Section A: Accelerators, Spectrometers, Detectors and Associated Equipment*. New Computing Techniques in Physics Research V 389.1 (Apr. 1997). ISSN: 0168-9002. DOI: 10.1016/S0168-9002(97)00048-X. URL: http://www.sciencedirect.com/science/article/pii/S016890029700048X.

[147] F. Gaede. "Marlin and LCCD—Software tools for the ILC". In: *Nuclear Instruments and Methods in Physics Research Section A: Accelerators, Spectrometers, Detectors and Associated Equipment*. Proceedings of the X International Workshop on Advanced Computing and Analysis Techniques in Physics Research 559.1 (Apr. 2006). ISSN: 0168-9002. DOI: 10.1016/j.nima.

2005.11.138. URL: http://www.sciencedirect.com/science/article/pii/S0168900205022643.

[148] Taikan Suehara and Tomohiko Tanabe. "LCFIPlus: A framework for jet analysis in linear collider studies". In: *Nuclear Instruments and Methods in Physics Research Section A: Accelerators, Spectrometers, Detectors and Associated Equipment* 808 (Feb. 2016). ISSN: 0168-9002. DOI: 10.1016/j.nima.2015.11.054. URL: http://www.sciencedirect.com/science/article/pii/S0168900215014199.

[149] Mikael Berggren. "SGV 3.0 - a fast detector simulation". In: (Mar. 2012). URL: http://arxiv.org/abs/1203.0217.

[150] Gerald R. Lynch and Orin I. Dahl. "Approximations to multiple Coulomb scattering". In: *Nuclear Instruments and Methods in Physics Research Section B: Beam Interactions with Materials and Atoms* 58.1 (May 1991). ISSN: 0168-583X. DOI: 10.1016/0168-583X(91)95671-Y. URL: http://www.sciencedirect.com/science/article/pii/0168583X9195671Y.

[151] R. E. Kalman. "A New Approach to Linear Filtering and Prediction Problems". In: *J. Basic Eng* 82.1 (Mar. 1960). ISSN: 0021-9223. DOI: 10.1115/1.3662552. URL: https://asmedigitalcollection.asme.org/fluidsengineering/article/82/1/35/397706/A-New-Approach-to-Linear-Filtering-and-Prediction.

[152] Max S. Zolotorev and Kirk T. McDonald. "Classical Radiation Processes in the Weizsacker-Williams Approximation". In: (Mar. 2000). URL: http://arxiv.org/abs/physics/0003096.

[153] E. Fermi. "Über die Theorie des Stoßes zwischen Atomen und elektrisch geladenen Teilchen". In: *Zeitschrift für Physik* 29.1 (Dec. 1924), pp. 315–327. ISSN: 0044-3328. DOI: 10.1007/BF03184853. URL: http://link.springer.com/10.1007/BF03184853.

[154] Stanley J. Brodsky, Toichiro Kinoshita, and Hidezumi Terazawa. "Two-Photon Mechanism of Particle Production by High-Energy Colliding Beams". In: *Phys. Rev. D* 4.5 (Sept. 1971). DOI: 10.1103/PhysRevD.4.1532. URL: http://link.aps.org/doi/10.1103/PhysRevD.4.1532.

[155] Daniel Shulte. *DESY - FLASH - TESLA Reports 1997*. 1996. URL: http://flash.desy.de/reports_publications/tesla_reports/tesla_reports_1997/ (visited on 05/25/2016).

[156] U. Amaldi et al. "The real part of the forward proton proton scattering amplitude measured at the CERN intersecting storage rings". In: *Physics Letters B* 66.4 (Feb. 1977). ISSN: 0370-2693. DOI: 10.1016/0370-2693(77)90022-3. URL: http://www.sciencedirect.com/science/article/pii/0370269377900223.

[157] M. Acciarri et al. "Total cross section in collisions at LEP". In: *Physics Letters B* 519 (Oct. 2001). ISSN: 0370-2693. DOI: 10.1016/S0370-2693(01)01072-3. URL: http://www.sciencedirect.com/science/article/pii/S0370269301010723.

[158] Ch. Berger et al. "Measurement of the total photon-photon cross section for the production of hadrons at small Q^2". In: *Physics Letters B* 149 (Dec. 1984). ISSN: 0370-2693. DOI: 10.1016/0370-2693(84)90437-4. URL: http://www.sciencedirect.com/science/article/pii/0370269384904374.

[159] S. E. Baru et al. "Total cross section of two-photon production of hadrons". In: *Z. Phys. C - Particles and Fields* 53 (1992). ISSN: 0170-9739, 1431-5858. DOI: 10.1007/BF01597557. URL: http://link.springer.com/article/10.1007/BF01597557.

[160] N. F. Nasrallah and K. Schilcher. "Charged pion pair production by two photons from a chiral sum rule". In: (Nov. 2002). URL: http://arxiv.org/abs/hep-ph/0211379.

[161] Jonathan L. Rosner. "Vector meson pair production in two-photon collisions near threshold". In: *Physical Review D* 70 (Aug. 2004). ISSN: 1550-7998, 1550-2368. DOI: 10.1103/PhysRevD.70.034028. URL: http://arxiv.org/abs/hep-ph/0404245.

[162] H. Albrecht et al. "A Spin parity analysis of $\gamma\gamma \to \rho^+\rho^-$". In: *Physics Letters B* 267.4 (Sept. 1991). ISSN: 0370-2693. DOI: 10.1016/0370-2693(91)90907-8. URL: http://www.sciencedirect.com/science/article/pii/0370269391909078.

[163] Argus Collaboration et al. "Observation of Spin Parity 2^+ Dominance in the Reaction $\gamma\gamma \to \rho^0\rho^0$ Near Threshold". In: *Z. Phys. C - Particles and Fields* 50 (). ISSN: 0170-9739, 1431-5858. DOI: 10.1007/BF01558550. URL: http://link.springer.com/article/10.1007/BF01558550.

[164] Hermann Kolanoski. *Two-Photon Physics at e^+e^- Storage Rings*. Vol. 105. Springer Tracts in Modern Physics 105. Berlin/Heidelberg: Springer-Verlag, 1984. ISBN: 978-3-540-13671-2. URL: http://link.springer.com/10.1007/BFb0045900.

[165] A.E. Kaloshin and V.V. Serebryakov. "Crystal ball experiment on $\gamma\gamma \to \pi^0\pi^0$ and neutral pion polarizability". In: *Physics Letters B* 278.1–2 (1992). ISSN: 0370-2693. DOI: 10.1016/0370-2693(92)90734-L. URL: http://www.sciencedirect.com/science/article/pii/037026939290734L.

[166] Howard Baer and Jenny List. "Post LHC8 SUSY benchmark points for ILC physics". In: *Phys. Rev. D* 88.5 (Sept. 2013). ISSN: 1550-7998, 1550-2368. DOI: 10.1103/PhysRevD.88.055004. URL: http://arxiv.org/abs/1307.0782.

[167] C.-H. Chen, M. Drees, and J. F. Gunion. "Searching for Invisible and Almost Invisible Particles at e^+e^- Colliders". In: *Phys. Rev. Lett.* 76.12 (Mar. 1996). ISSN: 0031-9007, 1079-7114. DOI: 10.1103/PhysRevLett.76.2002. URL: http://arxiv.org/abs/hep-ph/9512230.

[168] C. Hensel. "Search for nearly mass degenerate charginos and neutralinos in e^+e^- collisions". In: (2002). DOI: 10.3204/DESY-THESIS-2002-047.

[169] P. Chen. "Disruption, Beamstrahlung, AND Beamstrahlung PAIR CREATION". In: (1989). URL: https://inspirehep.net/literature/267815.

[170] M S Zolotorev, E A Kuraev, and V G Serbo. *Estimates of electromagnetic background processes for the VLEPP project*. IYAF-87-63-TRANS-E. SLAC-TRANS-0227. Novosibirsk, 1987. URL: https://cds.cern.ch/record/179155.

[171] G. Breit and John A. Wheeler. "Collision of Two Light Quanta". In: *Physical Review* 46 (Dec. 1934). ISSN: 1536-6065. DOI: 10.1103/PhysRev.46.1087. URL: http://adsabs.harvard.edu/abs/1934PhRv...46.1087B.

[172] H. Bethe, W. Heitler, and Paul Adrien Maurice Dirac. "On the stopping of fast particles and on the creation of positive electrons". In: *Proceedings of the Royal Society of London. Series A, Containing Papers of a Mathematical and Physical Character* 146.856 (Aug. 1934). DOI: 10.1098/rspa.1934.0140. URL: https://royalsocietypublishing.org/doi/abs/10.1098/rspa.1934.0140.

[173] Lev Davidovich Landau and E. Lifshitz. *On the theory of the dispersion of magnetic permeability in ferromagnetic bodies*. 1935. URL: https://doi.org/10.1016/B978-0-08-036364-6.50008-9.

[174] Matteo Cacciari, Gavin P. Salam, and Gregory Soyez. "FastJet user manual". In: *The European Physical Journal C* 72.3 (Mar. 2012). ISSN: 1434-6044, 1434-6052. DOI: 10.1140/epjc/s10052-012-1896-2. URL: http://arxiv.org/abs/1111.6097.

[175] *ILCSoft Home Page*. URL: https://ilcsoft.desy.de/portal.

[176] Benno List. *Why and When to Optimizize Efficiency times purity*. URL: https://www.desy.de/~blist/notes/whyeffpur.ps.gz.

A. Plots on different η values for the track algorithm

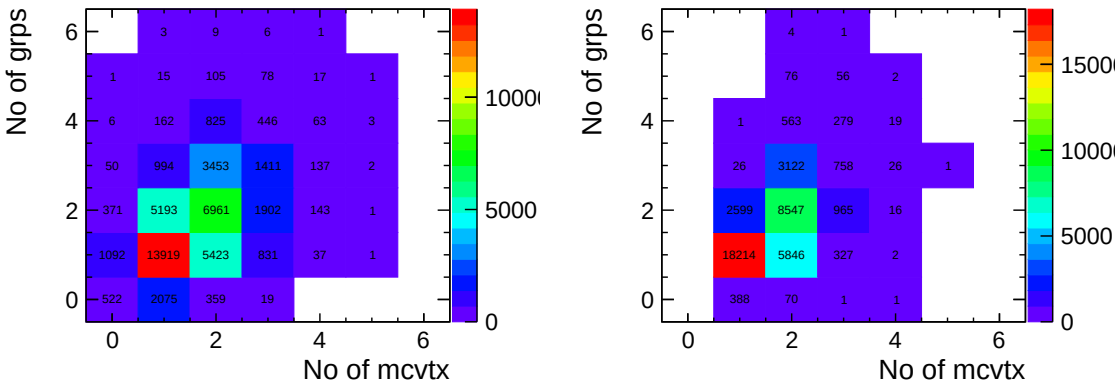

(a) (b)

Figure A.1.: Comparison of number of true Monte-Carlo vertices with track groups obtained from the algorithm for $\eta = 1.6$. a) dM770 benchmark scenario b) dM1600 benchmark scenario

.

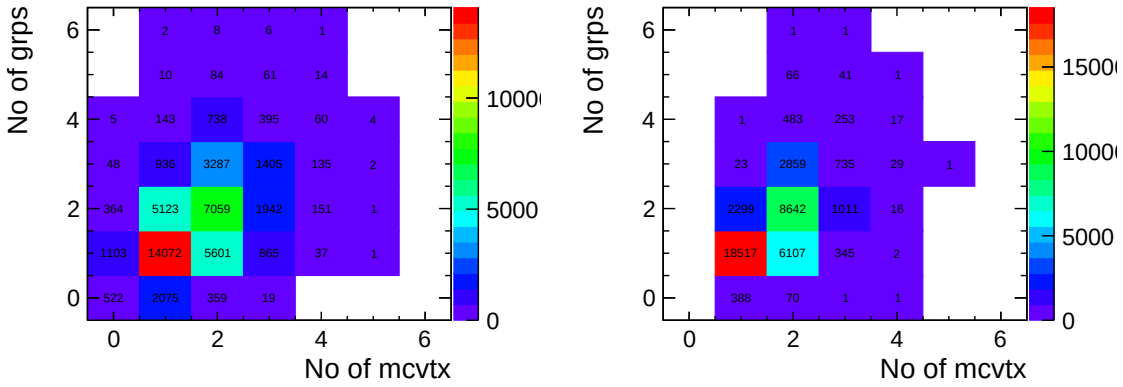

(a) (b)

Figure A.2.: Comparison of number of true Monte-Carlo vertices with track groups obtained from the algorithm for $\eta = 1.7$. a) dM770 benchmark scenario b) dM1600 benchmark scenario

.

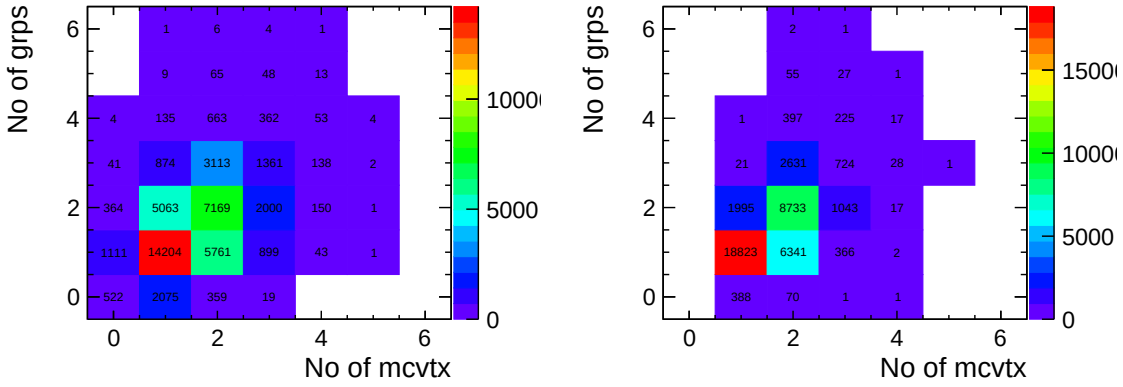

(a) (b)

Figure A.3.: Comparison of number of true Monte-Carlo vertices with track groups obtained from the algorithm for $\eta = 1.8$. a) dM770 benchmark scenario b) dM1600 benchmark scenario

.

B. Fits performed on different $\sqrt{s'}$ ranges

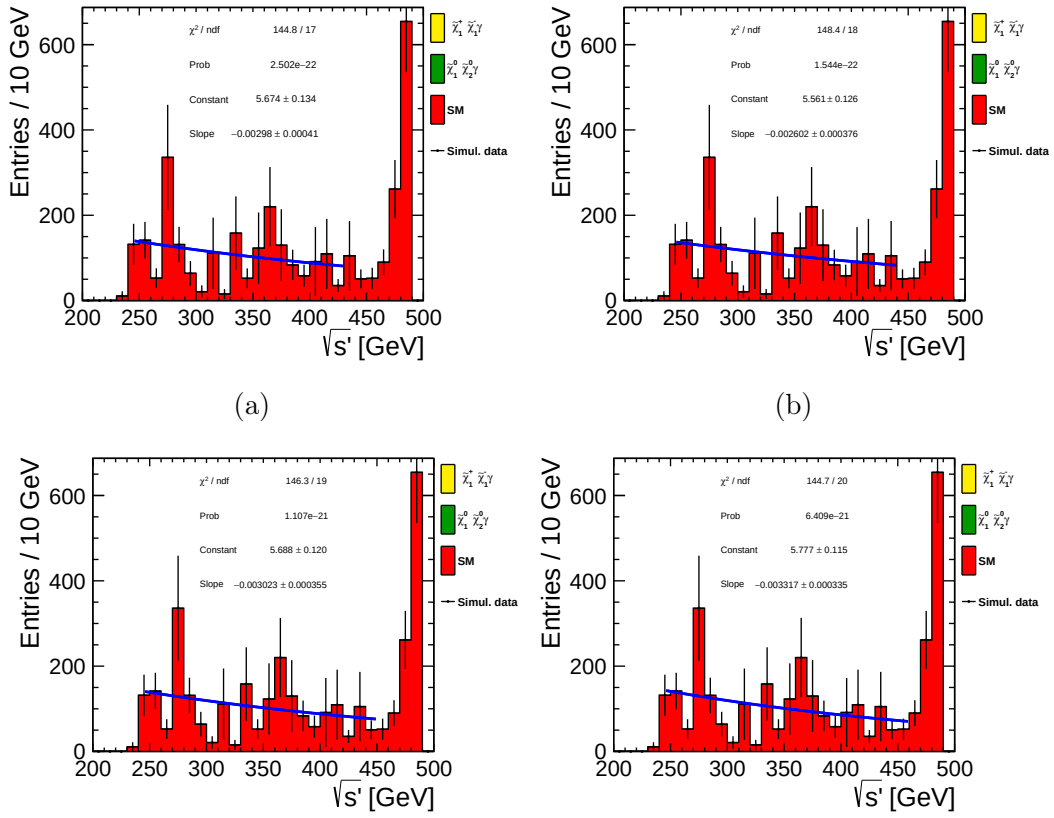

Figure B.1.: Fits performed on the $\sqrt{s'}$ distribution of the Standard Model background events for different ranges at $\sqrt{s} = 500$ GeV and $\int \mathcal{L} dt = 500$ fb^{-1} with $P(e^+, e^-) = (+30\%, -80\%)$ for dM1600. (a) $\sqrt{s'} = 245$ - 430 GeV. (b) $\sqrt{s'} = 245$ - 440 GeV. (c) $\sqrt{s'} = 245$ - 450 GeV. (d) $\sqrt{s'} = 245$ - 460 GeV.

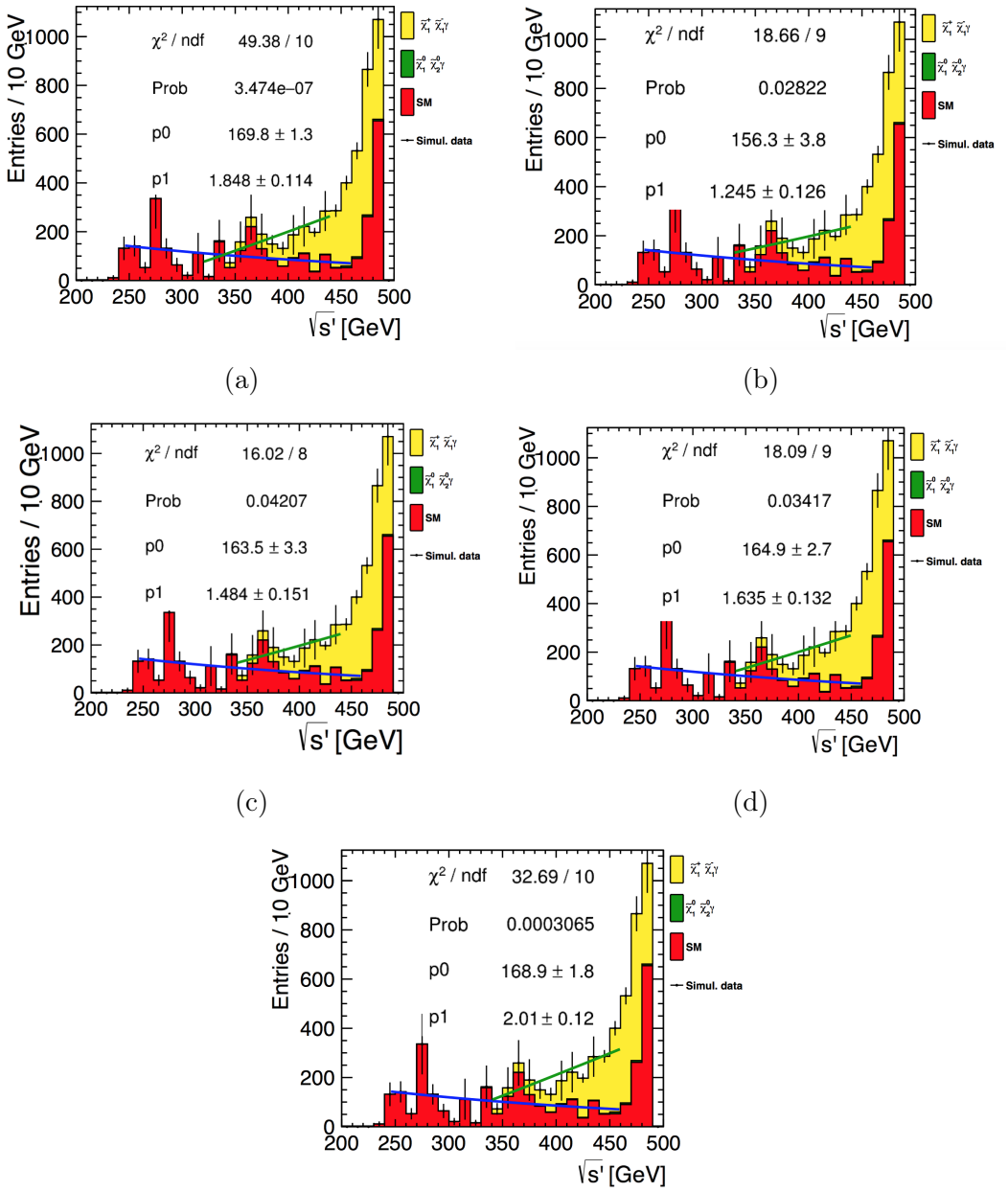

Figure B.2.: Fits performed on the $\sqrt{s'}$ distribution for the entire data for different ranges at $\sqrt{s} = 500$ GeV and $\int \mathcal{L}dt = 500$ fb^{-1} with $P(e^+, e^-) = (+30\%, -80\%)$ for dM1600.

List of Figures

List of Tables

Acknowledgements

Every Ph.D is a legend in itself and nobody has walked this journey alone. I too have my guardian angels and superheroes without whom this journey wouldn't have been possible. People who became the wind in my sail and the stars at night to show direction every time I felt lost in darkness. At this moment when I have crossed this ocean and stand on the other side, I would like to thank them all from the very bottom of my heart.

First and foremost I would like to extend my deepest gratitude to my supervisor Dr. Jenny List. Thank you for giving me this wonderful opportunity of doing a Ph.D with you. You have been such an amazing supervisor and I have grown so much as a scientist under your guidance. You have been a huge support not only in my project and my studies but also in my difficult personal life situations. Thank you very much for all your advices, for the extreme patience that you held for me and for that every extra mile you went to help me in my endeavers.

Another important person without whom this project would have not been the same is Dr. Mikael Berggren. Thank you very much Mikael for helping me understand the basic concepts, for giving me ideas to deal with the difficult parts of my project and for having your doors open for all the naive questions that I had. I am grateful to Dr. Tim Barklow for his contributions in the generator studies and for always being avalaible for the questions that I had. I am also very thankful to Dr. Frank Gaede for his inputs, advices and encouragements. Discussions with you always gave me a new perspective on that particular subject.

I would like to thank Prof. Gudrid Moortgat-Pick who is my second supervisor and my mentors Dr. Katja Krüger and Dr. Isabell Melzer-Pellmann for their support and advices in my project. I will always be grateful to Dr. Ties Behnke who gave me an opportunity to do a Ph.D in this group and for the ever encouraging attitude he held. I would also like to thank Dr. Karsten Büßer who was always willing to help me with the accelerator and machine related questions.

My deepest gratitude goes to my dear friend Dr. Hale Sert for helping me to take forward the research she started and for the huge support she had extended towards completion of my thesis. I will always remember how you were available on the other side of the Skype to answer my questions, particularly in the last stage, without even caring how late it was at night. Another person who I will be ever grateful to have both in my scientific as well as personal life is my beloved friend Dr. Madalina Chera. You taught me how to simplify complicated things, may it be a scientific theory or a life situation, and then to deal with it. Thank you for your unwavering love, support and care throughout the time. I would like to thank my officemate and my dear friend Jakob Beyer, the biggest witness to most of my stupidities (:D), for his huge support and encouragement in my scientific endeavers

and personal life especially in the last moments of panic of finalizing my thesis. It was a privilege to share an office with a brilliant mind like you. I am also very thankful to Dr. Rémi Eté, my partner in crime, for always cheering for me and largely for helping me with my Track Grouping Algorithm studies. Thank you very much for always being there and for the non-negotiable bars I received for every bug in my code which I came up with to your office door. I would also like to thank my dear friend Dr. Suvi-Leena Lehtinen whose scientific inputs, advises and constant support both in my career and in personal life helped me largely. I am also sending my gratitude to Dr. Moritz Habermehl for his ever encouraging attitude, for his valuable advises and mainly for helping me translate my abstract to german. I will also be ever grateful to Dr. Armando Bermudez Martínez who taught me the theoretical concepts of particle physics. It wouldn't have been easier without your help. I also want to thank Dr. Eldwan Brianne for motivating me, for the scientific advices and for constantly checking on the status of my thesis.

My special thanks goes to Dr. Yan Wang, Dr. Shin-Ichi Kawada, Dr. Shaujun Lu, Dr.Georgios Voutsinas, Paul Malek, Ulrich Einhaus, Dr. Maria Teresa Nunez Pardo de Vera, and Yasser Radkhorrami for their scientific inputs in my projects. I would also like to thank Dr. Ambra Provenza, Olin Pinto, Daniel Heuchel, Vladimir Bocharnikov, Dr. Engin Eren and Malinda De Silva for creating a joyful and fun filled environment during the stressful times of my Ph.D. Moreover, I would also want to thank Andrea Schrader our group secretary for all her help.

I would like to thank my professors at my home university, Prof. Dr. Manju Thankamoni, Prof. Malini Jayram, Prof. Vinod G and all my other teachers for constantly inspiring the younger generation. Thank you for motivating me and for believing in me. This thesis is dedicated to you.

Beyond my friends within the group, the presence of my Indian friends always made me feel at home. I would like to thank my dear friends Dr. Krishna Murari Agarwal, Dr. Rudrakant Sollapur, Dr. Jhilik Majumdar, Murali Krishna, Akshay Bankar, Chitra Nanaware, Dr. Sreevidya Thekkuveedu, Haritha Retnakaran, Dr. Mahesh Namboothiri and Meghnad Kayanatil for being there for me. I would specially like to mention Pragya Chopra whose constant efforts to keep me positive one or the other way always pushed me for better things. Thank you Pragya for all that love and care you showered on me. I would also like to thank my beloved friends back home in India. Thank you Rajeev eta, Rahul Ramesh, Sreedevi P. D, Parvathy Menon, Jasira Siraj and Sirajuddin.

Not always the inspiration to hold on comes from the real people in your life. Sometimes the fictional characters can have their fair shares too. I will always be grateful to Po, Tigress and Master Oogway from the Kung Fu Panda, Xiao Dre and Mr. Han from the Karate Kid and Captain Jack sparrow for always filling me up with a new strength.

Finally I would like to thank the inevitable characters of my life, my dearest beings on this planet. I would like to thank my best friend Dr. Mariyam Fatima for all that she has been for me. Your unfaltering love, immense support and care in my Ph.D life and in some of the biggest crises in my life will always make me ever grateful to you. I would also like to thank Aritra Mukhopadhyay, my Kung Fu Panda, for always giving that feeling of I have got your back. I am immensely grateful to have you both in my life. Thank

you for taking this one hell of a roller coaster ride with me. My deepest gratitude goes to Anoop Pullarkat for being one of the most beautiful human beings in my life. I will be ever indebted for the support that you gave in every phase of my life and for all the sacrifices that you bore to see me achieve this dream of mine. I will always be grateful to Dr. Pankaj Mishra for the endless love, for always believing in me, for the ever abiding support and for holding on when it was too difficult to.

I thank my aunt Shyji, uncle Manilal and my grandmother for their love and support. I am very thankful to my sister, Maneesha, who took the role of a mother and a best friend at the same time supporting in the most challenging times of my thesis. I am also ever grateful to my little brother, Balamurali, who always made me realize my strength. Above all, I bow down before the unconditional love, care and support that my parents bestowed upon me . Thank you Amma (Mom) and Achan (Dad) for being a part of this wonderful journey, for bearing all my tantrums in difficult times and for all those sacrifices you made so that such a day would dawn upon me.

Finally, I would like to thank my spiritual master Sadhguru Jaggi Vasudev whose self-transforming meditative tools always helped to be joyful and composed from within especially during the most challenging phases of my Ph.D.

Eidesstattliche Versicherung

Hiermit erkläre ich an Eides statt, dass ich die vorliegende Dissertationsschrift selbst verfasst und keine anderen als die angegebenen Quellen und Hilfsmittel benutzt habe.

I hereby declare, on oath, that I have written the present dissertation by my own and have not used other than the acknowledged resources and aids.

Kollassery Swathi Sasikumar

Hamburg, August 2020